STUDIES OF THE PETROLOGIC AND GEOCHEMICAL DIVERSITY OF THE LUNAR REGOLITH

by

Joshua Francis Snape

A thesis submitted to University College London (UCL)
for the degree of Doctor of Philosophy (PhD)

I, Joshua Francis Snape confirm that the work presented in this thesis is my own. Where information has been derived from other sources, I confirm that this has been indicated in the thesis.

Abstract

This study comprises petrologic investigations of the lunar meteorite Northeast Africa (NEA) 001 and 16 fragments from the Apollo 12 soil 12003. These samples are examples of the variety of materials found in lunar feldspathic highland and mare regoliths, and provide insights into the petrogenesis of different lithologies and regolith mixing processes. They have been analysed by electron microprobe and laser ablation inductively coupled plasma mass spectrometry.

NEA 001 is a feldspathic regolith breccia containing clasts of multiple lithologies including; feldspathic impact melt, ferroan noritic anorthosite, magnesian feldspathic clasts and low-Ti and very-low-Ti (VLT) basalts. Feldspathic impact lithologies in NEA 001 are more mafic than estimations for the composition of the upper feldspathic lunar crust, indicating that they have incorporated more mafic lower crustal material. The VLT basalt clasts have low incompatible trace elements (ITE) concentrations, and may represent products of primitive basaltic volcanism. The feldspathic nature of the sample, low-ITE concentrations, and the presence of magnesian feldspathic clasts suggest that the meteorite has been sourced from the Outer-Feldspathic Highlands Terrane, probably on the lunar farside.

Apollo 12 landed in the eastern region of Oceanus Procellarum. Previous studies of Apollo 12 samples identified three major basaltic suites (olivine, ilmenite and pigeonite basalts) local to the region. Examples of all three of these have been identified within the 12003 soil collected near the Lunar Module. Two samples are identified as possibly representing a previously unrecognised basaltic suite. One sample is identified as a possible addition to the feldspathic suite; a potential fourth basaltic suite currently consisting of only one other sample. Three non-igneous samples are identified, including two breccias and one impactite. The petrologic analysis of these samples forms part of an ongoing basaltic diversity study which will also include radioisotope dating of these and other Apollo 12 soil samples.

Alan Bean - *"It's beautiful out there."*

Pete Conrad - *"It's a nice place to land."*

Alan Bean - *"Those rocks have been waiting* $4\frac{1}{2}$ *billion years for us to come grab them."*

Pete Conrad - *"Think so, huh?"*

Alan Bean - *"Let's go grab a few."*

(Conversations between Apollo 12 astronauts, Charles "Pete" Conrad and Alan Bean, after landing in the Oceanus Procellarum and before their first extra-vehicular activities.)

Acknowledgements

This thesis would not have been possible without the support of a number of people. Firstly, Dr Ian Crawford has been a fantastically enthusiastic and patient supervisor. I also thank Dr Adrian Jones who has contributed his extensive petrologic knowledge and experience to this project. My lunar science experience began when Dr Katherine Joy took me under her wing at the end of my undergraduate studies. Since then, she has consistently gone above and beyond the call of duty as an advisor.

A considerable amount of my time on this project has been spent in the electron microprobe and LA-ICP-MS labs at UCL/Birkbeck. This was largely made possible by Dr Andrew Beard and Dr Andrew Carter, who provided valuable and very much appreciated technical assistance. During my studies I was also selected to take part in the NLSI Lunar Exploration intern program at the Lunar and Planetary Institute, as well as the NLSI Field Training and Research Program at Meteor Crater. These were hugely beneficial and enjoyable experiences and I thank Dr David Kring for allowing me to participate in them.

I have been fortunate to be part of an incredibly friendly and (mostly) studious office and extend very sincere thanks to all members of the Centre for Planetary Sciences with whom I have had the pleasure of working alongside. I am particularly grateful to Dr. Peter Grindrod who has always been willing to provide advice, especially when it comes to making aesthetically pleasing figures. It would also be remiss of me not to acknowledge my fellow "lunatics", Louise Alexander and Shoshana Weider, for many fruitful discussions and generally sharing a love of the Moon.

Most importantly, I thank my family for all the support they have provided throughout this process. Andy, for looking after his little brother while we were both living in London, and Matt, for always expressing an interest in what I was doing. Finally, I thank my parents who have been so important in bringing this project to fruition. They have both been a constant source of guidance; from encouraging me to develop an inquisitive and scientific mind at an early age to being such good and supportive company during the thesis writing process.

Contents

1 Introduction **14**

1.1 Lunar exploration 14

1.1.1 Lunar samples 15

1.1.2 Remote sensing datasets 16

1.2 An overview of lunar geology 17

1.2.1 Lunar mineralogy 18

1.2.2 Origin of the Moon 18

1.2.3 Lunar Magma Ocean 20

1.2.4 Non-mare igneous rocks 20

1.2.5 Lunar volatiles 25

1.3 Mare volcanism 25

1.3.1 Mare basalts 26

1.3.2 Pyroclastic volcanics 27

1.3.3 Cryptomare 28

1.3.4 Generation of mare basalts 30

1.4 The lunar regolith 32

1.4.1 Properties of the lunar soil 33

1.4.2 Regolith mixing processes 35

1.4.3 Regolith breccias 36

1.5 Aims of this project 36

2 Analytical Methods **38**

2.1 Samples 38

2.2 Sample Preparation 39

2.2.1 Lunar Meteorite NEA 001 39

2.2.2 Apollo 12 Fines 39

2.3 Electron Microprobe - Energy Dispersive Spectroscopy 42

2.3.1 BSE Imaging, elemental mapping and modal mineralogy 42

2.3.2 Bulk-sample major element chemistry 43
2.4 Electron Microprobe - Wavelength Dispersive Spectroscopy 46
2.5 Laser Ablation Inductively Coupled Plasma Mass Spectrometry 49

3 Lunar Meteorite Northeast Africa 001 55
3.1 Introduction 55
3.2 Results 56
3.2.1 Petrography and clast inventory 56
3.3 Discussion 74
3.3.1 Similarities to other lunar meteorites 75
3.3.2 Composition of impact melts and impact melt breccias: implications for composition of the lunar feldspathic crust 76
3.3.3 Source and petrogenesis of basalt in NEA 001 77
3.3.4 NEA 001 source region 83
3.4 Summary 85

4 Apollo 12 87
4.1 Mission overview 87
4.2 Apollo 12 samples 89
4.2.1 Mare basalts 89
4.2.2 Non-igneous rocks 99
4.3 Basaltic diversity study 100

5 Apollo 12 Calibration Samples 103
5.1 Introduction 103
5.2 Sample descriptions 103
5.3 Discussion 110

6 12003,308 113
6.1 Introduction 113
6.2 Results 113
6.2.1 Petrography and mineral chemistry 118
6.3 Discussion 133
6.3.1 Igneous samples 133
6.3.2 Non-igneous samples 146
6.4 Summary 147

7 12003 Chips **160**

7.1 Introduction . . . 160
7.2 Results . . . 160
7.2.1 12003,310 . . . 160
7.2.2 12003,311 . . . 170
7.2.3 12003,312 . . . 170
7.2.4 12003,314 . . . 175
7.2.5 12003,316 . . . 177
7.2.6 12003,317 . . . 179
7.3 Discussion . . . 180
7.3.1 Crystallisation history and equilibrium parent magma composition 180
7.3.2 Intersample comparisons . . . 187
7.3.3 Comparison with other Apollo 12 basalts . . . 190
7.4 Summary . . . 194

8 Summary **208**

8.1 Lunar meteorite Northeast Africa 001 . . . 208
8.2 Apollo 12 basaltic diversity . . . 209
8.3 Ongoing and future Work . . . 210

Electronic Appendix

A EDS bulk compositions - host phase density correction details
B NEA 001 - EMPA and LA-ICP-MS analyses
C 12003,308 - WDS analyses
D 12003,308 - LA-ICP-MS analyses
E 12003 chips - WDS analyses
F 12003 chips - LA-ICP-MS analyses

List of Tables

1.1 Average modal mineralogies of mare basalts 28

2.1 Sample inventory table 40
2.2 WDS settings 48

3.1 NEA 001 clast inventory table 58
3.2 Major, minor and trace element concentrations in NEA 001 clasts . . . 59
3.3 NEA 001 representative mineral chemistry 64

5.1 Modal mineralogies of Apollo 12 calibration samples 105
5.2 Bulk chemistries of Apollo 12 calibration samples 111

6.1 12003,308 - modal mineralogies 118
6.2 12003,308 - bulk chemistries 119
6.3 12003,308 - summary 147
6.4 12003,308 - representative pyroxene chemistries 148
6.5 12003,308 - representative plagioclase chemistries 152
6.6 12003,308 - representative olivine chemistries 154
6.7 12003,308 - representative ilmenite chemistries 156
6.8 12003,308 - representative spinel chemistries 157
6.9 12003,308 - miscellaneous silicate chemistries 158
6.10 12003,308 - representative phosphate mineral chemistries 158
6.11 12003,308 - representative metal and sulfide chemistries 159

7.1 12003 chips - modal mineralogies 161
7.2 12003 chips - bulk chemistries 162
7.3 12003 chips - summary 194
7.4 12003 chips - representative pyroxene chemistries 195
7.5 12003 chips - representative plagioclase chemistries 200
7.6 12003 chips - representative olivine chemistries 202

7.7 12003 chips - representative ilmenite chemistries 204
7.8 12003 chips - representative spinel chemistries 205
7.9 12003 chips - miscellaneous silicate phase chemistries 206
7.10 12003 chips - representative metal and sulfide chemistries 207

List of Figures

1.1 Locations of sample return mission landing sites 16
1.2 Maps of the lunar terranes 19
1.3 Lunar magma ocean cumulates 21
1.4 Mare basalt classification 27
1.5 Mare basalt textures 29
1.6 Dark-haloed craters 30
1.7 Idealised cross-section of the megaregolith 33
1.8 Optical, scanning electron and X-ray microscope images of an agglutinate particle 34

2.1 Image of the lunar meteorite NEA001 38
2.2 Photographs of 12003 regolith samples 39
2.3 Diagrammatic illustration of false colour element map generation 43
2.4 Illustration of technique for estimating modal mineralogy 44
2.5 Back scattered electron image illustrating raster beam analysis area scan technique 45
2.6 EDS measurements of the USGS BCR-2 basaltic glass standard 46
2.7 WDS measurements of the USGS BCR-2 basaltic glass standard 50
2.8 Back scattered and secondary electron images illustrating laser ablation inductively coupled plasma mass spectroscopy sampling 51
2.9 LA-ICP-MS measurements of the NIST SRM 612 glass reference material 53
2.10 LA-ICP-MS measurements of the NIST SRM 610 glass reference material 54

3.1 Photographs of NEA 001 hand samples 56
3.2 Back scatter electron and false colour element map of NEA 001 57
3.3 Mineral compositions of phases in NEA 001 clasts and matrix mineral grains 65
3.4 Back scatter electron image and false colour element map of clasts B1a and B1b 66

3.5 Back scatter electron images of NEA 001 basalt clasts 67
3.6 Chondrite normalised average concentrations of REE in NEA 001 clasts 69
3.7 NEA 001 bulk clast compositions 70
3.8 Ti# vs Fe# for pyroxene phases within basaltic clasts of NEA 001 . . . 71
3.9 Back scatter electron images of NEA 001 impact textures and feldspathic clasts 72
3.10 Mg# for pyroxene and olivine versus An# of plagioclase grains in Ferroan Noritic Anorthosite clasts and magnesian feldspathic clasts of NEA 001 74
3.11 TiO_2 (wt%) vs. Mg# for bulk clast compositions within NEA 001 . . . 78
3.12 Fe/Mn (atomic) for pyroxene and olivine phases vs. An# of plagioclase phases within NEA 001 basaltic clasts 79
3.13 Predicted crystallisation sequences for two basalt clasts in NEA 001 . . 83

4.1 Ages of mare basalts on the lunar nearside 88
4.2 Apollo 12 landing site map 90
4.3 Apollo 12 basalts - bulk Mg# vs Rb/Sr 93
4.4 Spatial distribution of Apollo 12 basalts 94
4.5 Cross-section of Apollo 12 site 95
4.6 Ages of Apollo 12 basalts 98
4.7 Components of the Apollo 12 regolith 101

5.1 BSE and element maps of 12022,304_C 104
5.2 BSE and element maps of 12038,263_A 107
5.3 BSE and element maps of 12063,330_A 109
5.4 Calibration sample modal mineralogies 110

6.1 BSE images and element maps of samples 12003,308_1-3A 114
6.2 BSE images and element maps of samples 12003,308_4-6A 115
6.3 BSE images and element maps of samples 12003,308_7-8A 116
6.4 BSE images and element maps of samples 12003,308_9-10A 117
6.5 Compositions of pyroxene phases within samples 12003,308_1-10A . . . 120
6.6 Pyroxene REE abundances in 12003,308 groups 1 and 2 121
6.7 Compositions of olivine and plagioclase phases within samples 12003,308_1-10A 122
6.8 Plagioclase REE abundances in 12003,308 groups 1 and 2 123
6.9 Compositions of spinel phases within samples 12003,308_1-10A 124
6.10 Compositions of pyroxene phases within samples 12003,308_1-10A . . . 126

6.11 Compositions of pyroxene phases within 12003,308 samples 127
6.12 Compositions of olivine phases within samples 12003,308_2-8A 129
6.13 Pyroxene REE abundances in 12003,308 groups 3 and 4 130
6.14 Plagioclase REE abundances in 12003,308 groups 3 and 4 131
6.15 Pyroxene REE abundances in non-igneous 12003,308 samples 134
6.16 Plagioclase REE abundances in non-igneous 12003,308 samples 135
6.17 12003,308 parent melt compositions 136
6.18 Ti/V ratios in 12003,308 mafic phases 138
6.19 12003,308 bulk compositions 142

7.1 BSE images and element maps of 12003 chips 163
7.2 BSE images and element maps of 12003 chips 164
7.3 Compositions of pyroxene phases within 12003 chips 165
7.4 Pyroxene REE abundances in 12003,310_1C;,311_1C;,312_C 166
7.5 Compositions of olivine and plagioclase phases within 12003 chips . . . 167
7.6 Plagioclase REE abundances in 12003,310_1C;,311_1C;,314_D 168
7.7 Compositions of spinel phases within the 12003 chips 169
7.8 BSE images and element maps of 12003 chips 171
7.9 BSE images of lamellae in 12003,311_1C 172
7.10 Compositions of pyroxene phases within the 12003 chips 173
7.11 Compositions of pyroxene phases within the 12003 chips 174
7.12 BSE images and element maps of 12003 chips 176
7.13 Pyroxene REE abundances in 12003,314_D;,316_C;,317_D 177
7.14 Plagioclase REE abundances in 12003,316_C;,317_D 178
7.15 Compositions of olivine phases within 12003 chips 181
7.16 12003 chips parent melt compositions 183
7.17 12003 chips bulk compositions 188
7.18 Ti/V ratios in mafic phases of the 12003 chips 189

8.1 Apollo 12 sample locations 212

Chapter 1

Introduction

1.1 Lunar exploration

The 20^{th} century saw a fundamental change in the way humans study the universe beyond the Earth's atmosphere. When the V-2 rocket became the first human-made object in space in 1942, it ushered in a new era for human space exploration. Over the following two decades a number of important milestones were reached. Amongst these were: the launch of the first scientific research flight and acquisition of the first pictures of Earth from space in 1946 by the United States, using a modified V-2 rocket; the launch of the first artificial satellite (Sputnik 1) by the USSR in 1957; and the first manned and orbital space flight by Yuri Gagarin in 1961.

A series of flyby and impacting missions (including the USSR Luna and Zond programs, and the US Ranger program) between 1959 and 1965 signalled the beginning of modern lunar exploration. In January 1966 the Luna 9 mission achieved the first successful soft landing on the Moon. This was followed by the first lunar orbital mission (Luna 10) in March of that year, and then by the US Surveyor 1 lander and Lunar Orbiter 1 mission. By this point, the Space Race between the Soviet Union and the United States was in full swing and, spurred on by the political climate, the progress towards a manned landing on the Moon was rapid. In 1968 the Apollo 8 mission achieved the first manned orbit of the Moon, paving the way for the historic Apollo 11 mission less than a year later in July 1969.

The end of the Apollo program in 1972, followed by that of the Luna program in 1976, led to a prolonged period of inactivity in lunar exploration. Although its primary target was not the Moon, the Galileo spacecraft performed two separate flybys in 1990 on its journey towards Jupiter. The next notable missions were the NASA Clementine probe in 1994 and Lunar Prospector mission in 1998, both of which obtained valuable

geochemical information about the Moon from lunar orbit.

With the turn of the 21^{st} century, there has been a renewed interest in the Moon. With the exception of the Japanese Hiten orbiter in 1990, lunar exploration had been dominated by the USSR and the United States up to this point. This changed in 2003 with the launch of the SMART-1 mission by the European Space Agency (ESA). The last five years in particular have seen a marked increase in the number of missions to the Moon, with at least one mission being launched per year. This has included the Japenese Kaguya (SELENE) and Chinese Chang'e 1 orbiters in 2007; the Indian Chandryaan-1 orbiter in 2008; the US Lunar Reconnaissance Orbiter and LCROSS impactor combined mission in 2009; the second Chinese orbiter (Chang'e 2) in 2010; and most recently, the US GRAIL mission which was launched in September 2011.

1.1.1 Lunar samples

Just under 382 kg of geologic samples were returned from the Moon by the six Apollo missions which successfully landed on the surface (Fig. 1.1; *Vaniman et al.* 1991). Each Apollo mission returned a larger mass of samples than the previous mission, beginning with the 22 kg returned by the Apollo 11 astronauts, and increasing to 111 kg from Apollo 17 (*Vaniman et al.*, 1991). A majority (∼70% of the total returned mass) of the samples collected during the Apollo missions were rocks (>10 mm in size), ∼24% of the samples were fines (<10 mm), and ∼5% were cores (*Vaniman et al.*, 1991). A further 0.3 kg were returned by the Luna 16, 20 and 24 missions (Fig. 1.1; *Vaniman et al.* 1991; *Stöffler and Ryder* 2001). As of 2012, the material provided by the Apollo and Luna missions represents the only geologic samples to be returned from targeted locations on the Moon. Prior to the Japanese Hayabusa mission, which sampled a near-Earth asteroid, it was also the only geologic material returned from targeted locations on a planetary surface other than the Earth.

Our knowledge of lunar geological diversity has also been extended by the study of lunar meteorites (*Korotev*, 2005). These rocks were ejected from the Moon by meteoroid impacts and have since landed on the Earth. They provide important new insights into the magmatic history, impact history and evolution of the Moon (*Warren and Kallemeyn*, 1991a,b; *Cohen et al.*, 2000; *Nyquist et al.*, 2006; *Terada et al.*, 2007; *Yamaguchi et al.*, 2010). These meteorites may have potentially sampled the entire range of lunar terranes, but in a random manner (*Warren and Kallemeyn*, 1991a; *Warren*, 1994; *Gallant et al.*, 2009) that makes identification of their source craters difficult to determine (*Korotev*, 2005).

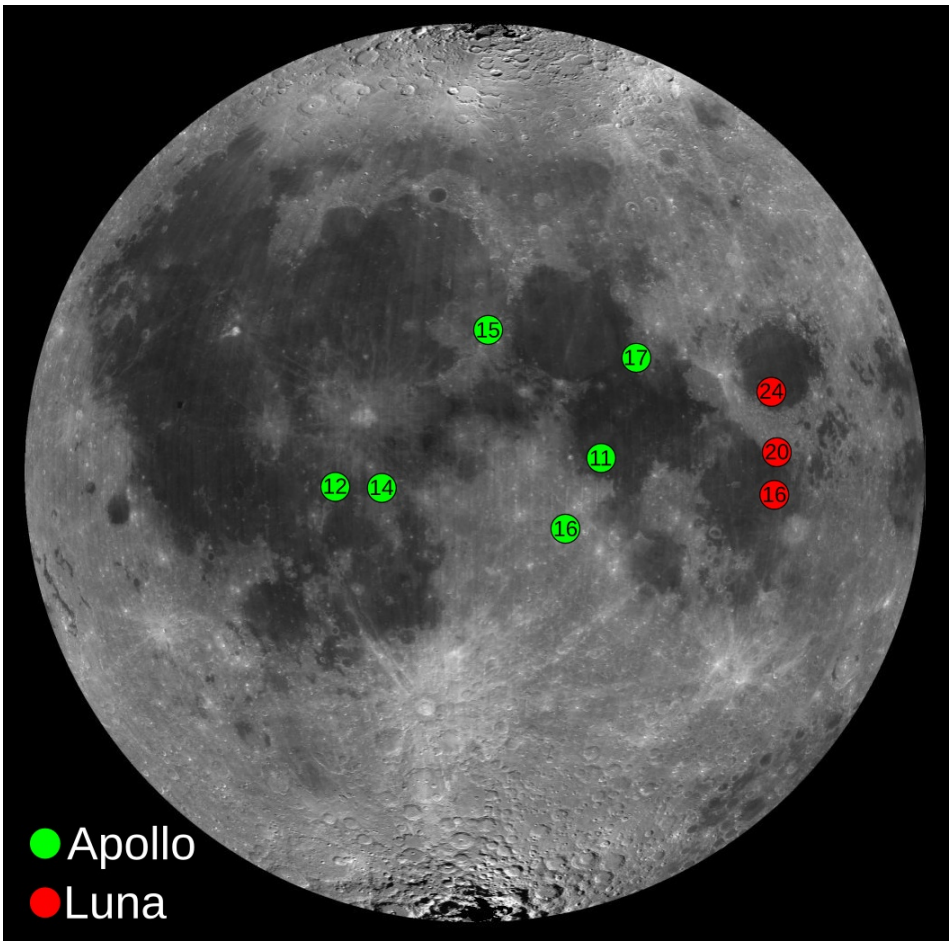

Figure 1.1: Locations of sample return mission landing sites. Background image is a global albedo map from the 750 nm filter of the Clementine UV-VIS camera (NASA/USGS).

The first lunar meteorites to be collected were the Yamato 791197, 793274 and 793169 stones collected in Antarctica in 1979 (*Yanai et al.*, 1984; *Yanai and Kojima*, 1985; *Korotev*, 2005). However, their lunar origin was not recognised at the time, and it was not until 1982 when the meteorite Allan Hills 81005 (ALHA 81005) became the first stone to be identified as a lunar meteorite (*Kallemeyn and Warren*, 1983; *Marvin*, 1983; *Score and Mason*, 1983; *Korotev*, 2005). As of December, 2012, there have been more than 160 individual stones identified as meteorites originating from the Moon (*Korotev*, 2012). Many of these stones may have come from the same parent meteoroid, and analysis of these stones suggests that they could be derived from ∼80 separate meteoroids (*Korotev*, 2012).

1.1.2 Remote sensing datasets

It is unclear when the next human mission to the Moon will occur, or from which country the next person on the Moon will come from. What is clear, from the remote sensing

missions that have flown since the Apollo and Luna programs of the 1960s and 1970s, is that the samples returned by those early forays have barely scratched the surface of lunar geology. Remote sensing data obtained by the Apollo orbital experiments (*Adler et al.*, 1973; *Davis*, 1980), the Galileo spacecraft (*Belton et al.*, 1992; *Pieters et al.*, 1993), Lunar Prospector (*Binder*, 1998; *Lawrence et al.*, 1998; *Jolliff et al.*, 2000; *Prettyman et al.*, 2006), Clementine (*Lucey et al.*, 1998, 2000; *Pieters et al.*, 2001; *Lucey*, 2004), and more recently the Kaguya (*Matsunaga et al.*, 2008), Chandrayaan-1 (*Dhingra et al.*, 2010; *Pieters et al.*, 2010) and Chang'e-1 (*Wu et al.*, 2012; *Yan et al.*, 2012) spacecraft, have revealed that the Moon is far more compositionally diverse than shown by the range of localities visited by the six Apollo and three Luna sample return missions (*Hiesinger and Head*, 2006).

1.2 An overview of lunar geology

Lunar rocks can be considered as comprising of three separate generations of lithologies (*Stöffler and Ryder*, 2001; *Hiesinger and Head*, 2006). The first generation consists of two groups of igneous rocks: (1) the primary lunar crustal rocks, which are interpreted as direct products of the planetary differentiation processes; and (2) volcanic rocks, which erupted on to the surface of the Moon at a later date, and include the basalts which form the distinctive lunar maria. Modification of these first generation lithologies by impact processes led to the second generation of lunar rocks. These include metamorphic rocks such as granulites, as well as impactites such as breccias and impact melts. Continued impact modification of the first and second generation rocks has since led to the production of increasingly lithologically complicated polymict breccias and the "impactoclastic sediment" or regolith which now covers a majority of the Moon's surface (*Stöffler and Ryder* 2001; see Section 1.4).

Despite the process of impact modification, much of the material on the Moon's surface is thought to represent primary crustal rocks formed in the early stages of the geologic evolution of the Moon >4 billion years ago (*Hiesinger and Head*, 2006). This is due to a lack of significant tectonic activity and recycling of crustal material, such as that which occurs of the Earth. As such, the Moon provides a unique opportunity to study the processes of planetary differentiation and crustal formation on terrestrial planets, as well as the impact history of the inner solar system (*Hiesinger and Head*, 2006; *Wieczorek et al.*, 2006).

One of the most immediately obvious aspects of lunar geology is the apparent dichotomy between the nature of the lunar nearside and farside. *Head* (1976) reported

that the lunar mare make up approximately 17% (by area) of the lunar surface and the vast majority of this (16%) is located on the nearside of the Moon. More recent observations including the contribution of buried "cryptomare" deposits (ancient mare which have since been buried by highland ejecta; see Section 1.3) suggest that the mare coverage of the Moon may actually exceed 20% (*Head and Wilson*, 1992; *Antonenko*, 1999).

The Clementine and Lunar Prospector data provided the basis for a more detailed evaluation of the different compositional regions of the Moon, and led to the definition of three major crustal terranes (*Jolliff et al.*, 2000). These include the Procellarum-KREEP Terrane (PKT), the Feldspathic Highlands Terrane (FHT) and the South Pole-Aitken Terrane (SPAT; see Fig. 1.2). The PKT and FHT are interpreted as being products of global-scale differentiation early in the Moon's history (see Section 1.2.3). The SPAT is located on the southern farside, and represents the largest (2000-2500 km) confirmed and most ancient lunar impact basin (*Head et al.*, 1993; *Wieczorek et al.*, 1999). It remains unclear whether the geochemical anomaly associated with the basin is due to the exposure of lunar mantle or lower crustal material (*Pieters et al.*, 1997, 2001; *Lucey*, 2004; *Cahill et al.*, 2009).

1.2.1 Lunar mineralogy

Lunar rocks are dominated by a few key minerals which are, for the most part, common to both terrestrial and lunar geology (*Papike et al.*, 1991). There is, however, a notable absence of hydrous minerals (such as the serpentine, clay and mica phyllosilicate groups) in lunar rocks. The most common minerals in lunar rocks are the silicate minerals: plagioclase feldspar, $(Ca,Na)(Al,Si)_4O_8$; pyroxene, $(Ca,Fe,Mg)_2Si_2O_6$; and olivine, $(Mg,Fe)_2SiO_4$. Also present are the various silica polymorphs (SiO_2; quartz, cristobalite and tridymite) and oxides such as ilmenite $(Fe,Mg)TiO_3$ and spinel. In addition to these, many lunar rocks contain accessory phases including sulfides (in particular troilite, FeS) and phosphate minerals (such as apatite and merrillite).

1.2.2 Origin of the Moon

The most widely accepted theory for the origin of the Moon is that it accreted from the ejecta of a large impact into the proto-Earth towards the end of its accretion (*Hartmann and Davis*, 1975; *Cameron and Ward*, 1976; *Hartmann et al.*, 1986). The size of the impactor involved is a matter of ongoing research, however, a Mars-sized body is commonly stated as being a likely candidate (*Cameron and Ward*, 1976; *Cameron*,

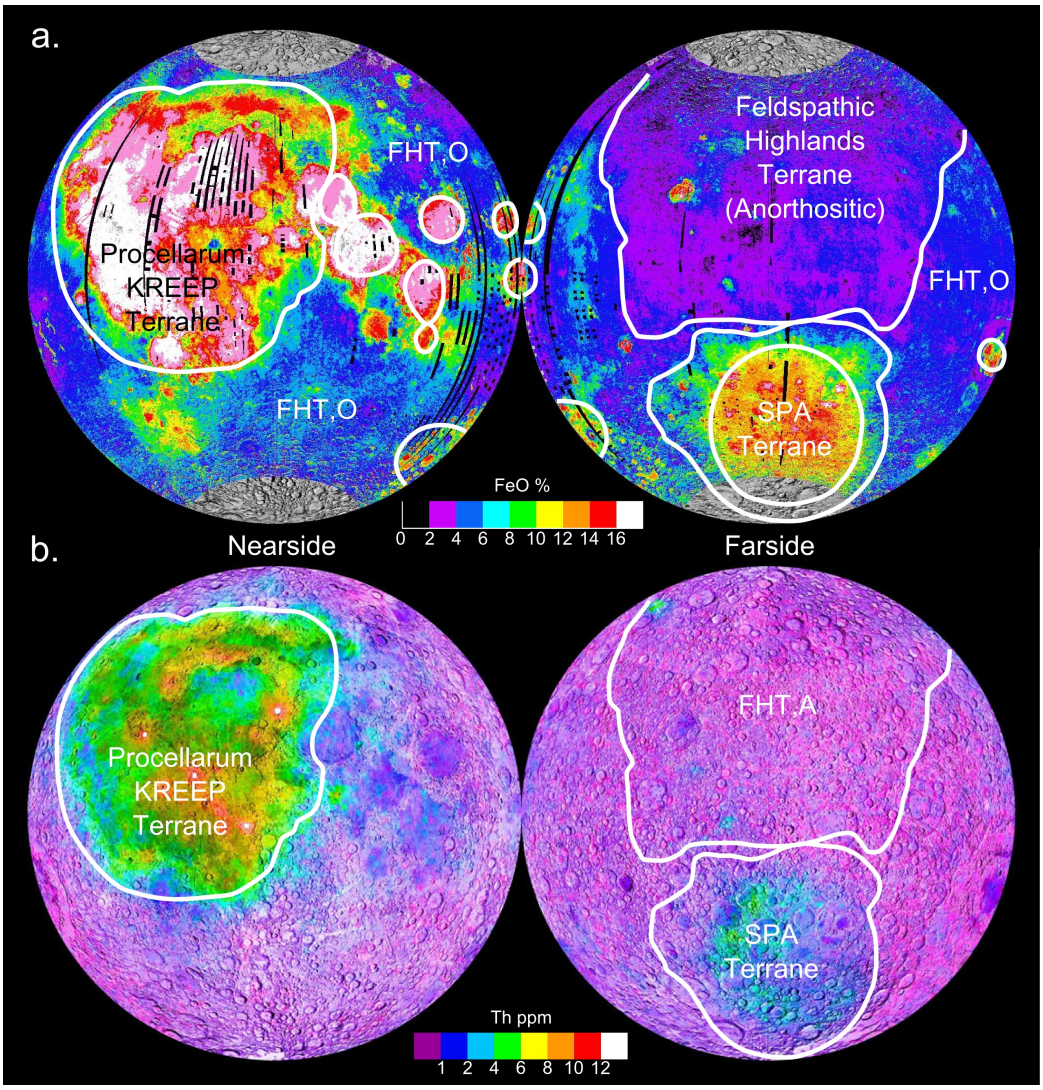

Figure 1.2: Locations of major lunar crustal terranes as proposed by *Jolliff et al.* (2000). The geochemical anomalies associated with the individual terranes are apparent in the (a) Clementine global FeO map (*Lucey et al.*, 2000) and the (b) global Th distribution as mapped by Lunar Prospector (*Gillis et al.*, 2004). FHT,A = anorthositic central region of the feldspathic highlands terrane; FHT,O = outer feldspathic highlands terrane. Reproduced by permission of the American Geophysical Union.

1997; *Canup*, 2004; *Reufer et al.*, 2012). The majority of the resulting ejecta from this collision went into orbit around the Earth, where it rapidly accreted into the early Moon (*Cameron and Benz*, 1991; *Canup and Esposito*, 1996; *Ida et al.*, 1997). Some studies have also raised the possibility that two bodies formed in this accretion process and that the smaller of these later collided with the main body, resulting in the observed dichotomy between the flatter maria dominating the lunar nearside and the more mountainous farside (*Canup et al.*, 1999; *Jutzi and Asphaug*, 2011).

1.2.3 Lunar Magma Ocean

The samples returned in 1969 by the Apollo 11 mission were predominantly basaltic (*LSPET* 1969). However, within those soils were a number of pieces of rock rich in Ca-rich plagioclase feldspar (>96% anorthite by volume). These anorthosites were identified as being material from the lunar highlands, introduced to the Apollo 11 landing site by meteoritic impact processes (*Wood et al.*, 1970a,b). The identification of anorthositic rock fragments led to the proposal of a primary lunar crust formed by the flotation of an anorthositic layer over more dense mafic cumulates in a lunar magma ocean (LMO; *Wood et al.* 1970a).

Shearer and Papike (1999) summarise the likely crystallisation sequence of the LMO as follows: olivine → orthopyroxene ± olivine → olivine + clinopyroxene ± plagioclase → clinopyroxene + plagioclase → clinopyroxene + plagioclase + ilmenite. While plagioclase floated to form the lunar crust, the mafic cumulates sank to form a cumulate pile, with olivine at the base and later forming cumulates towards the top (Fig. 1.3; *Taylor and Jakes* 1974; *Shearer and Papike* 1999). The final dregs of the LMO would have been rich in volatile and incompatible trace elements (ITEs) which are generally excluded from the crystal structures of the major silicate phases (*Taylor and Jakes*, 1974; *Warren*, 1985; *Shearer and Papike*, 1999). These include K, rare earth elements, P ("KREEP"), Th, U, Zr, Hf and Nb (*Meyer et al.*, 1971; *Wasson et al.*, 1977). This material, referred as urKREEP (*Warren and Wasson*, 1979) would then be concentrated below the anorthositic crust and above the mafic cumulates (Fig. 1.3; *Shearer and Papike* 1999).

Numerous studies have been performed in order to improve our understanding of how the LMO evolved and address challenges posed to this model (e.g. *Herbert et al.* 1978; *Shearer and Papike* 1999; *Elkins-Tanton et al.* 2011). One such challenge has been the source of primordial heating which could generate a global magma ocean. Early models of planetary accretion on the time scale of $\sim 10^7$ years do not appear to provide enough heat for such substantial melting (*Wetherill*, 1980). However, more recent models suggest that accretion of the giant impact ejecta may have occurred much more rapidly, possibly even within the space of a year (*Ida et al.*, 1997). As such, the heat source required for the LMO model can now be explained (*Shearer et al.*, 2006).

1.2.4 Non-mare igneous rocks

When discussing lunar lithologies it is convenient to maintain the top-level division between mare volcanic materials (see Section 1.3) and the non-mare igneous rocks.

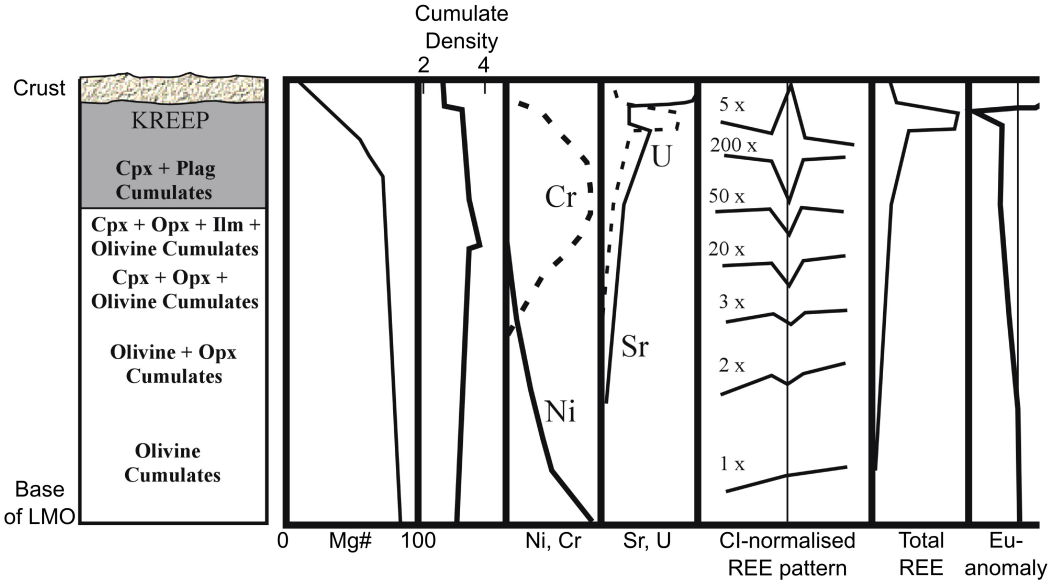

Figure 1.3: Schematic cross-section illustrating the crystallisation products of the LMO and their associated mineral and chemical characteristics (*Taylor*, 1982; *Shearer and Papike*, 1999; *Shearer et al.*, 2006). Reproduced by permission of the Mineralogical Society of America.

In addition to this, it is important to consider the role of impact processes which have reworked the original lunar crust and generated impact lithologies in the form of breccias and impact melt material (*Stöffler et al.* 1979; see also Section 1.4). This is particularly noticeable in the ancient non-mare highland rock suites, for which very few pristine (i.e. rocks unaltered by impact processes) samples have been identified (*Warren and Wasson*, 1977). When examining the issue of pristinity in non-mare rocks, *Warren* (1993) was able to identify 260 possibly pristine samples, however, only 89 of these were deemed to be "confidently pristine". Studies of the returned lunar samples and lunar meteorites have led to the definition of three types of non-mare lunar lithologies: the ferroan anothorsite, magnesian and alkali-rich suites (*Taylor*, 2009).

Ferroan anorthosite (FAN) suite

The anorthosites are compositionally distinct from other pristine non-mare rocks, having a lower Mg# (atomic Mg/[Mg+Fe]; hence them being referred to as "Ferroan") and lower concentrations of most ITEs (*Korotev et al.*, 2003; *Papike et al.*, 1998; *Taylor*, 2009). A majority of the samples are heavily brecciated, concealing the primary igneous textures (*Dowty et al.*, 1974). Where such igneous textures are visible they are characterised by large plagioclase crystals (up to 4 mm in size) surrounded by smaller anhedral pyroxene and olivine (*Lucey et al.*, 2006; *Taylor*, 2009).

Within the FAN suite, four subgroups of rocks are identified on the basis on plagioclase composition and abundance (*Taylor*, 2009). The most abundant rocks are

the ferroan anorthosites, defined by their calcic plagioclase ($An_{>95}$; An = atomic Ca/[Ca+Na+K]). Less common are the sodic anorthosites, which exhibit plagioclase compositions between An_{92-95}. FAN suite rocks with lower modal abundances of plagioclase include the mafic ferroan rocks (>80% plagioclase with $An_{>95}$) and the mafic magnesian rocks (>75% plagioclase with $An_{>95}$). It is currently unclear whether these subgroups are the products of multiple parent magmas or due to the fractionation of the LMO (*Taylor*, 2009). In addition to these four rock groups it has been suggested that magnesian anorthosites, which have higher Mg# than other FAN rocks but similarly low Na/Ca ratios and concentrations of ITEs, are linked with the FAN suite (*Takeda et al.*, 2006).

A further challenge to the LMO model is the wide range of ages (spanning ∼200 Myr) reported for the FAN rocks (e.g. *Nyquist et al.* 2006; *Borg et al.* 2011; *Elkins-Tanton et al.* 2011). A caveat of these ages is the difficulty of dating FAN samples due to their protracted exposure to meteorite impacts, which affects the isotopic systems which are typically employed (*Norman et al.*, 2003; *Meyer et al.*, 2010; *Borg et al.*, 2011). In order to circumvent this problem *Borg et al.* (2011) used multiple isotopic chronometers (including ^{207}Pb-^{206}Pb, ^{147}Sm-^{143}Nd and ^{146}Sm-^{142}Nd) to determine the age of a FAN sample from the Apollo 16 sample collection. Their age of 4.36±0.03 Ga is significantly younger than the modelled age of lunar magma ocean solidification (∼4.51 Ga; *Elkins-Tanton et al.* 2011). One explanation is that tidal heating of the Moon by the Earth (*Touma and Wisdom*, 1998; *Garrick-Bethell et al.*, 2006) may provide a mechanism to slow the solidification of the LMO and also melt and re-erupt portions of the crust (*Meyer et al.*, 2010; *Elkins-Tanton et al.*, 2011).

Magnesian suite

The Magnesian suite (Mg-suite) rocks are characterised by containing mafic silicates with high Mg# between ∼60-95, and coexisting plagioclase with An_{84-98} (*Wieczorek et al.*, 2006). The Mg-suite rocks include plagioclase cumulates (typically 50-65% plagioclase by volume) as well as mafic silicate phases: olivine in the case of troctolites; orthopyroxene in norites; augite and pigeonite in gabbronorites (*James and Flohr*, 1983; *Taylor*, 2009). Olivine-rich (>90% by volume) dunites are also included in the Mg-suite. Isotopic studies of samples in the Mg-suite have provided crystallisation ages of between 4.61±0.07 to 4.17±0.02 Ga (*Nyquist and Shih*, 1992). This has led to the suite being interpreted as representing a transition from magmatism associated with the LMO and post-magma ocean magmatism (*Shearer and Papike*, 1999; *Shearer and Papike*, 2005).

When compared with the FAN suite, the rocks of the Mg-suite are characterised by high Mg# and are enriched in KREEP, although their precise compositional range is not well defined (*Shearer and Papike*, 2005; *Lucey et al.*, 2006; *Wieczorek et al.*, 2006). In addition to this, the apparent restriction of these rocks close to the PKT suggests that KREEP may have played a significant role in the production of the Mg-suite (*Shearer and Papike*, 2005; *Taylor*, 2009). One theory is that low density mafic cumulates with high Mg# rose through the lunar mantle and assimilated KREEP material whilst passing through the urKREEP layer (*James and Flohr*, 1983; *Shearer and Papike*, 2005). An alternative to the assimilation theory is that mantle overturn, resulting from density instabilities in the LMO cumulates (*Hess and Parmentier*, 1995), led to the sinking of the urKREEP material which then mixed with the rising olivine-rich cumulates (*Shearer and Papike*, 1999; *Shearer and Papike*, 2005). The presence of heat-producing elements such as K, Th and U in the KREEP component could then have led to the partial melting and subsequent eruption of the olivine-rich cumulates.

Warren and Wasson (1979) proposed that the urKREEP layer is asymmetrically distributed below the lunar crust. If this is true, then the assimilation theory might predict the existence of farside KREEP-poor, apparently 'pristine', magnesian magmas (*Shearer and Papike*, 2005). Clasts of KREEP-poor magnesian lithologies were identified in the lunar meteorite Dhofar 489 by *Takeda et al.* (2006). As such, *Takeda et al.* have proposed that these clasts do indeed represent farside magnesian lithologies. *Nyquist et al.* (2011) determined an age of 4.36±0.07 Ga for Dhofar 489; within the range of other Mg-suite samples. However, if the Mg-suite volcanism was initiated by mantle overturn and mixing of urKREEP and olivine-rich cumulates, then this form of magmatism would have been restricted to the PKT region (*Shearer and Papike*, 2005).

Alkali suite

Most lunar rocks contain plagioclase that is very calcic (such as that in ferroan anorthosites = $An_{>95}$) and have low bulk rock Na/Ca ratios. The evolved highland rocks or alkali suite rocks are an exception to this trend and contain plagioclase which typically has compositions of $An_{<86}$ (*Warren*, 1993). These include alkali anorthosites, alkali gabbronorites, quartz monzodiorites and felsites (*Warren*, 1993; *Lucey et al.*, 2006). The crystallisation ages determined for the alkali suite rocks (4.37±0.03 to 3.88±0.03 Ga) overlap with those of the Mg-suite and KREEP basalts (*Nyquist and Shih*, 1992; *Shearer and Papike*, 1999).

Another indicative feature of the alkali suite rocks is that they tend to be enriched in incompatible trace elements (*Warren*, 1993; *Shearer and Papike*, 1999). This has been

interpreted as evidence that they may be petrogenetically related to KREEP (*Hubbard et al.*, 1971; *Warren*, 1993; *Shearer and Papike*, 1999; *Shervais and McGee*, 1999; *Lucey et al.*, 2006). Further evidence of this relationship has been identified by isotopic studies reporting similar ratios of $^{147}Sm/^{144}Nd$ between the alkali suite rocks, KREEP basalts and Mg-suite rocks (*Snyder et al.*, 1995; *Shearer et al.*, 2006).

For these reasons, it has been suggested that the alkali suite may be part of a continuum of crystallisation products (including the Mg-suite) of basaltic magmas similar to the KREEP basalts (*Snyder et al.*, 1995; *Shearer and Papike*, 1999; *Shervais and McGee*, 1999). Models by *Snyder et al.* (1995) suggest a possible crystallisation sequence, beginning with an Apollo 15 KREEP basalt composition: Mg-suite (0-43% crystallisation) → alkali anorthosites, alkali norites (43-74% crystallisation) → alkali gabbros, alkali norites (74-90% crystallisation) → quartz monzodiorites (90-99.8% crystallisation). However, this hypothesis conflicts with that of the Mg-suite becoming enriched in KREEP by assimilation in the urKREEP layer. An alternative hypothesis is that the Mg-suite and alkali suite rocks were formed by separate episodes of basaltic magmatism, and that the alkali suite rocks formed from comparatively shallow mantle melts which also assimilated KREEP material (*Shearer and Papike*, 1999).

KREEP basalts

KREEP-bearing materials have been identified in samples from all of the Apollo sites, however, KREEP basalts are most common in the Apollo 15 and Apollo 17 samples (*Hubbard et al.*, 1971; *Wieczorek et al.*, 2006; *Taylor et al.*, 2012). These typically have higher Al and lower Fe concentrations (13-16 wt% Al_2O_3; 9-15 wt% FeO) than most mare basalts (*Taylor et al.*, 1991; *Wieczorek et al.*, 2006). The crystallisation ages determined for the KREEP basalts are between 3.82-4.08 Ga (*Nyquist and Shih*, 1992; *Wieczorek et al.*, 2006; *Shearer et al.*, 2006).

If (as previously discussed) the KREEP basalts were parental to the Mg- and alkali suites, it is hard to reconcile the ages of the KREEP basalts with those of the Mg- and alkali suite samples (*Shearer et al.*, 2006). An independent model for the formation of KREEP basalts is that they are the product of impact-induced volcanism during the Late Heavy Bombardment (LHB) between ∼3.9-4.2 Ga (*Hawke and Head*, 1978; *Nyquist and Shih*, 1992; *Elkins-Tanton et al.*, 2004; *Norman*, 2009; *Taylor et al.*, 2012).

1.2.5 Lunar volatiles

Analysis of the lunar samples has indicated that the Moon is depleted in volatiles relative to the Earth (*LSPET* 1969; *Taylor et al.* 2006; *Taylor et al.* 2006). This is thought to be due to the high temperatures during the energetic formation of the Moon (*Cameron and Benz*, 1991; *Canup and Esposito*, 1996; *Ida et al.*, 1997). However, the concept of a completely dry Moon has been subject to considerable debate in recent years. Several studies have suggested that the lunar interior contains more water than originally thought (*Saal et al.*, 2008; *Boyce et al.*, 2010; *McCubbin et al.*, 2010; *Greenwood et al.*, 2011).

Saal et al. (2008) studied the volatile content within very low-Ti (VLT; <1 wt% TiO_2) and low-Ti basaltic (1-6 wt% TiO_2) volcanic glasses from the Apollo 15 sample suite and high-Ti glasses (>6 wt% TiO_2) collected during the Apollo 17 mission. By modelling the degassing processes during eruption of these glasses *Saal et al.* (2008) were able to estimate that the original water content of the beads would have been between 70-745 ppm. *McCubbin et al.* (2010) attempted to investigate the water budget of the lunar interior by analysing the water content of apatites within a range of lunar samples. Based on the volatile partitioning behaviour in apatites, they were able to calculate the water content within the parental melts from which these samples originated. Conservative estimates based on these calculations suggest that the parental melts from which these samples formed would have had a water content between 64 ppb and 21 ppm (*McCubbin et al.*, 2010). This is significantly more than the <1 ppb estimate of the water content of the bulk Moon provided by *Taylor et al.* (2006).

1.3 Mare volcanism

The most visible volcanic products on the Moon are the mare lavas that infilled the majority of the large impact basins on the nearside of the Moon, covering much of the Procellarum KREEP Terrane (*Jolliff et al.*, 2000). Initial analysis of the Apollo and Luna samples led to the conclusion that the first generation igneous lunar rocks were formed during two distinct periods in lunar geologic history: the formation of the lunar highland rocks (>4.40 Ga), and the eruption of mare basalts (<3.95 Ga; *Taylor* 1982; *Taylor et al.* 1983). This is consistent with the majority of mare basalts returned by the Apollo and Luna missions, which have a range of crystallisation ages between ∼3.8-3.0 Ga (*Grove and Krawczynski*, 2009). However, subsequent studies have identified evidence of significantly older (4.35-3.95 Ga) "mare-type" volcanism, and identified regions of comparatively young (∼1.2 Ga) mare basalts (*Taylor et al.*, 1983; *Schultz*

and Spudis, 1983; *Hiesinger et al.*, 2003; *Terada et al.*, 2007; *Sokol et al.*, 2008).

Taylor et al. (1983) identified a high-Al basalt clast in an Apollo 14 breccia which was found to have a crystallisation age of 4.23±0.05 Ga. In addition to this, studies of similar Apollo 14 and Luna 16 basalts have reported a range of ages between 3.96-4.33 Ga (*Dasch et al.*, 1987; *Neal and Kramer*, 2006), although it remains unclear whether the basalts represent ancient mare basalts, a form of non-mare basaltic magmatism or basaltic impact melts (*Shearer et al.*, 2006). Studies of the basaltic meteorite Kalahari 009 by *Terada et al.* (2007) and *Sokol et al.* (2008) have also provided evidence of ancient volcanic activity (4.35±0.15 Ga and 4.29±0.10 Ga respectively).

The youngest basalt samples identified in the Apollo and Luna samples were collected from the Apollo 12, Apollo 15 and Luna 24 landing sites, and have crystallisation ages of 3.16-3.40 Ga (*Shearer et al.*, 2006). However, a younger crystallisation age (3.12±0.01 Ga) has been determined for the basaltic lunar meteorite Northwest Africa (NWA) 2977 (*Zhang et al.*, 2010). In addition to this, remote sensing studies utilising crater size frequency relationships have identified nearside mare basalt units with estimated ages of ∼1.1-1.2 Ga (*Schultz and Spudis*, 1983; *Hiesinger et al.*, 2003, 2008). If these crater-count model ages are correct, and if the Apollo 14 and Kalahari 009 samples represent true mare basalts, then mare volcanism was active for more than 3.2 Gyr (*Shearer et al.*, 2006).

1.3.1 Mare basalts

The range of compositions seen in lunar mare basalts is larger than that observed in terrestrial basalts, basaltic samples from Mars or other basaltic meteorites (*Shearer et al.*, 2006). The mare basalts are commonly classified according to several specific aspects of their chemical composition (*Neal and Taylor*, 1992). The first basaltic classification is made according to the TiO_2 content of the basalts and identifies three separate groups of mare basalt: very low-Ti (VLT) basalts (<1 wt% TiO_2), low-Ti basalts (1-6 wt% TiO_2) and high-Ti basalts (>6 wt% TiO_2). A secondary classification is defined by the concentration of Al, where <11 wt% Al_2O_3 is considered to be low-Al and >11 wt% Al_2O_3 is considered to be high-Al. Finally, basalts with <2000 ppm of K are considered to be low-K and those with >2000 ppm of K are classified as high-K. This classification scheme, and how it relates to the Apollo and Luna samples, is illustrated in Fig. 1.4.

Although highly variable, the average modal mineralogies of the mare basalts are pyroxene ∼53%, plagioclase ∼31%, opaques ∼10% and olivine ∼6% (Table 1.1; *Papike and Vaniman* 1978a; *Lucey et al.* 2006). Mare basalts also exhibit a wide variety of

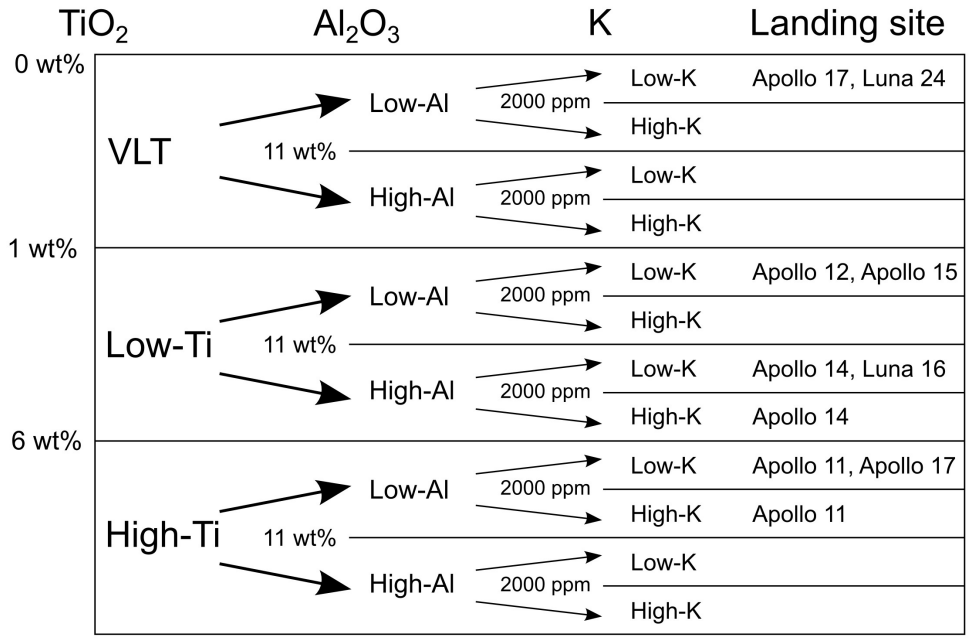

Figure 1.4: Mare basalt classification scheme, as proposed by *Neal and Taylor* (1992). Modified with permission of Elsevier.

textures, from fine-grained vitrophyres to coarse grained ophitic and cumulate textures (Fig. 1.5; *Taylor et al.* 1991). These textural variations are attributed to different cooling rates (*Taylor et al.*, 1991; *Neal and Taylor*, 1992).

1.3.2 Pyroclastic volcanics

Glass beads are a common component in the lunar soil (*Butler*, 1978; *Delano*, 1986; *Lucey et al.*, 2006). Although many of these were formed by impact melting (*Delano and Livi*, 1981), some have been identified as the products of pyroclastic fire fountains (*Butler*, 1978; *Delano*, 1986; *Elkins-Tanton et al.*, 2003). The most well-known examples of these are the Apollo 17 orange glasses discovered by Harrison "Jack" Schmitt (*LSPET* 1973).

The picritic glasses are found to have higher Mg# than most fine-grained mare basalts, indicating that they have undergone less fractionation than most mare basalts (*Delano*, 1986). Individual picritic glasses are noted as being compositionally homogeneous (*Delano*, 1986). This is due to the fact they originate from magmatic reservoirs which were at high temperatures during their ascent through the mantle, allowing them to remain chemically uniform up until eruption, at which point they are rapidly quenched. This is true, with the exception of volatile elements (e.g. S, Na, K and Rb) which are mobilised during eruption (*Delano*, 1986).

Table 1.1: Average modal mineralogies of mare basalts (*Papike and Vaniman*, 1978a; *Lucey et al.*, 2006).

Basalt type	Opaques	Pyroxene	Feldspar	Olivine
A17 high-Ti	24.4	47.7	23.4	4.6
A11 high-K/high-Ti	20.6	57.5	21.7	0.1
A17 low-K/high-Ti	15.1	51.6	33.3	-
A11 low-K/high-Ti	14.6	50.9	32.2	2.3
A12 ilmenite	9.3	61.1	25.9	3.6
A12 pigeonite	9.1	68.4	21.1	1.4
A12 olivine	7.1	53.5	19.2	20.2
A15 olivine-normative	5.5	63.3	24.1	7.0
A15 quartz-normative	3.7	62.5	33.8	-
Luna 16 high-Al	7.1	51.5	41.2	0.1
A14 high-Al	9.0	37.1	43.9	10.0
A14 VHK/high-Al	8.0	33.2	46.8	12.0
Luna 24 VLT	1.8	48.6	39.1	10.4
A17 VLT	1.0	61.7	31.9	5.4

Opaque minerals include ilmenite, spinel, troilite and native FeNi metal

Another key feature, which was identified in the Apollo 15 green and Apollo 17 orange glasses, is the presence of thin coatings of volatile and chalcophile elements (e.g. Zn, Ga, Pb, Cu, Tl, S, F and Cl; *Meyer et al.* 1975). These are interpreted as forming via a process of sublimation and then condensation on the surfaces of the glass droplets (*Butler*, 1978; *Delano*, 1986). *Elkins-Tanton et al.* (2003) suggested that it was the degassing of these volatiles, once the parent melt neared the surface, which drove the fire-fountaining process.

Evidence of pyroclastic materials has also been identified remotely in the form of dark mantle deposits (*Pieters et al.*, 1973; *Heiken et al.*, 1974; *Head*, 1974). For example, *Pieters et al.* (1973, 1974) reported such deposits in the Taurus-Littrow region from which the Apollo 17 orange glasses originated. In addition to their low-albedo, the magnesian nature of the dark mantle deposits is reflected in high Mg/Al ratios relative to surrounding mare regoliths (*Schonfeld and Bielefeld*, 1978). The dark mantle deposits are often located near the edges of the maria and in association with large vents and sinuous rilles (*Hiesinger and Head*, 2006).

1.3.3 Cryptomare

Schultz and Spudis (1979) identified multiple "dark-haloed" craters (Fig. 1.6). These were interpreted as indicators of volcanic units which had been buried by impact ejecta and subsequently exposed by further impacts. *Antonenko* (1999) reviewed all of the known cryptomare deposits and calculated their maximum surface area at $\sim 3.6 \times 10^6$ km^2. This is equal to half the surface area of the previously identified lunar mare, and would amount to $\sim$25% of the Moon's surface being covered by mare basalts. On the

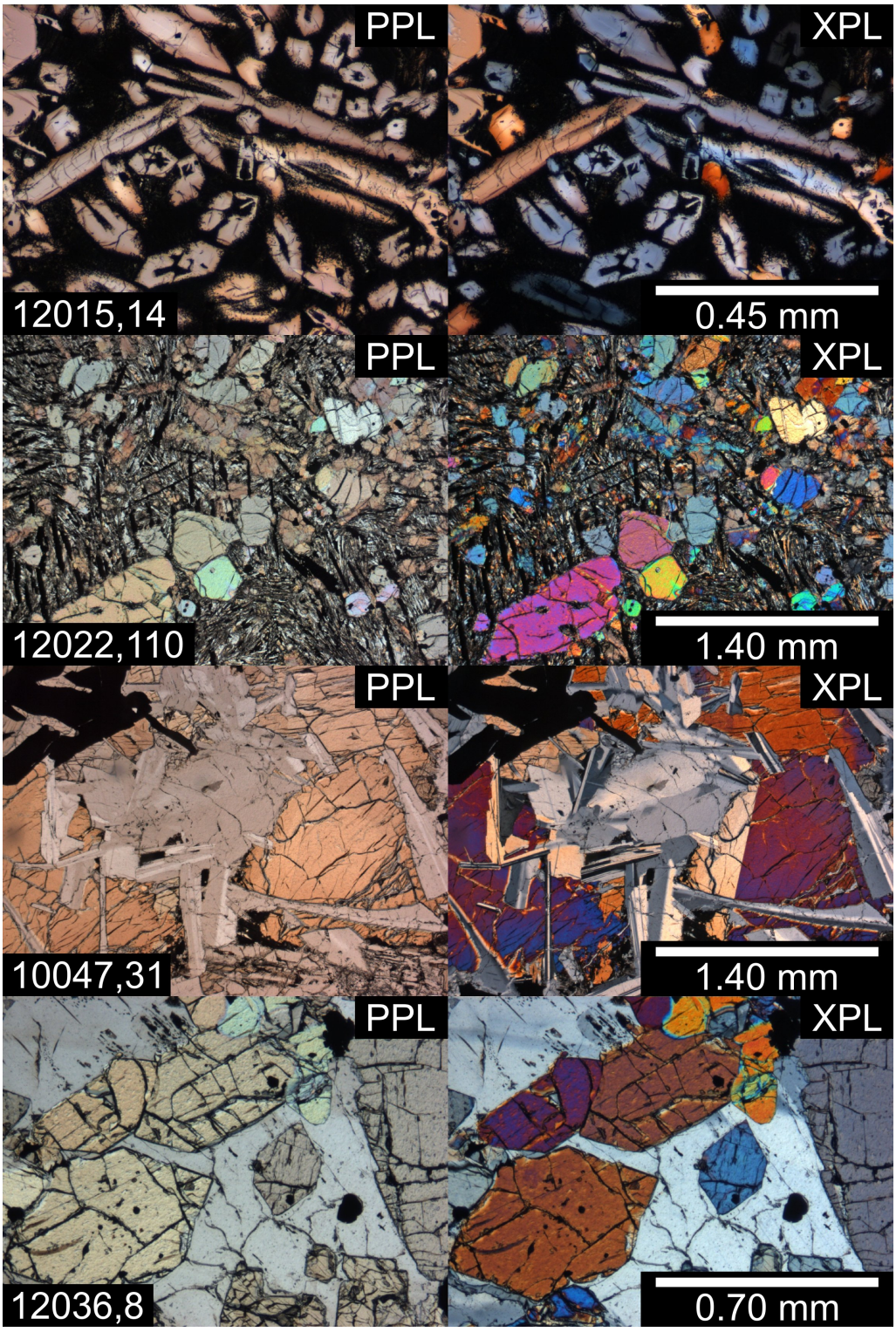

Figure 1.5: Examples of common textures observed in mare basalts viewed in plane (PPL) and cross (XPL) polarised light (images from the Lunar Sample Atlas, LPI-JSC). 12015 is an olivine vitrophyre. The very fine-grained matrix appears to be opaque in thin-section, and is the result of rapid quenching. 12022 has a porphyritic texture, with mafic phenocrysts embedded in a fine-grained matrix. 10047 is a medium-grained subophitic basalt. 12036 has a coarse-grained cumulate texture, due to less-rapid crystallisation.

basis of known stratigraphic relationships, *Antonenko* (1999) also estimated the ages of the cryptomare deposits as being between 3.2-4.1 Ga.

Spectral analysis of dark-haloed craters indicate that cryptomare deposits are of low-Ti to VLT composition (*Giguere et al.*, 2003; *Hawke et al.*, 2005a,b). In a separate study, U-Pb and Lu-Hf dating of the VLT basaltic meteorite Kalahari 009 yielded crystallisation ages of 4.35±0.15 Ga (U-Pb; *Terada et al.* 2007) and 4.29±0.10 Ga (Lu-Hf; *Sokol et al.* 2008). Based on this information, it has been suggested that the VLT basaltic meteorite Kalahari 009 may be a sample of cryptomare basalt, and represent some of the earliest mare volcanism (*Terada et al.*, 2007; *Sokol et al.*, 2008).

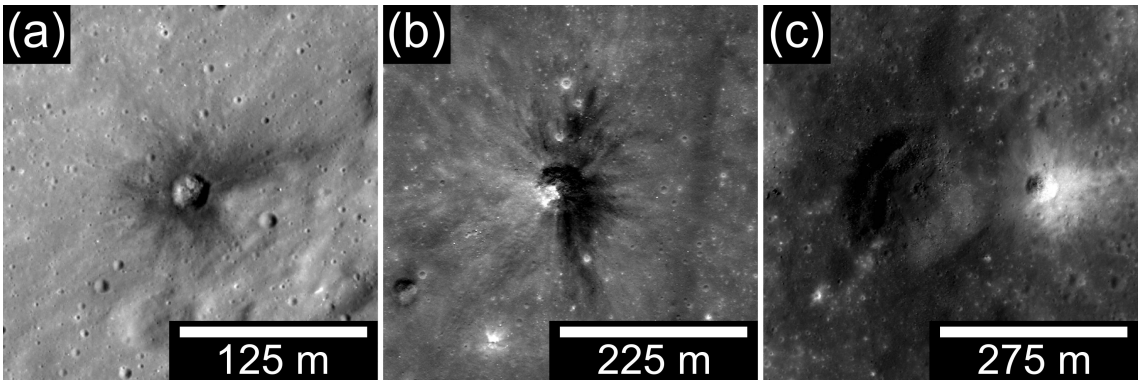

Figure 1.6: Examples of dark-haloed craters, imaged by the Lunar Reconnaissance Orbiter Narrow Angle Camera (LROC NAC; NASA/GSFC/Arizona State University): (a) on the ejecta of the Censorinus A crater (LROC NAC frame M144409490L); (b) in Mare Humorum (LROC NAC frame M140203430R); and (c) in the Orientale basin adjacent to a smaller, bright crater (LROC NAC frame M138188186).

1.3.4 Generation of mare basalts

Terrestrial and martian basalts can be modelled as the crystallisation products of melts derived from mantle sources with relatively uniform compositions. However, the wide Al and Ti variations in the lunar mare basalts implies much more compositionally variable sources (*Grove and Krawczynski*, 2009). Mare basalts are thought to represent the products of partial melting of mafic cumulates which crystallised from the LMO (*Taylor and Jakes*, 1974). The composition of the residual LMO liquid would have evolved as these cumulates formed, which would in turn have led to the compositional evolution of subsequent cumulates. For example, Ti is moderately incompatible in pyroxene and highly incompatible in olivine, and will be more concentrated in late stage ilmenite-bearing cumulates (*Shearer and Papike*, 1999; *Shearer et al.*, 2006). This will result in a stratified cumulate pile with the early low-Ti, Mg-rich cumulates towards the bottom, and more Fe-rich, high-Ti cumulates towards the top (Fig. 1.3; *Shearer and Papike* 1999). Variable compositions of the mare basalts could, therefore, be explained

by the composition of the cumulate phases which were melted as well as the depth, temperature and degree of partial melting (*Taylor and Jakes*, 1974).

With the exception of several VLT basalts collected at the Apollo 17 and Luna 24 sites, and identified in lunar meteorites (Chapter 3; *Laul et al.* 1978; *Ma et al.* 1978; *Warren and Kallemeyn* 1993; *Joy et al.* 2008; *Sokol et al.* 2008; *Liu et al.* 2009; *Snape et al.* 2011a), the mare basalts have REE abundances between ∼10-100 ×CI values (*Anders and Grevesse*, 1989), and Eu abundances which are depleted relative to other REE (*Shearer et al.*, 2006). Due to the reducing conditions of the LMO, Eu was present as Eu^{2+} which can substitute for Ca in plagioclase (*Haskin et al.*, 1970). As such, the negative Eu-anomaly of the mare basalts has been attributed to the fractionation of plagioclase in the LMO to form the lunar crust (*Haskin et al.*, 1970; *Philpotts and Schnetzler*, 1970; *Taylor and Bence*, 1975). Further evidence of this is seen in the results of crystallisation experiments for Apollo 11 and Apollo 12 basalts, which showed that mafic silicate phases (e.g. olivine and pyroxene) are the first to crystallise, while plagioclase only crystallises after significant cooling of the parent melt (*Ringwood and Essene*, 1970; *Green et al.*, 1971). This indicates that plagioclase was not present in the source region from which the Apollo 11 and 12 basaltic parent melts were derived (*Grove and Krawczynski*, 2009).

It is possible to model the high-Ti basalts as products of melts originating from shallow, late-stage cumulates (*Taylor and Jakes*, 1974; *Grove and Krawczynski*, 2009). However, petrologic studies of the high-Ti picritic glasses indicate that they formed from parent melts which originated from greater depths than those of the high-Ti basalts or that are predicted in the LMO model (*Delano*, 1980; *Krawczynski and Grove*, 2008). One explanation for this is the overturn of cumulates in the lunar mantle (*Ringwood and Kesson*, 1976; *Spera*, 1992; *Hess and Parmentier*, 1995). Modelling of mafic cumulates by *Hess and Parmentier* (1995) indicates that the higher density of the shallow late-stage cumulates would result in them sinking through the less dense early mafic cumulates, forming a deep reservoir of Ti-rich cumulates.

A number of theories have arisen to explain the source of heat responsible for generating the parent melts of the mare basalts. For example, a consequence of the cumulate overturn model is the concentration of incompatible heat-producing radioactive elements at the bottom of the lunar mantle (*Ringwood and Kesson*, 1976; *Hess and Parmentier*, 1995). Several external heat sources have also been proposed. *Elkins-Tanton et al.* (2004) presented a model of impact-induced volcanism as a result of the late heavy meteorite bombardment. It has also been suggested that the Moon's orbit may have previously been significantly more eccentric than it is currently, resulting in

tidal heating of the lunar interior (*Touma and Wisdom*, 1998; *Garrick-Bethell et al.*, 2006).

1.4 The lunar regolith

Merrill (1897) first defined the term "regolith" when referring to the fragmental and unconsolidated material that overlies solid bedrock and is generated through the weathering of larger rocks. The Moon is covered by a global layer of regolith, which has been generated by continuous meteoritic bombardment of the lunar crust since its formation (*McKay et al.*, 1991; *Lucey et al.*, 2006). The top regolith layer is believed to form part of a larger 'megaregolith'; a structure which extends beneath the surface of the Moon to ∼25 km (Fig. 1.7; *Hörz et al.* 1991). Below ∼10 km the crustal material is thought to be largely in situ, albeit fractured by impacts. Above this, the megaregolith is composed of chaotically mixed material, from large (>1 m) blocks, to the more fine-grained regolith layer in the top ∼10 m (*Hörz et al.*, 1991; *McKay et al.*, 1991; *Shkuratov and Bondarenko*, 2001). The average thickness of these individual megaregolith layers and the depth to which the lunar crust is disturbed by impacts is not well constrained (*Hiesinger and Head*, 2006). Variations in the thickness of the megaregolith at different locations will be dependent on the age of the underlying bedrock and the distribution of impact craters. For example, *Shkuratov and Bondarenko* (2001) identified an average regolith thickness of 12 m for the highlands and 5 m for the younger mare. A more recent survey, using images from the Lunar Reconnaissance Orbiter Camera, determined slightly lower median regolith depths in mare and non-mare regions (2-4 m and 6-8 m, respectively; *Bart et al.* 2011).

All of the Apollo and Luna samples were collected from the regolith, and all direct measurements and experiments conducted on the Moon were performed on or in the regolith (*McKay et al.*, 1991). Techniques used for remotely sensing the composition of the lunar surface have penetration depths between ∼1 μm for multispectral imaging and 50-100 cm for various neutron spectroscopy measurements (*Lucey et al.*, 2006). Therefore, all remotely sensed data also comes from the regolith. As such, it is important to understand the nature of the lunar regolith and how it relates to the underlying lunar geology.

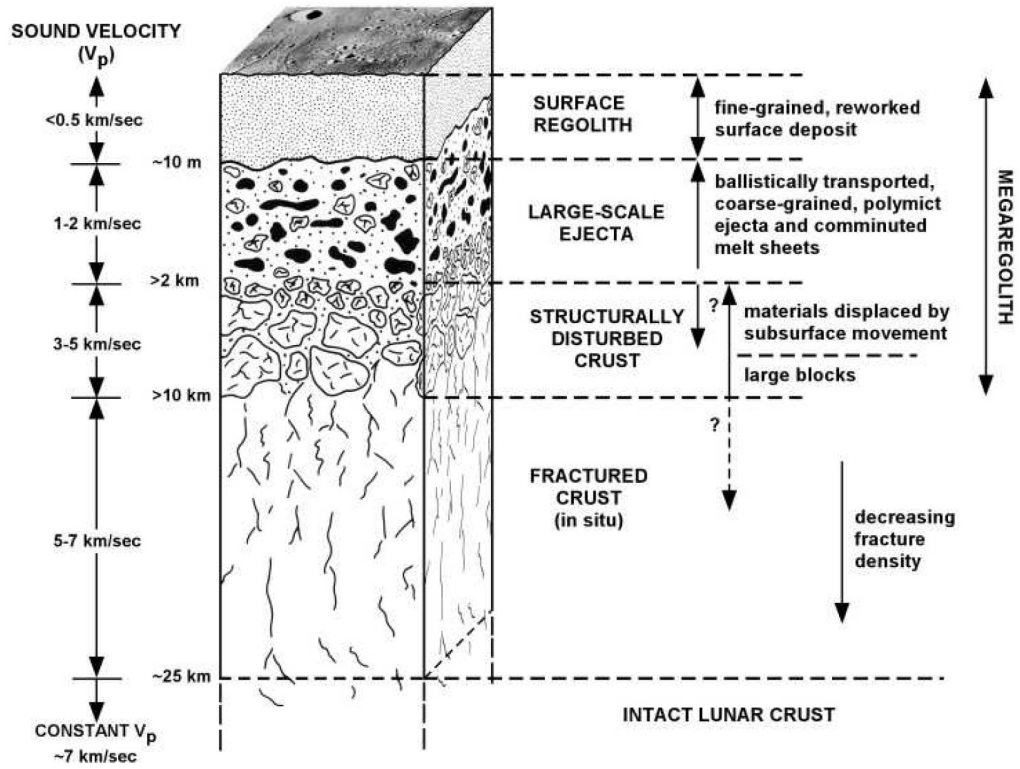

Figure 1.7: An idealised cross section of the lunar megaregolith, illustrating the relative depths of the individual components in the structure (*Hörz et al.*, 1991; *Hiesinger and Head*, 2006). Reproduced with permission of the Lunar and Planetary Institute.

1.4.1 Properties of the lunar soil

The major component of the surficial regolith layer is the subcentimeter fraction referred to as the lunar soil (*McKay et al.*, 1991). Soil on the Earth is generated by a range of mechanisms from atmospheric weathering to biological processes which generally tend to result in creating more rounded particles and well-sorted soils over time. Due to the lack of a significant atmosphere on the Moon the primary soil-forming mechanism is meteoroid impact, the result of which is poorly sorted soils composed of more angular particles (*Carrier et al.*, 1991; *McKay et al.*, 1991; *Lucey et al.*, 2006; *Kiely et al.*, 2011). The mean grain size of lunar soil samples is variable (between 40-800 μm), however, most are between 45-100 μm (*McKay et al.*, 1991).

The Earth's surface is protected from small meteoroids, which burn up in the terrestrial atmosphere. The Moon, however, is constantly subjected to "micrometeorite" impacts that have the effect of fracturing, melting and fusing together particles in the regolith. This results in the generation of irregularly shaped glass-bonded aggregates, known as agglutinates (Fig. 1.8; *Duke et al.* 1970; *McKay et al.* 1970, 1972; *Heiken* 1975; *Kiely et al.* 2011). These particles make up a high proportion (~25-30% on av-

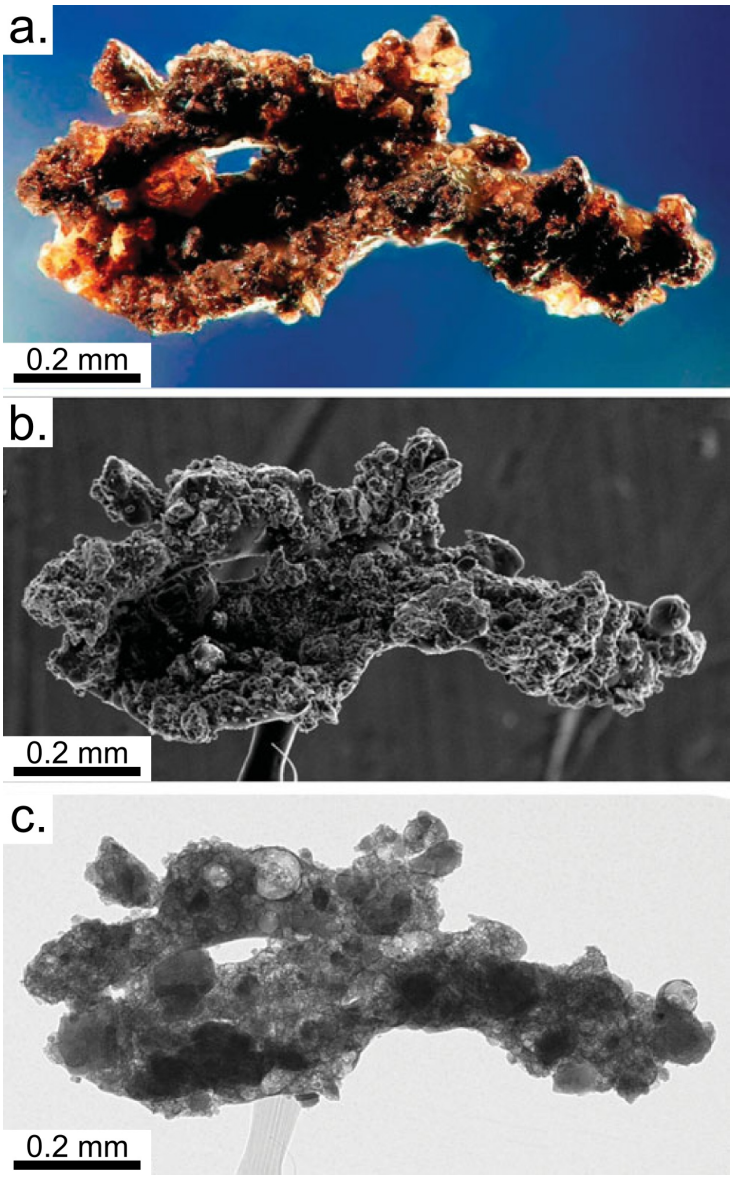

Figure 1.8: Optical (a), scanning electron (b) and X-ray (c) microscope images of an agglutinate particle (taken from *Kiely et al.* 2011). Reproduced with permission of Cambridge University Press.

erage) of lunar soils. The proportion of agglutinates in lunar soils increases with soil maturity, with agglutinates comprising up to ∼65% of the lithic fragments in mature lunar soils (*McKay et al.*, 1991; *Lucey et al.*, 2006).

Several less common components have also been identified in lunar soil samples, including: impact glasses, shocked minerals and volcanic glasses (*McKay et al.*, 1991). Impact glasses are reported in all lunar soils (∼3-5% by volume). These are present as small beads and irregular pieces of glass, formed by impact melting of pre-existing regolith (*Heiken*, 1975; *Delano and Livi*, 1981; *McKay et al.*, 1991; *Kiely et al.*, 2011). The compositions of these glasses are consistent with this theory, and commonly represent mixtures of various rock types (*Naney et al.*, 1976; *Meyer*, 1978; *Korotev et al.*,

2011). A subset of the impact glasses, which are also common to all lunar soils, are ropy glasses. These are broken pieces of twisted glass, containing inclusions of soil grains and skeletal crystals (*Meyer et al.*, 1971; *Fruland et al.*, 1977; *McKay et al.*, 1991). Unlike the various impact glasses, volcanic glasses have more uniform chemical compositions, lack schlieren textures and inclusions, and are not enriched in siderophile elements by meteoritic contamination (*Delano* 1986; see Section 1.3).

1.4.2 Regolith mixing processes

Impacts also act to mix regolith material, both laterally and vertically, and on a range of scales. The continued bombardment of the lunar surface by submillimeter-sized particles has the effect of churning the regolith in a process referred to as "gardening" (*Morris*, 1978). Models of this process by *Gault et al.* (1974) and *Arnold* (1975) indicate a 50% probability that regolith will be re-worked to a depth of 1 cm during a period of 5-10 Myr. Subsequent analysis of core samples from Apollo 15, 16 and 17 by *Morris* (1978) indicates a more rapid gardening process, such that regolith would be re-worked to a depth of ∼5 cm in just over 10 Myr. However, for timescales in excess of 100 Myr there is better agreement between the observations of *Morris* (1978) and the *Arnold* (1975) model, indicating that regolith would be re-worked to a depth of ∼50 cm in ∼500 Myr.

Larger impacts are less frequent, but will result in more significant mixing of regolith material and may also mobilise larger bedrock fragments (*McKay et al.*, 1991). Because impacts have a random spatial distribution, this process complicates the study of samples from the regolith and can make the provenance of particular lunar lithologies hard to determine, even if they were collected from known locations (e.g. *Hubbard et al.* 1971; *Meyer et al.* 1971; *Wasson and Baedecker* 1972; *Bogard et al.* 1994; *Wentworth et al.* 1994; *Korotev et al.* 2011). Conversely, lateral and vertical mixing of regolith can also be a benefit to lunar geologists, as samples obtained from a particular location may originate from regions of the Moon which were not visited by the Apollo or Luna missions. Lateral mixing of regolith may also have the effect of blurring the boundaries between geologic units which are observed remotely. For example, *Giguere et al.* (2000) used Clementine UV-VIS data to map the Ti concentration of mare basalt units and identified evidence of mixing over distances of 2-10 km.

Several studies have investigated the effects of lateral regolith mixing by impacts (e.g. *Arvidson et al.* 1975; *Li and Mustard* 2005; *Petro and Pieters* 2007). Early attempts at modelling lateral mixing suggested that regolith is largely locally derived, with ∼1% of regolith being derived from distances of >10 km for a given location

(*Arvidson et al.*, 1975; *Quaide and Oberbeck*, 1975). However, *Rhodes* (1977) noted a discrepancy between these results and the observations of 'exotic' highland materials in regoliths collected at mare locations. In addition to this, petrographic studies of Apollo 16 regolith samples have provided evidence of mixing on scales of 220-600 km (*Zeigler et al.*, 2006). More recent modelling by *Li and Mustard* (2005) is in better agreement with these observations, suggesting that lateral mixing is efficient enough for ∼20-30% of regolith material to be derived from distances of >100 km away. By calculating the cumulative effect of lateral mixing since the major basin-forming impacts (i.e. in the last ∼3.85 Gyr), *Petro and Pieters* (2007) determined that ∼10-20% of regolith material is derived from >500 km away and that most of the foreign component will originate from within 1000 km.

1.4.3 Regolith breccias

About 50% of the identified lunar meteorites have been formed from fused pieces of feldspathic lunar regolith (*Korotev et al.*, 2009). These samples are known as regolith breccias. *Stöffler et al.* (1979) define regolith breccias as rocks formed by shock lithification (*Kieffer*, 1975) of rock, mineral and glass fragments, glass spherules, and agglutinates within a regolith. Regolith breccias are particularly important as they are evidence of conditions in both ancient (associated with the basin-forming epoch) and younger (post basin-forming epoch) regolith environments (*McKay et al.*, 1986a; *Joy et al.*, 2011a), which have been preserved by lithification. They are also important due to their polymict structure, which makes them more representative of the heterogeneous average surface compositions of the areas in which they formed than monomict and pristine samples (*Lucey et al.*, 2006). In the case of regolith breccia meteorites, this can assist in the identification of launch localities for an individual meteorite of known composition through comparison with remote sensing data (*Gnos et al.*, 2004; *Arai et al.*, 2010; *Joy et al.*, 2010, 2011b).

1.5 Aims of this project

This project aims to investigate the diversity of materials in the lunar regolith. The samples analysed represent both feldspathic (lunar meteorite Northeast Africa 001; Chapter 3) and mare (Apollo 12 soils; Chapters 4-7) regoliths. As a polymict regolith breccia, Northeast Africa 001 provides insights into the petrogenesis of multiple lithologies, and the effects of regolith mixing processes responsible for bringing those lithologies

together. The second half of this project focuses on the basaltic diversity represented in soil samples collected during the Apollo 12 mission, in an attempt to improve our understanding of the basalts that formed at the Apollo 12 site, and potentially identify examples of 'exotic' lithologies introduced to the site by lateral regolith mixing.

Chapter 2

Analytical Methods

2.1 Samples

The samples analysed in these investigations include a sample of the lunar feldspathic regolith breccia meteorite Northeast Africa (NEA) 001 (Fig. 2.1) and a number of 1-10 mm lunar regolith particles which were hand selected from the Apollo 12 sample collection at Johnson Space Center (JSC) (Fig. 2.2a-b; Table 2.1).

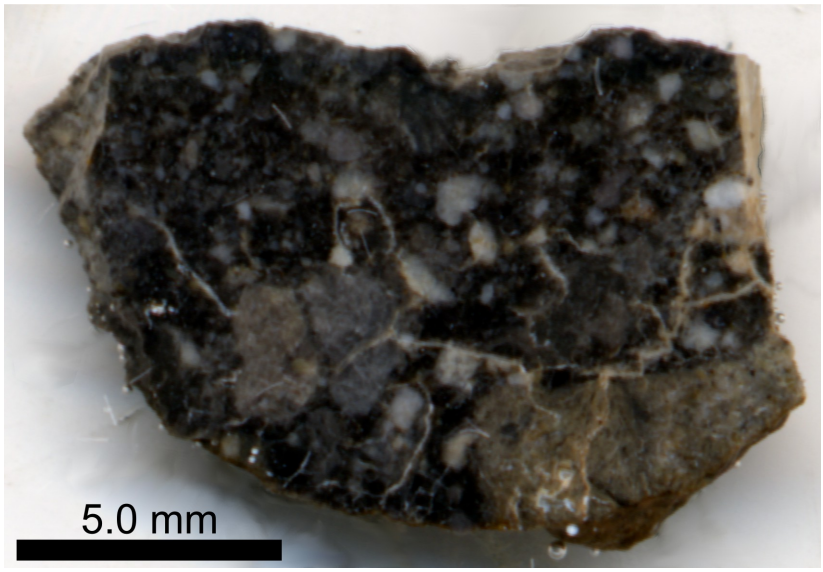

Figure 2.1: Image of the section of lunar meteorite Northeast Africa 001 discussed in Chapter 3.

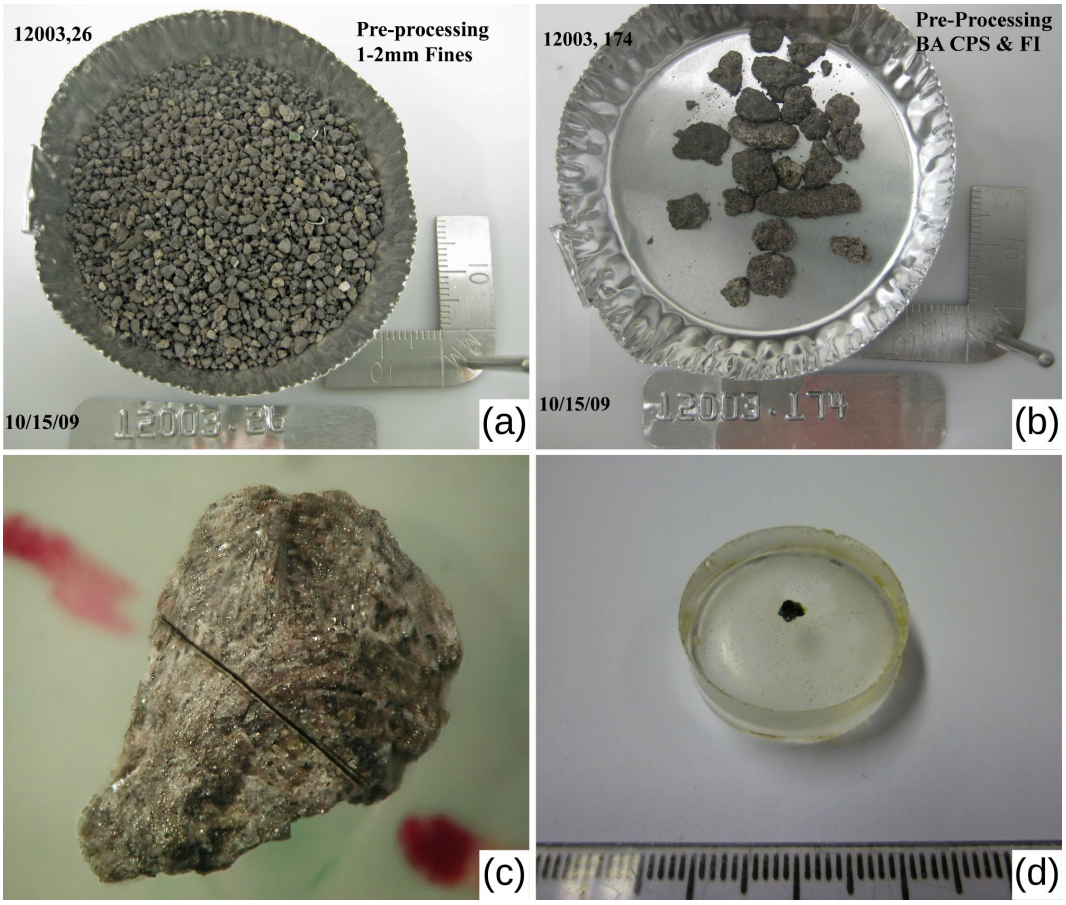

Figure 2.2: (a) and (b) Photographs of the parent samples from which the 12003,308 (a) and 12003,310;,311;,316;,317 (b) were selected by Joshua Snape and Drs Ian Crawford and Katherine Joy (images provided by the staff at the Lunar Sample Curation Facility at Johnson Space Center). (c) 12003,308_1 after laser cutting (the sample is approximately 2 mm along its longest axis). (d) An example of a sample mounted in an EPOTEK resin block (scale bar tick marks are at 1 mm increments).

2.2 Sample Preparation

2.2.1 Lunar Meteorite NEA 001

Lunar meteorite NEA 001 was purchased from a meteorite dealer (*Hupe - www.lunarrock.com*) as a small chip (362 mg). The chip was mounted in an EPOTEK epoxy resin block and polished using varying grades of aluminium polishing paste. The surface was imaged (Fig. 2.1) using an optical microscope. Finally, the polished sample was coated with carbon to facilitate electron microprobe analysis (EMPA).

2.2.2 Apollo 12 Fines

For the Apollo 12 samples an attempt was made to select particles which appeared to be of basaltic nature (i.e. crystalline, with mafic and felsic phases present) and

Table 2.1: Inventory of all samples analysed. Samples in *italics* were mounted in EPOTEK epoxy resin blocks. The Apollo 12 "B-splits" were retained for $^{40}Ar/^{39}Ar$ radiometric age dating.

Generic	Parent	Specific	Sample	Mass (g)	Generic	Parent	Specific	Sample	Mass (g)
12003	*26*	*308_1*	*A*	*0.0062*	12003	174	311_1	A	0.0203
12003	26	308_1	B	0.0033	12003	174	311_1	B	0.0047
12003	*26*	*308_2*	*A*	*0.0090*	*12003*	*174*	*311_1*	*C*	*0.0160*
12003	26	308_2	B	0.0023	12003	174	311_2	A	0.0092
12003	*26*	*308_3*	*A*	*0.0062*	12003	174	311_2	B	0.003
12003	26	308_3	B	0.0020	*12003*	*174*	*311_2*	*C*	*0.0057*
12003	*26*	*308_4*	*A*	*0.0083*					
12003	26	308_4	B	0.0030	12003	174	316	A	0.0756
12003	*26*	*308_5*	*A*	*0.0075*	12003	174	316	B	0.0044
12003	26	308_5	B	0.0029	*12003*	*174*	*316*	*C*	*0.0139*
12003	*26*	*308_6*	*A*	*0.0079*					
12003	26	308_6	B	0.0042	12003	174	317	A	0.0814
12003	*26*	*308_7*	*A*	*0.0052*	12003	174	317	B	0.0052
12003	26	308_7	B	0.0017	12003	174	317	C	0.0064
12003	*26*	*308_8*	*A*	*0.0061*	*12003*	*174*	*317*	*D*	*0.0162*
12003	26	308_8	B	0.0024					
12003	*26*	*308_9*	*A*	*0.0064*	12003	176	312	A	0.0916
12003	26	308_9	B	0.0030	12003	176	312	B	0.0040
12003	26	308_9	C	0.0014	*12003*	*176*	*312*	*C*	*0.0418*
12003	*26*	*308_10*	*A*	*0.0062*					
12003	26	308_10	B	0.0017	12003	178	314	A	0.0290
					12003	178	314	B	0.0031
12003	174	310_1	A	0.0188	12003	178	314	C	0.0151
12003	174	310_1	B	0.0024	*12003*	*178*	*314*	*D*	*0.0199*
12003	*174*	*310_1*	*C*	*0.0076*					
12003	174	310_2	A	0.0244	12022	84	304	A	0.1206
12003	174	310_2	B	0.0033	12022	84	304	B	0.0192
12003	174	310_2	C	0.0010	*12022*	*84*	*304*	*C*	*0.024*
12003	*174*	*310_2*	*D*	*0.0122*					
12003	*174*	*310_3*	*A*	*0.0078*	*12038*	*255*	*263*	*A*	*0.099*
12003	174	310_3	B	0.0031	12038	255	263	B	0.0135
12003	174	310_3	C	0.0048					
12003	*174*	*310_4*	*A*	*0.0055*	*12063*	*290*	*330*	*A*	*0.0877*
12003	174	310_4	B	0.0030	12063	290	330	B	0.0065
12003	174	310_4	C	0.0042					

would, therefore, be most useful to a project studying basaltic diversity in the lunar regolith. This selection was made primarily with the aid of a relatively low magnification optical microscope in the Apollo sample curation laboratory at JSC. However, such identification is extremely difficult without the benefit of any additional information (e.g. electron microscopy images, modal mineralogy or geochemical data) especially when dealing with such small samples. As such, several non-igneous samples were mistakenly selected (see Chapter 6).

The Apollo 12 regolith grains required several additional preliminary preparation stages. Prior to all other processing, these samples were weighed and then photographed using a Sony α330 digital camera attached to an Olympus SZX12 optical microscope. Repeat weighings with several test samples of similar masses to the Apollo 12 fines indicated an accuracy of 10^{-4} g for the weighing balance. The samples were then split into at least two parts, in order to obtain one sample to use for petrologic analysis and a second ("B-split") sample which could be retained for radiometric age dating (see Table 2.1). For the smallest (<2 mm) samples, a New Wave 213 nm laser with a beam width of 25 μm was used to begin the cutting process in order to reduce the overall mass loss (Fig. 2.2c). Where necessary, the samples were then split with a fine scalpel blade. For samples much larger than 2 mm this method was impractical due to limitations of the laser system and splitting was performed entirely with either a scalpel or a pair of surgical bone cutters. The samples were then photographed and weighed a second time in order to establish any mass loss during the processing. In order to minimise the chance of cross contamination between the samples, all of the instruments used in these procedures (e.g. tweezers, scalpel blades and bone cutters) were cleaned thoroughly with acetone after each sample was processed.

The samples to be used for petrologic analysis (Table 2.1) were mounted in EPOTEK epoxy resin blocks (Fig. 2.2d). Any surficial resin was ground away with silicon carbide paper in order to expose the samples. The exposed sample surfaces were then polished with either aluminium oxide or diamond paste on pellon cloths using an alcohol-based lubricant. The pellon cloths used were only used in the preparation of lunar samples in order to minimise contamination from terrestrial rock samples. Polishing was initially performed by hand, however, a final polish was achieved with an Struers Planopol-V automated rotational polisher. Finally, the samples were coated with carbon to facilitate electron microprobe analysis (EMPA).

2.3 Electron Microprobe - Energy Dispersive Spectroscopy

A majority of the Energy Dispersive Spectroscopy (EDS) analysis of the samples was performed using a JEOL JXA-8100 electron microprobe analyser at UCL/Birkbeck with an accompanying Oxford Instruments EDS probe and INCA software package (*Oxford Instruments*, 2006). The probe was operated at a 15 kV accelerating voltage, with a 10 nA beam current. This included the acquisition of back scattered electron (BSE) images, elemental mapping and bulk sample and area compositions. The only exception to this was the elemental mapping of NEA 001 (see Chapter 3), which was performed at the Natural History Museum, London, using a LEO 1455VP SEM, with an Oxford Instruments INCA EDS X-ray microanalyser system, operated at a 20 kV accelerating voltage, with a 2 nA beam current.

2.3.1 BSE Imaging, elemental mapping and modal mineralogy

The EMPA of the samples began with the acquisition of BSE images. Multiple high resolution (typically ×200) BSE images were obtained for each sample using the INCA software package (*Oxford Instruments*, 2006). These were then montaged using the GNU Image Manipulation Program (*GIMP*) to form complete maps of the samples.

The elemental concentrations within the samples were mapped using the EDS system and INCA software (*Oxford Instruments*, 2006). This process provides a series of maps for each sample, where the concentration of a single element is represented by varying greyscale tones. These maps were then "colourised" and combined using the *GIMP* in order to generate false colour element maps (Fig. 2.3).

Modal mineralogies of the Apollo samples and NEA 001 clasts were obtained from the BSE images and X-ray element maps using the *GIMP*. A majority of the individual phases within each sample were automatically identified based on their greyscale tone in the BSE images (Fig. 2.4). This technique was effective in many cases where the tonal differences between the phases were clear. However, for phases with very similar greyscale tones in the BSE images (for example pyroxenes and olivines), or in the case of very compositionally zoned phases, it was often necessary to use the elemental maps to refine the selection. Having identified the phases within a given sample or area, it was then possible to use the *GIMP* to count the pixels associated with each phase and calculate the modal mineralogies from these pixel counts. The accuracy and reproducibility of this method was demonstrated with several well characterised Apollo

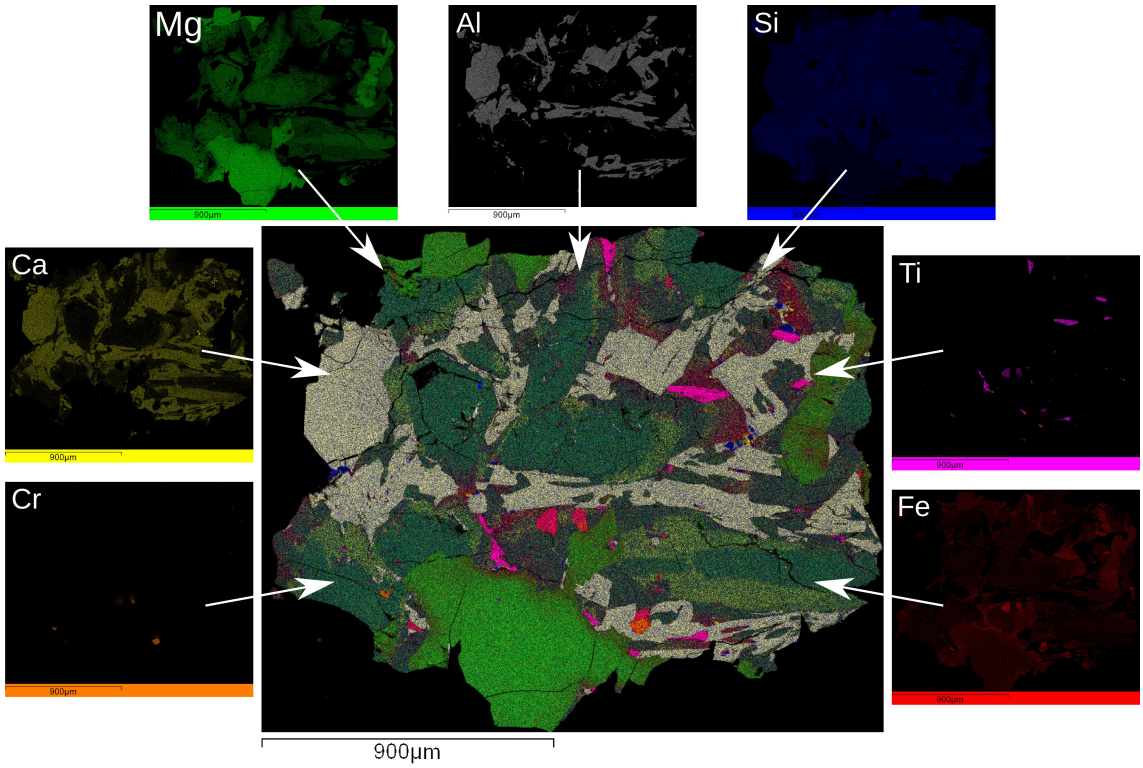

Figure 2.3: Colourised individual element maps used to generate the false colour element map of 12003,308_8A. Each image was imported as a separate layer within a single file in the *GIMP*. These were then combined using the program's 'Addition' function.

12 basalts (see Chapter 5; *Snape et al.* 2011b).

2.3.2 Bulk-sample major element chemistry

The bulk sample and area compositions were measured using the EDS probe and INCA software package by performing multiple raster beam analyses (RBA) across the sample areas (Fig. 2.5; see also *Joy et al.* 2010, 2011b; *Snape et al.* 2011b). This method provides a relatively simple and non-destructive way to make in-situ measurements of the bulk sample compositions in crystalline basalts and individual clast compositions in brecciated samples. Prior to each set of measurements, the EDS detector was calibrated by analysing a Co standard. RBA acquisition times of 50 seconds were used for the clasts within NEA 001 and 480 seconds for the Apollo 12 regolith samples. Repeat RBA were averaged together and the mean result was normalised to reduce the effects of void spaces, mineral edge effects and small fractures. The errors quoted for these average values are the 1σ standard deviations between the individual RBA, and therefore indicate the instrumental precision of the measurements. Samples which were too large to fit within the maximum field of view of the electron microprobe were divided into multiple areas within which the area scans were performed. The sizes of these areas

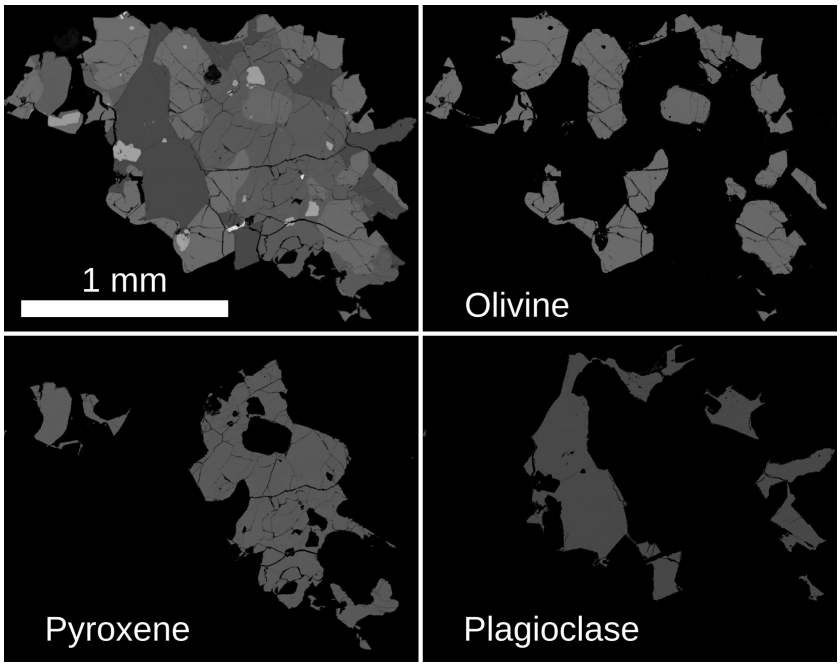

Figure 2.4: Back scattered electron images illustrating the selection of major silicate phases within 12003,308_3A using the *GIMP*. The numbers of pixels within these images were then used to calculate the sample's modal mineralogy.

were then measured using the image processing program *ImageJ* and used to weight each set of area scan results (based on their relative sizes) prior to combining them to obtain an overall sample composition.

In order to monitor and assess the accuracy and precision of the EDS system, measurements were obtained from a section of the United States Geological Survey (USGS) BCR-2 basaltic glass standard (*USGS*, 2009) before and after each set of sample analyses. Comparison of these measurements with the composition reported by the USGS indicates a relative error of <6% for almost all elements present at concentrations >0.1 wt% (including Na, Mg, Al, Si, K, Ca, Ti, Cr, Mn and Fe; see Fig. 2.6). An exception to this is P for which accurate measurements at low concentrations are difficult to obtain by EDS due to an overlap between the P Kα and Si Kα X-ray emission lines (Fig. 2.6).

A potentially significant error associated with RBA and similar defocused or broad beam analyses (DBA) is known to occur when analysing non-homogeneous multiphase samples (*Dowty et al.*, 1973; *Albee et al.*, 1977). This is due to the differences in densities between individual phases within the area being analysed which are not accounted for in conventional matrix corrections (*Nazarov et al.*, 1982). These invariably lead to underestimations for concentrations of heavy elements such as Mg and Fe, and overestimations of lighter elements such as Al (*Dowty et al.*, 1973). *Warren* (1997) attempted

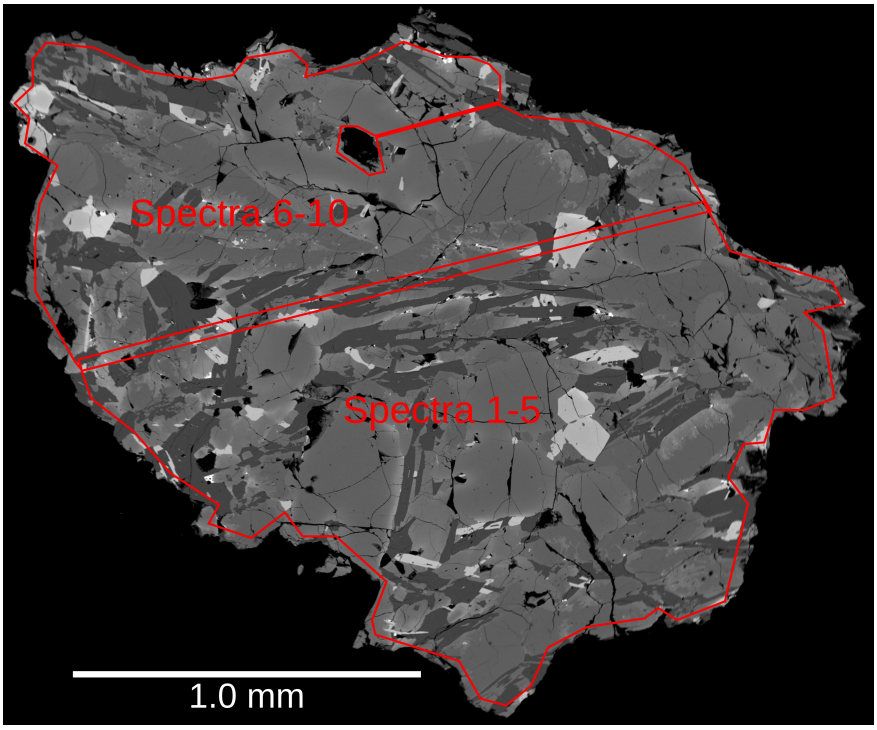

Figure 2.5: Back scattered electron image illustrating raster beam analysis area scan locations within Apollo sample 12003,310_4A.

to provide a correction for the "Unequal Host-Phase Density Effect" which has been used since in multiple studies (*Warren*, 1997; *Arai and Warren*, 1999; *Grossman et al.*, 2000; *Cohen et al.*, 2004; *Joy et al.*, 2010). Although *Lindstrom* (1999) have cited deficiencies in the model of *Warren* (1997), it is still preferable to using uncorrected data (*Carpenter et al.*, 2009a,b). As such, this method has been used when processing all the RBA data presented in this work.

In order to generate correction factors for each set of RBA, average compositions of the individual phases within the clasts and samples were calculated from the mineral chemistry data obtained by Wavelength Dispersive Spectroscopy (WDS; see Section 2.4). It was also necessary to provide an estimate of the densities for the phases within each clast or sample. For phases which typically have quite limited compositional ranges within lunar materials, canonical literature values for density were used (in the case of plagioclase, for example, the calculated density of anorthite was used: see *Mindat*; *Webmineral* websites). The densities of phases with more variable compositions (such as pyroxene and olivine) were calculated based on the average mineral chemistries within each sample and published variations between mineral compositions and physical properties (*Bloss* 1952; *Brown* 1960; *Mindat*; *Webmineral*). Typical correction factor ranges are Si = 0.98-1.02; Ti = 1.03-1.55; Al = 0.84-1.00; Fe = 1.04-1.31; Mg = 1.03-1.28; Ca = 0.91-1.04; K = 0.82-1.07; Na = 0.88-1.02 (i.e. the raw measured

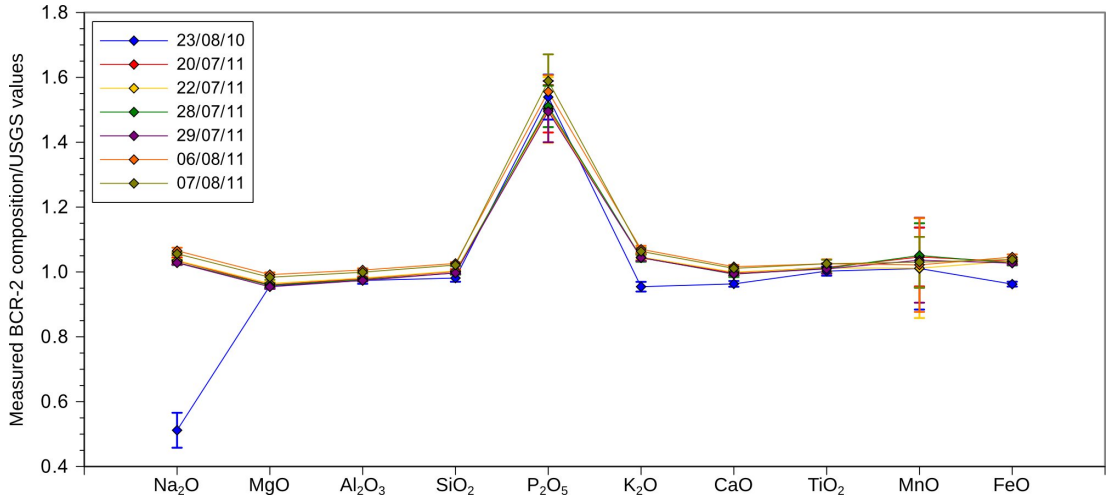

Figure 2.6: EDS measurements of the USGS BCR-2 basaltic glass standard normalised to the elemental composition published by the USGS. Each set of values represents the average of the BCR-2 measurements taken over a given day (the errors plotted represent 1σ standard deviations of the measurements for that day).

values were multiplied by these factors to allow for the phase density differences). The implementation of *Warren*'s (1997) method used in this study has been tested with the well characterised Apollo 12 basalts 12022, 12038 and 12063 (see Chapter 5; *Snape et al.* 2011b) for which bulk compositions have also been acquired using a range of different analytical techniques in previous studies. In general, these tests show good agreement between the RBA and the literature values. A noticeable improvement in this correlation is also observed when the density correction is applied (Electronic Appendix A).

Significant discrepancies between the bulk sample compositions obtained by RBA and those obtained by alternative techniques are largely attributed to the analysed samples not being representative of the parent rocks from which they originated. This hypothesis is supported by observed differences in the modal mineralogies obtained for these samples when compared with those from previous studies.

2.4 Electron Microprobe - Wavelength Dispersive Spectroscopy

Major and minor element analyses of individual mineral phases were performed with the JEOL JXA-8100 electron microprobe Wavelength Dispersive Spectroscopy (WDS) system. Measurements were made using a 15 kV accelerating voltage, a 25 nA beam current and a 1 μm diameter beam. A peak acquisition time of 20 seconds (with a background measurement time of 10 seconds) was used for a majority of the elements

analysed. Table 2.2 provides a summary of the settings used for the WDS analyses, including the acquisition times, diffracting crystals and standards used for each element.

The WDS results were subjected to several checks in order to assess the quality of the data. An initial check was performed on the totals of all the measured elements (in oxide weight percent) within each analysis. Measurements with analytical totals of less than 97.5% or greater than 102.5% were rejected. The remaining measurements were then subjected to stoichiometric checks in order to confirm the compositions agreed with canonically accepted mineral formulae (*Deer et al.*, 1966; *Papike et al.*, 1991). As with the EDS RBA, the USGS BCR-2 basaltic glass standard (*USGS*, 2009) was used as an external standard to allow the accuracy and precision of the data to be monitored and assessed. Multiple measurements of the BCR-2 standard were obtained throughout the course of each set of analyses. A majority of these measurements are within the errors quoted by the *USGS* (2009) for the standard glass for elements present at concentrations >0.1 wt%. The relative errors between the measured concentrations and the *USGS* (2009) values are also consistently below 6% for a majority of these elements (Fig. 2.7). An exception to this is Na for which accurate measurements are difficult to obtain due to the element's volatility upon interaction with the electron beam (Fig. 2.7).

Table 2.2: Summary of settings used for WDS analyses.

Element	Na	K	Mg	P	Al	Ca	Si	Ti
Peak measurement time (sec)	10	20	20	20	20	20	20	20
Background measurement time (sec)	5	10	10	10	10	10	10	10
Diffracting crystal	TAP	PET	TAP	PET	TAP	PET	PET	LIF
Standard name	BCR-2	ORTH2008	BCR-2	apFara	BCR-2	BCR-2	ORTH2008	uclrutile
Standard type	Basaltic glass	Orthoclase	Basaltic glass	Apatite	Basaltic glass	Basaltic glass	Orthoclase	Ti oxide
Element	Cr	Mn	Fe	Ni	V	Co	Ba	Zn
Peak measurement time (sec)	20	20	20	40	40	40	40	20
Background measurement time (sec)	10	10	10	20	20	20	20	10
Diffracting crystal	LIF	LIF	LIF	LIF	LIF	LIF	LIF	LIF
Standard name	Cr	MnO	ol1ucl	Ni	V	Co	Ba_lif	Zn
Standard type	Pure metal	Oxide	Olivine	Pure metal	Pure metal	Pure metal	Barium sulfide	Pure metal
Element	Cu	F	Cl	Nd	Ce	La	Y	Sr
Peak measurement time (sec)	20	20	20	20	20	20	20	20
Background measurement time (sec)	10	10	10	10	10	10	10	10
Diffracting crystal	LIF	TAP	PET	LIF	LIF	LIF	PET	PET
Standard name	Cu	apFara	ApatiteNHM	NdF3	CeAl2	LaB6	YAG	SrSO4
Standard type	Pure metal	Apatite	Apatite	Neodymium fluoride	Kondo lattice compound	Lanthanum hexaboride	Yttrium aluminium garnet	Strontium sulfate

Diffracting crystals used were: Thallium acid pthalate (TAP) Pentaerythritol (PET) Lithium fluoride (LIF).

2.5 Laser Ablation Inductively Coupled Plasma Mass Spectrometry

Mineral trace element chemistries and bulk compositions of clasts and samples were determined using a laser ablation inductively coupled plasma mass spectrometer (LA-ICP-MS), with a similar analytical procedure as described by *Joy et al.* (2010, 2011b). The instrumental setup consisted of a New Wave 213 aperture imaged frequency quintupled laser ablation system (213 nm) coupled to an Agilent 750a quadrupole-based ICP-MS with a shield torch to reduce polyatomic interferences. The laser source was operated with a pulse frequency of between 10-20 Hz and a fluence of 3-5 mJ cm^{-2}. Instrumental background levels were established by analysing the mixed He gas (flow rate of 100%) and Ar carrier gas with the laser off for 30 seconds. The sample was then ablated for 30 seconds. The system was purged with He for 30 seconds between analyses and left for at least a further 2 minutes to flush out the system before proceeding to the next analysis.

Data were collected for a total of 60 s, during which time the abundance of 45 elements were monitored. The ICP-MS system performs these measurements by cycling a detector across the mass ranges of the selected elements over a given period of time. The number of elements measured does not increase the overall analysis duration. However, if the detector is having to measure more elements within a given acquisition time, the quality of the data will not be as good as there will be less repeat cycles per element. For this reason, care was taken in order to establish a suitable element list. The initial selection of elements was based largely on those used in other trace element studies of lunar samples (*Shearer et al.*, 1989; *Schnare et al.*, 2008; *Joy et al.*, 2008). In addition to this, an attempt was made to further refine this list by investigating which elements may help answer specific geochemical questions about the samples being studied.

Trace element mineral data were acquired by ablating sample material from 55 μm spots. Where the mineral grains were large enough, multiple measurements were made within a single phase including lines of measurements from mineral core to rim (Figs. 2.8a-b). Bulk-clast trace element compositions within NEA 001 were acquired by ablating sample material in elongated tracks (80 $\times$ 200 μm) from adjacent portions of the same clast (within the area previously studied by EMP RBA techniques; see Figs. 2.8c-d). Results for each track were averaged together to provide a representative value of the clast's bulk composition. The errors listed in Table 3.2 represent the 1σ standard deviation variation of all data collected within a single clast. Therefore, clasts with large errors represent clasts that were more mineralogically heterogeneous or coarsely grained

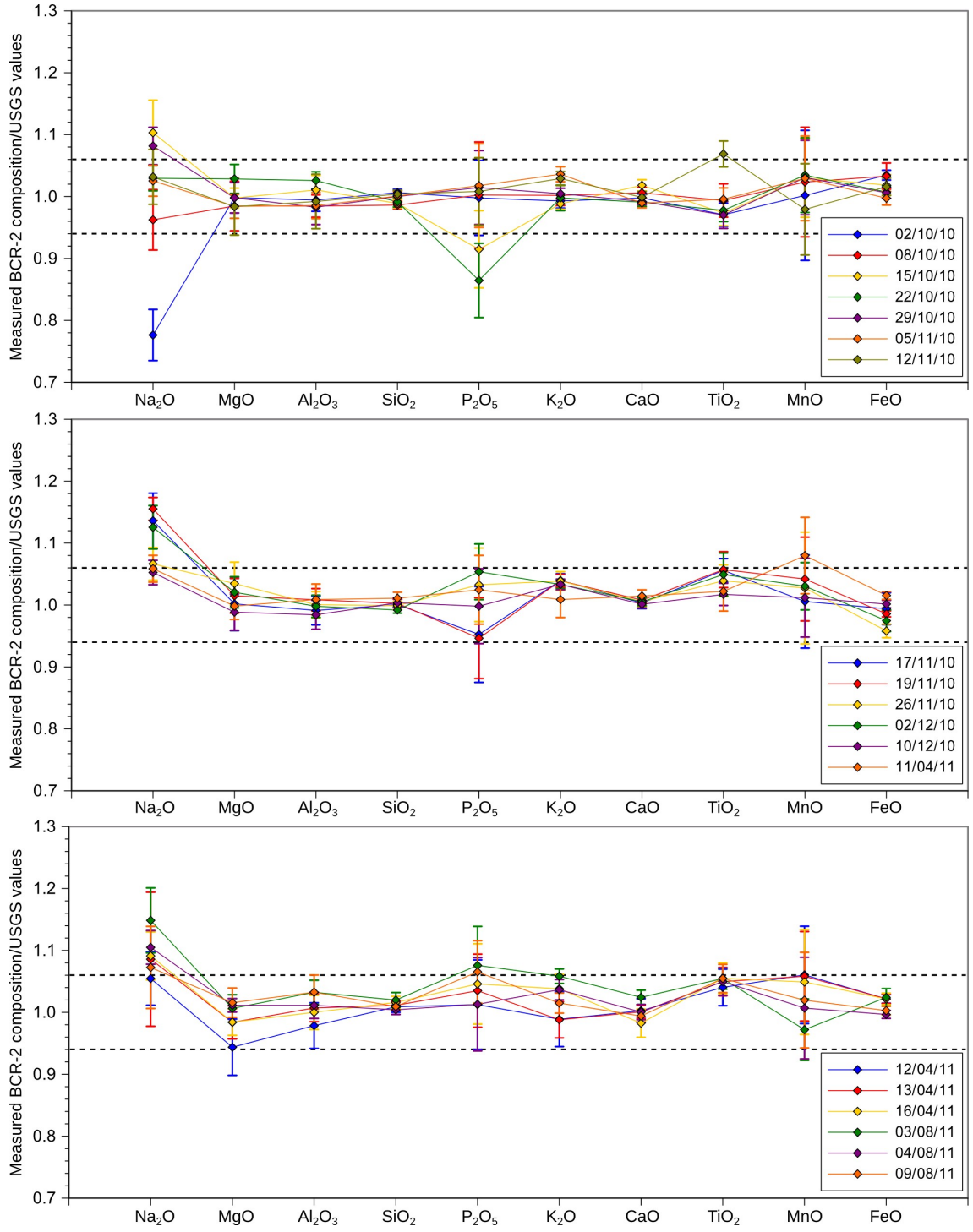

Figure 2.7: WDS measurements of the USGS BCR-2 basaltic glass standard normalised to the elemental composition published by the USGS. Each set of values represents the average of the BCR-2 measurements taken over a given analytical run (the errors plotted represent 1σ standard deviations of the measurements for that run). Note that, with the exception of Na, a majority of the measurements are within $\pm 6\%$ of the USGS values.

(where one measurement may be rather unrepresentative of the total clast composition, increasing the elemental variability measured by this study), and smaller errors indicate finer grained (i.e. all phases were easily sampled) or more homogeneous material.

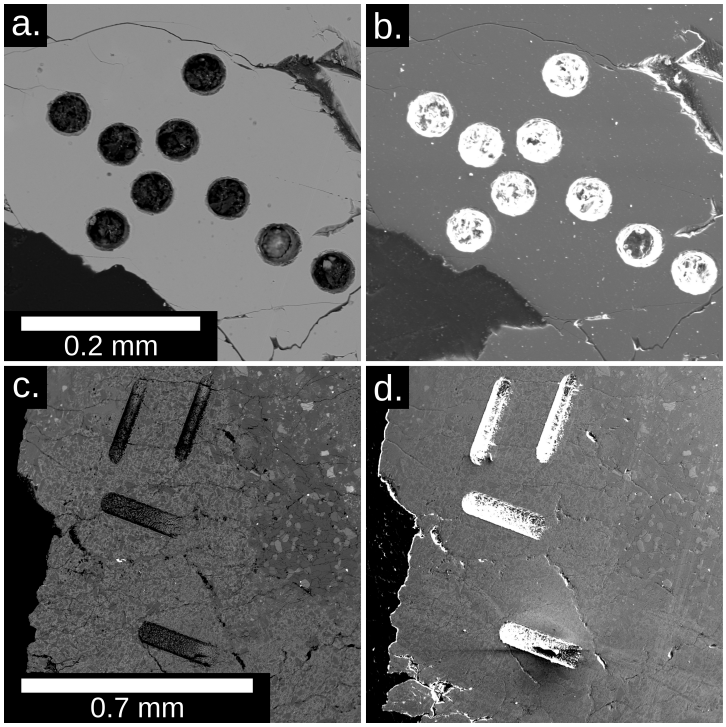

Figure 2.8: (a) Back scattered electron (BSE) image and (b) secondary electron image (SEI) illustrating trace element mineral chemistry analysis by laser ablation inductively coupled plasma mass spectroscopy. (c) BSE image and (d) SEI illustrating trace element bulk clast composition analysis within lunar meteorite Northeast Africa 001.

Data were reduced using the *GEMOC* (2002) Glitter software program. Analyses were calibrated with both an internal and external standard measurement of a particular element. The values used as internal standards were obtained from the WDS EMPA for the mineral grain trace element measurements and the EDS RBA for the bulk trace element analyses. The external standards used were the NIST SRM 610 and NIST SRM 612 glass reference materials (*Pearce et al.*, 1997). Measurements of these materials were made using identical analytical conditions as the sample measurements, including the dimensions of the laser tracks and spots, acquisition times and other instrumental settings. The standard element and external reference material selected for calibrating the trace element mineral chemistries was varied depending on the phase being analysed, so that the concentrations of the standard elements within both the sample and the external reference material were similar. In the cases of plagioclase and pyroxene, CaO was used and external standard measurements were made on the NIST SRM 612 glass. For spinel analyses, Al_2O_3 was used and the analyses were again

calibrated with the NIST SRM 612 glass. Olivine and ilmenite analyses were calibrated with MnO, using the NIST SRM 610 glass as an external standard. CaO was used as an internal standard for bulk clast trace element compositions and the NIST SRM 612 glass was analysed as an external standard.

Several elements (e.g. Mg, Al, Ti, Cr and Mn) whose concentrations have been previously measured during EDS RBA and WDS EMPA, but which were not being used as calibration standards, were also measured by LA-ICP-MS so that the results from the two techniques could be compared against each other for consistency (Appendices B;D;F). The relative standard deviation of all the NIST 610 standard repeat measurements had a total range of between 2% and 15% (1σ) for all elements analysed except Au and Cu. The relative standard deviation of all the NIST 612 standard repeat measurements was less than 15% (1σ) for a majority of the elements analysed. However, several elements (e.g. Zn, Au and U) appear to be less reproducible, with relative standard deviations of between 3% and 28%. These measurements were compared to the preferred average NIST 610 and 612 element concentrations reported by *Pearce et al.* (1997) in order to assess their accuracy. The difference between the values in this study and the *Pearce et al.* (1997) values was <10% for all elements analysed, and typically <5% (Figs. 2.9;2.10).

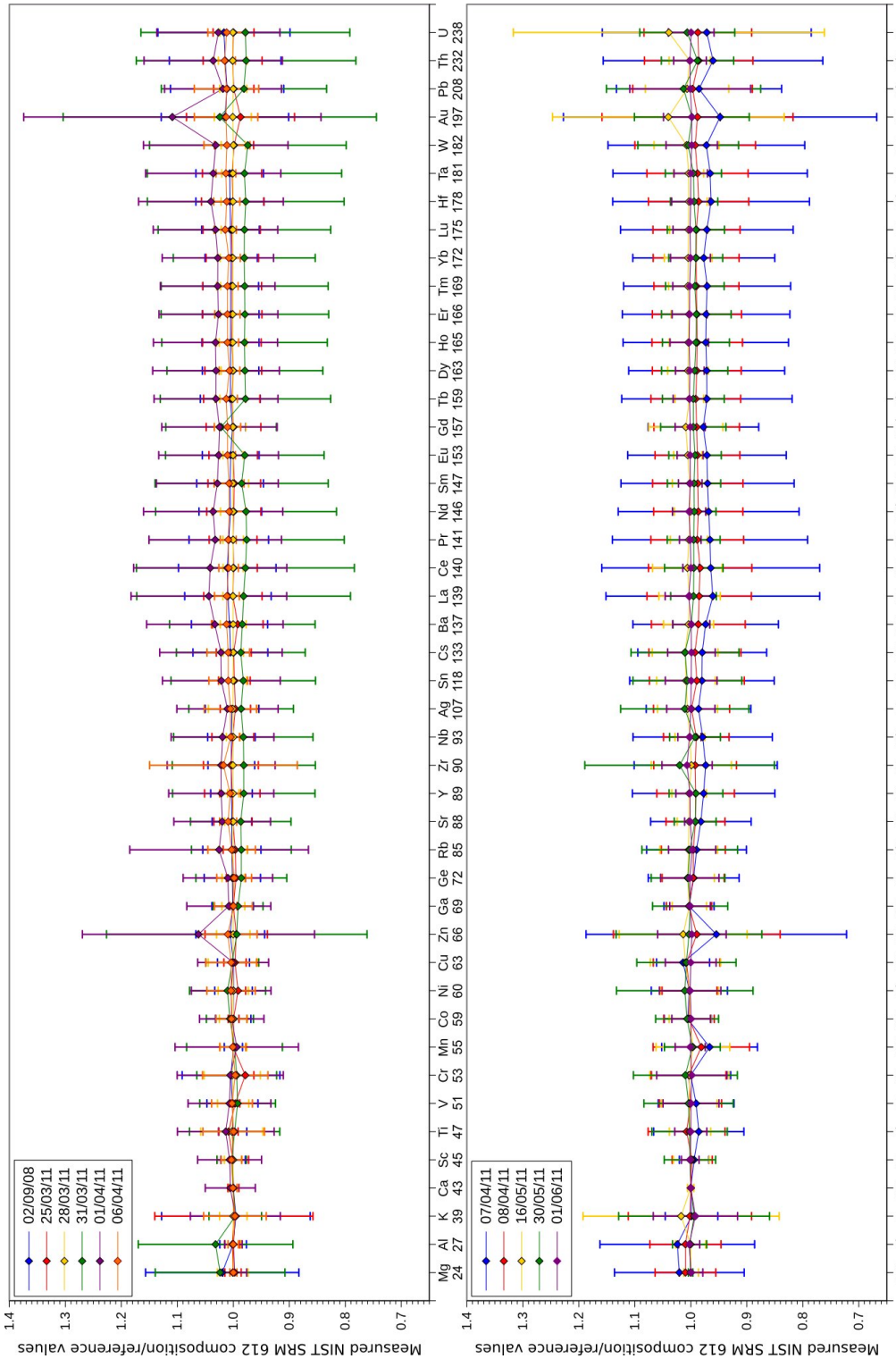

Figure 2.9: LA-ICP-MS measurements of the NIST SRM 612 normalised to the preferred average values provided by *Pearce et al.* (1997). Each set of values represents the average of the NIST SRM 612 measurements taking over a given day (the errors plotted represent averages of the 1σ standard deviations of the measurements for that day). Note that the measurements are within ±10% of the published values for all elements analysed, and typically within ±5%.

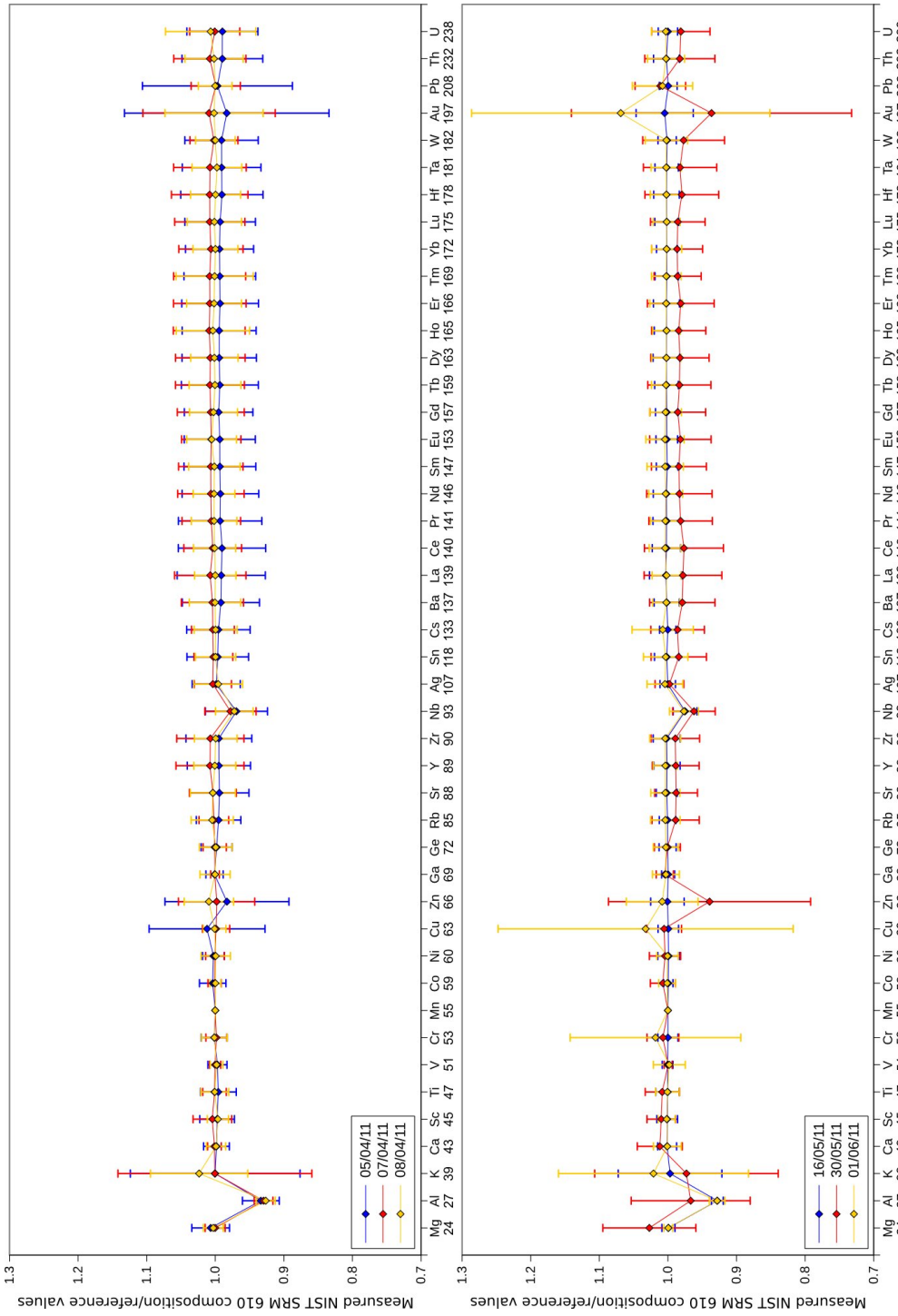

Figure 2.10: LA-ICP-MS measurements of the NIST SRM 610 normalised to the preferred average values provided by *Pearce et al.* (1997). Each set of values represents the average of the NIST SRM 610 measurements taking over a given day (the errors plotted represent 1σ standard deviations of the measurements for that day). Note that the measurements are within $\pm 10\%$ of the published values for all elements analysed, and typically within $\pm 5\%$.

Chapter 3

Lunar Meteorite Northeast Africa 001

3.1 Introduction

Northeast Africa (NEA) 001 was collected in northern Sudan in 2002, and is classified in the Meteoritical Bulletin (*Russell et al.*, 2005) as a lunar anorthositic regolith breccia. The original stone weighed 262 g, is reported to have had a brownish, grey colour, and lacked a fusion crust (*Russell et al.*, 2005); (Fig. 3.1). The sample was classified as a polymict feldspathic regolith breccia by *Haloda et al.* (2005) and *Korotev and Irving* (2005) following the scheme of *Stöffler et al.* (1979). It is a heterogeneous, clast-rich meteorite, consisting of clasts ranging in size from <0.1 to 6.0 mm, supported by a microcrystalline feldspathic matrix. This study presents the petrography and mineralogy of a 362 mg section (∼11.7 × 8.6 mm) of NEA 001 in order to characterise this as yet little studied lunar meteorite, and use this characterisation to elucidate several different aspects of lunar geology and evolution.

The majority of this chapter was published in *Snape et al.* (2011a). Permission to reproduce this material has been granted by John Wiley and Sons, Inc.

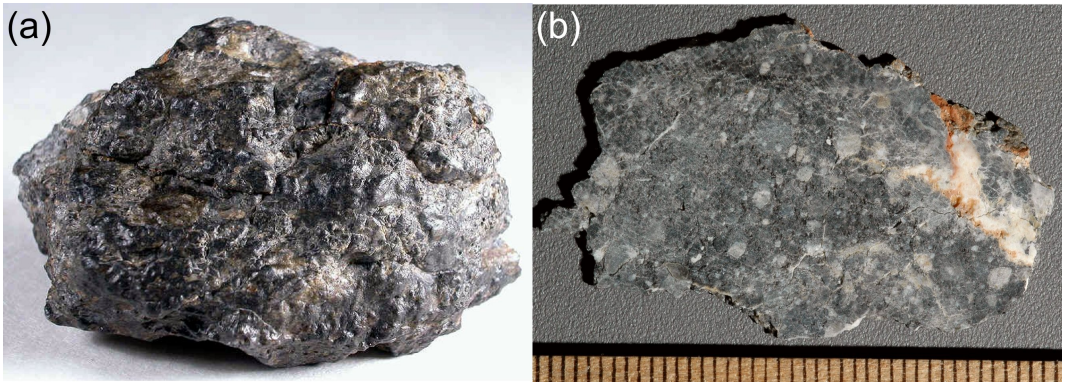

Figure 3.1: (a) Hand specimen of the NEA 001 meteorite. (b) A sawn face of NEA 001. The scale bar tick marks are at 1 mm increments. Image source: *Korotev* (2012).

3.2 Results

3.2.1 Petrography and clast inventory

NEA 001 consists of a dark black/brown matrix with clasts ranging in colour from grey to light brown. These clasts vary in size from <0.1-6.0 mm (Fig. 3.2). The clasts which were identified within NEA 001 make up 42% of the total surface area of the sample. Amongst these are impact melt clasts and impact melt breccias (23%), basaltic clasts (15%), ferroan noritic anorthosites (3%) and magnesian feldspathic clasts (1%). Table 3.1 summarises the characteristics of all the clasts studied within the sample. The matrix is well consolidated and is composed of glass and small (<0.15 mm) individual mineral grains. Also observed within the matrix are small glass spherules (0.05-0.15 mm; Fig. 3.2; Table 3.2), consistent with the sample being a regolith breccia (*Stöffler et al.*, 1979).

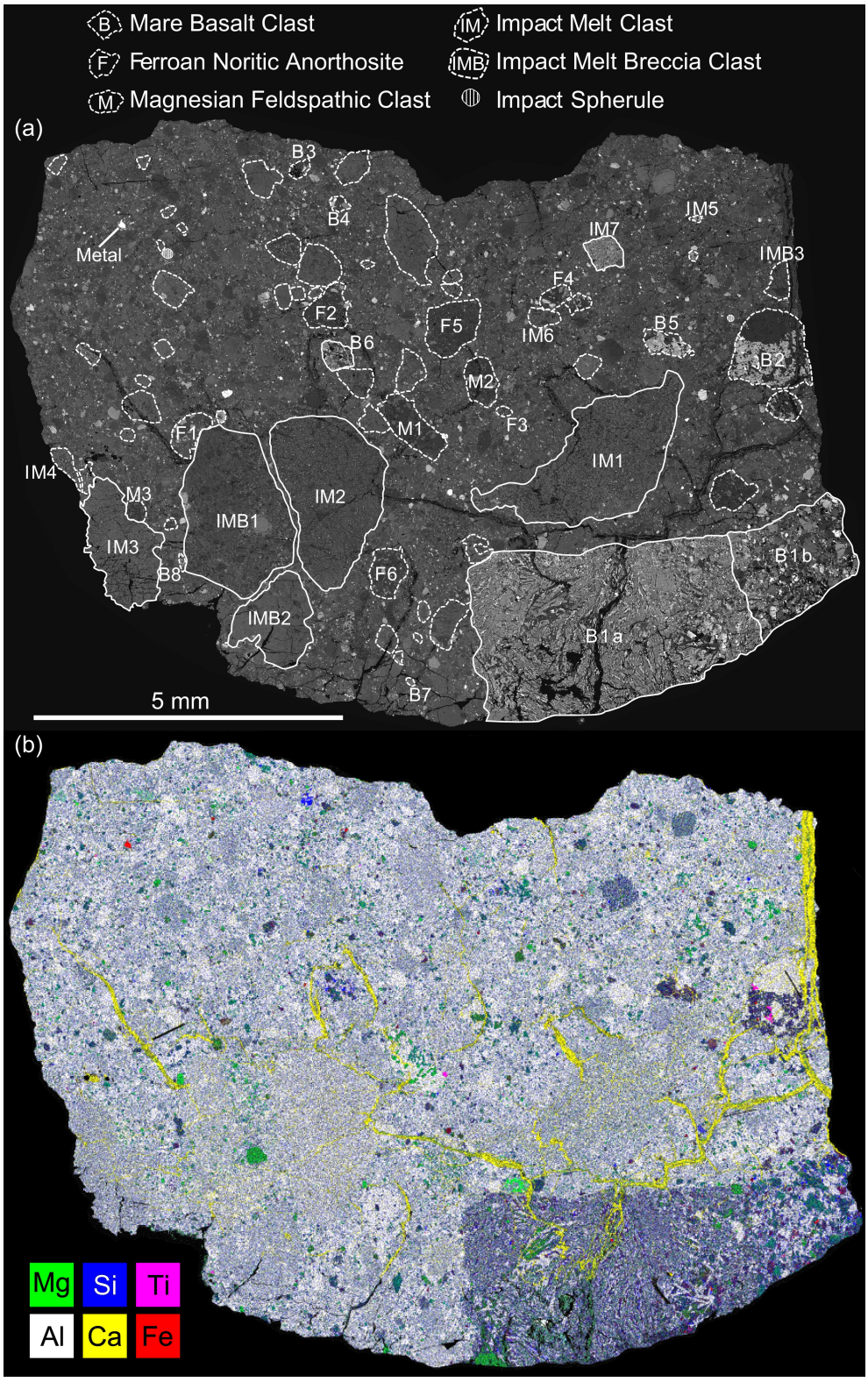

Figure 3.2: (a) Montaged back scatter electron (BSE) image of NEA 001 section with clasts of interest denoted. Clast dimensions, modal mineralogies, mineral chemistry and, in some cases, bulk compositions were obtained for clasts which have been allocated identifiers. Clasts which have been outlined, but remain unnamed, were used to establish approximate modal proportions of clast and matrix material within the sample. Trace element data were collected for clasts with solid outlines. (b) Montaged false colour elemental map of NEA 001 where colours represent element distribution and concentration: Si = blue, Al = white, Mg = green, Fe = red, Ca = yellow and Ti = pink.

Table 3.1: Inventory table of all clasts identified and named within NEA 001.

	Dimensions	Grainsize		Pyroxene			Plagioclase	Olivine
Clast	(mm)	(mm)	Approximate Modal Mineralogy	Wo	En	Fs	An-range	Fo-range
B1a	4.42 × 2.60	<0.01-0.25	58% Plag, 32% Pyx (CPX; OPX), 10% Ol, <1% Ilm	14-35	17-54	30-67	96-97	64-75
B1b	1.86 × 1.51	0.05-0.33	48% Plag, 40% Pyx (CPX; OPX), 5% Ol, 7% Sil	4.9-37	4.7-72	23-78	94-98	n.m.
B2	1.21 × 1.26	0.01-0.71	66% Plag, 33% Pyx (CPX; OPX), 1% Ilm	4.4-42	33-44	25-54	89-94	32
B3	0.37 × 0.25	0.01-0.21	60% Plag, 12% Pyx (CPX), 26% Sil, 2% Ilm	36-42	6.7-39	19-53	95	n.m.
B4	0.35 × 0.25	0.01-0.14	50% Plag, 29% Pyx (CPX), 15% Ol, 6% Ilm	22-45	17-39	16-53	n.m.	n.m.
B5	0.77 × 0.35	0.02-0.28	38% Plag, 56% Pyx (CPX; OPX); 5% Ol	8.7-35	29-58	29-47	94-97	78
B6	0.46 × 0.45	0.01-0.19	50% Plag, 41% Pyx (OPX), 8% Sil, 1% Ilm	4.2-5.7	60-71	24-34	n.m.	n.m.
B7	0.17 × 0.09	<0.01-0.05	21% Plag, 72% Pyx, 7% Ilm	n.m.	n.m.	n.m.	91	n.m.
B8	0.09 × 0.32	<0.01-0.06	56% Plag, 39% Pyx (CPX; OPX), 5% Ilm	9.0-23	35-41	42-50	n.m.	n.m.
IM1	3.46 × 1.94	<0.01-0.14	63% Plag, 37% mafic melt	n.m.	n.m.	n.m.	n.m.	n.m.
IM2	2.86 × 1.55	0.01-0.18	83% Plag, 17% mafic melt	n.m.	n.m.	n.m.	n.m.	n.m.
IM3	1.07 × 2.19	<0.01-0.14	46% Plag, 54% mafic melt	n.m.	n.m.	n.m.	96	n.m.
IM4	0.21 × 0.77	0.01-0.08	68% Plag, 32% mafic melt	20	49	32	n.m.	n.m.
IM5	0.21 × 0.10	0.01-0.08	37% Plag, 63% mafic melt	7.2-19	44-48	37-45	n.m.	n.m.
IM6	0.49 × 0.28	0.01-0.14	38% Plag, 62% mafic melt	n.m.	n.m.	n.m.	95	n.m.
IM7	0.71 × 0.66	0.01-0.05	40% Plag, 36% Pyx (CPX), 21% Ol, 3% Sil, 1% Ilm	20-26	18-49	25-61	95-97	68
IMB1	2.83 × 1.59	<0.01-0.27	84% Plag, 6% Pyx, 10% melt	n.m.	n.m.	n.m.	n.m.	n.m.
IMB2	1.49 × 1.44	<0.01-0.19	54% Plag, 10% Pyx, 36% mafic melt	n.m.	n.m.	n.m.	n.m.	n.m.
IMB3	0.23 × 0.61	0.01-0.20	73% Plag, 27% mafic melt	n.m.	n.m.	n.m.	95-96	n.m.
F1	0.42 × 0.77	0.01-0.25	75% Plag, 25% Pyx (OPX)	3.3-7.1	54-68	28-39	95-97	n.m.
F2	0.69 × 0.41	<0.01-0.16	86% Plag, 12% Pyx (CPX; OPX), 1%Ol	7.7-43	31-44	26-52	92-96	54
F3	0.30 × 0.21	<0.01-0.10	83% Plag, 15% Pyx, 2% Ol	n.m.	n.m.	n.m.	97	53-79
F4	0.70 × 0.35	0.01-0.21	75% Plag, 20% Pyx (CPX; OPX), 4% Ol, 1% Ilm	6.6-42	41-49	16-44	96	52-53
F5	1.12 × 0.87	<0.01-0.30	89% Plag, 11% Pyx	n.m.	n.m.	n.m.	n.m.	n.m.
F6	0.54 × 0.81	<0.01-0.30	89% Plag, 11% Pyx (CPX; OPX)	5.3-16	46-49	38-46	96	n.m.
M1	0.47 × 1.23	0.02-0.42	82% Plag, 4% Pyx, 12% Ol, 1% Ilm	4.6	80	16	95-96	81-82
M2	0.46 × 0.84	0.01-0.23	76% Plag, 16% Pyx (OPX), 8% Ol	2.9-3.5	72-74	23-24	90-97	70-71
M3	0.32 × 0.32	<0.01-0.14	85% Plag, 8% Pyx (OPX), 7% Ol	3.6	77	20	96	76

Wo = Pyroxene wollastonite value calculated as atomic Ca/[Ca+Fe+Mg]×100; En = Pyroxene enstatite value calculated as atomic Mg/[Ca+Fe+Mg]×100; Fs = Pyroxene (Pyx) ferrosilite value calculated as atomic Fe/[Ca+Fe+Mg]×100; An-range = Plagioclase (Plag) anorthite range calculated as atomic Ca/[Ca+K+Na]×100; Fo-range = Olivine (Ol) forsterite range calculated as atomic Mg/[Mg+Fe]×100; CPX = Clinopyroxene; OPX = Orthopyroxene.

There are fractures running throughout the sample, with apparently random orientation. These fractures have been subject to terrestrial mineral deposition, in the form of high concentrations of $CaCO_3$ (see Fig. 3.2b where Ca is highlighted as yellow). When analysing individual mineral grain chemistries, phases located away from fractures and holes in the sample were selected to avoid the effects of such terrestrial contaminants.

It was harder to avoid such fractures and holes when acquiring clast bulk chemistries, and therefore it should be assumed that these data may be affected by terrestrial contaminants. The work of *Crozaz et al.* (2003) suggests that enrichments of Sr and Ba will occur in feldspathic material due to terrestrial alteration. Materials containing a large amount of mafic minerals are believed to be more susceptible to alteration of rare earth element (REE) abundances due to terrestrial contamination (*Crozaz et al.*, 2003). This is supported by *Shih et al.* (2002) who ascribed disturbances in the Rb-Sr and Sm-Nd systems within the mare basalt component of the lunar meteorite Dhofar 287 to terrestrially altered material.

Detailed mineral chemistries of a number of individual clasts are described below.

Table 3.2: Major, minor and trace element concentrations in NEA 001 clasts, as identified in Fig. 3.2a Major and minor element concentrations are given as oxide wt% values. To correct for unequal host-phase density effects these values were multiplied by correction factors generated using the method described by *Warren* (1997). Minor and trace element concentrations measured by LA-ICP-MS are given as ppm values. LA-ICP-MS values for Ti, Cr, and Mn have also been presented as oxide wt% values in order to facilitate comparison with the raster beam analyses. Errors for major elements are 1σ standard deviations. Errors for trace elements are 1σ standard deviation variations between the tracks measured in each clast.

Table 3.2

	B1a	B1b	B2	B3	B5	B6
Major and minor elements measured by raster beam analyses (wt%)						
SiO_2	45.42 ± 0.43	47.85 ± 0.40	42.70 ± 0.03	74.50 ± 17.40	45.74 ± 1.14	50.52 ± 0.15
TiO_2	0.55 ± 0.11	0.40 ± 0.13	2.24 ± 0.15	0.33 ± 0.06	0.61 ± 0.16	1.60 ± 0.56
Al_2O_3	15.85 ± 0.19	17.74 ± 0.32	18.74 ± 0.28	12.39 ± 9.92	9.50 ± 2.29	15.14 ± 0.67
Cr_2O_3	0.41 ± 0.09	0.42 ± 0.07	0.10 ± 0.07	b.d.	0.38 ± 0.13	0.35 ± 0.01
FeO	16.54 ± 0.20	12.21 ± 0.28	13.36 ± 0.39	3.92 ± 1.90	20.50 ± 2.04	13.64 ± 1.00
MnO	0.22 ± 0.05	b.d.	0.09 ± 0.07	b.d.	0.21 ± 0.17	0.14 ± 0.01
MgO	9.61 ± 0.28	9.27 ± 0.16	5.75 ± 0.15	1.26 ± 0.32	8.63 ± 1.61	7.64 ± 0.59
CaO	11.86 ± 0.37	11.12 ± 0.24	16.08 ± 0.20	8.31 ± 5.91	14.58 ± 1.13	10.23 ± 0.10
K_2O	b.d.	b.d.	0.08 ± 0.05	b.d.	0.05 ± 0.03	0.18 ± 0.06
Na_2O	0.30 ± 0.04	0.35 ± 0.06	0.64 ± 0.04	0.25 ± 0.10	0.27 ± 0.03	0.40 ± 0.13
P_2O_5	b.d.	b.d.	0.26 ± 0.09	0.25 ± 0.09	b.d.	0.27 ± 0.05
Total	100.76	99.35	100.04	101.22	100.47	100.10
Mg#	50.90	57.51	43.43	36.49	42.91	49.97
Na_2O+K_2O	0.30	0.35	0.72	0.25	0.32	0.58
No. of raster beam analyses	9	4	4	4	4	2
Minor and trace elements measured by LA-ICP-MS (ppm; wt% for TiO_2, Cr_2O_3 and MnO)						
Sc	50.6 ± 11.1	37.3 ± 31.4	n.m.	n.m.	n.m.	39.1 ± 10.4
Ti	2749 ± 1071	1540 ± 1020	n.m.	n.m.	n.m.	4351 ± 2432
TiO_2	0.46 ± 0.18	0.26 ± 0.17	n.m.	n.m.	n.m.	0.73 ± 0.41
V	125 ± 28	b.d.	n.m.	n.m.	n.m.	105 ± 63
Cr	2404 ± 495	b.d.	n.m.	n.m.	n.m.	2566 ± 1932
Cr_2O_3	0.35 ± 0.07	b.d.	n.m.	n.m.	n.m.	0.38 ± 0.28
Mn	2217 ± 290	1575 ± 1414	n.m.	n.m.	n.m.	1420 ± 442
MnO	0.29 ± 0.04	0.20 ± 0.18	n.m.	n.m.	n.m.	0.18 ± 0.06
Co	31.2 ± 10.1	21.3 ± 19.2	n.m.	n.m.	n.m.	29.3 ± 16.1
Ni	1.48 ± 0.42	10.6 ± 2.1	n.m.	n.m.	n.m.	46.1 ± 39.5
Cu	4.09 ± 1.38	4.68 ± 2.21	n.m.	n.m.	n.m.	b.d.
Zn	11.4 ± 2.4	14.2 ± 7.0	n.m.	n.m.	n.m.	6.41 ± 1.32
Ga	5.94 ± 2.08	12.9 ± 11.8	n.m.	n.m.	n.m.	22.2 ± 12.7
Rb	0.28 ± 0.11	0.50 ± 0.03	n.m.	n.m.	n.m.	b.d.
Sr	109 ± 24	166 ± 40	n.m.	n.m.	n.m.	118 ± 13
Y	7.59 ± 3.39	4.67 ± 1.88	n.m.	n.m.	n.m.	50.1 ± 35.6
Zr	9.13 ± 4.96	6.71 ± 2.36	n.m.	n.m.	n.m.	222 ± 204
Nb	0.32 ± 0.17	0.42 ± 0.20	n.m.	n.m.	n.m.	18.6 ± 17.2
Ba	65 ± 33	b.d.	n.m.	n.m.	n.m.	316 ± 187
La	0.35 ± 0.15	0.56 ± 0.08	n.m.	n.m.	n.m.	20.2 ± 17.0
Ce	1.11 ± 0.46	1.42 ± 0.22	n.m.	n.m.	n.m.	50.3 ± 41.8
Pr	0.20 ± 0.09	0.27 ± 0.02	n.m.	n.m.	n.m.	6.71 ± 5.42
Nd	1.05 ± 0.48	1.04 ± 0.21	n.m.	n.m.	n.m.	28.2 ± 23.7
Sm	0.49 ± 0.24	0.36 ± 0.12	n.m.	n.m.	n.m.	7.23 ± 5.78
Eu	0.31 ± 0.03	0.44 ± 0.05	n.m.	n.m.	n.m.	0.70 ± 0.18
Gd	0.74 ± 0.36	0.53 ± 0.18	n.m.	n.m.	n.m.	7.81 ± 6.11
Tb	0.16 ± 0.08	0.11 ± 0.03	n.m.	n.m.	n.m.	1.39 ± 1.01
Dy	1.28 ± 0.53	0.86 ± 0.35	n.m.	n.m.	n.m.	9.73 ± 7.02
Ho	0.30 ± 0.13	0.19 ± 0.08	n.m.	n.m.	n.m.	1.96 ± 1.42
Er	0.91 ± 0.42	0.57 ± 0.24	n.m.	n.m.	n.m.	5.73 ± 4.13
Tm	0.15 ± 0.06	0.09 ± 0.03	n.m.	n.m.	n.m.	0.86 ± 0.55
Yb	1.15 ± 0.56	0.63 ± 0.29	n.m.	n.m.	n.m.	5.78 ± 3.89
Lu	0.18 ± 0.08	0.11 ± 0.05	n.m.	n.m.	n.m.	0.82 ± 0.53
Hf	0.37 ± 0.17	0.24 ± 0.11	n.m.	n.m.	n.m.	5.58 ± 4.93
Pb	0.40 ± 0.05	0.58 ± 0.11	n.m.	n.m.	n.m.	1.70 ± 1.27
Th	0.03 ± 0.02	0.09 ± 0.02	n.m.	n.m.	n.m.	4.92 ± 4.20
U	0.04 ± 0.03	0.14 ± 0.12	n.m.	n.m.	n.m.	1.43 ± 0.87
No. of LA-ICP-MS analyses	6	3				3

Table 3.2 (continued)

	IM1	IM2	IM3	IM4	IM7
Major and minor elements measured by raster beam analyses (wt%)					
SiO_2	43.32 ± 0.32	44.20 ± 0.17	45.49 ± 0.21	46.32 ± 0.27	47.72 ± 0.19
TiO_2	0.23 ± 0.15	0.29 ± 0.09	0.25 ± 0.16	0.32 ± 0.07	0.38 ± 0.07
Al_2O_3	23.78 ± 0.34	26.99 ± 0.29	22.80 ± 0.50	23.92 ± 0.26	13.51 ± 0.66
Cr_2O_3	0.16 ± 0.14	0.10 ± 0.08	b.d.	0.23 ± 0.10	0.56 ± 0.00
FeO	6.44 ± 0.32	4.74 ± 0.15	6.09 ± 0.29	6.97 ± 0.11	15.75 ± 0.46
MnO	b.d.	b.d.	0.06 ± 0.05	0.12 ± 0.08	0.24 ± 0.08
MgO	6.86 ± 0.25	4.28 ± 0.13	6.04 ± 0.25	6.25 ± 0.17	11.69 ± 0.49
CaO	17.23 ± 0.36	18.26 ± 0.15	15.72 ± 0.27	14.62 ± 0.20	9.34 ± 0.31
K_2O	0.07 ± 0.04	0.11 ± 0.02	0.05 ± 0.02	0.04 ± 0.03	b.d.
Na_2O	0.39 ± 0.07	0.47 ± 0.05	0.36 ± 0.07	0.34 ± 0.04	0.26 ± 0.04
P_2O_5	0.22 ± 0.10	0.19 ± 0.09	0.18 ± 0.04	0.19 ± 0.08	0.15 ± 0.07
Total	98.69	99.63	97.05	99.30	99.59
Mg#	65.52	61.72	63.86	61.53	56.97
Na_2O+K_2O	0.46	0.58	0.41	0.38	0.26
No. of raster beam analyses	5	4	3	4	5
Minor and trace elements measured by LA-ICP-MS (ppm; wt% for TiO_2, Cr_2O_3 and MnO)					
Sc	17.5 ± 0.8	13.0 ± 0.8	18.1 ± 2.3	n.m.	46.0 ± 2.0
Ti	2175 ± 96	2040 ± 310	2005 ± 392	n.m.	2098 ± 286
TiO_2	0.36 ± 0.02	0.34 ± 0.05	0.33 ± 0.07	n.m.	0.35 ± 0.05
V	33.2 ± 1.4	17.6 ± 1.0	34.1 ± 2.8	n.m.	145 ± 1
Cr	941 ± 29	527 ± 42	880 ± 98	n.m.	3152 ± 305
Cr_2O_3	0.14 ± 0.01	0.08 ± 0.01	0.13 ± 0.01	n.m.	0.46 ± 0.04
Mn	779 ± 44	598 ± 51	817 ± 118	n.m.	2112 ± 50
MnO	0.10 ± 0.01	0.08 ± 0.01	0.11 ± 0.02	n.m.	0.27 ± 0.01
Co	13.1 ± 1.3	8.9 ± 1.23	12.5 ± 1.6	n.m.	36.5 ± 5.4
Ni	46.8 ± 7.3	7.6 ± 1.85	46.5 ± 5.1	n.m.	41.6 ± 10.7
Cu	5.26 ± 0.85	4.77 ± 0.31	5.89 ± 1.24	n.m.	4.02 ± 0.13
Zn	9.88 ± 1.28	7.99 ± 1.09	8.18 ± 0.94	n.m.	21.6 ± 8.2
Ga	9.74 ± 3.09	8.49 ± 1.30	6.48 ± 2.05	n.m.	4.00 ± 0.12
Rb	0.61 ± 0.12	0.49 ± 0.06	0.52 ± 0.09	n.m.	0.24 ± 0.06
Sr	224 ± 23	259 ± 10	159 ± 20	n.m.	92 ± 0.27
Y	7.85 ± 0.30	6.99 ± 0.38	6.69 ± 1.22	n.m.	5.58 ± 1.12
Zr	22.7 ± 1.0	19.8 ± 1.9	18.8 ± 3.4	n.m.	8.5 ± 0.35
Nb	1.97 ± 0.09	1.50 ± 0.27	1.68 ± 0.34	n.m.	0.46 ± 0.09
Ba	109 ± 43	99.2 ± 20.0	71.1 ± 35.9	n.m.	41.4 ± 2.6
La	2.05 ± 0.12	b.d.	1.66 ± 0.32	n.m.	0.41 ± 0.06
Ce	5.19 ± 0.34	b.d.	4.18 ± 0.71	n.m.	1.07 ± 0.16
Pr	0.75 ± 0.06	b.d.	0.58 ± 0.11	n.m.	0.17 ± 0.03
Nd	3.22 ± 0.16	2.58 ± 0.22	2.69 ± 0.57	n.m.	0.87 ± 0.19
Sm	0.93 ± 0.05	0.89 ± 0.11	0.77 ± 0.11	n.m.	0.37 ± 0.08
Eu	0.81 ± 0.03	0.86 ± 0.04	0.70 ± 0.07	n.m.	0.24 ± 0.03
Gd	0.99 ± 0.10	1.06 ± 0.13	0.85 ± 0.18	n.m.	0.53 ± 0.13
Tb	0.22 ± 0.03	0.20 ± 0.05	0.17 ± 0.04	n.m.	0.11 ± 0.02
Dy	1.51 ± 0.08	1.38 ± 0.06	1.21 ± 0.16	n.m.	0.88 ± 0.13
Ho	0.34 ± 0.02	0.31 ± 0.02	0.26 ± 0.06	n.m.	0.22 ± 0.04
Er	0.99 ± 0.07	0.78 ± 0.05	0.79 ± 0.14	n.m.	0.71 ± 0.06
Tm	0.16 ± 0.02	0.14 ± 0.01	0.12 ± 0.02	n.m.	0.11 ± 0.02
Yb	1.04 ± 0.07	0.88 ± 0.08	0.87 ± 0.18	n.m.	0.86 ± 0.19
Lu	0.15 ± 0.02	0.13 ± 0.01	0.13 ± 0.02	n.m.	0.14 ± 0.03
Hf	0.66 ± 0.08	0.54 ± 0.07	0.54 ± 0.14	n.m.	0.28 ± 0.05
Pb	0.63 ± 0.14	b.d.	0.49 ± 0.09	n.m.	0.71 ± 0.06
Th	0.34 ± 0.03	b.d.	0.26 ± 0.04	n.m.	0.05 ± 0.00
U	0.32 ± 0.08	b.d.	0.21 ± 0.11	n.m.	0.05 ± 0.01
No. of LA-ICP-MS analyses	4	4	4		2

Table 3.2 (continued)

	IMB1	IMB2	IMB3	Glass Beads
Major and minor elements measured by raster beam analyses (wt%)				
SiO_2	44.80 ± 0.30	46.06 ± 0.19	42.40 ± 0.24	46.18 ± 0.24
TiO_2	0.36 ± 0.10	0.32 ± 0.09	0.34 ± 0.18	0.41 ± 0.03
Al_2O_3	24.15 ± 2.83	24.00 ± 0.34	25.19 ± 0.21	21.16 ± 0.89
Cr_2O_3	0.09 ± 0.01	0.15 ± 0.10	0.17 ± 0.07	0.21 ± 0.04
FeO	6.47 ± 2.37	5.24 ± 0.09	5.95 ± 0.21	7.63 ± 0.50
MnO	0.09 ± 0.08	0.12 ± 0.11	0.09 ± 0.03	0.12 ± 0.02
MgO	9.74 ± 4.32	5.70 ± 0.23	6.02 ± 0.16	8.08 ± 0.36
CaO	14.94 ± 2.27	15.30 ± 0.39	18.35 ± 0.33	13.88 ± 0.26
K_2O	b.d.	0.05 ± 0.04	0.09 ± 0.05	b.d.
Na_2O	0.47 ± 0.05	0.39 ± 0.02	0.42 ± 0.02	0.11 ± 0.09
P_2O_5	0.14 ± 0.04	0.19 ± 0.06	0.25 ± 0.11	0.03 ± 0.01
Total	101.25	97.52	99.28	97.81
Mg#	72.87	66.01	64.32	65.39
Na_2O+K_2O	0.47	0.45	0.51	0.11
No. of raster beam analyses	4	4	4	
Minor and trace elements measured by LA-ICP-MS (ppm; wt% for TiO_2, Cr_2O_3 and MnO)				
Sc	12.3 ± 4.1	13.9 ± 1.2	n.m.	n.m.
Ti	2131 ± 849	1936 ± 129	n.m.	n.m.
TiO_2	0.36 ± 0.14	0.32 ± 0.02	n.m.	n.m.
V	28.4 ± 12.6	28.6 ± 2.8	n.m.	n.m.
Cr	730 ± 312	840 ± 42	n.m.	n.m.
Cr_2O_3	0.11 ± 0.05	0.12 ± 0.01	n.m.	n.m.
Mn	578 ± 196	670 ± 47	n.m.	n.m.
MnO	0.07 ± 0.03	0.09 ± 0.01	n.m.	n.m.
Co	9.82 ± 3.76	15.7 ± 1.6	n.m.	n.m.
Ni	17.8 ± 2.8	120 ± 16	n.m.	n.m.
Cu	3.60 ± 0.63	4.44 ± 0.61	n.m.	n.m.
Zn	9.00 ± 2.39	5.53 ± 0.81	n.m.	n.m.
Ga	9.30 ± 1.57	4.50 ± 0.58	n.m.	n.m.
Rb	0.67 ± 0.19	0.85 ± 0.06	n.m.	n.m.
Sr	209 ± 14	140 ± 5	n.m.	n.m.
Y	7.20 ± 3.52	9.90 ± 1.57	n.m.	n.m.
Zr	26.2 ± 15.7	32.8 ± 6.0	n.m.	n.m.
Nb	4.08 ± 3.90	3.10 ± 0.55	n.m.	n.m.
Ba	110 ± 16	45.2 ± 8.7	n.m.	n.m.
La	b.d.	2.78 ± 0.51	n.m.	n.m.
Ce	b.d.	7.35 ± 1.41	n.m.	n.m.
Pr	b.d.	1.02 ± 0.20	n.m.	n.m.
Nd	3.49 ± 1.51	4.34 ± 0.96	n.m.	n.m.
Sm	0.95 ± 0.47	1.31 ± 0.22	n.m.	n.m.
Eu	0.87 ± 0.08	0.75 ± 0.05	n.m.	n.m.
Gd	1.10 ± 0.49	1.49 ± 0.31	n.m.	n.m.
Tb	0.23 ± 0.10	0.25 ± 0.04	n.m.	n.m.
Dy	1.43 ± 0.70	1.83 ± 0.34	n.m.	n.m.
Ho	0.37 ± 0.17	0.38 ± 0.08	n.m.	n.m.
Er	0.88 ± 0.38	1.08 ± 0.21	n.m.	n.m.
Tm	0.15 ± 0.04	0.16 ± 0.02	n.m.	n.m.
Yb	0.91 ± 0.42	1.21 ± 0.16	n.m.	n.m.
Lu	0.14 ± 0.05	0.17 ± 0.03	n.m.	n.m.
Hf	0.71 ± 0.40	0.83 ± 0.17	n.m.	n.m.
Pb	b.d.	0.34 ± 0.09	n.m.	n.m.
Th	b.d.	0.50 ± 0.12	n.m.	n.m.
U	b.d.	0.22 ± 0.07	n.m.	n.m.
No. of LA-ICP-MS analyses	4	4		

Table 3.2 (continued)

	F1	F6	M1	M2
Major and minor elements measured by raster beam analyses (wt%)				
SiO_2	46.39 ± 0.08	45.90 ± 0.13	41.04 ± 0.68	39.81 ± 1.96
TiO_2	0.35 ± 0.08	0.17 ± 0.05	b.d.	0.23 ± 0.10
Al_2O_3	23.63 ± 0.53	30.15 ± 0.02	27.10 ± 0.43	21.09 ± 2.15
Cr_2O_3	0.16 ± 0.04	0.05 ± 0.04	b.d.	0.15 ± 0.10
FeO	7.38 ± 0.57	2.99 ± 0.10	4.20 ± 0.51	10.86 ± 2.98
MnO	0.08 ± 0.08	0.07 ± 0.01	b.d.	0.11 ± 0.08
MgO	6.64 ± 0.43	2.58 ± 0.08	9.52 ± 0.77	14.63 ± 3.29
CaO	13.60 ± 0.24	17.16 ± 0.08	16.68 ± 1.53	12.86 ± 1.00
K_2O	b.d.	b.d.	0.07 ± 0.04	0.06 ± 0.02
Na_2O	0.33 ± 0.06	0.39 ± 0.02	0.45 ± 0.04	0.43 ± 0.06
P_2O_5	0.15 ± 0.02	0.19 ± 0.04	0.21 ± 0.07	0.20 ± 0.08
Total	98.70	99.64	99.29	100.42
Mg#	61.61	60.61	80.19	70.62
Na_2O+K_2O	0.33	0.39	0.52	0.49
No. of raster beam analyses	4	3	5	5

Acronyms used to describe the clasts are as follows: IM = Impact Melt; IMB = Impact Melt Breccia; F = Ferroan Anorthosite; M = Magnesian Anorthosite; B = Basaltic. Values which were below instrument detection limits (b.d.) or not measured (n.m.) have been indicated.

Matrix and Individual Mineral Grains

The section studied has a relatively fine-grained (<0.01 mm) matrix, containing individual mineral grains (up to ∼0.15 mm). These include plagioclase (∼72% by modal abundance), pyroxene (∼25%) and olivine (∼3%) mineral fragments that are within the compositional ranges of the minerals within lithic clasts in the sample, indicating a common origin (Table 3.3; Fig. 3.3).

Other less common mineral grains (<1% modally) include very small (<0.05 mm) oxide and sulphide grains. The oxides within the section are all ilmenites (53.1-56.3 TiO_2 wt%; 34.7-42.5 FeO wt%; Table 3.3). The sulfide grains observed within the sample are mostly subhedral with typical lunar troilite compositions (61.7-63.5 Fe wt%; 35.9-37.5 S wt%).

In addition to the silicate, oxide, and sulfide phases, a minor (<<1%) metallic component is observed in the sample matrix. This is represented by small (<0.1 mm), often anhedral, grains of predominantly iron-nickel composition (87.9-98.4 Fe wt%; 0.4-10.6 Ni wt%; 0.6-1.6 Co wt%). The largest of these (∼0.1 mm) is visible in Fig. 3.2a as a bright grain in the top left corner of the image (labelled as 'Metal'). The metal grain with the lowest Ni content (0.4 wt%) is possibly lunar in origin (*Papike et al.*, 1991). The higher nickel content (∼10 wt%) of the remaining grains is suggestive of a meteoritic origin. Owing to their small size, it was not possible to perform further siderophile element analyses of these grains that might provide a definitive indication of their origin (i.e. lunar or meteoritic; *Papike et al.* 1991; *Day et al.* 2010).

Table 3.3: Representative chemical compositions of minerals within the clasts and matrix of NEA 001.

	Basaltic Clasts	Impact Melt Clasts	Impact Melt Breccia Clasts	Ferroan Noritic Anorthosite Clasts	M1	M2	M3	Matrix mineral grains
Olivine								
SiO_2	36.61	38.07	n.m.	36.21	39.36	37.77	38.54	36.74
TiO_2	0.05	0.06	n.m.	0.03	0.02	0.07	0.05	0.11
Al_2O_3	0.04	0.66	n.m.	0.11	0.13	0.26	0.03	0.03
Cr_2O_3	0.08	0.07	n.m.	0.02	0.06	b.d.	0.02	0.03
FeO	31.39	26.55	n.m.	38.59	17.40	25.80	21.61	34.03
MnO	0.42	0.25	n.m.	0.43	0.21	0.28	0.28	0.35
MgO	31.49	33.32	n.m.	25.29	44.07	35.44	38.12	29.16
CaO	0.32	0.62	n.m.	0.18	0.09	0.10	0.21	0.11
Na_2O	b.d.	0.03	n.m.	b.d.	b.d.	0.01	b.d.	0.01
K_2O	b.d.	0.01	n.m.	b.d.	b.d.	0.01	b.d.	b.d.
Total	100.39	99.62	n.m.	100.85	101.34	99.73	98.87	100.56
Mg#	64.13	69.10	n.m.	53.87	81.87	71.00	75.87	60.43
Pyroxene								
SiO_2	50.00	51.58	n.m.	51.62	55.42	53.48	53.31	50.86
TiO_2	0.40	0.58	n.m.	0.19	0.77	0.65	0.68	0.21
Al_2O_3	1.76	1.47	n.m.	1.06	1.10	1.50	2.46	1.50
Cr_2O_3	0.72	0.22	n.m.	0.55	0.55	0.39	0.36	0.76
FeO	24.65	24.34	n.m.	25.01	10.60	14.92	12.30	21.18
MnO	0.48	0.37	n.m.	0.46	0.21	0.28	0.21	0.43
MgO	13.33	15.81	n.m.	14.39	30.20	26.43	26.97	14.54
CaO	8.02	6.86	n.m.	6.28	2.44	1.64	1.76	9.67
Na_2O	0.02	0.04	n.m.	b.d.	0.01	0.03	b.d.	0.01
K_2O	b.d.	b.d.	n.m.	0.01	b.d.	b.d.	0.01	b.d.
Total	99.37	101.26	n.m.	99.58	101.28	99.31	98.06	99.16
Mg#	49.08	53.66	n.m.	50.63	83.55	75.95	79.62	55.03
En	40.49	45.96	n.m.	43.69	79.68	73.46	76.77	43.56
Wo	17.50	14.33	n.m.	13.70	4.63	3.28	3.59	20.83
Fs	42.01	39.70	n.m.	42.61	15.69	23.26	19.64	35.60
Plagioclase								
SiO_2	45.34	45.38	44.11	44.61	44.25	44.04	44.34	44.26
TiO_2	b.d.	0.05	0.06	0.01	0.05	0.06	0.05	0.02
Al_2O_3	32.63	33.50	34.64	34.14	33.25	33.16	33.28	33.78
Cr_2O_3	b.d.	0.02	b.d.	b.d.	0.01	b.d.	0.01	b.d.
FeO	0.11	0.23	0.23	0.26	0.21	0.25	0.16	0.19
MnO	b.d.	b.d.	0.03	b.d.	0.02	0.02	0.02	0.01
MgO	0.04	0.16	0.26	0.03	0.62	0.15	0.29	0.10
CaO	18.80	19.12	19.19	19.61	19.18	19.53	19.23	19.55
Na_2O	0.94	0.53	0.53	0.45	0.47	0.37	0.41	0.43
K_2O	0.08	0.02	0.05	0.02	0.07	0.01	0.04	0.01
Total	97.95	99.02	99.10	99.12	98.12	97.58	97.84	98.35
An#	91.25	95.12	94.93	95.89	95.41	96.63	96.02	96.15

	B2	M1	Matrix mineral grains
Ilmenite			
SiO_2	0.09	0.06	0.09
TiO_2	53.89	56.28	53.87
Al_2O_3	0.04	0.03	0.05
Cr_2O_3	0.07	0.22	0.16
FeO	42.27	35.14	40.92
MnO	0.38	0.43	0.41
MgO	1.69	7.60	2.66
CaO	0.35	0.07	0.46
Na_2O	0.01	b.d.	0.01
K_2O	b.d.	b.d.	b.d.
Total	98.79	99.84	98.63
Fe#	93.36	72.18	89.61

An# = atomic Ca/[Ca+Na+K]×100; Mg# = atomic Mg/[Mg+Fe]×100 and Fe# = atomic Fe/[Mg+Fe]×100.

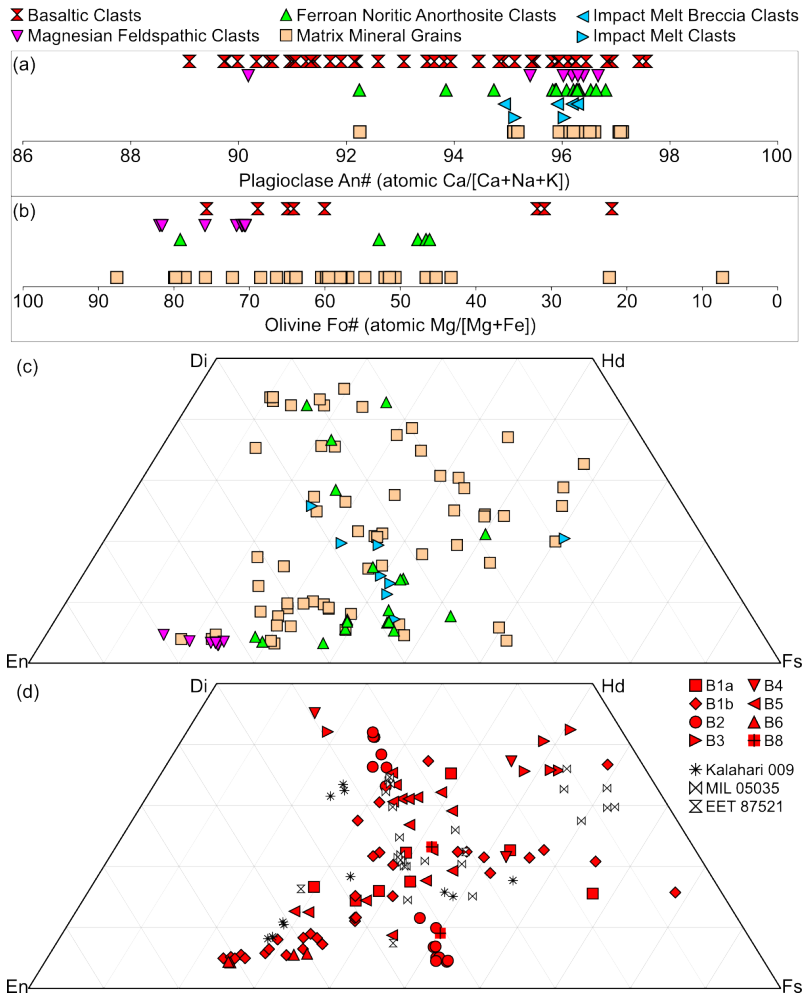

Figure 3.3: Mineral compositions of phases in NEA 001 clasts and matrix mineral grains. (a) Range of plagioclase anorthite content (An: atomic Ca/[Ca + Na + K]×100) and (b) olivine forsterite content (Fo: atomic Mg/[Mg+Fe]×100). (c) Pyroxene compositions projected onto a pyroxene quadrilateral. (d) Compositions of pyroxene phases within basaltic clasts in NEA 001. Basaltic pyroxene compositions have been compared with those of the VLT basatic lunar meteorites Kalahari 009, Miller Range (MIL) 05035 and Elephant Moraine (EET) 87521 (*Arai et al.*, 2006; *Sokol et al.*, 2008; *Joy et al.*, 2008). Di = diopside; Hd = hedenbergite; En = enstatite; Fs = ferrosilite.

Basaltic Clasts (clasts B1a, B1b, B2, B3, B5, B6)

Basalt Clast 1 (B1a and B1b): The largest clast within the section is ∼6 × 4 mm in size (Fig. 3.2). The textures seen within this clast are highly variable and the clast is divided into two sub-areas based on this textural diversity (Fig. 3.4). The largest area of the clast (B1a; 4.4 × 2.6 mm) is dominated by textures typical of crystalline basaltic material which has been shocked (Fig. 3.5a-c), whereas the smaller area (B1b; 1.9 × 1.5 mm) exhibits a more brecciated texture (Fig. 3.4). Both sections of the clast contain evidence of shock metamorphism, in the form of irregular fractures within olivine, pyroxene and plagioclase grains, and some planar fractures within olivine and pyroxene grains, indicating that the phases have witnessed shock pressures of at least

5-10 GPa (*Stöffler et al.*, 1979; *Rubin et al.*, 1997). The boundary separating the brecciated and crystalline portions of the clast is gradual and poorly defined (Fig. 3.4). Both sections of the clast are compositionally similar, but not identical (Table 3.2).

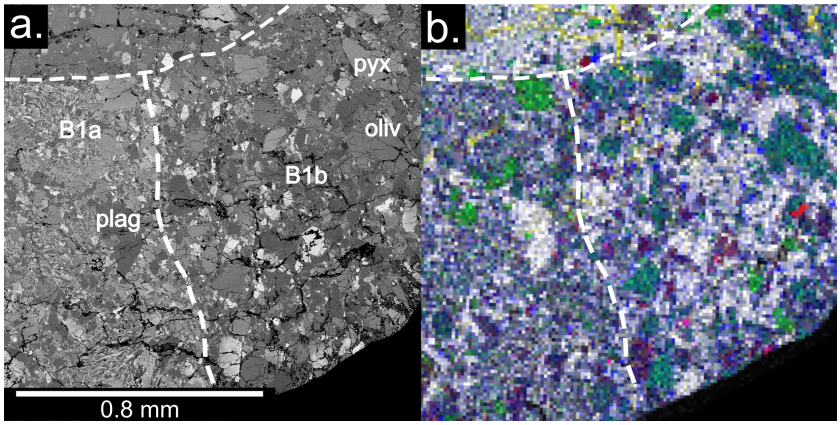

Figure 3.4: (a) BSE image of the boundary between clasts B1a (left) and B1b (right) - a brecciated basaltic clast, exhibiting less lath-like plagioclase crystals than B1a. (b) Montaged false-colour elemental map of the same area (colour scheme is the same as in Fig. 3.2b).

The larger section of the clast (B1a) is predominantly composed of anhedral pyroxene grains subophitically enclosing plagioclase laths. Pyroxene compositions are diverse within this clast (Wo_{14-35} En_{17-54} Fs_{30-67}). The plagioclase grains (An_{96-97}) typically form subhedral laths, however finer grained plumose and dendritic textures are also observed (Figs. 3.5a-b). Olivine is also present (10% by modal abundance) and exhibits normal compositional zonation (Fo_{60-76}). Many of the olivine grains within the clast have undulatory contacts with the pyroxene grains around them. These features are observed on a variety of scales, with both fine (∼0.01 mm) and coarse (∼0.5 mm) grains.

The smaller section (B1b) of the clast has a more brecciated texture and is generally coarser grained than the rest of the clast (Fig. 3.4). Plagioclase grains (An_{94-98}) in this half of the clast are generally larger and less needle-like. The pyroxene component exhibits a larger compositional range (Wo_{5-37} En_{5-72} Fs_{23-78}) than that of B1a.

Both sections of the clast have very low-Ti (VLT) compositions (i.e. where bulk TiO_2 = <1 wt%; *Neal and Taylor* 1992): see Table 3.2. REE concentrations obtained by LA-ICP-MS reveal that both sections of the clast have lower light-rare earth element (LREE) concentrations in comparison with heavy-rare earth element (HREE) abundances (B1a: 0.2 La_{cn}/Lu_{cn}; B1b: 0.5 La_{cn}/Lu_{cn}; where $_{cn}$ implies chondrite normalised values using the CI concentrations reported by *Anders and Grevesse* 1989). Both sections also have positive Eu-anomalies (Fig. 3.6a: B1a = 1.6 Eu/Eu*; B1b = 3.1 Eu/Eu*; where Eu/Eu* is calculated as $Eu_{cn}/\sqrt{[Sm_{cn} \times Gd_{cn}]}$). Compared with

other basaltic lunar meteorites (e.g. *Warren and Kallemeyn* 1993; *Anand et al.* 2003; *Fagan et al.* 2003; *Barrat et al.* 2005; *Day et al.* 2006a; *Joy et al.* 2006, 2008; *Liu et al.* 2009; *Arai et al.* 2010) and VLT basalts from the Apollo and Luna collection (e.g. *Laul et al.* 1978; *Ma et al.* 1978; *Blanchard and Budahn* 1979; *Wentworth et al.* 1979), clast B1 also has lower concentrations of other trace elements such as Th (B1a = 0.04±0.02 ppm; B1b = 0.10±0.01 ppm) and Sm (B1a = 0.52±0.25 ppm; B1b = 0.38±0.12 ppm: Figs. 3.7a-b).

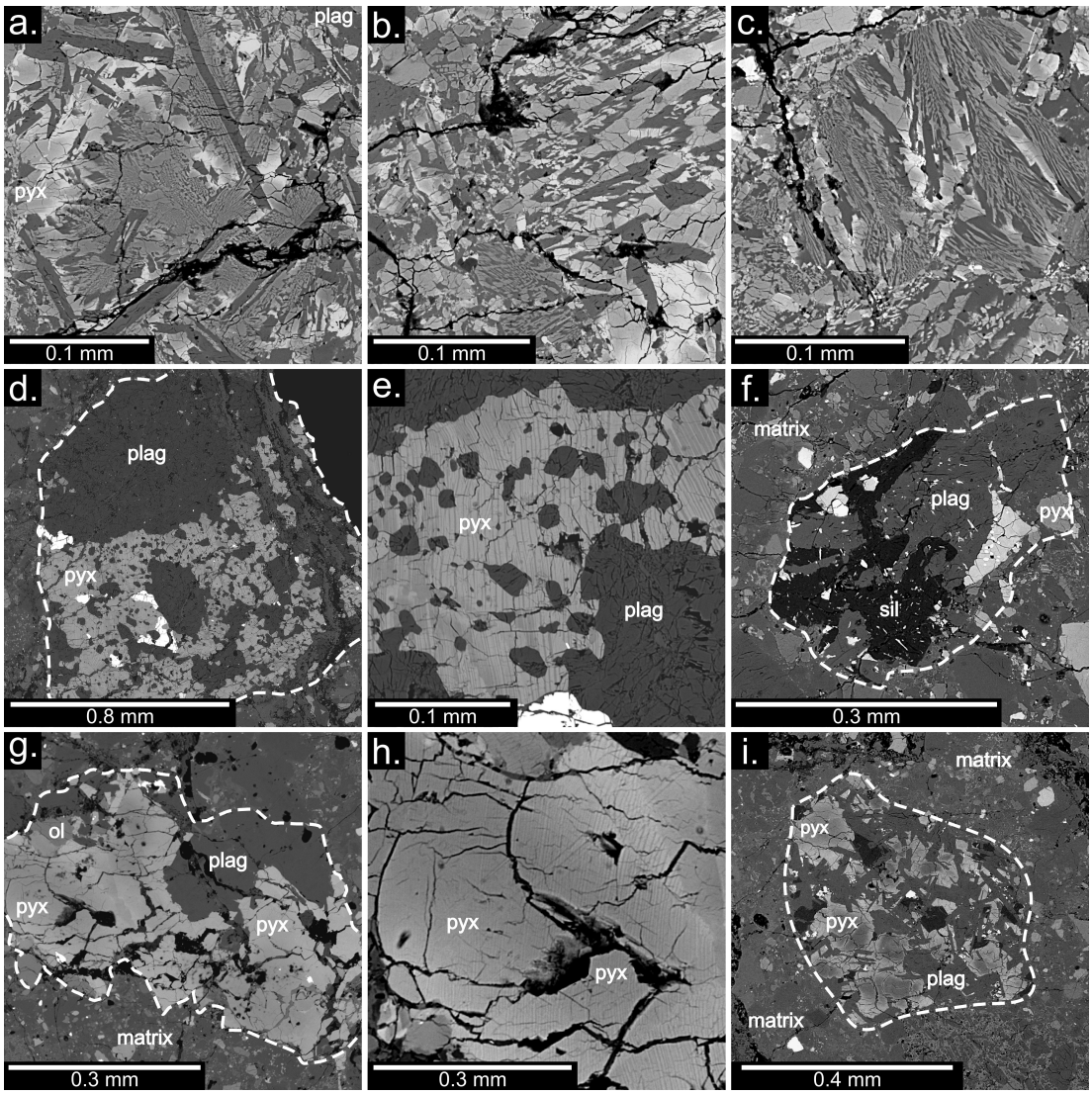

Figure 3.5: Close up BSE images of several analysed basalt clasts. (a-c) B1a - basaltic clast dominated by zoned pyroxene grains and plagioclase laths. (d) B2 - low-Ti gabbroic clast containing mostly homogeneous plagioclase and anhedral pyroxene grains with prominent exsolution lamellae; these are visible in (e). (f) B3 - siliceous basaltic clast. (g) B5 - fractured VLT basaltic clast containing zoned pyroxene with fine lamellae, possibly due to shock; these are visible in (h). (i) B6 - basaltic clast, consisting of zoned pyroxene grains subophitically enclosing plagioclase crystals.

Basalt Clast 2: The mare basalt clast component of the NEA 001 section is almost

entirely of VLT composition (Table 3.2). Two clasts, however, are identified as having low-Ti compositions (i.e. where bulk TiO_2 = 1-6 wt%; *Neal and Taylor* 1992), including a large (1.2 × 1.3 mm) gabbroic clast (B2; Fig. 3.5d). The clast is mostly composed of anhedral pyroxene (Wo_{4-42} En_{33-44} Fs_{25-54}) grains and a plagioclase component (An_{89-94}). The pyroxene grains have prominent exsolution lamellae (∼1-5 μm thick; Fig. 3.5e) and compositions which are consistent with pyroxenes reported in low-Ti basalts in other lunar meteorites (Fig. 3.8). The clast is comparatively richer in Ti (2.24±0.15 TiO_2 wt%; Table 3.2) than the NEA 001 VLT basalt component as it contains several anhedral ilmenite grains (∼50-100 μm), which occur next to pyroxene. The compositions of several of these ilmenite grains were measured and were found to have a Mg# range of 6-7 (Mg# = atomic Mg/[Fe + Mg]). Smaller (∼10 μm) troilite grains and rare bead-like olivine (Fo_{32}) inclusions in the pyroxene are also observed within the clast.

Basalt Clast 3: The most compositionally distinct clast in the sample is a siliceous basaltic fragment (0.4 × 0.3 mm; Table 3.2; Fig. 3.5f). Bulk clast composition data reveals the clast to have a lower Mg# (36.5), and less CaO (8.31 wt%), than all of the other clasts (Mg# range = 42.7-57.5; CaO range = 9.34-16.08 wt%; Table 3.2). Individual plagioclase grains, however, are quite calcic (An_{95}). About 26% (by modal abundance) of the fragment's surface area is formed by silica. This clast is interpreted as representing the mesostasis portion of a VLT basaltic lava, as pyroxene Ti# (atomic Ti/[Ti+Cr]) and Fe# (atomic Fe/[Mg+Fe]) values are similar to the range shown by lunar VLT lavas (Fig. 3.8).

Basalt Clast 5: B5 (0.8 × 0.4 mm) is a fractured VLT (0.63±0.16 TiO_2 wt%; Table 3.2; Fig. 3.5g) basalt fragment, with a crystalline texture. The clast consists of ∼55% pyroxene (Wo_{9-35} En_{29-58} Fs_{29-47}), ∼40% plagioclase (An_{94-96}), and ∼5% olivine (Fo_{78}) by surface area. Some of the pyroxene phases are zoned with rims that are slightly more Fe-rich than the cores of the grains. Whilst the bulk TiO_2 composition of the clast is within the range of VLT basalt, several of the analyses obtained from the less Fe-rich areas of the pyroxene phases display compositions more akin to pyroxenes from low-Ti lunar lavas (Fig. 3.8). Fine grained (∼0.5-1.0 μm) lamellae are also noted within the pyroxene component of B5 that may be due to shock deformation (Fig. 3.5h).

Basalt Clast 6: B6 (0.5 × 0.5 mm) is a coarse grained (>0.1 mm) low-Ti (1.6±0.56 TiO_2 wt%) basaltic clast, consisting of zoned pyroxene grains (Wo_{4-6} En_{60-71} Fs_{24-34}) subophitically enclosing plagioclase laths (Fig. 3.5i). These phases make up a majority of the clast (∼40% plagioclase and ∼50% pyroxene, by modal abundance). Occasional

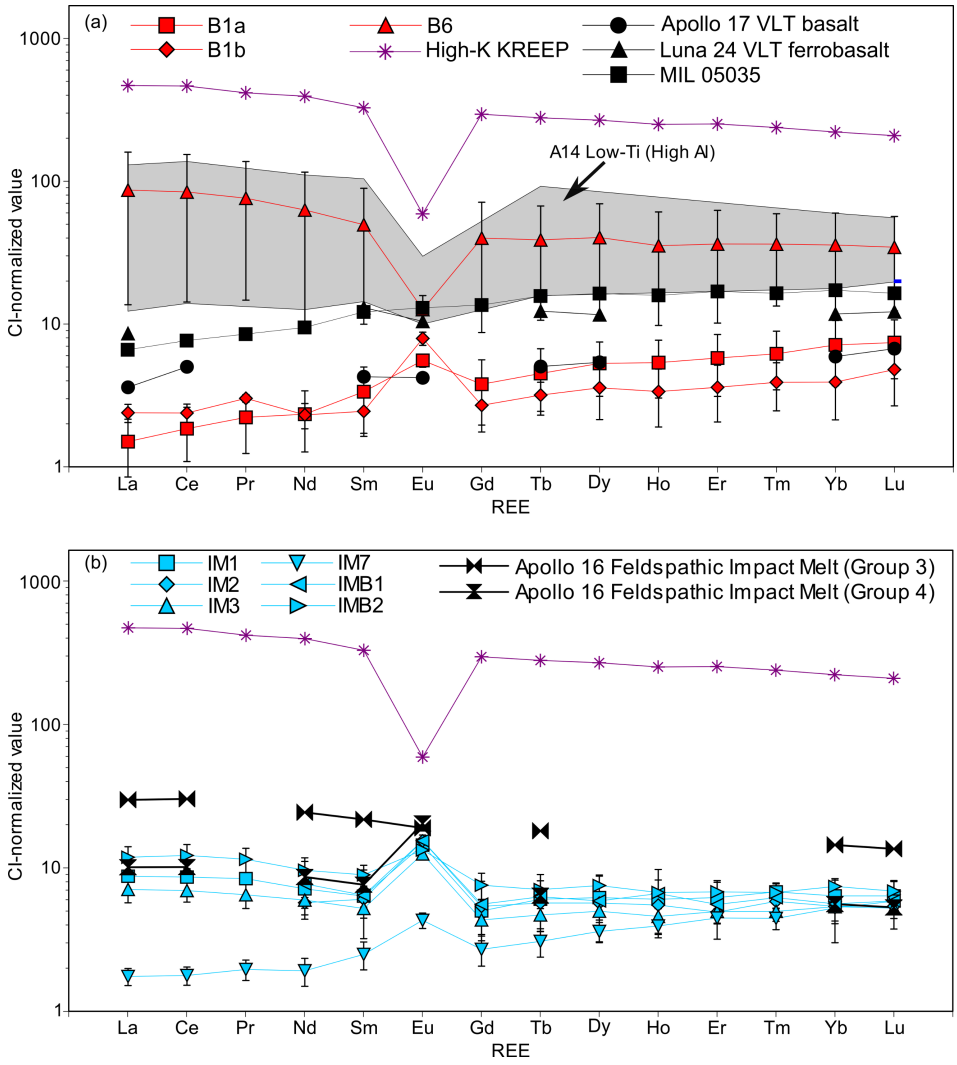

Figure 3.6: Chondrite normalised (*Anders and Grevesse*, 1989) average clast concentrations of REE in (a) basaltic clasts and (b) impact melt clasts. Error bars reflect 1σ standard deviation variations between the tracks measured in each clast (i.e. clast heterogeneity). Basaltic clast concentrations are compared with values for Apollo 14 low-Ti basalts (*Shervais et al.*, 1985; *Neal et al.*, 1988), Apollo 17 VLT basalts (*Blanchard and Budahn*, 1979; *Wentworth et al.*, 1979), a Luna 24 VLT ferrobasalt (*Ma et al.*, 1978); high-K KREEP (*Warren*, 1989) and lunar meteorite MIL 05035 (*Joy et al.*, 2008). Impact melt clast concentrations are compared with the mean composition of the Group-4 Apollo 16 Feldspathic Impact Melts (*Korotev*, 1994) and high-K KREEP (*Warren*, 1989).

(~5% by modal abundance) subhedral silica crystals are present, as well as rare grains of ilmenite (<5% by modal abundance). B6 exhibits trace element concentrations (Th = 4.9±4.2 ppm; Sm = 7.2±5.8 ppm; Sc = 39.1±10.4 ppm; Table 3.2) more similar to those of Apollo low-Ti basalts (Fig. 3.7; see also *Dickinson et al.* 1985; *Shervais et al.* 1985; *Neal et al.* 1988, 1989) and other lunar low-Ti basaltic meteorites (*Warren and Kallemeyn*, 1993; *Anand et al.*, 2003; *Fagan et al.*, 2003; *Barrat et al.*, 2005; *Day et al.*, 2006a; *Joy et al.*, 2006) than the other basaltic clasts in NEA 001 (Fig. 3.7).

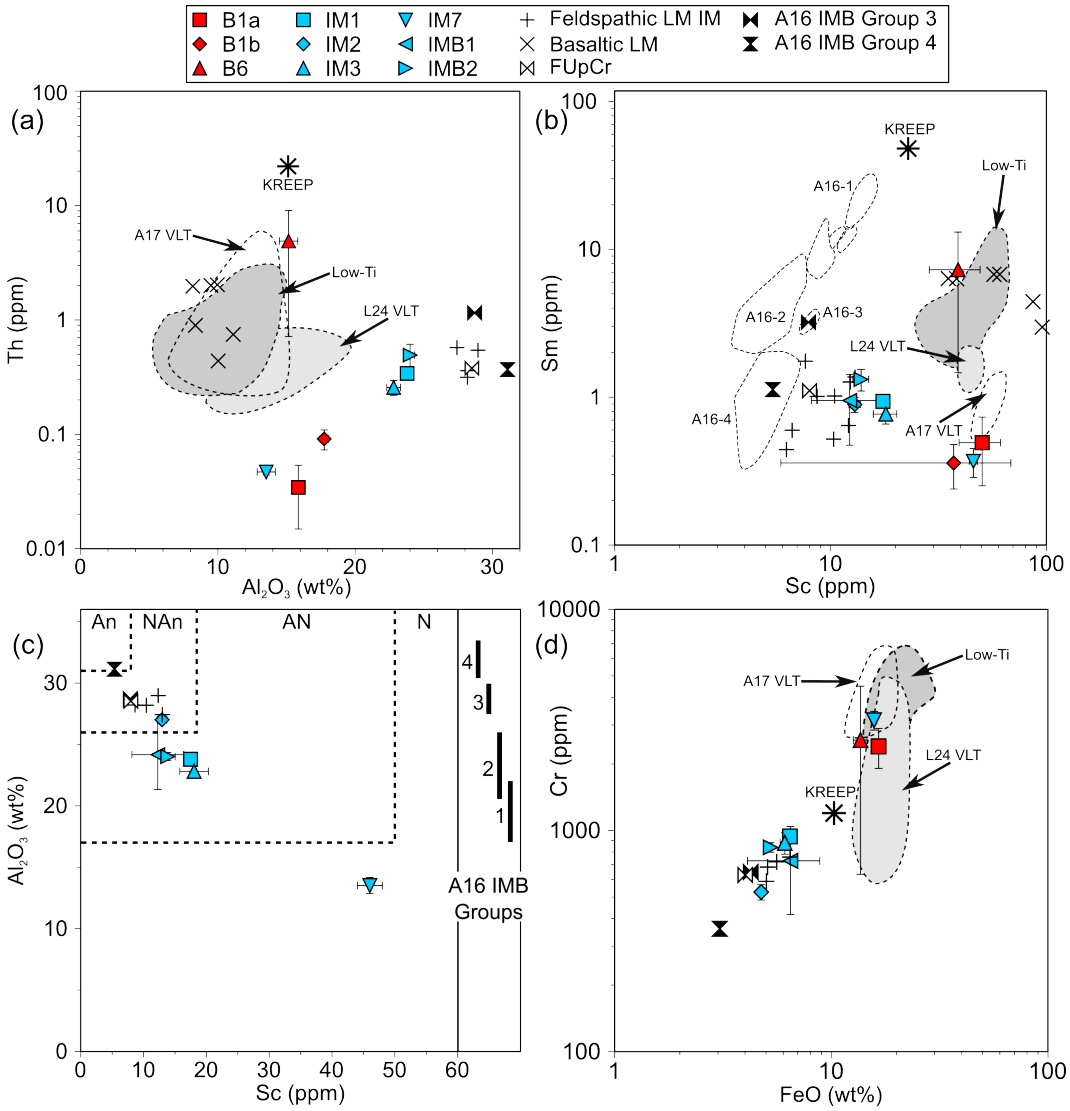

Figure 3.7: NEA 001 bulk clast compositions compared with Apollo 16 Group-3 and Group-4 impact melt groups (A16 IMB; *Korotev* 1994), Apollo low-Ti basalts (*Dickinson et al.*, 1985; *Shervais et al.*, 1985; *Neal et al.*, 1988, 1989), Apollo 17 VLT basalts (*Blanchard and Budahn*, 1979; *Wentworth et al.*, 1979), Luna 24 VLT basalts (*Laul et al.*, 1978; *Ma et al.*, 1978) and literature values for several basaltic lunar meteorites (*Warren and Kallemeyn*, 1993; *Anand et al.*, 2003; *Fagan et al.*, 2003; *Barrat et al.*, 2005; *Day et al.*, 2006a; *Joy et al.*, 2006, 2008), impact melt clasts in other feldspathic meteorites (*Joy et al.*, 2010) and the estimated composition of the upper feldspathic lunar crust (FUpCr; *Korotev et al.* 2003). (a) Th (ppm) vs Al_2O_3 (wt%) in NEA 001. (b) Sm (ppm) vs Sc (ppm). (c) Al_2O_3 (wt%) vs Sc (ppm) in NEA 001 IM and IMB clasts. An = Anorthosite; NAn = Noritic Anorthosite; AN = Anorthositic Norite; N = Norite. (d) Cr (ppm) vs FeO (wt%) in NEA 001 clasts.

Impact Melt and Melt Breccia Clasts (clasts IM1, IM2, IM3, IM4, IM7, IMB1, IMB2, IMB3)

The most commonly occurring clasts in this section of NEA 001 are derived from material formed by impact melting processes. This is in agreement with the observations of *Haloda et al.* (2005). These make up ∼23% of the total sample, by surface area. Major and trace element data were acquired from a number of these clasts, mostly

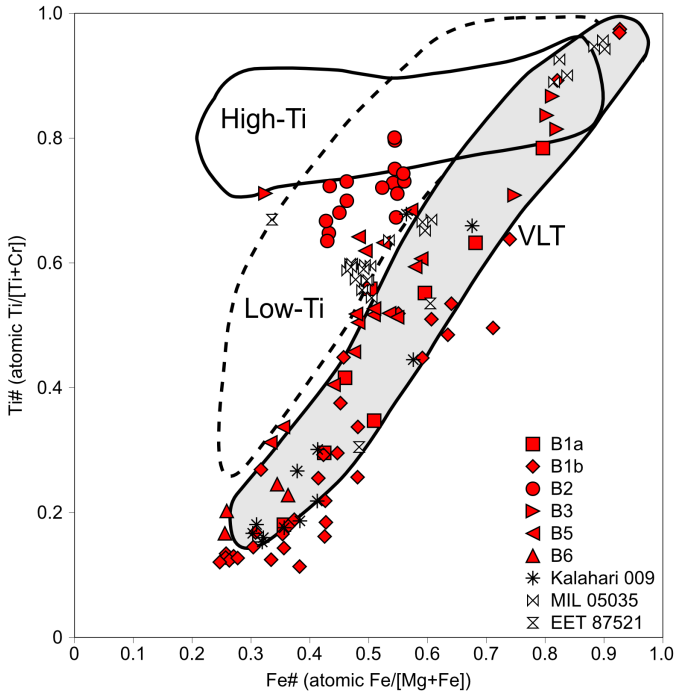

Figure 3.8: Ti# (atomic Ti/[Ti+Cr]) vs Fe# (atomic Fe/[Mg+Fe]) for pyroxene phases within basaltic clasts of NEA 001. NEA 001 pyroxene compositions are compared with those of the VLT basatic lunar meteorites Kalahari 009, Miller Range (MIL) 05035 and Elephant Moraine (EET) 87521 (*Arai et al.*, 2006; *Sokol et al.*, 2008; *Joy et al.*, 2008). High-Ti, Low-Ti and VLT fields are taken from *Nielsen and Drake* (1978); *Arai et al.* (1996) and *Robinson and Treiman* (2010).

anorthositic norites or noritic anorthosites by composition (Fig. 3.7c). A range of impact melt textures are observed. Non-clastic impact melt (IM) clasts with intersertal textures are commonly observed, with tabular and lath-like plagioclase grains (∼0.1 × ∼0.01 mm) within a mafic melt matrix (Figs. 3.9a-c). There are also clastic-feldspathic impact melt breccia (IMB) clasts containing various sizes (∼0.1-0.25 mm) of anorthosite grains and brecciated lithic fragments, held within a devitrified mafic melt matrix (Fig. 3.9d). A single basaltic IM clast (IM7; 0.7 × 0.7 mm) is identified. It is a fine grained (<0.01 mm) clast, consisting of anhedral plagioclase (An_{95}), pyroxene (Wo_{20-26} En_{18-49} Fs_{25-61}), and olivine (Fo_{69}) crystals (Fig. 3.9e).

Trace element analyses were performed on four impact melt clasts (IM1, IM2, IM3 and IM7; Fig. 3.2) and two impact melt breccia clasts (IMB1 and IMB2) and the results of these analyses are shown in Table 3.2. The IM and IMB Clasts have varying amounts of Sr (between 92±3 to 259±10 ppm) and Ba (between 41±0.3 to 110±16 ppm), that are attributed to addition by terrestrial weathering.

The chondrite normalised REE patterns (Fig. 3.6b) show that both of the IM and IMB clasts have slightly higher concentrations of LREE than HREE (1.4-1.7 La_{cn}/Lu_{cn}) and have positive Eu-anomalies (1.6-2.7 Eu/Eu*). Concentrations of other trace ele-

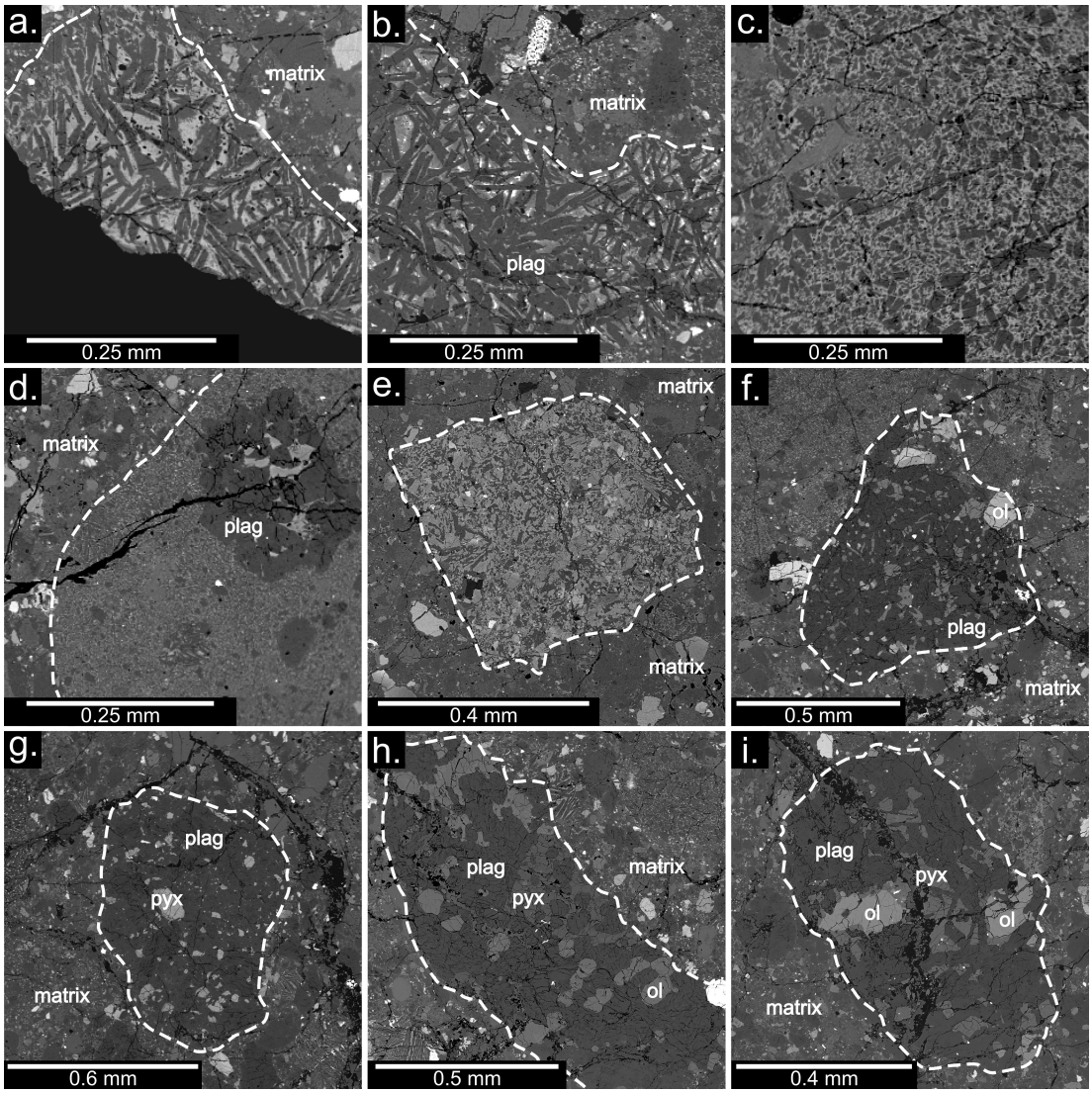

Figure 3.9: Close up BSE images of several analysed clasts. (a) microcrystalline intersertal impact melt clast; (b) Non-clastic impact melt clast with small plagioclase laths enclosing mafic melt matrix. (c) Small tablet-shaped anorthosite 'clasts' in an aphanitic mafic melt matrix. (d) Clastic-feldspathic impact melt clast with large, but relatively sparse feldspathic lithic clasts. (e) IM7 - fine grained (<0.01 mm) basaltic impact melt clast, consisting mostly of anhedral pyroxene and plagioclase crystals. (f) F2 - anorthositic clast with a poikilitic texture of plagioclase enclosing mostly pyroxene and some olivine grains. (g) F6 - ferroan noritic anorthosite clast dominated by homogeneous shocked plagioclase, within which small pyroxene phenocrysts are distributed. (h-i) M1 and M2 - magnesian feldspathic clasts containing plagioclase, pyroxene and sub-rounded olivine.

ments in the IM clasts (Th = 0.3±0.04 ppm; Sm = 0.9±0.1ppm; Sc = 16.2±1.3 ppm) and IMB clasts (Th = 0.5±0.1 ppm; Sm = 1.1±0.4 ppm; Sc = 13.1±2.7 ppm) are similar to those observed in other feldspathic lunar meteorites (Figs. 3.7a-b; see also *Joy et al.* 2010). Siderophile element concentrations (i.e. Ni, Cr and Co) within the feldspathic IM and IMB clasts are similar to those identified in the Apollo 16 feldspathic Group-3 (and to a lesser extent, Group-4) impact melts (*Korotev*, 1994); (Fig. 3.7d) and several feldspathic impact clasts identified in other lunar meteorites (*Joy et al.*,

2010). As with the largest basaltic clast in NEA 001 (clast B1), the basaltic impact melt clast (IM7) has low LREE relative to HREE concentrations (0.3 La_{cn}/Lu_{cn}), has a positive Eu-anomaly (1.7 Eu/Eu*) and similar low concentrations of Th (0.05±0.01 ppm) and Sm (0.40±0.08 ppm).

Feldspathic Non-Impact Clasts (F1, F2, F6, M1, M2, M3)

Ferroan Noritic Anorthosite Clasts: Several clasts within the sample are composed mostly (∼75-90%) of calcic plagioclase ($An_{>94}$). The clast termed 'F6' (as shown in Fig. 3.2) displays the textures typical of these clasts (Fig. 3.9g). F6 consists of pyroxene phenocrysts (Wo_{5-16} En_{46-49} Fs_{38-46}; Table 3.1) within homogeneous plagioclase. Several anorthositic gabbro clasts (e.g. clast F2) also occur within the meteorite. These have poikilitic textures, consisting mostly of blocky plagioclase (An_{92-96}; Table 3.1) enclosing pyroxene (Wo_{8-43} En_{31-44} Fs_{26-52}; Table 3.1) and, to a lesser extent, olivine grains (Fo_{54}; Table 3.1; Fig. 3.9f). *Haloda et al.* (2005) identified a number of similar clasts of anorthositic composition in a separate section of NEA 001, which they classified as non-mare igneous rocks.

Magnesian Feldspathic Clasts: Three clasts in the section have particularly magnesium-rich ($Mg\#_{>70}$) bulk compositions. The largest (0.47 × 1.23 mm) of the three clasts (M1) has a granulitic texture composed mostly (80%) of plagioclase (An_{95-96}), poikilitically enclosing pyroxene (Wo_5 En_{80} Fs_{16}), and sub-rounded olivine. Ilmenite is also seen in this clast, in the form of two larger sub-rounded grains (∼0.05 mm) on the edge of the clast ($Mg\#_{28}$), and small (0.01 mm) ilmenite flecks within the clast (Fig. 3.9h). Comparison of the An values for the plagioclase in this clast, with the Mg# of olivine ($Mg\#_{81-82}$) and pyroxene ($Mg\#_{80}$) grains (Fig. 3.10), shows the clast to have a similar composition to the magnesian anorthosites and spinel troctolite identified in the lunar meteorite Dhofar 489 (*Takeda et al.*, 2006).

Clast M2 is smaller (0.46 × 0.84 mm) than M1 and consists of more angular and blocky grains (Fig. 3.9i). It is also composed mostly (∼75%) of plagioclase (An_{90-97}). Pyroxene (Wo_{3-4} En_{72-74} Fs_{23-24}; $Mg\#_{73}$) accounts for a further 15% of the clast by modal abundance, and is present both around the rims of large (0.1 mm) olivine ($Mg\#_{71}$) grains, and as individual grains within the clast.

The third clast (M3) is smaller than M1 and M2 (0.32 × 0.32 mm). It is dominated by (85%) homogeneous plagioclase (An_{96}), within which, sub-rounded olivine ($Mg\#_{76}$) and pyroxene (Wo_4 En_{77} Fs_{20}; $Mg\#_{77}$) grains are seen. It has mineralogical and compositional affinities to magnesian anorthosite clasts identified in other lunar samples (*Korotev*, 2006; *Takeda et al.*, 2006, 2007; *Arai et al.*, 2008).

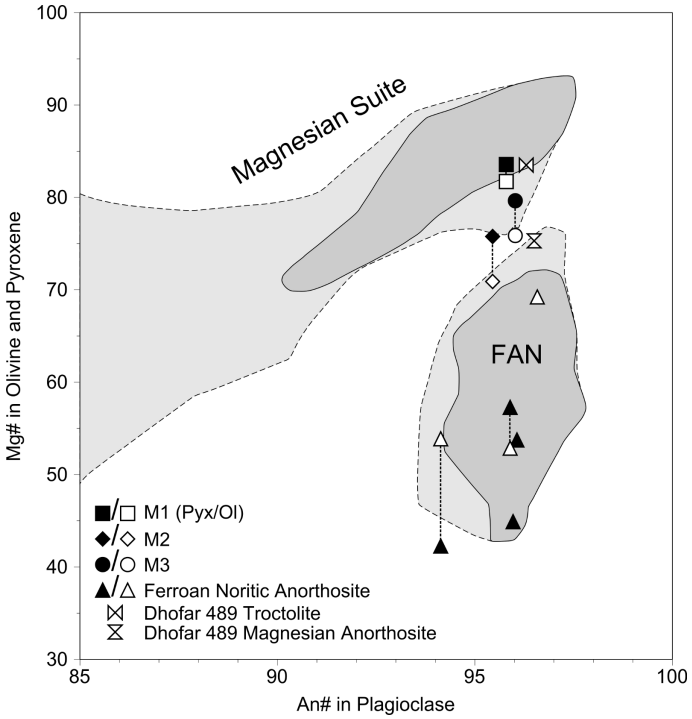

Figure 3.10: Comparison of plagioclase An# (atomic Ca/[Ca+Na+K]×100) with Mg# (atomic Mg/[Mg+Fe]×100) for pyroxene (filled symbols) and olivine (open symbols) grains in Ferroan Noritic Anorthosite clasts and magnesian feldspathic clasts (M). Vertical lines join grains from the same clasts. NEA 001 data are compared with values for magnesian anorthite and troctolite clasts in Dhofar 489 (data taken from *Takeda et al.* 2006). FAN and Mg-Suite fields are taken from *Yamaguchi et al.* (2010) and are based on the prisitinity index of *Warren* (1993), where the darker gray fields with solid outlines indicate a pristinity of ≥ 7 and the lighter gray fields with dashed outlines indicate a prisitinity of ≥ 6. The prisitinity index ranges from 9 for samples which are most likely to be pristine, down to 3 for samples which are least likely to be pristine.

3.3 Discussion

The range of clast sizes and the presence of multiple large (>1.0 mm) clasts within this section of NEA 001 is suggestive of the relatively immature nature of the regolith from which the meteorite was formed as regolith processing would result in a more consistently fine grain size (*McKay et al.*, 1974, 1978). The relatively low occurrence of impact spherules when compared with other feldspathic regolith breccias (only two impact melt beads were identified), and the absence of agglutinate particles within the meteorite, provide further evidence that NEA 001 originates from an immature regolith.

Fractures within the sample may be the result of the meteorite's exposure to at least one major impact event, resulting in its ejection from the lunar surface, and probably several other previous impact events. It is also possible that these fractures could have developed during the meteorite's descent to Earth.

3.3.1 Similarities to other lunar meteorites

NEA 001 has not been conclusively paired with any other lunar meteorites. *Korotev and Irving* (2005) draw comparisons between it and the meteorites Yamato-791197 (*Yanai and Kojima*, 1991), Yamato-82192/3 (*Yanai and Kojima*, 1985), Allan Hills (ALHA) 81005 (*Kallemeyn and Warren*, 1983; *Marvin*, 1983; *Score and Mason*, 1983) and Pecora Escarpment (PCA) 02007 (*Day et al.*, 2006b; *Korotev et al.*, 2006; *Joy et al.*, 2010). *Korotev and Irving*'s (2005) suggestion is that these stones are compositionally alike, for example, bulk Al_2O_3 concentrations are ∼26 wt% in all three meteorites (*Korotev*, 2005). However, discrepancies in values such as the Sc and Cr data of NEA 001 and Yamato 791197 (*Korotev and Irving*, 2005) suggest that the meteorites are not related. These geochemical discrepancies may also be explained by heterogeneity within the meteorites and the degree to which the samples studied were representative of the parent stones from which they originated. It is also noted that Yamato-791197 contains the greatest proportion of mare volcanic material (including VLT and low-Ti basalt; *Goodrich and Keil* 1987), of any known feldspathic lunar meteorite, which is relevant when one considers the large amount of mare basalt material observed in NEA 001. Whilst cosmic-ray exposure data provide ejection ages for Yamato-791197 and ALHA 81005 that allows possible pairing of these meteorites (*Warren*, 1994; *Eugster*, 2003; *Korotev*, 2005), there is (as of December, 2012) no published cosmic-ray exposure data for NEA 001. *Korotev and Irving* (2005) conclude that NEA 001 could have originated from a feldspathic regolith similar to ALHA 81005, but with a more significant VLT mare basalt component, which is consistent with the results presented here.

Compositional similarities can be seen with other meteorites not noted in the two previous studies of NEA 001. For example, Kalahari 009 is (as of December, 2012) the only other lunar meteorite in which positive Eu-anomalies have been noted in basaltic clasts (*Sokol et al.*, 2008). Kalahari 009 is a monomict breccia with a VLT mare basalt composition, which is paired with a second meteorite, Kalahari 008 (an anorthositic breccia). The basaltic component of Kalahari 009 bears compositional and textural similarities to the basaltic clasts in NEA 001 (Table 3.2; *Sokol et al.* 2008). NEA 001 also contains a non-impact feldspathic component, including ferroan noritic anorthosite clasts similar in appearance to several clasts identified in PCA 02007 (*Day et al.*, 2006b) and a magnesian feldspathic clast component similar to that reported in several other feldspathic breccia meteorites (*Korotev et al.*, 2006; *Takeda et al.*, 2006; *Day et al.*, 2006b; *Gross and Treiman*, 2010).

3.3.2 Composition of impact melts and impact melt breccias: implications for composition of the lunar feldspathic crust

The range of impact melt textures provides a clue as to the geological history of the local NEA 001 parent lunar regolith environment and provides important information about the nature of the lithologies in proximity to the regolith site. The majority of impact melt clasts identified, regardless of texture, have feldspathic compositions (Table 3.2; Figs. 3.7; 3.11) and REE patterns, typical of plagioclase-dominated materials (Fig. 3.6b). The glass impact spherules identified in NEA 001 also have compositions which, when averaged over the five measurements obtained for two separate beads, are indicative of melting feldspathic target rocks (Table 3.2). This indicates that the impacts responsible for creating this material occurred in a predominantly feldspathic crustal environment. The range of major, minor and trace element compositions within the feldspathic impact melts of NEA 001 (Table 3.2) is less diverse than those seen within individual groups of impact melt rocks from the Apollo 16 landing site (*McKinley et al.*, 1984; *Korotev*, 1994). In particular, the REE concentrations of the NEA 001 impact melt and impact melt breccia clasts are very similar, suggesting they may have originated from the same impact melt sheet.

The impact-derived material in NEA 001 shows little evidence of meteoritic contamination. Bulk clast compositions have Ni concentrations that are mostly below 50 ppm, with only one clast (IMB2) containing more than >100 ppm. The Co concentrations are all less than 20 ppm, with the exception of the basaltic impact melt clast (IM7) that has similar Co concentrations (36 ppm) to the basaltic clasts in NEA 001 (Table 3.2). These Ni and Co concentrations are lower than those observed in many Apollo impact melts (Ni = 10-1090 ppm, Co = 19-66 ppm; *Korotev* 1994; *Jolliff* 1998) and similar to estimations for the composition of the upper feldspathic lunar crust (Ni = ∼16 ppm, Co = 10 ppm; *Korotev et al.* 2003).

The major element Al_2O_3 and FeO compositions of the feldspathic impact melt and impact melt breccia clasts within NEA 001 are most similar to Apollo 16 Group-3 (*Korotev* 1994; Fig. 3.7) feldspathic impact melts. However, they have lower concentrations of incompatible trace elements (ITE) that are more similar to the Apollo 16 Group-4 (*Korotev*, 1994) feldspathic impact melts (Figs. 3.7a-b). This indicates that the NEA 001 impact melts and impact melt breccia target rocks, like the Group-4 melts, did not include a KREEP component. However, like the feldspathic impact melts in other lunar meteorites (*Lindstrom et al.*, 1986; *Cahill et al.*, 2004; *Joy et al.*, 2010) the NEA 001 impactites have greater Sc abundances (Sc = 12-19 ppm: Figs. 3.7b-c) than the

Apollo 16 Group-4 impact melts (average Sc = 5.4 ppm; *Korotev* 1994). This suggests that the feldspathic crust sampled by the Apollo 16 Group 4 impact melts may have been more anorthositic (Sc-poor) compared with the regions from which the impact melt in NEA 001 and several other meteorites originated.

The feldspathic impact material in NEA 001 actually has greater concentrations of Sc and lower concentrations of Al than (i) in the feldspathic impact melts in other lunar meteorites (*Joy et al.* 2010; Fig. 3.7b-c) and (ii) the estimated composition of the upper feldspathic lunar crust (*Korotev et al.*, 2003). One explanation for this observation is that the NEA 001 impact melts represent material that has been excavated from lower crustal material, which is more mafic than that of the upper feldspathic crust (*Pieters et al.*, 1997; *Wieczorek and Zuber*, 2001). This is consistent with melting in basin-forming sized impact events. It is noted that this melted lower crustal component must have been relatively KREEP-free (as is evident by the low concentrations of Th and Sm; Figs. 3.7a-b). This implies a notable difference from the near-side melted lower crust material sampled by the Apollo mafic impact melt groups (*Jolliff*, 1998) that are KREEP-bearing and all have greater amounts of incompatible trace elements (>4 ppm Th; >13 ppm Sm). This difference provides evidence that the upper (feldspathic) and lower (more mafic) crust in the region where NEA 001 was formed must have been deficient in KREEP-bearing lithologies and evolved rocks.

Another possible explanation for the observed differences in Sc and Al concentrations between the NEA 001 impact melts and other feldspathic impact melts (Fig. 3.7a-b) could be the incorporation of basaltic components (e.g. mare basalts) into the melt material (see also *Joy et al.* 2010). However, the LREE to HREE CI-normalised gradients for the NEA 001 impact melts (1.4-1.7 La_{cn}/Lu_{cn}; Fig. 3.6b) are relatively flat compared to the positive gradient of the basaltic impact melt clast IM7 (0.3 La_{cn}/Lu_{cn}; Fig. 3.6b) and VLT basalt clasts in NEA 001 (0.2-0.5 La_{cn}/Lu_{cn}; Fig. 3.6a). This argues against significant mixing of a NEA 001-like VLT mare-basaltic component into the NEA 001 feldspathic impact melt clasts.

3.3.3 Source and petrogenesis of basalt in NEA 001

Both of the previous studies of NEA 001 (*Haloda et al.*, 2005; *Korotev and Irving*, 2005) noted the contribution of basaltic material in the meteorite, citing this as a reason for the more mafic bulk composition of the meteorite (high Fe, Sc and Cr) when compared with other feldspathic lunar meteorites. The section analysed in this study appears to contain a higher volume (15% area of section) of basaltic material than previously studied sections: *Korotev and Irving* (2005) report a value of 2%. Based on the bulk

TiO_2 compositions measured for the basaltic clasts, they mostly have a VLT mare basalt affinity, consistent with the observation of *Haloda et al.* (2005). The Fe# and Ti# of the pyroxenes analysed within some of these clasts (B1a, B1b, B3) are also suggestive of a VLT mare basalt affinity (Fig. 3.8; see also *Nielsen and Drake* 1978; *Arai et al.* 1996). An exception to this is B5, which has pyroxene compositions more consistent with low-Ti basalt. This may be due to sampling less Fe-rich areas of the zoned pyroxenes within this clast, or due to obtaining a bulk composition from a small but coarse grained clast which is potentially unrepresentative of its parent rock.

Two clasts (B2, B6) have a low-Ti bulk composition (Fig. 3.11). The Fe# and Ti# of the pyroxenes within B2 are suggestive of a low-Ti affinity, however, this is less clear in the case of B6 (Fig. 3.8). The olivine and pyroxene phases within the basalt clasts of NEA 001 have similar ratios of Fe/Mn to mafic minerals as other lunar basalts. However, the plagioclase phases found within the same clasts are found to be slightly more anorthositic (An_{95} on average) than those in other lunar mare basalts (Fig. 3.12; *Papike et al.* 2003).

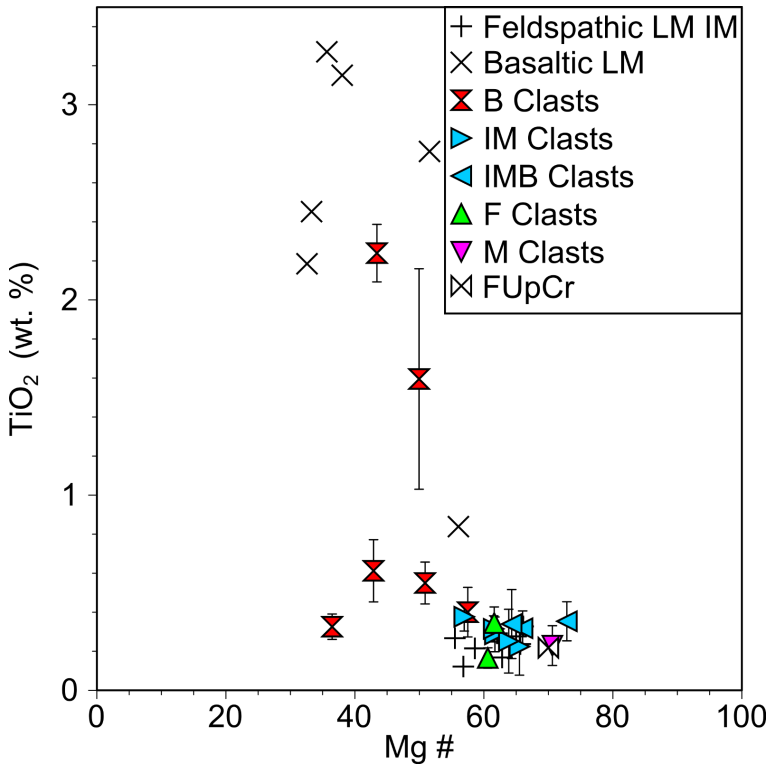

Figure 3.11: TiO_2 (wt%) vs. Mg# (atomic Mg/[Mg+Fe]×100) for bulk clast compositions within NEA 001. NEA 001 values are compared with those from the references cited in Fig. 3.7. for meteoritic samples and the estimated composition of the upper feldspathic lunar crust (FUpCr). LM IM = lunar meteorite impact melt.

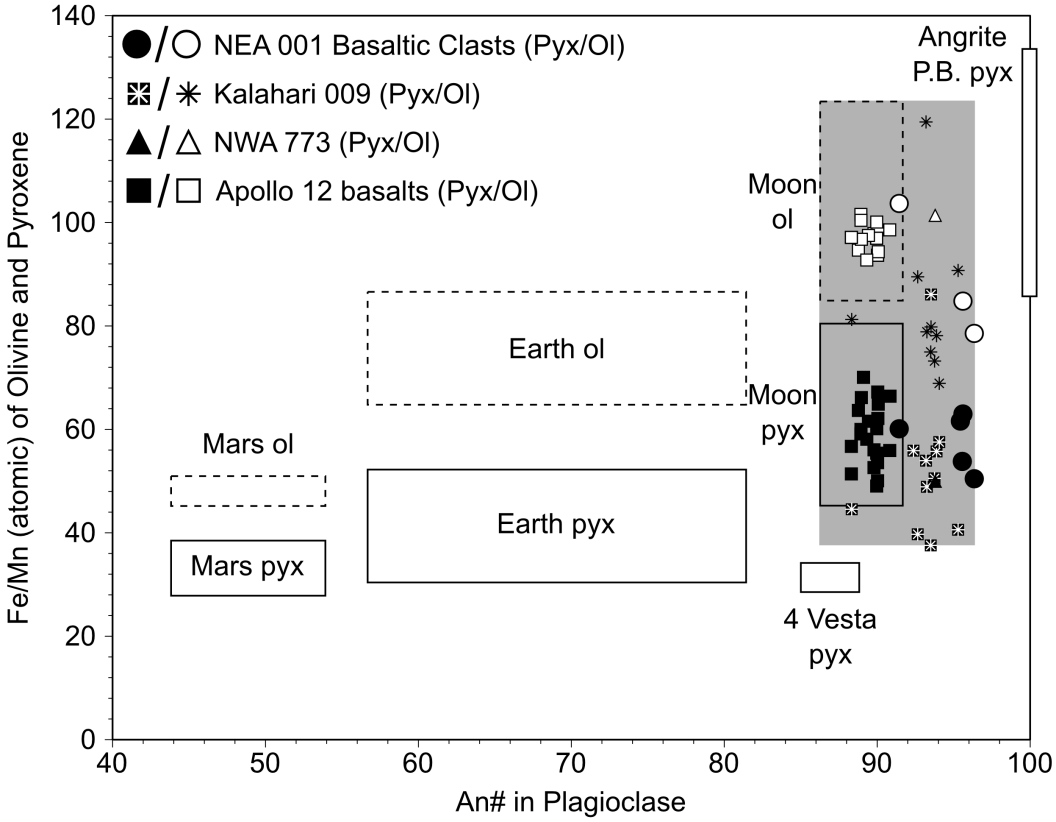

Figure 3.12: Ratio of Fe/Mn (atomic) for pyroxene (filled circles) and olivine (open circles) phases vs. An# (atomic Ca/[Ca+Na+K]×100) of plagioclase phases within NEA 001 basaltic clasts. The fields (taken from *Papike et al.* 2003) represent the average compositions of basalts from different planetary bodies. The plagioclase within the NEA 001 clasts tend to have higher An# values ($\sim An_{95}$) than the range for lunar basalts (An_{89}). However, this range was obtained from analyses of Apollo samples (*Karner et al.*, 2004) that were collected from a limited region of the lunar surface (for example the low-Ti Apollo 12 basalts - see Chapters 6 and 7). It may, therefore, not be fully representative of basalts from other lunar lithologies. Compositions of phases from the VLT basaltic meteorites Northwest Africa (NWA) 773 and Kalahari 009 (*Jolliff et al.*, 2003a; *Sokol et al.*, 2008) also suggest that the range of lunar mineral chemistries is wider than was previously recognised (as indicated by the grey rectangle).

VLT basalt

The basalt clasts in NEA 001 have predominantly VLT compositions. VLT basalts were only sampled to a limited extent by the Apollo 17 (*Blanchard and Budahn*, 1979; *Wentworth et al.*, 1979) and Luna 24 (*Haskin*, 1978; *Laul et al.*, 1978; *Ma et al.*, 1978) missions. Remote sensing observations, however, have shown them to have a widespread distribution across the lunar surface (*Gillis et al.*, 2003). In contrast with the Apollo and Luna collection, VLT basalts occur as or in several other lunar meteorites (e.g. Northwest Africa 773, Dhofar 287 and Miller Range (MIL) 05035: *Arai et al.* 1996; *Fagan et al.* 2003; *Jolliff et al.* 2003b; *Demidova et al.* 2003; *Joy et al.* 2008; *Liu et al.* 2009). VLT basalts sampled by the Kalahari 009 lunar meteorite are of particular

interest as they are likely to represent some of the oldest basaltic lavas that flowed on the Moon (*Terada et al.*, 2007; *Sokol et al.*, 2008). It is thought that VLT basalts like these represent extensive cryptomaria deposits, now buried by subsequent ejecta blankets (*Antonenko et al.*, 1995; *Anand and Terada*, 2008). Therefore VLT basalt clasts in lunar meteorites like NEA 001 shed new light on lunar VLT basalt petrogenesis from regions that were not sampled by the Apollo and Luna missions. In particular, they may reveal the nature of ancient (>4 Ga) melting and volcanism on the Moon (*Terada et al.*, 2007).

The VLT clasts (B1a, B1b) have concentrations of trace elements lower than those found in most Apollo low-Ti and high-Ti mare basalts (Table 3.2; Fig. 3.7; *Haskin and Warren* 1991). The trace element concentrations in the NEA 001 VLT clasts are similar to several Apollo 17 and Luna 24 VLT basalts (Fig. 3.7; *Ma et al.* 1978; *Blanchard and Budahn* 1979; *Wentworth et al.* 1979). However, the VLT clasts within NEA 001 have much lower concentrations of Th than Apollo 17 and Luna 24 VLT basalts (Fig. 3.7a) and are also relatively Sm-poor (Fig. 3.7b).

B1a and B1b also exhibit positive Eu-anomalies (Table 3.2; Fig. 3.6a). Positive Eu-anomalies are highly unusual for mare basalt material, but small positive, or essentially flat, Eu-anomalies have been reported for rare Luna 24 ferrobasalt samples (*Laul et al.*, 1978; *Ma et al.*, 1978), and in VLT lunar meteorites Kalahari 009; MIL 05035 and Asuka 881757 (*Warren and Kallemeyn*, 1993; *Joy et al.*, 2008; *Sokol et al.*, 2008; *Liu et al.*, 2009). The unusual REE patterns exhibited in some of the basalt clasts in NEA 001 have implications with regard to their petrogenesis.

Laul et al. (1978) proposed several theories for the occurrence of both positive and negative Eu-anomalies in Luna 24 ferrobasalts. These include: (1) biases introduced due to the small size of samples analysed relative to the grain sizes of the rocks (i.e. 1-2 mm fragments of rock with 1-3 mm grain size); (2) higher feldspar concentration due to processes such as accumulation, assimilation or remelting; (3) the presence of phosphates with high Eu-concentrations; (4) varying degrees of partial melting or variation in the source composition; (5) reduction and an increased Eu/Eu* and REE fractionation during cooling.

As *Laul et al.* (1978) discuss, low concentrations ($<10_{cn}$ abundances) of REE in small-sized samples mean that slight changes in Eu concentration and phase distribution, can greatly affect any apparent Eu-anomalies. In this study of NEA 001 LA-ICP-MS trace element data was obtained by analysing several multiphase regions of reasonably fine grained basaltic material, where crystal size <150 μm (e.g. Figs. 3.4a; 3.5a-c). This approach, therefore, ensured that representative areas of the clasts were sampled,

and as the clasts are fine grained, they are likely to be representative of quenched regions of their parent lava flow. For this reason the first of *Laul et al.*'s (1978) explanations is not adequate to explain the results of this study. Their suggestion regarding the importance of phosphates is also discounted: this investigation revealed no evidence of either apatites or merrillites within the basalt clasts. Furthermore, phosphates typically have negative Eu-anomalies. If one is to infer crustal assimilation as an explanation for the unusual REE patterns of these basalt fragments, based on the fact that their low concentrations of REE makes features such as the Eu-anomalies susceptible to even slight changes in mineralogy, then it is still necessary to explain why the basalts are so ITE-poor in the first place. Therefore, crustal assimilation does not fully explain the nature of the REE trends seen in these clasts.

Low ITE-concentrations in the NEA 001 VLT basalt clasts suggest that the parent melts of these basalt clasts originated from an ITE-poor source and that there was no urKREEP (magma ocean residue; *Warren and Wasson* 1979) or KREEP-rich rocks (e.g. KREEP-bearing impactites, High-Alkali Suite rocks, Mg-Suite rocks; *Lucey et al.* 2006) assimilated by the melts during ascent. One other possible source for the parent melts would be early pyroxene and olivine cumulates in the lunar magma ocean (LMO), such as those proposed by *Joy et al.* (2008) and *Liu et al.* (2009) as a source for VLT basalts within the lunar meteorite MIL 05035. These cumulates would have crystallised prior to the large-scale precipitation of plagioclase (responsible for Eu-removal), late stage ilmenite crystallisation, and the concentration of KREEP-rich melts in the upper LMO. These could therefore provide a possible source for low-ITE, VLT basalts such as those discussed here.

Low-Ti basalt

Low-Ti basalt is less common in NEA 001, but is represented by clasts B2 and B6 (2.2 and 1.6 wt% TiO_2 bulk clast composition respectively: Table 3.2). The gabbroic B2 clast is relatively coarse grained and therefore the clast chemistry reported in Table 3.2 is not believed to be truly representative of the parent rock bulk composition. Clast B6 however, although small in size, is reasonably fine grained (<150 μm) suggesting that the clast is more representative of its parent lava. B6 has high-ITE concentrations compared with other basalts and impact melt in NEA 001 (Table 3.2; Figs. 3.6a; 3.7a-b) indicating that it may be material that has been introduced to the NEA 001 parent regolith from a distant KREEP-rich mare basalt source. The clast is compositionally akin to low-Ti basalts such as those from the Apollo 14 mission (*Dickinson et al.*, 1985; *Shervais et al.*, 1985; *Neal et al.*, 1988, 1989).

Basalt petrogenesis

The liquidus temperature and plausible crystallisation (equilibrium and fractional) sequences of basalts sampled by NEA 001 have been investigated here using the MELTS modelling code (*Ghiorso and Sack*, 1995; *Asimow and Ghiorso*, 1998). All modelling was performed assuming a system pressure of 1 bar (i.e. near-surface lava flow crystallisation; varying the pressure between 0 and 1 bar has no apparent effect on the crystallisation sequence) and an oxygen fugacity (fO_2) equal to one log unit below the IW buffer (*Righter et al.*, 2005). The bulk clast compositions (Table 3.2) were used as the starting composition and the plausible crystallising phases were limited to typical mare basalt mineral species (olivine, orthopyroxene, clinopyroxene, feldspar, cristobalite and ilmenite). After calculating the liquidus temperature the model was run in 5°C steps noting when minerals appeared on the liquidus. The results of these models are summarised in Fig. 3.13.

Of the two basalt fragments for which the crystallisation sequences were modelled, the VLT clast B1a has the highest liquidus temperature (1213°C in both fractional and equilibrium models: Fig. 3.13). Olivine is the first phase to crystallise in B1a, followed by feldspar and then clinopyroxene. The observed subophitic texture within B1a is in broad agreement with the crystallisation of feldspar before clinopyroxene. Ilmenite is the last phase to crystallise in B1a during both equilibrium and fractional crystallisation sequences.

Low-pressure (0-1 bar) equilibrium crystallisation experiments performed on Apollo and Luna basaltic samples show that olivine typically crystallises before pyroxene and plagioclase in low-Ti and VLT basalts. These experiments also show a range of liquidus temperatures (∼1150-1300°C) for the Apollo and Luna basalts under low oxygen fugacity conditions. The modelled mineral precipitation sequence and liquidus temperature (Fig. 3.13) for NEA 001 clast B1a are consistent with these experiments (*Walker et al.*, 1972; *Walker et al.*, 1976a, 1977; *Grove and Vaniman*, 1978).

MELTS crystallisation modelling of the low-Ti basalt B6 indicates that it has a relatively low liquidus temperature (1193°C) compared with B1a (Fig. 3.13). Orthopyroxene is the first phase to crystallise in B6, followed by feldspar and then clinopyroxene. As with B1a, the crystallisation of plagioclase before clinopyroxene is consistent with the subophitic texture seen in the clast. The final phases to crystallise in B6 are ilmenite and then cristobalite (in the fractional crystallisation sequence only) and olivine. Both ilmenite and a silica phase are observed in B6, however, olivine is not (Table 3.1).

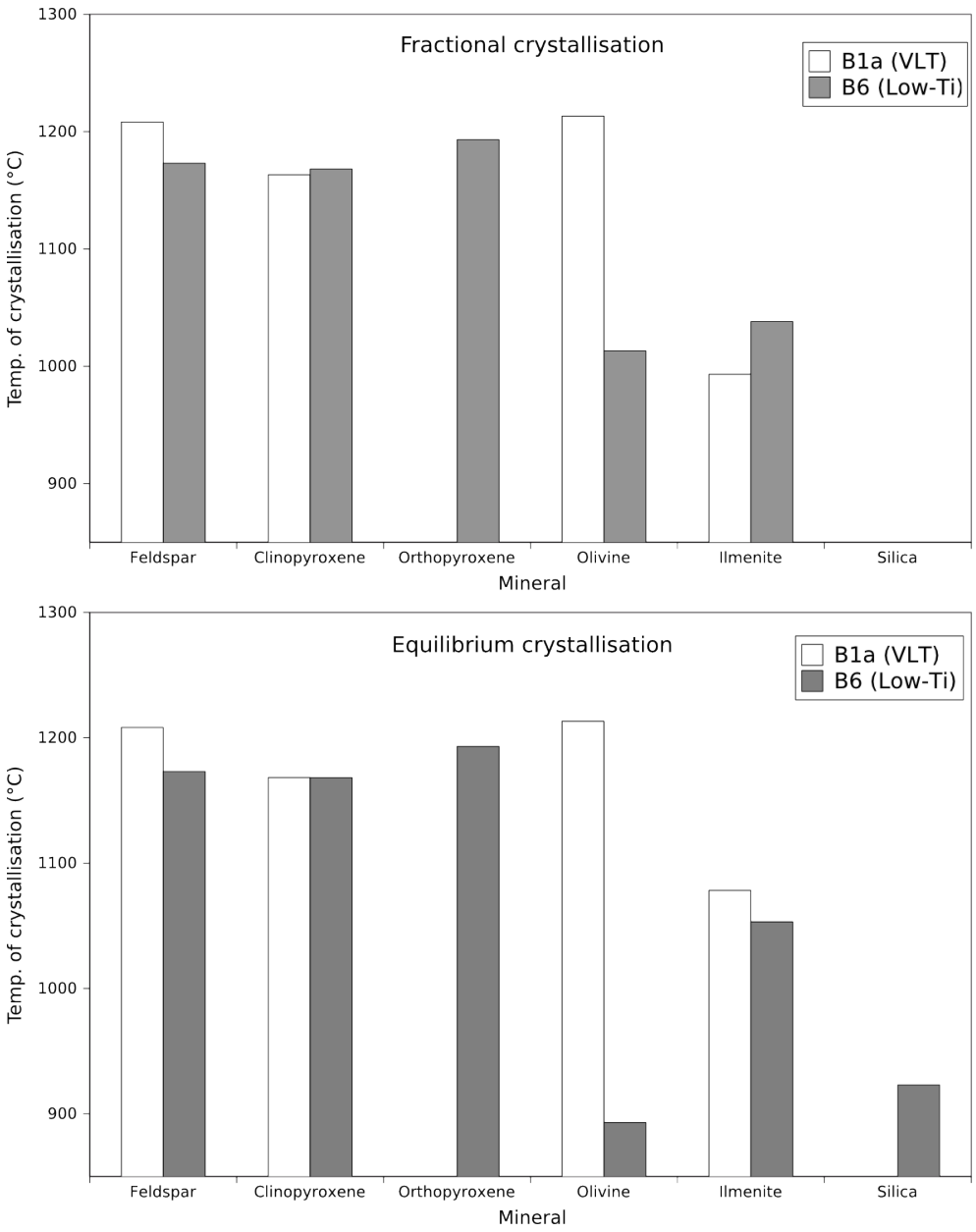

Figure 3.13: Predicted fractional and equilibrium crystallisation sequences as modelled by the MELTS thermodynamic software (*Ghiorso and Sack*, 1995; *Asimow and Ghiorso*, 1998). Models were performed for two of the basalt clasts in NEA 001 including B1a (VLT) and B6 (low-Ti). Tops of the bars indicate the temperature at which mineral phases first appear on the liquidus.

3.3.4 NEA 001 source region

NEA 001 is predominantly a feldspathic sample and therefore the basalt clast component was most likely introduced into NEA 001's parent regolith source region by impact ejecta mixing processes. Attempts have been made to model the effects of lateral regolith mixing by impacts which have occurred since the major basin-forming events, (*Li and Mustard*, 2005; *Petro and Pieters*, 2007). The model of *Li and Mustard* (2005) indicates that in certain cratering conditions lateral mixing is efficient enough that

20-30% of ejecta could be distributed to distances greater than 100 km away. *Petro and Pieters* (2007) estimate that ∼10 to 20% of the regolith at any given location on the Moon will be foreign material from >500 km away, and that most of the foreign component will originate from within 1000 km. Evidence of lateral mixing, albeit on smaller scales than these models suggest, has also been observed in Clementine data. For example, *Giguere et al.* (2000) observed mixing of high-Ti and low-Ti units, and noted the most extensive mixing occurring within 2 km of the geological contact, with less mixing occurring within 10 km. Petrographic studies of basalt fragments within Apollo 16 regolith samples (*Zeigler et al.*, 2006) have provided evidence of lateral impact mixing on larger (220-600 km) scales.

As noted above, with the exception of two clasts (B2 and B6), the mare basalt component observed in the sample has a VLT composition (Table 3.2). Therefore the presence of a mare basalt component constrains the lunar source locality of NEA 001, to an area within a relatively close proximity to a source of VLT mare basalt. Elemental maps of Ti distribution across the lunar surface (*Lucey et al.*, 1998, 2000; *Spudis et al.*, 2002; *Prettyman et al.*, 2006) indicate some possible sources of low-Ti and VLT material to be the farside mare regions and the peripheral regions of the near side impact basins. The work of *Gillis et al.* (2003) highlights the northern regions of Oceanus Procellarum, large areas of Mare Serenitatis and areas of Mare Crisium, as locations containing VLT mare basalt. However the location of these basins near and within the Procellarum KREEP Terrane (PKT; *Jolliff et al.* 2000) does not fit the ITE-poor (i.e. KREEP-poor) nature of the basaltic clasts identified in NEA 001. On the other hand, it is possible that buried cryptomare deposits (*Antonenko et al.*, 1995; *Terada et al.*, 2007; *Anand and Terada*, 2008) could provide a source of VLT basaltic material for a feldspathic breccia such as NEA 001.

Based on the studies of lateral mixing previously mentioned, it seems highly unlikely that NEA 001 could have formed more than 1000 km away from a source of VLT ITE-poor basaltic material. In addition to a source of VLT basaltic material, it is likely that NEA 001 formed within a similar distance of a source of low-Ti basaltic material, from which the clasts B2 and B6 could have originated. Taking into account the dominance of the KREEP signature around nearside mare basalts, it is suggested that the basalts in NEA 001 are more likely to have originated in the Outer-Feldspathic Highlands Terrane (FHT-O; *Jolliff et al.* 2000), most likely on the lunar farside.

3.4 Summary

A detailed petrographic and mineralogical study of a section of the lunar feldspathic regolith breccia NEA 001 has been performed. The principal conclusions of this study are as follows:

1. The sample is petrographically heterogeneous, containing clasts of feldspathic impact melt and impact melt breccias, ferroan noritic anorthosites, magnesian feldspathic clasts, and low-Ti and VLT basalts (Table 3.2).

2. The Sc-rich nature of impact melt and impact melt breccia clasts within NEA 001 suggests that they might have formed from a more mafic region of the lunar crust than that sampled by the Group-3 and Group-4 Apollo 16 feldspathic impact melts (*Korotev*, 1994). It is also possible that the clasts incorporate a component of mafic (Sc-rich) lower crustal material (*Pieters et al.*, 1997; *Wieczorek and Zuber*, 2001) and/or basaltic material (*Joy et al.*, 2010). The concentrations of other ITEs (such as Th and Sm) within the NEA 001 impact melts are significantly less than those found in lower crustal material sampled by Apollo mafic impact melts (*Jolliff et al.*, 1998). This provides evidence that the meteorite originated from a KREEP-poor region of the Moon.

3. Feldspathic non-impact related clasts in NEA 001 are identified as both ferroan noritic anorthosites and magnesian feldspathic clasts. The ferroan noritic anorthosite clasts are believed to be fragments of primary igneous materials from the feldspathic crust (*Haloda et al.*, 2005). The magnesian feldspathic clasts within the meteorite may be more representative of farside feldspathic highland material than the ferroan noritic anorthosite clasts (*Arai et al.*, 2008). They may also represent lower crustal material as has been suggested for similar materials identified in the Dhofar 489 meteorite (*Takeda et al.*, 2006).

4. The VLT basaltic clasts identified in NEA 001 are all REE poor and exhibit positive Eu-anomalies. It is argued here that the low ITE abundances and positive Eu-anomalies could provide evidence that the source regions of these clasts formed prior to significant plagioclase separation in the LMO. This may be consistent with the VLT material being a product of some of the earliest lunar volcanism, and could be similar to that proposed to constitute cryptomaria (*Terada et al.*, 2007; *Anand and Terada*, 2008).

5. The feldspathic nature of the sample, together with the KREEP-poor nature of the vast majority of material within the meteorite and the presence of magnesian feldspathic clasts, suggest an origin in the farside lunar highlands. Given the limited range (<1000 km) of impact-driven lateral mixing processes in the lunar regolith, this would imply the presence of a buried near-surface reservoir of VLT deposits (i.e. VLT cryptomaria) within the farside crust.

Chapter 4

Apollo 12

4.1 Mission overview

The Apollo 12 mission launched from Kennedy Space Center on November 14^{th} 1969. The mission was manned by Commander, Charles "Pete" Conrad; Command Module Pilot, Richard Gordon; and Lunar Module Pilot, Alan Bean. Five days after launching, on November 19^{th}, Conrad and Bean touched down on Mare Cognitium in the eastern region of Oceanus Procellarum on the lunar nearside (Fig. 4.1). The Intrepid Lunar Module landed on the northwest rim of Surveyor crater (∼200 m diameter) at 23.34°W and 2.45°S, approximately 180 m away from the Surveyor 3 probe which had landed there three years earlier (Fig. 4.2). In doing so, the mission had achieved one of its key objectives, by demonstrating the capability of precision landings on the Moon. In addition to Surveyor, several other craters were visited by Conrad and Bean. The largest crater of these were Middle-Crescent Crater (∼400 m diameter), Head Crater (∼100 m), Bench Crater (∼60 m) and Sharp Crater (∼15 m).

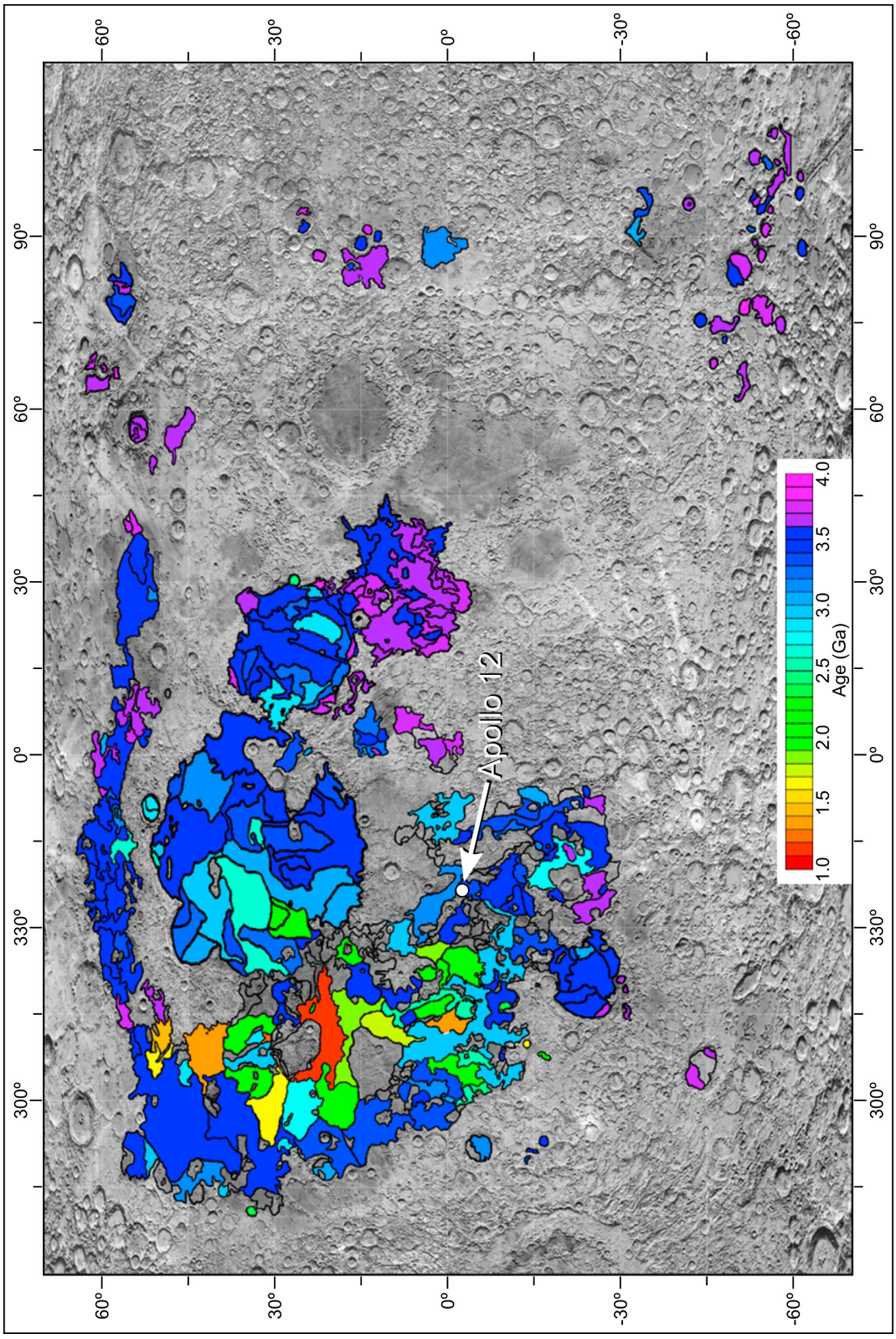

Figure 4.1: Ages and spatial distribution of mare basalts on the lunar nearside as mapped by *Hiesinger et al.* (2000, 2003, 2010). Reproduced by permission of the American Geophysical Union.

Four stratigraphic units of basaltic material were identified in the Oceanus Procellarum by *Whitford-Stark and Head* (1980). The Apollo 12 landing site is located within the Hermann Formation, the second youngest of these units (estimated to be ∼3.0-3.6 Ga by crater counting methods; *Whitford-Stark and Head* 1980). It is due north of the center of Mare Cognitium, lying on a ray of ejecta material from the crater Copernicus. By measuring the exposed rim heights of craters partially buried by mare basalts *De Hon* (1979) constructed an isopach map of basalt thickness, indicating that the basalt flows in the Oceanus Procellarum region have an average cumulative thickness of ∼400 m. Further evidence for this has since been provided by observations of ejecta compositions made using the Clementine UV-VIS camera (*Weider et al.*, 2010; *Korotev et al.*, 2011).

Geologic mapping by *Hiesinger et al.* (2000, 2003, 2010) and *Morota et al.* (2011) indicates that a large number of individual basaltic flows are located within the Oceanus Procellarum including some of the youngest mare basalts (∼1.5 Ga) on the Moon (Fig. 4.1). Given the location of the Apollo 12 landing site within the eastern region of this maria, and the potential for lateral transport of material across the lunar surface by impact processes (*Li and Mustard*, 2005; *Petro and Pieters*, 2007), it is possible that some of this young basaltic material may have been sampled by the mission. For this reason, further characterisation of the Apollo 12 sample collection may provide new insights to the duration of lunar volcanism and the magmatic evolution of the Moon.

4.2 Apollo 12 samples

A total of 34.3 kg of samples were returned by the Apollo 12 mission (*LSPET* 1970a; *Hiesinger and Head* 2006). This included 5.9 kg of fines (material <1 cm) and chips (between 1-4 cm), 27.7 kg of rocks and 0.8 kg of special samples (including cores, the lunar environment sample container and the gas analysis sample container). Of the forty-seven rocks collected, forty-three are mare basalts, three (12010, 12034 and 12073) are regolith breccias and one (12013) is a dilithologic breccia (*Quick et al.*, 1977; *Neal et al.*, 1994a; *Meyer*, 2005; *Korotev et al.*, 2011).

4.2.1 Mare basalts

Basaltic suites

The Lunar Sample Preliminary Examination Team (*LSPET* 1970a) identified a wider range of textures, modal mineralogies and chemical compositions in the crystalline

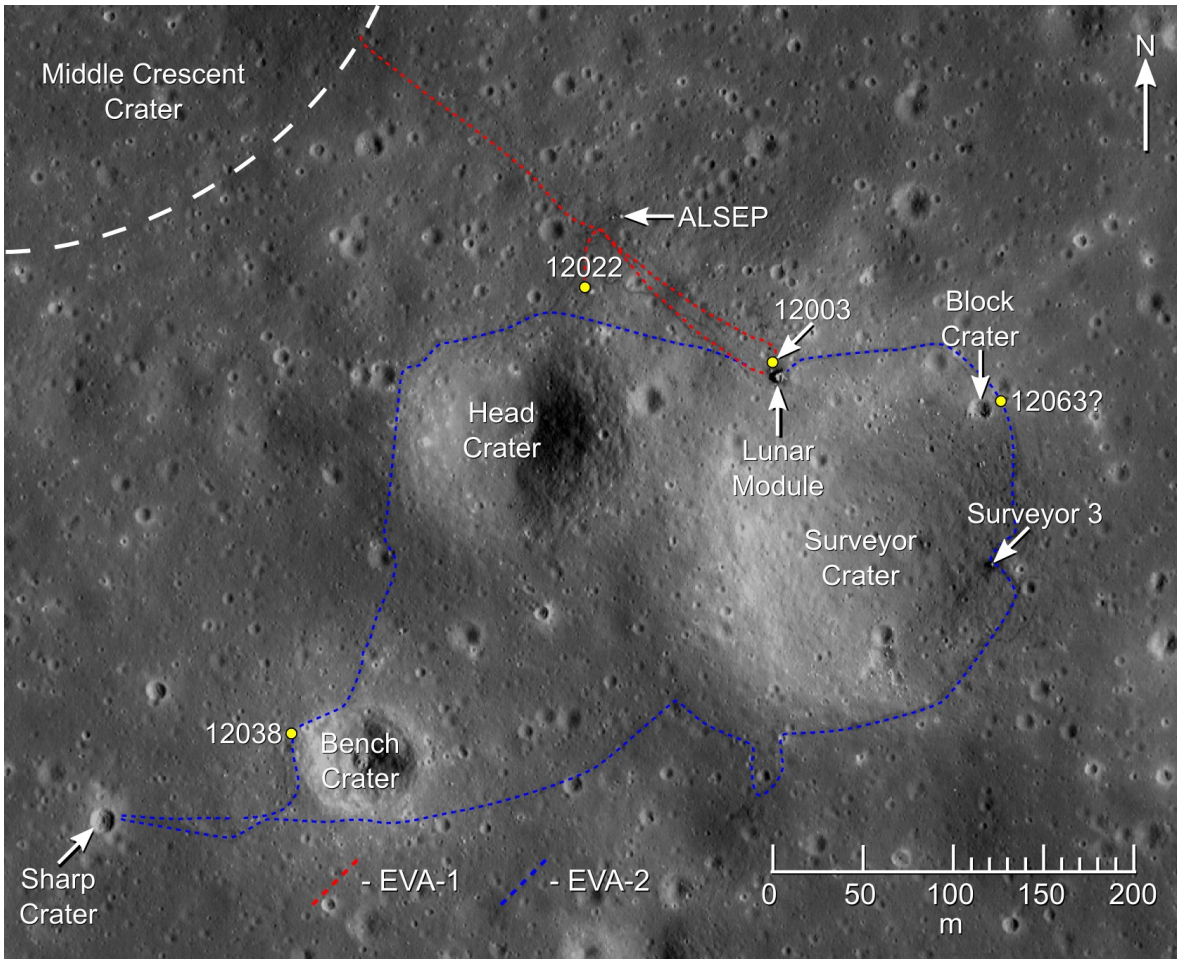

Figure 4.2: Map of the Apollo 12 landing site indicating the collection locations for the samples being analysed in the following chapters. Background image from the Lunar Reconnaissance Orbiter Narrow Angle Camera frame M175428601R (NASA/GSFC/Arizona State University). Sample locations have been based on maps of the landing site produced by the *Lunar Sample Preliminary Examination Team* (*LSPET* 1970a; 1970b) and additional information in the Apollo 12 Preliminary Science Report (*LSPET* 1970b). The location at which 12063 was collected is not certain but has based on inferences made by the *LSPET* (1970b) and *Rhodes et al.* (1977).

Apollo 12 samples compared with those collected during the Apollo 11 mission from Mare Tranquilitatis. As with the basalts collected during the Apollo 11 mission, the Apollo 12 basalts consist predominantly of clinopyroxene and plagioclase (*LSPET* 1969, 1970a). Olivine is also present in many of the Apollo 12 samples, forming a major constituent of some rocks (*James and Wright*, 1972).

Warner (1970, 1971) made one of the first attempts to divide the crystalline rocks into separate groups. Based on textural characteristics of the Apollo 12 samples, *Warner* recognised two distinct textural types: (1) rapidly crystallised, porphyritic basalts; and (2) slowly crystallised, ophitic basalts. These groups were compared with textures identified in the Apollo 11 samples, which also include a number of ophitic basalts, in addition to a third textural group; (3) intersertal basalts. Despite the over-

lapping textures of the ophitic Apollo 11 and Apollo 12 samples, the chemistries of the samples from each mission are different. The Apollo 11 basalts have TiO_2 contents between 9.1-12.2 wt% and form two distinct chemical groups of high and low alkali rocks (*Compston et al.*, 1970; *Warner*, 1971). By contrast, the Apollo 12 basalts have lower TiO_2 contents (2.6-5.0 wt%) and distinct chemical groups were not identified (*Warner*, 1971).

With new data available, *James and Wright* (1972) performed a more detailed review of the variety of basaltic materials collected at the Apollo 12 site. The samples were referred to as either basalts or gabbros. These classifications were given further mineral modifiers, including: "ilmenite", "olivine" or "pigeonite", where the respective minerals form more than 10% of the rock, or are important characterising accessories; "olivine-bearing", where olivine is present but makes up <5%; "olivine-poor" and "olivine-free"; and "ilmenite-bearing", where ilmenite is a characterising accessory forming between ∼4-10% of the rock. This resulted in the identification of three major Apollo 12 basalt suites: olivine and pigeonite basalts/gabbros; ilmenite basalts/gabbros; and feldspathic basalts (*James and Wright*, 1972).

More than half the samples were classified as olivine-pigeonite basalts and gabbros (*James and Wright*, 1972). These were described as having similar textural characteristics, with the basalts exhibiting porphyritic textures with mafic phenocrysts in variolitic groundmass, while the gabbros exhibit hypidiomorphic granular textures and coarsely variolitic textures similar to the groundmass of the basalts. Ilmenite basalts and gabbros were the next most common type of sample identified by *James and Wright* (1972). The textures of these samples are more variable than those of the olivine-pigeonite basalts and gabbros, from porphyritic through to subophitic and coarsely graphic. The ilmenite samples were also noted as having higher ratios of TiO_2/MgO and FeO/MgO, and lower ratios of SiO_2/MgO. Two samples (12006 and 12038) were identified as feldspathic basalts. At the time of the study only 12038 had been analysed in detail and it was recognised as having higher ratios of Na_2O/MgO and Al_2O_3 than the other Apollo 12 samples, due to its high modal plagioclase content, and lower FeO/MgO.

The classification of Apollo 12 mare basalts was re-assessed by *Papike et al.* (1976) and *Rhodes et al.* (1977), who confirmed the identification of separate basaltic suites. *Papike et al.* (1976) recognised the olivine and pigeonite suites as compositionally distinct, although maintained that there was a probable petrogenetic link between them. *Rhodes et al.* (1977) greatly extended the number of basalts studied from the Apollo 12 site, presenting major and trace element bulk compositions which largely supported the findings of *James and Wright* (1972), although several samples were reclassified.

Notably, 12006 was removed from the feldspathic suite into the olivine suite, and 12031 (initially classed as an ilmenite basalt by *James and Wright* 1972) was identified as either a plagioclase-enriched pigeonite basalt or a second feldspathic basalt. A key component of the *Rhodes et al.* (1977) study was the use of incompatible trace element ratios (as opposed to absolute abundances) which would not be significantly affected by fractionation processes or unrepresentative sampling in coarse grained basalts.

The most recent detailed assessment of the Apollo 12 basaltic suites was performed by *Neal et al.* (1994a). They established a new set of criteria to discriminate between the olivine, pigeonite and ilmenite basalts based on bulk Mg# (atomic Mg/[Mg+Fe]) and Rb/Sr ratios (Fig. 4.3). Based on that work several further changes were made to the basaltic groupings, however, the classifications of *Rhodes et al.* (1977) were mostly upheld. As is clear in Fig. 4.3, this classification scheme still relies heavily on the representative nature of the samples being analysed, resulting in some samples (in this case 12031 and 12040) lying outside the expected compositional ranges. If one applies the *Neal et al.* (1994a) classification to all of the Apollo 12 basalts currently studied, the number of samples in each suite is as follows:

- Olivine basalts - 16 samples (37%)
- Pigeonite basalts - 12 samples (28%)
- Ilmenite basalts - 14 samples (33%)
- Feldspathic basalts - 1 sample (2%)

It remains unclear whether the feldspathic basalt suite represents a lava flow local to the Apollo 12 site or if the paucity of identified samples suggests that the feldspathic basalts were introduced to the site as impact ejecta (*Neal et al.*, 1994a; *Snyder et al.*, 1997). Three samples previously identified as possible feldspathic basalts (12006, 12031 and 12072; *James and Wright* 1972; *Rhodes et al.* 1977; *Beaty et al.* 1979) have since been re-classified (*Neal et al.*, 1994a; *Nyquist et al.*, 1979). However, it is clear from isotopic studies by *Nyquist et al.* (1979); *Nyquist et al.* (1981) that 12038 is distinct from the other Apollo 12 basalts.

Basalt distribution at the Apollo 12 site

Warner (1971) noted a correlation between the locations from which the Apollo 12 basalts were collected and the textural groups he had identified. Based on the samples which had been classified at the time, there appeared to be an association between

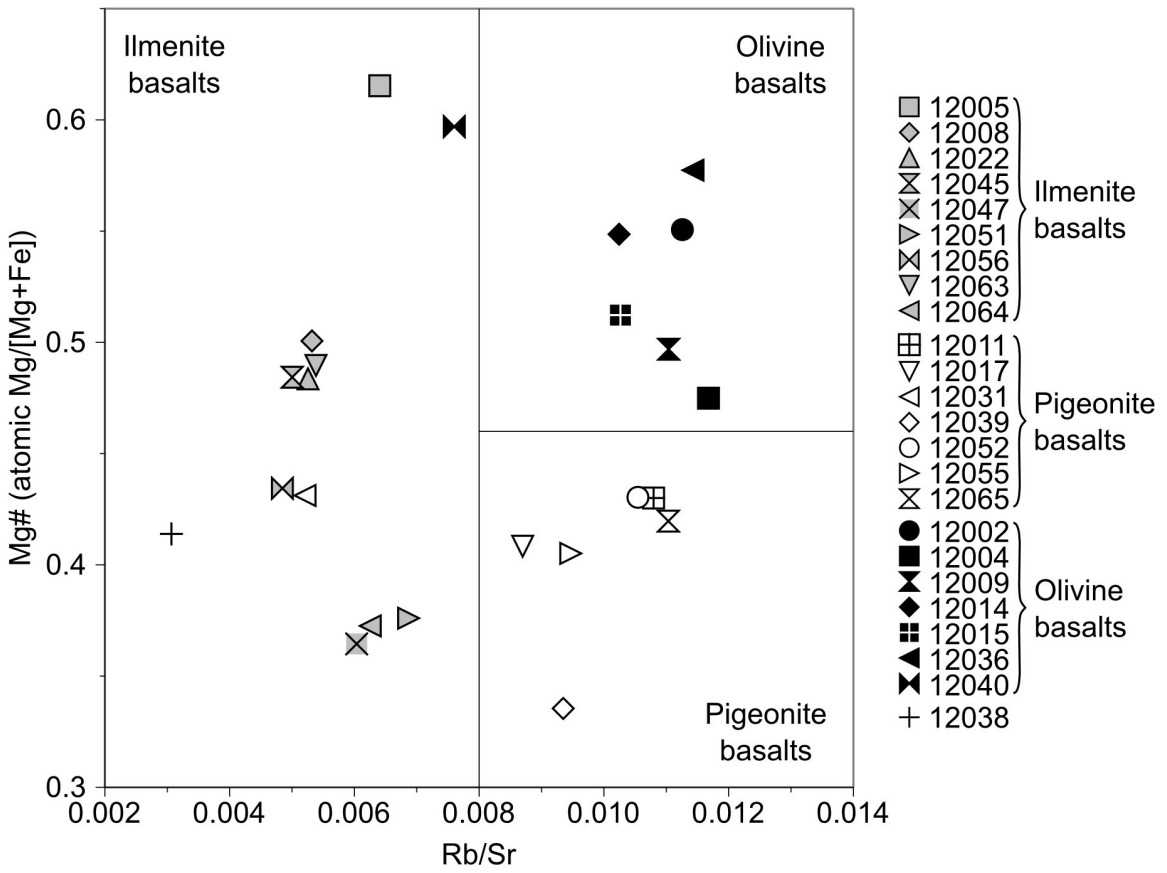

Figure 4.3: Bulk Mg# (atomic Mg/[Mg+Fe]) vs Rb/Sr for Apollo 12 basalts, illustrating the classification scheme of *Neal et al.* (1994a). Literature data is taken from *Papanastassiou and Wasserburg* (1970, 1971a); *Kushiro and Haramura* (1971); *Maxwell and Wiik* (1971); *Murthy et al.* (1971); *Wakita and Schmitt* (1971); *Willis et al.* (1971); *Rhodes et al.* (1977); *Nyquist et al.* (1977); *Nyquist et al.* (1979); *Nyquist et al.* (1981); *Warren et al.* (1986).

the largest crater at the Apollo 12 site (Middle Crescent Crater; Fig. 4.2) and the porphyritic basalts. *Warner* also noted that the four Apollo 12 breccias were within the area dominated by porphyritic basalts. This was interpreted as evidence that the Apollo 12 site was covered by ejecta from Middle Crescent Crater which had excavated at least two underlying lava flows or groups of lava flows; the stratigraphically lower unit(s) made up of the porphyritic basalts, with the ophitic basalts above. The inversion of this sequence in the Middle Crescent ejecta blanket exposed the porphyritic basalts, while the smaller craters in the area (e.g. Head and Surveyor) subsequently disturbed the Middle Crescent ejecta.

Although the basalt groupings of *Warner* (1971) were later revised (*James and Wright*, 1972; *Rhodes et al.*, 1977; *Neal et al.*, 1994a), mapping of probable ejecta blankets in the area indicates that the Apollo 12 site is indeed covered by the continuous ejecta blanket of Middle Crescent Crater (*Sutton and Schaber*, 1971). *Rhodes et al.* (1977) calculated the Middle Crescent ejecta blanket thickness to be between 1-10 m,

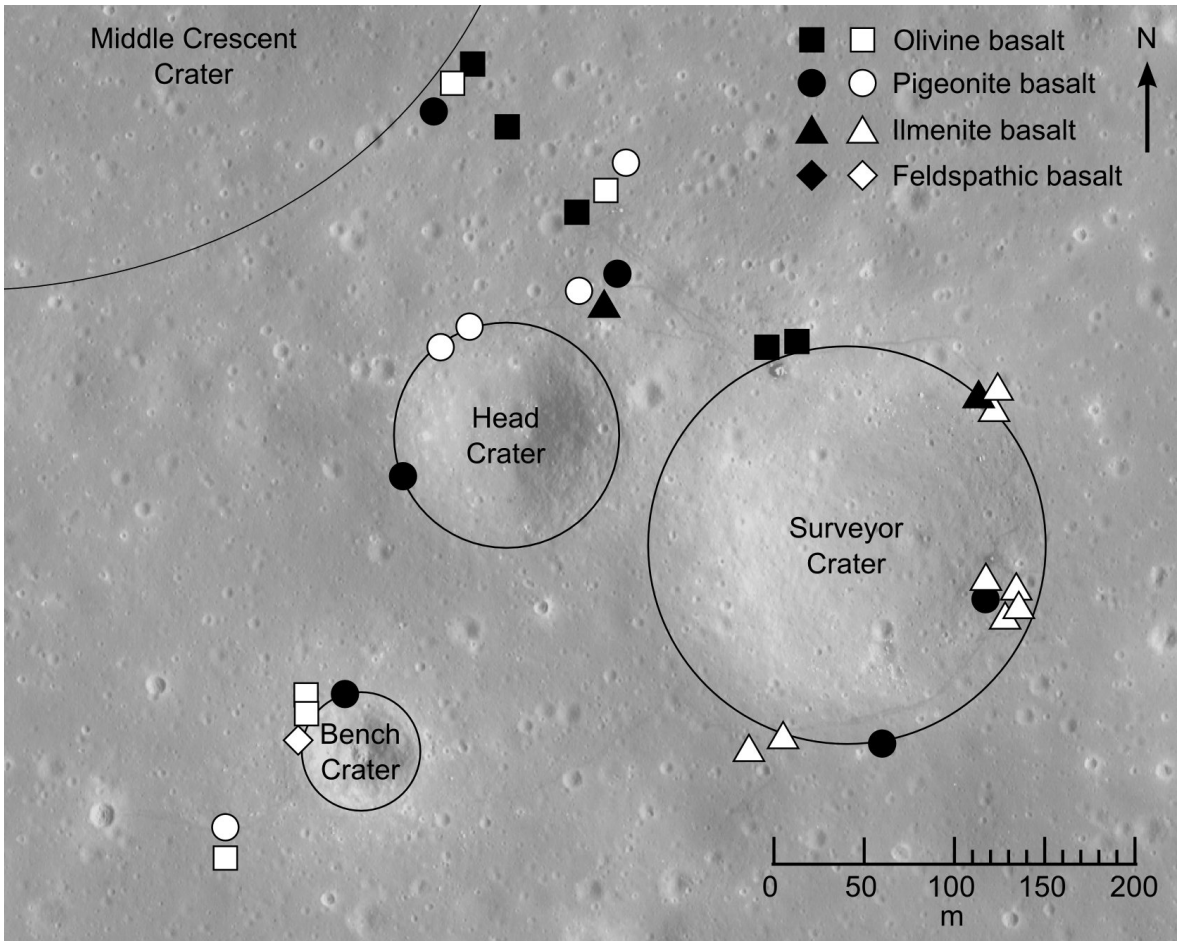

Figure 4.4: Spatial distribution of Apollo 12 basalts. Adapted from the map presented in *Rhodes et al.* (1977) with additional and modified symbols to account for more investigations of the Apollo 12 basaltic suites by *Neal et al.* (1994a). Black symbols represent more rapidly cooled vitrophyres and basalts with a variolitic groundmass, white symbols represent more slowly cooled samples with ophitic and gabbroic textures.

using the model of *McGetchin et al.* (1973). By comparison, estimates of excavation depth for the Surveyor and Head Craters (40 m and 20 m, respectively; *Rhodes et al.* 1977) suggest that Middle Crescent ejecta would have been significantly disrupted by these later impact events.

Rhodes et al. (1977) also assessed spatial relationships of the four Apollo 12 basaltic suites. They identified associations between: (1) the ilmenite basalts and Surveyor Crater in the south east of the landing site, as well as (2) the olivine basalts and Middle Crescent Crater in the north west of the area. Fig. 4.4 is modified from the sample distribution map of *Rhodes et al.* (1977), and reflects changes in basalt classifications and additional samples analysed since that study (*Nyquist et al.*, 1979; *Neal et al.*, 1994a). These modifications remain consistent with the spatial relationships originally identified. *Rhodes et al.* attempted to understand the underlying stratigraphy at the Apollo 12 site by combining these spatial relationships with calculations regarding crater

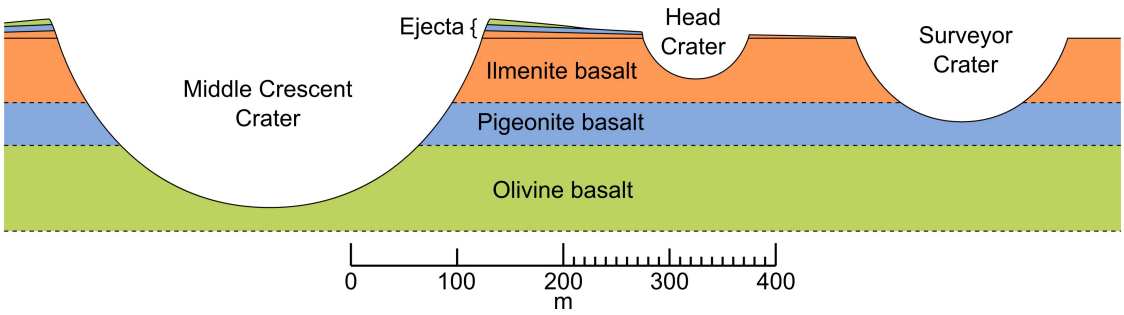

Figure 4.5: Simplified cross-section of Apollo 12 site, indicating stratigraphic sequence of the three main basaltic suites as inferred by *Rhodes et al.* (1977) and the estimated excavation depths of the three largest craters at the landing site. Scale is approximate with a ∼2× vertical exaggeration applied. A more detailed cross-section, examining possible stratigraphic positions of significant impact ejecta units is proposed in *Korotev et al.* (2011).

excavation, ejecta thickness, and the work of *Walker et al.* (1976b) investigating basalt flow thickness required to generate observed petrologic textures. The cross-section in Fig. 4.5 has been constructed using their descriptions (*Rhodes et al.*, 1977).

Petrogenesis of Apollo 12 basalts

The *LSPET* (1970a) first suggested that the varying textures and mineralogies of the Apollo 12 igneous rocks could be explained by fractional crystallisation and mineral accumulation within cooling basaltic magmas. The first detailed evaluation of this hypothesis was performed by *Compston et al.* (1971), who analysed the major and trace element chemistries and crystallisation ages of thirteen Apollo 12 basalts. In that study, the composition of 12009 (an olivine vitrophyre) was used to represent a primary liquid, and the effects of adding and removing assumed liquidus phases (i.e. olivine and Cr-spinel) were calculated. Although the compositions of some basalts could be recreated in this manner, varying trace element abundances (particularly Rb, Sr, Y and Zr) in other samples could not be explained by accumulation or fractionation of olivine and Cr-spinel. This led *Compston et al.* to conclude that the basalts had crystallised from at least six separate parent melts formed by individual episodes of partial melting in the lunar mantle. Initial ratios of $^{87}Sr/^{86}Sr$ calculated for the basalts were also found to be consistent with this conclusion.

Rhodes et al. (1977) later reviewed these findings, noting that the observed discrepancies may have been due to inter-laboratory bias in trace element determinations or sampling bias. One source of sampling bias arises from the fact that the trace elements used by *Compston et al.* to distinguish between different basalts are typically concentrated in accessory mesostasis assemblages. In addition to this, these trace elements

are inherently concentrated in residual liquids during crystallisation. Subsequent mobilisation of these liquids could then lead to trace elements being unevenly distributed throughout an individual basalt flow (*Rhodes et al.*, 1976; *Rhodes*, 1977). By contrast, REE abundances, Rb/Sr ratios and initial $^{87}Sr/^{86}Sr$ isotope ratios determined for the olivine and pigeonite basalts by *Nyquist et al.* (1977, 1979; 1981) are indistinguishable, whereas those of the ilmenite and feldspathic basalts are clearly distinct.

The combination of the olivine and pigeonite basalts and gabbros by *James and Wright* (1972) into a single basaltic suite was supported by trends in major, minor and trace element bulk compositions. Variations of elements such as MgO, SiO_2, Al_2O_3, TiO_2 and Cr_2O_3 in the olivine and pigeonite samples were found to fall along trends which can be explained by near-surface fractionation and accumulation of early-crystallised minerals, particularly olivine (*James and Wright*, 1972; *Rhodes et al.*, 1977). The ilmenite and feldspathic basalts, however, form separate compositional trends which cannot be explained by this process. It was suggested that these intergroup variations are indicative of basalts crystallising from separate parent melts generated by varying degrees of partial melting of the lunar interior at different depths (*Kushiro and Haramura*, 1971; *Green et al.*, 1971; *James and Wright*, 1972).

Several studies have identified problems with the co-magmatic nature of the olivine and pigeonite basalts. *Papike et al.* (1976) noted the lack of metallic iron inclusions in the pigeonite basalts, which are a characteristic feature of the olivine basalts. To explain this observation they suggested that fractionation of the basalts may have occurred at depth prior to reaching the reducing conditions of the lunar surface. More significantly, *Baldridge et al.* (1979) could not reconcile the compositional differences of the two suites with the textures they exhibited. It had previously been demonstrated that the composition of the fine-grained olivine vitrophyre 12009 had existed as a liquid at or close to the lunar surface and was close to that of the parent magma for the olivine basalts (*Green et al.*, 1971). When examining such vitrophyre samples, *Baldridge et al.* (1979) identified a discrepancy between the pigeonite and olivine basalt suites in normative olivine contents of $\sim$10% which is incompatible with the samples originating from a single homogeneous magma body.

More detailed modelling of the compositional evolution of the three main basaltic suites has provided further evidence against the co-magmatic nature of the pigeonite and olivine basalts. *Neal et al.* (1994a,b) used the compositions of vitrophyre samples from each suite, representing the suites' parental melt compositions, to determine their fractionation sequences. The results of these models were then used to generate fractionation and accumulation paths of compositional evolution, against which the bulk

compositions of other samples were compared. These demonstrated that the olivine and pigeonite suites are unrelated by fractionation or accumulation, and are derived from separate and distinct source regions. Assimilation of anorthositic crustal material was shown to be necessary to generate the pigeonite basalt compositions (up to 3% assimilation and 10% crystal fractionation). The compositions of the olivine and ilmenite basalts can be explained by variable degrees of partial melting (4-8% and 5-10% respectively) of sources containing olivine, pigeonite, augite and (in the case of the ilmenite basalts) plagioclase (*Neal et al.*, 1994b).

The minerals in these sources represent both early- and late-stage Lunar Magma Ocean (LMO) cumulates, formed after 82-94% crystallisation of the LMO. These are believed to have been brought together by overturn of the lunar interior (*Ringwood and Kesson*, 1976; *Spera*, 1992; *Neal et al.*, 1994b; *Hess and Parmentier*, 1995). Experimental studies have determined that the olivine and pigeonite basalt sources were located at a similar depth to other basaltic magmas (100-200 km; *Longhi* 1992a; *Snyder et al.* 1997). However, the ilmenite basalt source was likely located at a greater depth (350-400 km) comparable with that determined for the high-Ti picritic glasses (*Longhi*, 1992b; *Snyder et al.*, 1997).

Crystallisation ages

Initial efforts to determine the crystallisation ages of the Apollo 12 basalts by K-Ar radiometric dating resulted in values of 1.7-2.7 Ga (*LSPET* 1970a). However, several problems were identified with the use of the K-Ar method to date the samples, including; high levels of ^{40}Ar in some of the analysed materials, inhomogeneous distribution of K in the samples and the presence of phases with low Ar retentivity (*Papanastassiou and Wasserburg*, 1970; *Turner*, 1970a, 1971). As such, these ages have since been superceded by a number of studies utilising the ^{40}Ar-^{39}Ar, Rb-Sr and Sm-Nd dating methods (e.g. *Papanastassiou and Wasserburg* 1970; *Turner* 1971; *Murthy et al.* 1971; *Compston et al.* 1971; *Nyquist et al.* 1977; *Nyquist et al.* 1979). These studies have provided crystallisation ages of between 2.9-3.6 Ga for the Apollo 12 basalts (Fig. 4.6).

If the basalts within a given suite are related by magmatic processes, there should be agreement between crystallisation ages of the samples. With this reasoning, *Snyder et al.* (1997) calculated weighted-average ages for each of the basaltic suites (Fig. 4.6). These ages indicate that all three of the major suites were formed between ∼3.18-3.20 Ga. It is noticeable that the relative ages of the suites (oldest → youngest: ilmenite → olivine → pigeonite) conflict with the accepted stratigraphic sequence of the Apollo 12 basalts (Fig. 4.5; *Rhodes et al.* 1977; *Korotev et al.* 2011). However, this is almost

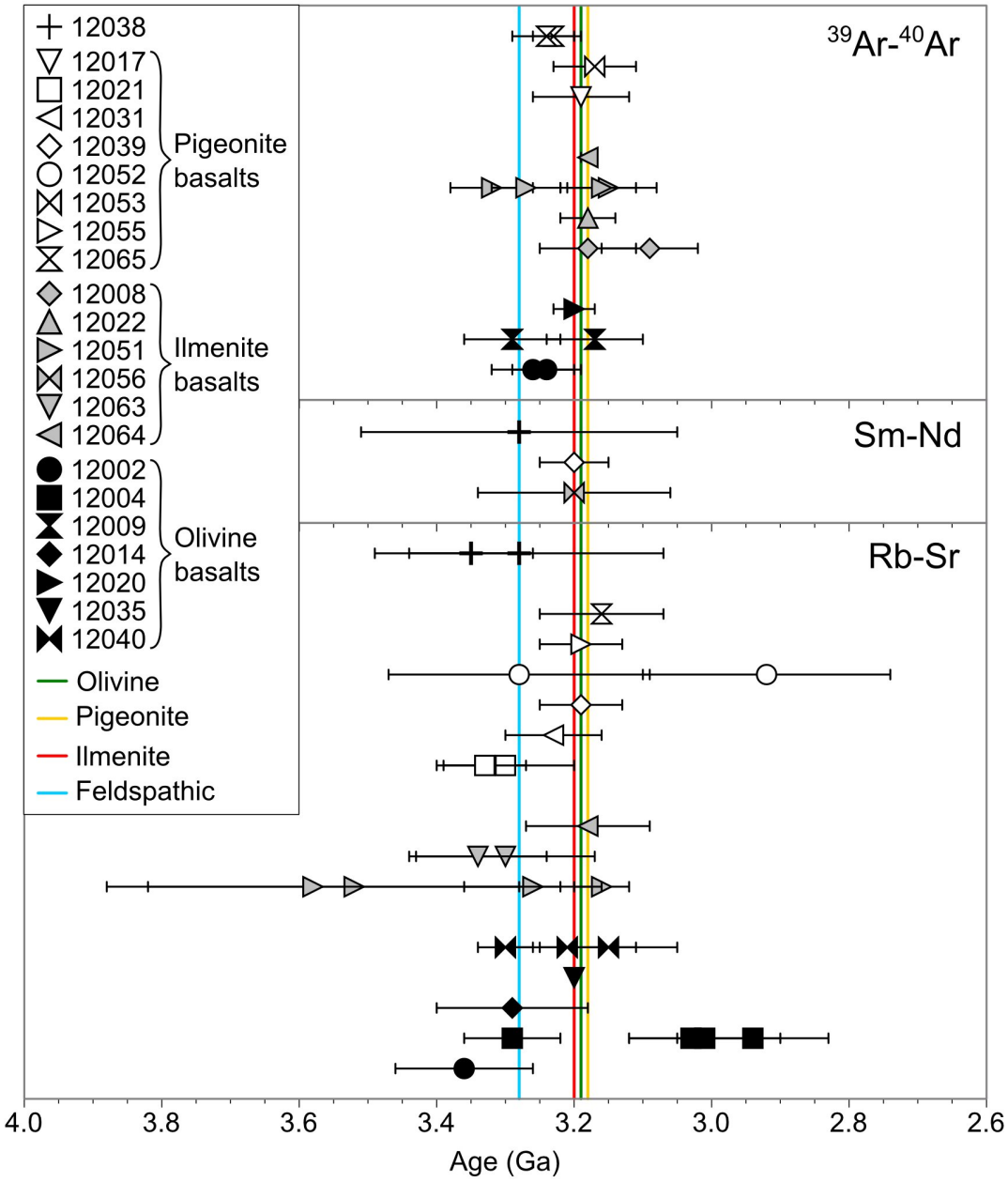

Figure 4.6: Ages of Apollo 12 basalts determined by ^{39}Ar-^{40}Ar, Sm-Nd and Rb-Sr radioisotope dating methods (*Papanastassiou and Wasserburg*, 1970, 1971b,a; *Cliff et al.*, 1971; *Compston et al.*, 1971; *Murthy et al.*, 1971; *Turner*, 1971; *Alexander et al.*, 1972a; *Stettler et al.*, 1973; *Horn et al.*, 1975a,b; *Nyquist et al.*, 1977; *Nyquist et al.*, 1979; *Nyquist et al.*, 1981). Coloured lines represent the weighted-average ages calculated by *Snyder et al.* (1997) for each of the basaltic suites.

certainly not significant given the similarity in these average ages and the errors reported for the original measurements. Possibly more significant is the older average age (3.28 Ga) reported for the feldspathic basalt 12038, providing additional evidence that the sample is indeed from a distinct parent melt to the other Apollo 12 basalts.

4.2.2 Non-igneous rocks

The *LSPET* (1970a) identified fewer breccias in the Apollo 12 samples than the Apollo 11 samples. This was interpreted as evidence that the regolith at the Apollo 12 landing site was less mature and not as thick as that at Tranquility Base. Preliminary study and comparison of the different types of material collected in the Oceanus Procellarum revealed a compositional similarity between the fine regolith material and the breccias, although both are compositionally distinct from the crystalline rocks (*LSPET* 1970a; *Meyer et al.* 1971; *Hubbard et al.* 1971). In addition to lunar lithologies, a carbonaceous chondrite was identified in the soil sample 12037 collected at Bench Crater (*McSween*, 1976; *Fitzgerald and Jones*, 1977).

Hubbard et al. (1971) first coined the term "KREEP" to describe material in the Apollo 12 soil which was found to be rich in K, Rb, P and rare-earth elements. They suggested the Copernican ray or extensive lateral mixing of material from the Fra Mauro region as possible sources of the materials. *Meyer et al.* (1971) divided the Apollo 12 KREEP component into glasses and annealed cataclastic breccias. Although Copernicus was identified as a probable source for the glass, the cataclastic nature of the breccias was interpreted as the result of a much larger impact event such as the one which produced the Fra Mauro Formation. The case for a Copernican origin of the KREEP glasses has since been reinforced by several other studies (e.g. *Bogard et al.* 1994; *Wentworth et al.* 1994; *Barra et al.* 2006). *Wasson and Baedecker* (1972) also suggested the Reinhold crater as an additional source of KREEP material.

Simon and Papike (1985) studied a range of Apollo 12 breccias, including the three regolith breccias (12010, 12034 and 12073) and eight smaller breccias selected from the coarse fines. Two of the breccias were found to be composed of anorthositic soils, derived from either the local crust underlying the basaltic flows or from highland regions distant from the Apollo 12 site. The remaining breccias were identified as "mare/KREEPy" breccias. Two of these were interpreted as being exotic to the Apollo 12 site, while the majority of them had compositions which could be modelled as mixtures of Apollo 12 mare basalts and medium-K KREEP with minor anorthositic components.

More recently, *Korotev et al.* (2011) performed a comprehensive study of Apollo 12 regolith samples, including 358 lithic fragments (2-4 mm sized) and 15 soils (<1

mm fines). Regarding the lithic fragments, *Korotev et al.* identified four lithological categories including: (1) mare basalts (∼33% of the lithic fragments), (2) regolith breccias (∼15%), (3) uncommon nonmare lithologies (∼5%), and (4) KREEP impact-melt breccias and glass (∼33%). The mare basalt fragments were largely found to be compositionally similar to examples of the three main basaltic suites already discussed, while the regolith breccias were reported to have compositions similar to the typical Apollo 12 regolith. The uncommon nonmare fragments were identified as alkali-suite rocks, ranging in composition from alkali anorthosite to alkali norite. Several of these fragments were found to have high concentrations of incompatible trace elements, although the ratios of specific trace elements were distinct from those typically associated with KREEP. The nonmare materials also include six feldspathic fragments which were identifed as originating from the feldspathic highlands. The KREEP impact-melt breccias and glass were found to be mostly crystalline impact-melt breccias and impact-melt rocks, with some glassy and crystalline rocks. Most of the KREEP material (which *Korotev et al.* refer to as "typical" Apollo 12 KREEP material) is reported as having compositions similar to KREEP material identified at the Apollo 14 site, although some were noted as containing a mare basalt component. Less common are a collection of crystalline impact-melt breccias with ITE concentrations ∼1.8× that of the typical Apollo 12 KREEP fragments, which were referred to as high-Th material.

Korotev et al. (2011) analysed the compositions of the <1 mm fines and used them in a series of mass-balance models in order to calculate the contributions of different materials to the "typical" Apollo 12 regolith (these results are summarised in Fig. 4.7). These models indicate that ∼29% of the typical Apollo 12 regolith is composed of a nonmare Procellarum KREEP Terrane component, incorporating the alkali noritic anorthosite, the typical KREEP material and the hi-Th KREEP material. The variety of nonmare lithologies in the regolith led *Korotev et al.* to propose that multiple craters were likely responsible for introducing material to the Apollo 12 site, with the Copernicus and Reinhold craters being likely sources of the typical KREEP material and hi-Th KREEP material respectively.

4.3 Basaltic diversity study

In an attempt to better characterise the basaltic material collected at the Apollo 12 site, eleven samples were selected for study from the 12003, 12023, 12030 and 12070 soils. This basaltic diversity study is comprised of two major components: (1) a detailed petrologic evaluation of the samples and identification of any compositionally distinct

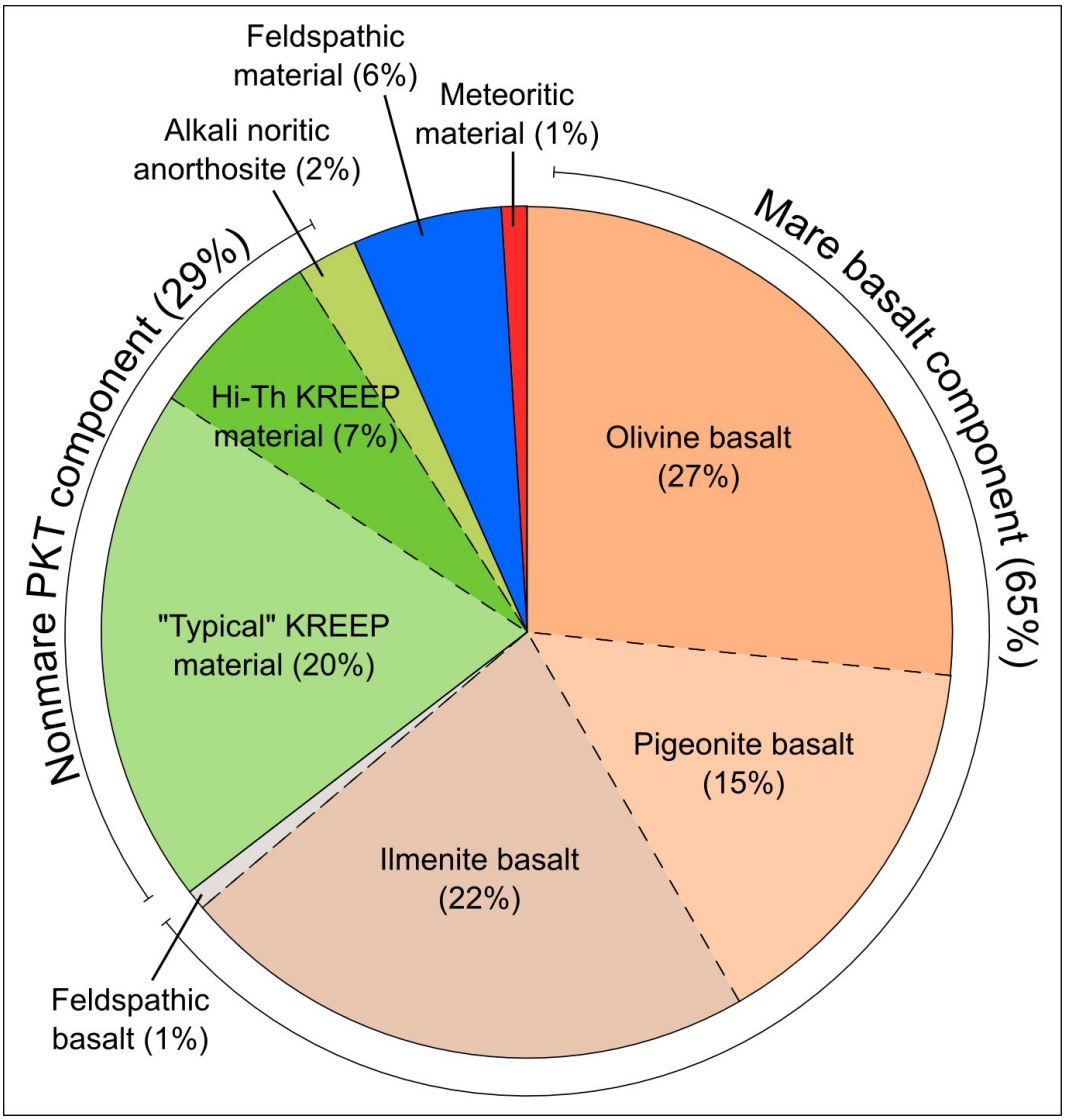

Figure 4.7: Summary of the mass-balance models of *Korotev et al.* (2011), indicating the components of "typical" Apollo 12 regolith.

basalts which may be exotic to the Apollo 12 site, and (2) radioisotope dating of the samples. In addition to the soil samples, three previously well-studied Apollo 12 basalts (12022, 12038 and 12063) were allocated to the project by the Curation and Analysis Planning Team for Extraterrestrial Materials (CAPTEM) in order to test the analytical techniques being employed in the study (Chapter 5).

Chapters 6 and 7 outline the initial results and conclusions of the petrologic evaluation of seven samples from the 12003 soil. 12003 originally had a mass of 0.30 kg and consists of fines and 1 cm pieces which were separated from the larger 12001 sample (originally 2.22 kg). These samples were collected near the Lunar Module (Fig. 4.2) at the end of the first of two extra vehicular activities (EVA-1) completed during the mission (*LSPET* 1970b).

All three of the main previous attempts to classify the Apollo 12 basalts have relied on bulk-rock characteristics (i.e. texture, modal mineralogy and bulk compositions; *James and Wright* 1972; *Rhodes et al.* 1977; *Neal et al.* 1994a). Although such measurements have been made in this study, the small sizes of the samples being analysed raises questions as to whether they are representative of the parent rocks from which they originated. As such, a major focus of this work has been to identify trends in major, minor and trace element mineral chemistry which are characteristic of individual basaltic suites. *Fagan et al.* (2012) have identified a relationship involving the ratio of Ti/V contents in olivine phases that appears to distinguish between ilmenite and olivine basalts. However, despite a large number of previous studies reporting mineral chemistries of the Apollo 12 basalts (e.g. *Bence et al.* 1970, 1971; *Grove et al.* 1973; *Dungan and Brown* 1977), few such trends have been identified.

Chapter 5

Apollo 12 Calibration Samples

5.1 Introduction

The following chapters outline the results of a study which aims to better characterise the diversity of basaltic flows at the Apollo 12 landing site, by analysing a selection of previously unstudied regolith particles (*Snape et al.*, 2011c). Detailed petrologic analyses of these samples utilised electron microprobe analysis and laser ablation inductively coupled plasma mass spectrometry, by the methods outlined in Chapter 2. In addition to the regolith particles, the Curation and Analysis Planning Team for Extraterrestrial Materials (CAPTEM) allocated three previously well-studied Apollo 12 basalt fragments, namely the ilmenite basalts 12022 and 12063, and the feldspathic basalt 12038. These were primarily to act as calibration samples for the ^{40}Ar-^{39}Ar radiosotope dating process which will form a fundamental component of the basaltic diversity project. The techniques employed to obtain modal mineralogies and bulk chemistries were also tested on these three samples. The results of these tests are discussed here.

5.2 Sample descriptions

12022

12022 was initially classified as an "ilmenite-bearing olivine basalt" by *James and Wright* (1972) on the basis of petrography and major element chemistry. *Neal et al.* (1994a) have since re-classified the sample as an ilmenite basalt, according to their whole-rock chemistry classification scheme where ilmenite basalts have Rb/Sr ratios which are <0.008. The basalt has been described as having a medium to fine grained porphyritic texture, composed of elongate augite and subhedral olivine phenocrysts en-

closed in a variolitic groundmass of intergrown plagioclase, pyroxene and ilmenite (*Brett et al.*, 1971a; *Weill et al.*, 1971). A crystallisation age of 3.18±0.04 Ga was determined by *Alexander et al.* (1972b) for 12022 by ^{40}Ar-^{39}Ar radioisotope dating.

The 12022 sample analysed in this study (12022,304_C) is consistent with previous petrographic descriptions (Fig. 5.1). It is predominantly composed of mafic minerals (pyroxene = 47% by mode; olivine = 14%; Table 5.1), with olivine and pyroxene phenocrysts ranging in size between ~100-800 μm. The pyroxene and plagioclase groundmass phases are typically between ~10-100 μm in size, although some plagioclase laths are >400 μm long.

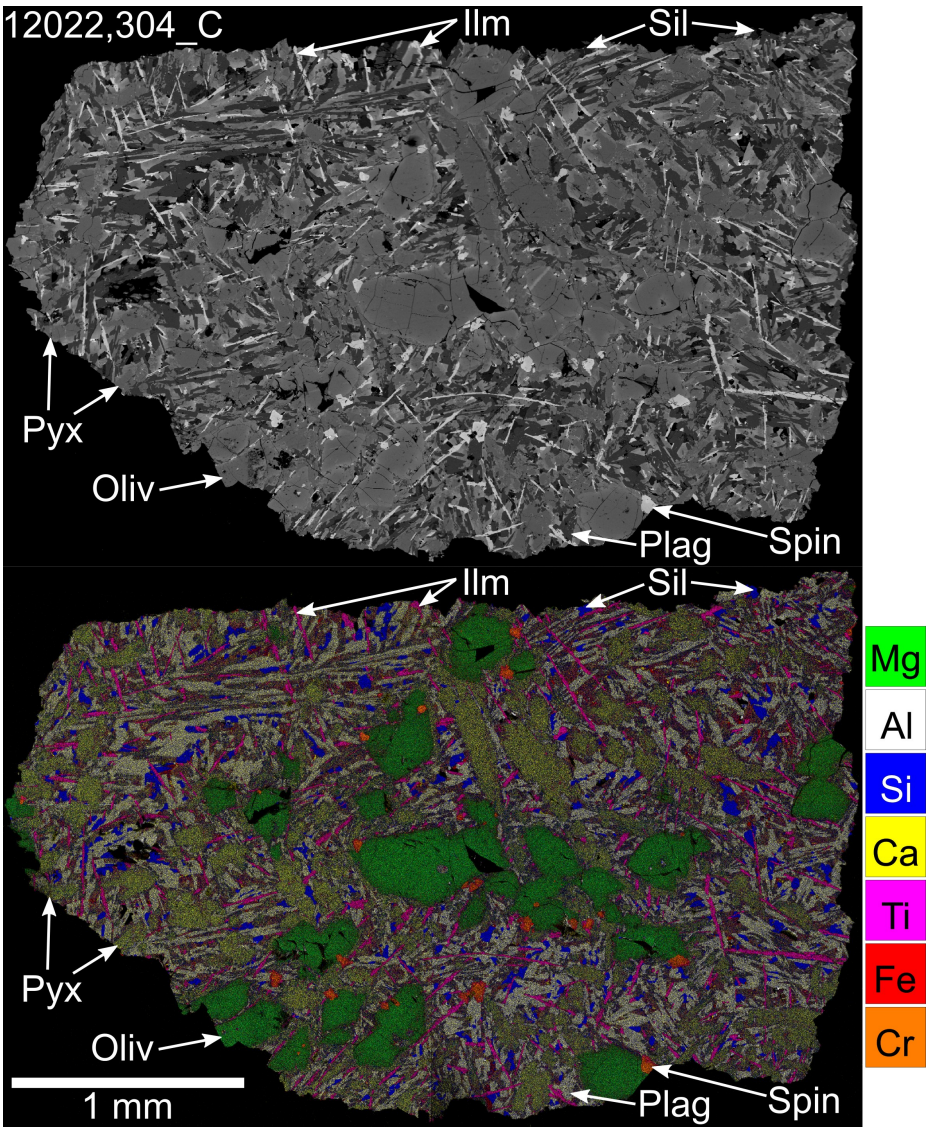

Figure 5.1: Backscattered electron (BSE) and false colour element maps 12022,304_C. The colours of the element maps represent distribution and concentration of the following elements: Si = blue, Al = white, Mg = green, Fe = red, Ca = yellow, Ti = pink and Cr = orange. Examples of the major and minor phases within the sample have been indicated. Pyx = pyroxene; Plag = plagioclase; Oliv = olivine; Sil = silica; Ilm = ilmenite; Spin = spinel.

Table 5.1: Modal mineralogies of the 3 calibration samples 12022, 12038 and 12063. The results from this study have been compared with those reported by previous authors. The literature values were largely obtained from thin section samples by point counting. Those reported by *McGee et al.* (1977) represent ranges of previous studies. Those reported by *Dungan and Brown* (1977) represent averages of previous studies.

12022,304												
Reference	Sample number	Pyx.	Plag.	Oliv.	Sil.	Spin.	Ilm.	FeNi	Tr.	Glass/Meso.	Opaques*	
This study	12022,304_C	51.0	25.8	14.4	3.8	0.6	4.2	<0.1	0.1	<0.1	-	
Brett et al. 1971a	12022,12	58.6	12.0	16.5	-	1.5	8.3	<0.1	1.5	1.6	-	
Engel et al. 1971	12022,54	49.0	24.0	20.2	-	-	-	-	-	-	23.4	
McGee et al. 1977	Not specified	30-59	12-26	16-33	-	-	9-23	-	-	1.0	-	
Neal et al. 1994a	Not specified	56.0	12.2	19.5	0.2	2.8	6.3	0.4	0.3	2.3	-	

12038,263													
Reference	Sample number	Pyx.	Plag.	Oliv.	Sil.	Spin.	Ilm.	FeNi	Tr.	Glass/Meso.	Phos.	Fa.	K-feld.
This study	12038,263_A	50.0	43.6	-	2.8	0.0	2.9	<0.1	0.2	0.3	0.2	-	-
Christie et al. 1971	12038,32	55.0	30.0	-	<5**	-	10.0	-	-	-	-	-	-
Beaty et al. 1979	12038,4	48.9	44.0	<0.1	2.7	0.1	3.5	<0.1	0.1	0.1	0.3	0.2	0.2
Neal et al. 1994a	Not specified	48.8	43.8	0.1	2.7	0.2	3.5	0.1	0.1	0.7	-	-	-

12063,330													
Reference	Sample number	Pyx.	Plag.	Oliv.	Sil.	Spin.	Ilm.	FeNi	Tr.	Glass/Meso.	Phos.	Fa.	Opaques*
This study	12063,330_A	54.1	33.4	6.2	0.7	0.4	4.4	<0.1	0.1	0.6	0.1	-	-
Taylor et al. 1971a	12063,9	56.8	27.1	6.6	2.0	-	-	-	-	1.5	-	1.2	4.8
Papike et al. 1976	Not specified	63.7	22.2	2.8	1.6	-	-	-	-	1.6	-	-	8.1
McGee et al. 1977	Not specified	56-64	22-28	3-9	-	-	-	-	-	2-7	-	-	8.0
Dungan and Brown 1977	Not specified	60.0	25.0	6.0	1.6	2.0	-	-	-	5.0	-	-	6.0
Neal et al. 1994a	Not specified	64.6	21.6	2.8	0.1	3.4	4.6	0.1	0.3	2.5	-	-	-

Pyx. = pyroxene; Plag. = plagioclase; Oliv. = olivine; Sil. = silica; Spin. = spinel; Ilm. = ilmenite; FeNi = FeNi metal grains; Tr. = troilite
Meso. = mesostasis; Phos. = phosphates; Fa. = fayalite
*Opaques include ilmenite, spinel, troilite and metal.
**<5 cristobalite and other minor phases.

Ilmenite is the most common minor phase (5%), and forms needles (up to 500 μm long and typically ~10 μm wide) which cross-cut the other groundmass phases. A silica polymorph is relatively common throughout the groundmass (4%) and occurs as interstitial grains (~20-50 μm) between the plagioclase and pyroxene crystals. Subhedral spinel grains (~30-65 μm; 1% by mode) are also present in the sample, and are typically adjacent to or enclosed in the olivine phenocrysts. The element map of 12022,304_C indicates that the spinel grains which are enclosed in olivine have more homogeneous chromite compositions, whereas those which are adjacent to the phenocrysts or in the groundmass of the sample appear to have chromite cores with ulvöspinel rims (Fig. 5.1).

Accessory phases in the sample include a sulfide mineral (0.1%) and FeNi metal (<0.1%). These form small (<15 μm) grains which are commonly associated with the most Fe-rich pyroxene compositions and rare (<0.1%) interstitial areas of mesostasis.

12038

Early studies of the Apollo 12 basalts identified 12038 as being compositionally distinct from the other samples (*LSPET* 1970a;*Compston et al.* 1971; *Cuttitta et al.* 1971; *Haskin et al.* 1971; *Keil et al.* 1971; *Kushiro and Haramura* 1971). The unusually high Al_2O_3 (>12 wt%) and low FeO (<18 wt%) content led to the sample being classified as a feldspathic basalt by *James and Wright* (1972). Although several other Apollo 12 basalts were also initially considered to be members of the feldspathic suite (12006, 12031 and 12072; *James and Wright* 1972; *Beaty et al.* 1979), more recent work by *Neal et al.* (1994a) suggests that 12038 is the only known feldspathic basalt in the Apollo 12 sample collection. As such, *Neal et al.* (1994a) suggested that it might represent an exotic sample placed at the Apollo 12 site as impact ejecta. Rb-Sr radiometric dating by *Compston et al.* (1971) yielded a crystallisation age of 3.28±0.21 Ga. This is within error of the ages reported by *Nyquist et al.* (1981) using both Rb-Sr (3.35±0.09 Ga) and Sm-Nd (3.28±0.23 Ga) dating methods.

The 12038,263_A subsplit is composed mostly of pyroxene (50% by mode) and plagioclase (44%) which form similarly sized grains (up to ~2 mm; Table 5.1; Fig. 5.2). This is consistent with modal mineralogies reported by *Beaty et al.* (1979) and *Neal et al.* (1994a). The plagioclase forms large laths which partially enclose the pyroxenes. The pyroxenes are prominently zoned from more magnesian to more Fe-rich compositions.

Ilmenite and a silica polymorph are present as minor phases in the sample (both ~3% by mode). The ilmenite forms needles which are typically between 20-30 μm thick,

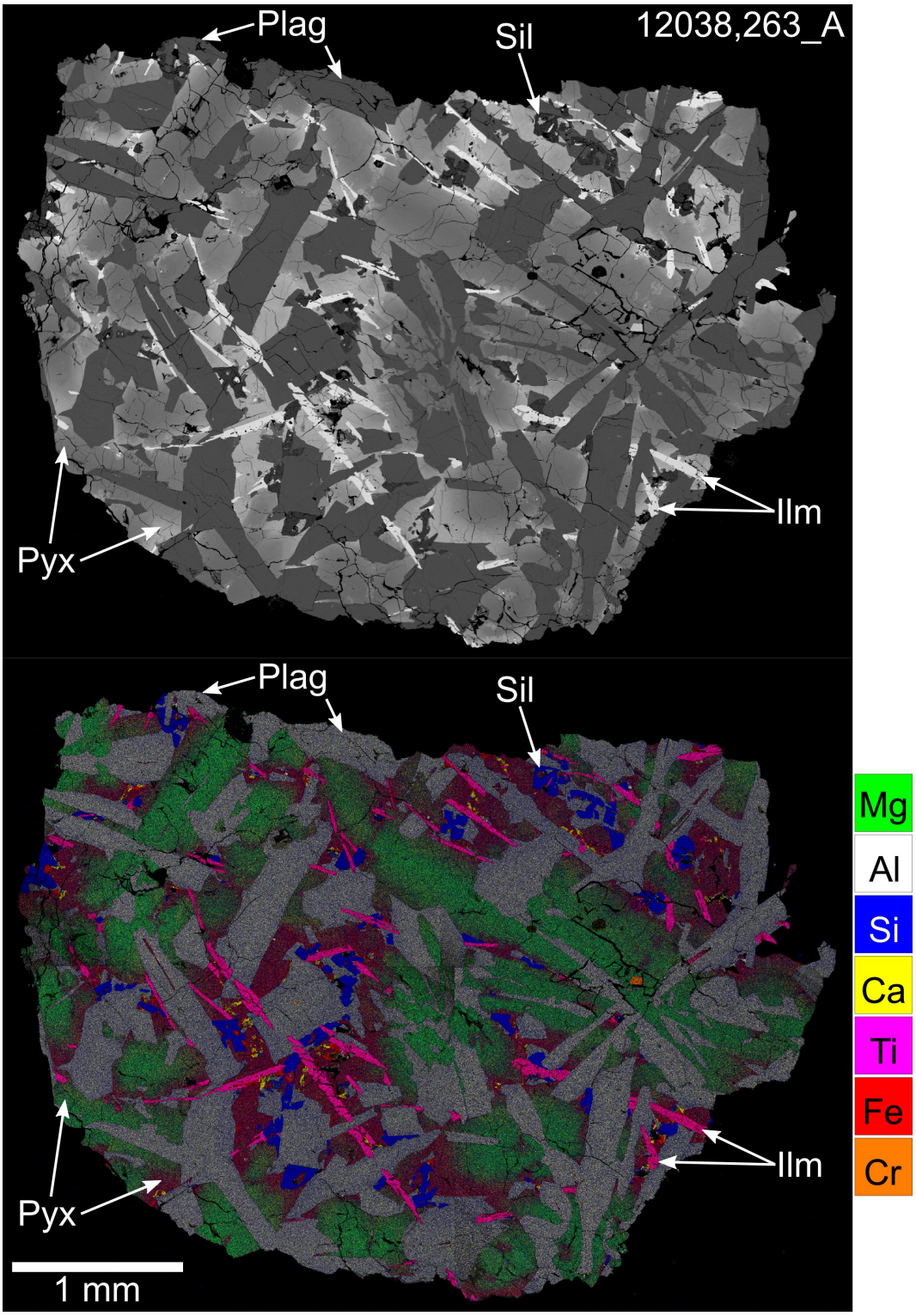

Figure 5.2: Backscattered electron (BSE) and false colour element maps 12038,263_A. The colours of the element maps represent distribution and concentration of the following elements: Si = blue, Al = white, Mg = green, Fe = red, Ca = yellow, Ti = pink and Cr = orange. Examples of the major and minor phases within the sample have been indicated. Pyx = pyroxene; Plag = plagioclase; Sil = silica; Ilm = ilmenite.

and in some cases >500 μm long. The silica forms anhedral-subhedral grains (∼50-150 μm) which are interstitial to the plagioclase and pyroxene. Several of the silica grains form hopper crystals which exhibit cruciform shapes.

Several accessory phases are commonly associated with areas of mesostasis, including phosphates (0.2%), sulfides (0.2%) and FeNi metal grains (<0.1%). These form anhedral grains which are between ∼5-50 μm in size. Two grains of chromite are also identified in the sample. The smaller of these (20 μm) is enclosed in plagioclase, while the larger grain (50 μm) is enclosed in a Mg-rich pyroxene phase.

12063

There is some discrepancy in the petrographic descriptions of the ilmenite basalt, 12063 (*Taylor et al.*, 1971a; *McGee et al.*, 1977; *Meyer*, 2005). *Taylor et al.* (1971a) described it as a microgabbro containing subhedral grains of forsteritic olivine and laths of plagioclase enclosed by pyroxene. However, *McGee et al.* (1977) describe it as a "porphyritic olivine, pyroxene basalt," containing phenocrysts of rounded olivine and euhedral to subhedral pyroxene in a matrix of intergrown plagioclase, pyroxene and opaque minerals. *Papanastassiou and Wasserburg* (1971a) and *Murthy et al.* (1971) determined the age of 12063 as 3.30±0.13 Ga and 3.34±0.10 Ga respectively, by Rb-Sr radioisotope dating.

The sample analysed in this study (12063,330_A) more closely fits the description of *Taylor et al.* (1971a), although plagioclase in the sample is only subophitically enclosed by pyroxene (Fig. 5.3). Pyroxene is the most abundant phase in 12063,330_A (54% by mode) and forms grains which vary in size from <0.1 mm up to ∼1.1 mm. The element map of the sample (Fig. 5.3) indicates compositional zoning of the pyroxenes, which appears to be broadly consistent with that described by *Hollister et al.* (1971) in 12063. Plagioclase is the next most abundant phase in the sample (33%) and forms less lathlike crystals (up to ∼700 μm) than are described by *Taylor et al.* (1971a) in 12063,9. Olivine occurs as subhedral to anhedral grains (∼0.2 mm; 6%). The ilmenite in 12063,330_A (4%) varies considerably from more lathlike crystals (typically ∼300×40 μm) to more irregular shapes (∼40-90 μm).

Spinel is less abundant (0.5%) in 12063,330_A than is reported in other 12063 samples (Table 5.1; *Dungan and Brown* 1977; *Neal et al.* 1994a), and forms subhedral grains (∼30-80 μm) with chromite cores and ulvöspinel rims. Other accessory phases in the sample include silica (0.7%), sulfides (0.1%), FeNi metal grains (<0.1%) and phosphates (<0.1%). These phases occur as ∼5-20 μm grains in interstitial sites between plagio-

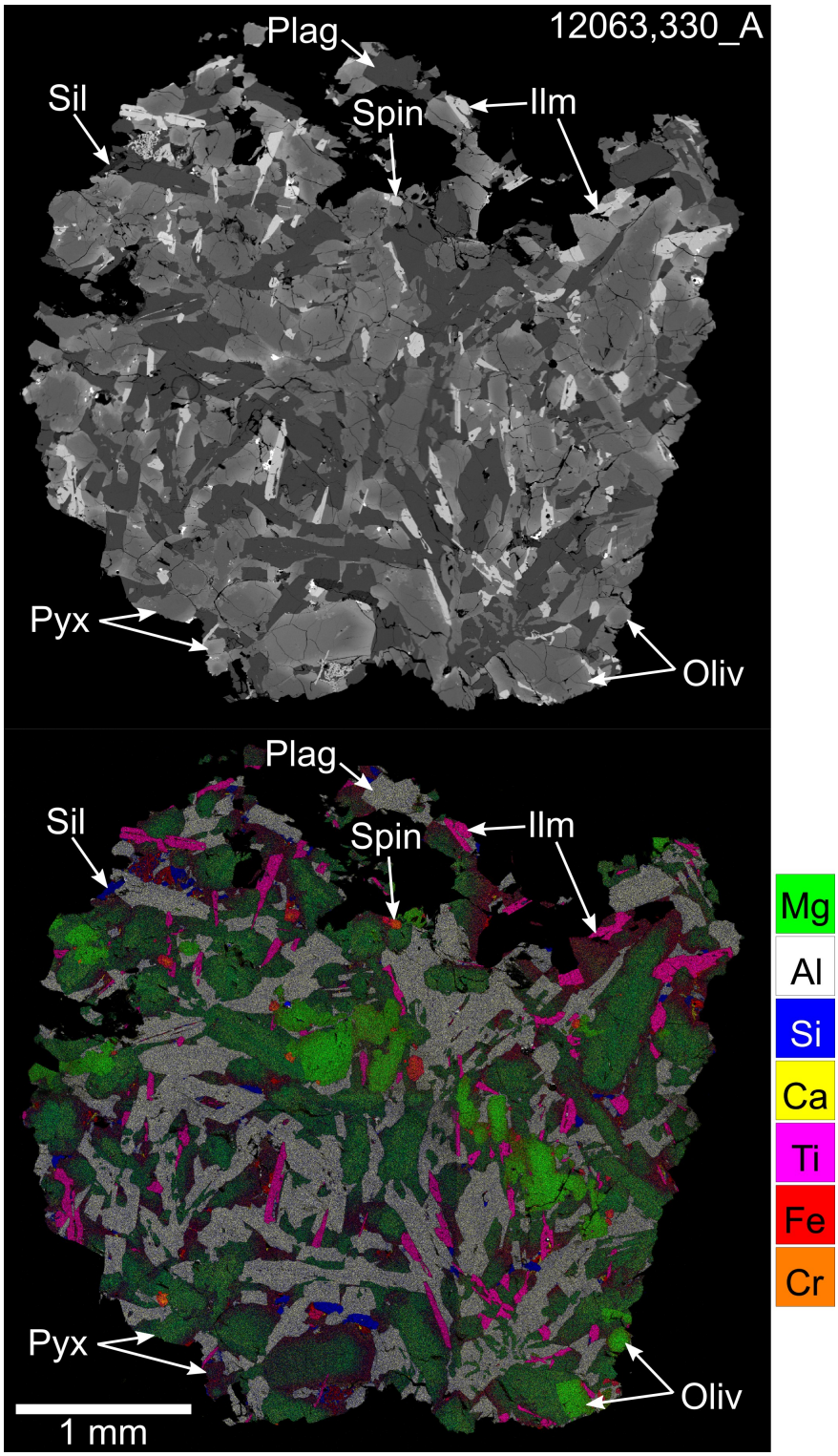

Figure 5.3: Backscattered electron (BSE) and false colour element maps 12063,330_A. The colours of the element maps represent distribution and concentration of the following elements: Si = blue, Al = white, Mg = green, Fe = red, Ca = yellow, Ti = pink and Cr = orange. Examples of the major and minor phases within the sample have been indicated. Pyx = pyroxene; Plag = plagioclase; Oliv = olivine; Sil = silica; Ilm = ilmenite; Spin = spinel.

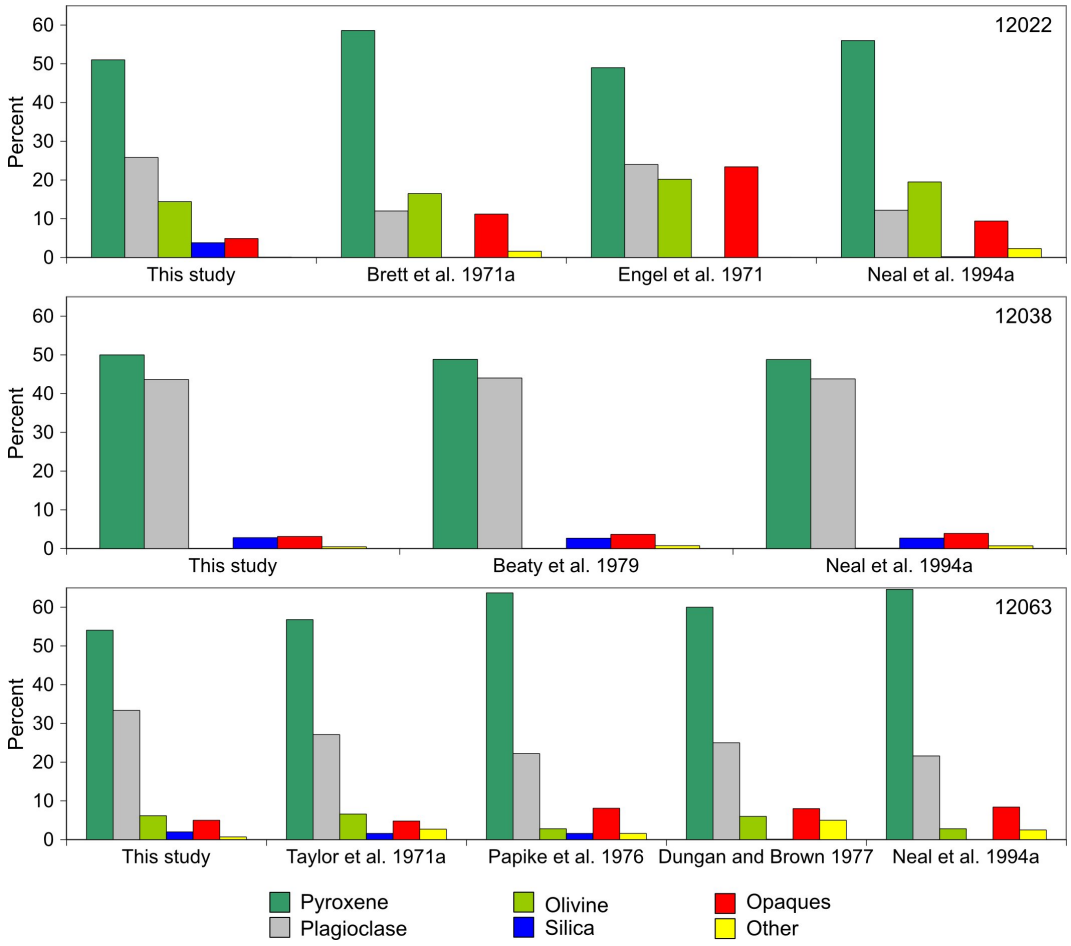

Figure 5.4: Histograms illustrating the modal mineralogies of the three calibration samples examined in this study compared with the literature data reported in Table 5.1. Opaques include ilmenite, spinel, FeNi metal and troilite. Other phases include glass/mesostasis, phosphates, fayalite and K-feldspar.

clase and the most Fe-rich pyroxenes. They are commonly associated with mesostasis assemblages and larger (0.1-0.2 mm) intergrowths of fayalite and silica.

5.3 Discussion

The techniques used for establishing modal mineralogy and bulk composition of these samples have produced results which are broadly comparable with those reported previously (Tables 5.1; 5.2; Fig. 5.4). Some discrepancies are observed between the results of this investigation and those of previous studies.

For example, a higher abundance of plagioclase was measured in 12063,330_A than in other 12063 samples, and lower abundances of mafic phases in both 12022,304_C and 12063,330_A (Table 5.1). However, these discrepancies are consistent with higher bulk concentration of Al_2O_3 in 12063,330_A, and lower bulk MgO values within both of these samples (Table 5.2). As such, these are interpreted to be the result of variability

Table 5.2: Major and minor element bulk chemistries of the 3 calibration samples 12022, 12038 and 12063. Values are reported as oxide wt%. Errors for the samples analysed in this study are 1σ standard deviations of repeated raster beam analyses.

12022							
Reference	This study	i	ii	iii	iv	v	v
Sample no.	12022,304_C	Not specified	12022,98	12022,56	Not specified	12022,232	12022,232
SiO_2	43.6 ± 0.1	36.0	42.3	43.2	42.3	43.4	43.0
TiO_2	5.37 ± 0.04	5.10	4.54	5.16	4.85	5.17	4.84
Al_2O_3	10.0 ± 0.1	11.0	9.12	9.04	8.20	9.45	7.94
Cr_2O_3	0.41 ± 0.03	0.39	0.56	0.56	-	0.47	0.53
FeO	21.2 ± 0.1	22.0	22.1	21.4	21.6	21.2	21.6
MnO	0.27 ± 0.02	0.17	0.26	0.25	0.31	0.27	0.28
MgO	8.83 ± 0.03	13.0	11.6	10.4	11.9	9.62	11.1
CaO	9.61 ± 0.03	11.0	9.37	9.56	9.00	9.93	9.51
Na_2O	0.42 ± 0.01	0.36	0.29	0.47	0.23	0.26	0.25
K_2O	0.08 ± 0.01	0.07	0.07	0.07	0.06	0.07	-
P_2O_5	0.21 ± 0.02	-	0.02	0.13	-	-	-
Total	100.0	99.1	100.2	100.3	98.5	99.9	99.1
Mg#	42.6	51.3	48.4	46.5	49.6	44.7	47.8
Analytical method	a	b	c	c	d + e	e	e

12038							
Reference	This study	i	vi	ii	vii	viii	ix
Sample no.	12038,263_A	Not specified	12038,44	12038,54	12038,28	Not specified	12038,77
SiO_2	47.2 ± 0.1	49.0	47.1	47.1	47.1	46.6	46.6
TiO_2	3.26 ± 0.04	3.20	3.28	3.22	3.17	3.31	3.25
Al_2O_3	13.3 ± 0.1	12.0	13.0	12.1	12.8	12.5	12.5
Cr_2O_3	0.30 ± 0.03	0.32	-	0.34	0.31	0.27	0.32
FeO	17.2 ± 0.1	17.0	17.7	17.9	17.4	18.0	17.8
MnO	0.25 ± 0.02	0.26	0.25	0.24	0.24	0.27	0.25
MgO	6.22 ± 0.03	6.50	6.60	7.09	6.50	6.71	6.83
CaO	11.1 ± 0.1	11.0	11.4	11.5	11.4	11.6	11.5
Na_2O	0.80 ± 0.01	0.60	0.69	0.64	0.64	0.66	0.67
K_2O	0.08 ± 0.01	0.06	0.06	0.07	0.04	0.07	0.07
P_2O_5	0.30 ± 0.02	-	0.14	0.02	0.17	0.14	0.12
Total	100.0	99.9	100.3	100.2	99.8	100.1	99.8
Mg#	39.2	40.6	39.9	41.4	40.0	40.0	40.7
Analytical method	a	b	c	c	f	d	d

12063						
Reference	This study	x	xi	xii	xiii	xiv
Sample no.	12063,330_A	12063,52	12063,70	12063,53	12063,60	12063,69
SiO_2	43.8 ± 0.1	43.5	42.8	41.9	43.2	44.7
TiO_2	4.77 ± 0.04	5.00	5.00	4.17	-	4.67
Al_2O_3	11.0 ± 0.1	9.27	9.10	11.5	7.99	9.33
Cr_2O_3	0.44 ± 0.02	0.44	0.41	0.45	-	0.38
FeO	19.8 ± 0.1	21.3	21.2	21.7	20.5	21.5
MnO	0.27 ± 0.02	0.28	0.27	0.26	-	0.28
MgO	8.92 ± 0.04	9.56	11.4	9.12	10.8	8.38
CaO	10.3 ± 0.1	10.5	10.8	12.0	-	13.0
Na_2O	0.44 ± 0.01	0.31	0.28	0.59	-	0.29
K_2O	0.06 ± 0.01	0.06	-	0.08	-	0.08
P_2O_5	0.18 ± 0.02	0.14	-	-	-	-
Total	100.0	100.3	101.3	101.9	-	102.6
Mg#	44.6	44.5	49.0	42.8	48.5	41.0
Analytical method	a	d	e	g	e	e

i. *LSPET* 1970a; ii. *Kushiro and Haramura* 1971; iii. *Engel et al.* 1971; iv. *Smales et al.* 1971; v. *Warren et al.* 1986; vi. *Biggar et al.* 1971; vii. *Cuttitta et al.* 1971; viii. *Compston et al.* 1971; ix. *Willis et al.* 1972; x. *Willis et al.* 1971; xi. *Wakita and Schmitt* 1971; xii. *Bouchet et al.* 1971; xiii. *Ehmann and Morgan* 1971; xiv. *Wänke et al.* 1971

a = EMP Raster beam analyses; b = optical spectrographic techniques; c = conventional wet chemistry; d = X-ray fluorescence; e = instrumental neutron activation analysis; f = mixed microchemical and X-ray fluorescence; g = spark mass spectrometry

between the samples in this study and those analysed in previous investigations. This observation highlights the higher uncertainties associated with data obtained from small (<1 cm surface area studied) samples which may not necessarily be representative of their parent rocks.

There appears to be a systematic overestimation of P_2O_5 (by ∼24-64%) and possibly also of Na_2O (by ∼16-26%) by the electron microprobe raster beam analyses (Table 5.2). Unlike the discrepancies described above, the modal mineralogies do not provide a clear explanation for these. As discussed in Chapter 2, energy dispersive spectroscopy (EDS) measurements of P are known to be problematic, due to problems resolving the element's X-ray emission peak. Indeed, the overestimation of P_2O_5 is consistent with the errors identified with EDS analyses of the USGS BCR-2 basaltic glass standard (Fig. 2.6).

The volatile nature of Na can lead to problems with electron microprobe measurements. However, this would typically lead to underestimations of Na and, therefore, seems like an unlikely explanation for an overestimation of Na_2O. EDS measurements of Na can also be affected by X-ray emission peak ovelaps with Zn. Due to the generally low abundance of Zn in lunar materials (*Haskin and Warren*, 1991) this is also considered to be an unlikely explanation. The most likely explanation for the overestimation of Na_2O abundances appears to be that the "Unequal Host-Phase Density Effect" (*Albee et al.*, 1977; *Nazarov et al.*, 1982) for Na is not adequately corrected by the method of *Warren* (1997).

Nevertheless, the broad agreement of these results with previous studies indicates that the approaches used here provide appropriate non-destructive methods for investigating the bulk characteristics of the unstudied fines (1-2 mm chips) which are discussed in the following chapters.

Chapter 6

12003,308

6.1 Introduction

Ten 1-2 mm fragments were selected from the 12003,26 regolith fine fraction of the Apollo 12 sample collection. These ten fragments (with a combined mass of 0.11 g) were allocated the identifier 12003,308 by the Lunar Sample Laboratory at the NASA Johnson Space Center. Each fragment was then split into two sub-sections, in order to obtain an "A-split" to use for petrologic analysis and a second "B-split" sample which could be retained for radiometric dating (see Chapter 2). This chapter will focus entirely on the petrologic examination of the ten "A-splits".

The primary aim of this study is to assess the petrologic variety of these samples and their relation (if any) to previously studied Apollo 12 samples (*James and Wright*, 1972; *Rhodes et al.*, 1977; *Neal et al.*, 1994a; *Meyer*, 2005). The small sizes of the 12003,308 samples require that caution is used when assessing the importance of their modal mineralogies and bulk compositions, and how representative such values may be of the parent rocks from which these samples originated. This is of particular concern for the coarser grained samples where their grain sizes are of a similar order of magnitude to their overall size. As such, this investigation will largely rely on the mineral chemistries of the samples.

6.2 Results

Initial observations by both optical and electron microscopy revealed textural differences between the ten samples. The variety of modal mineralogies and major and minor element bulk compositions of the samples are also broadly consistent with these

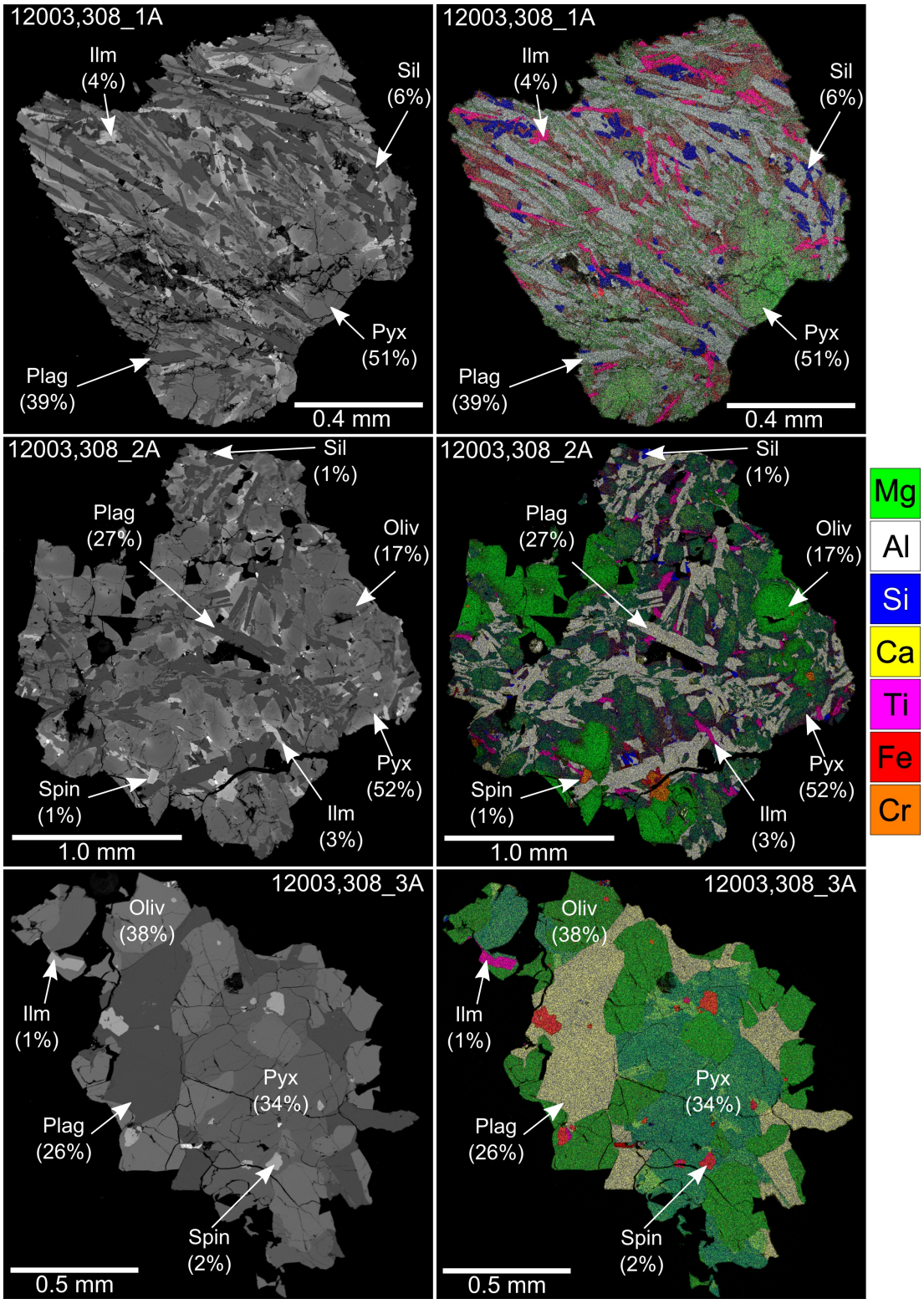

Figure 6.1: Backscattered electron (BSE) images and false colour element maps of samples 12003,308_1-3A. The colours of the element maps represent distribution and concentration of the following elements: Si = blue, Al = white, Mg = green, Fe = red, Ca = yellow, Ti = pink and Cr = orange. Examples of the major phases within the samples have been indicated along with their modal abundances. Pyx = pyroxene; Plag = plagioclase; Oliv = olivine; Sil = silica; Ilm = ilmenite; Spin = spinel.

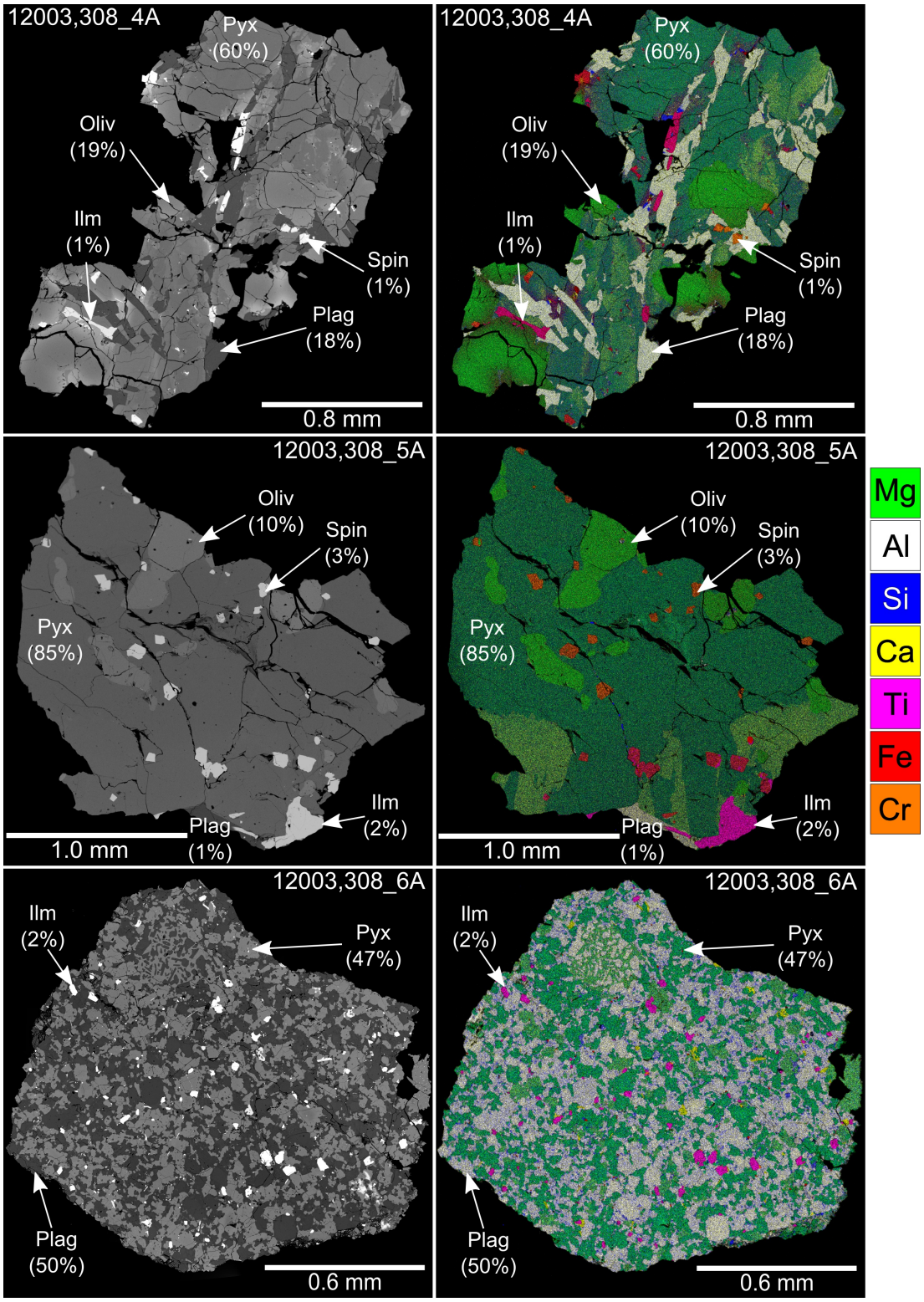

Figure 6.2: Backscattered electron (BSE) images and false colour element maps of samples 12003,308_4-6A. The colours of the element maps represent distribution and concentration of the following elements: Si = blue, Al = white, Mg = green, Fe = red, Ca = yellow, Ti = pink and Cr = orange. Examples of the major phases within the samples have been indicated along with their modal abundances. Pyx = pyroxene; Plag = plagioclase; Oliv = olivine; Sil = silica; Ilm = ilmenite; Spin = spinel.

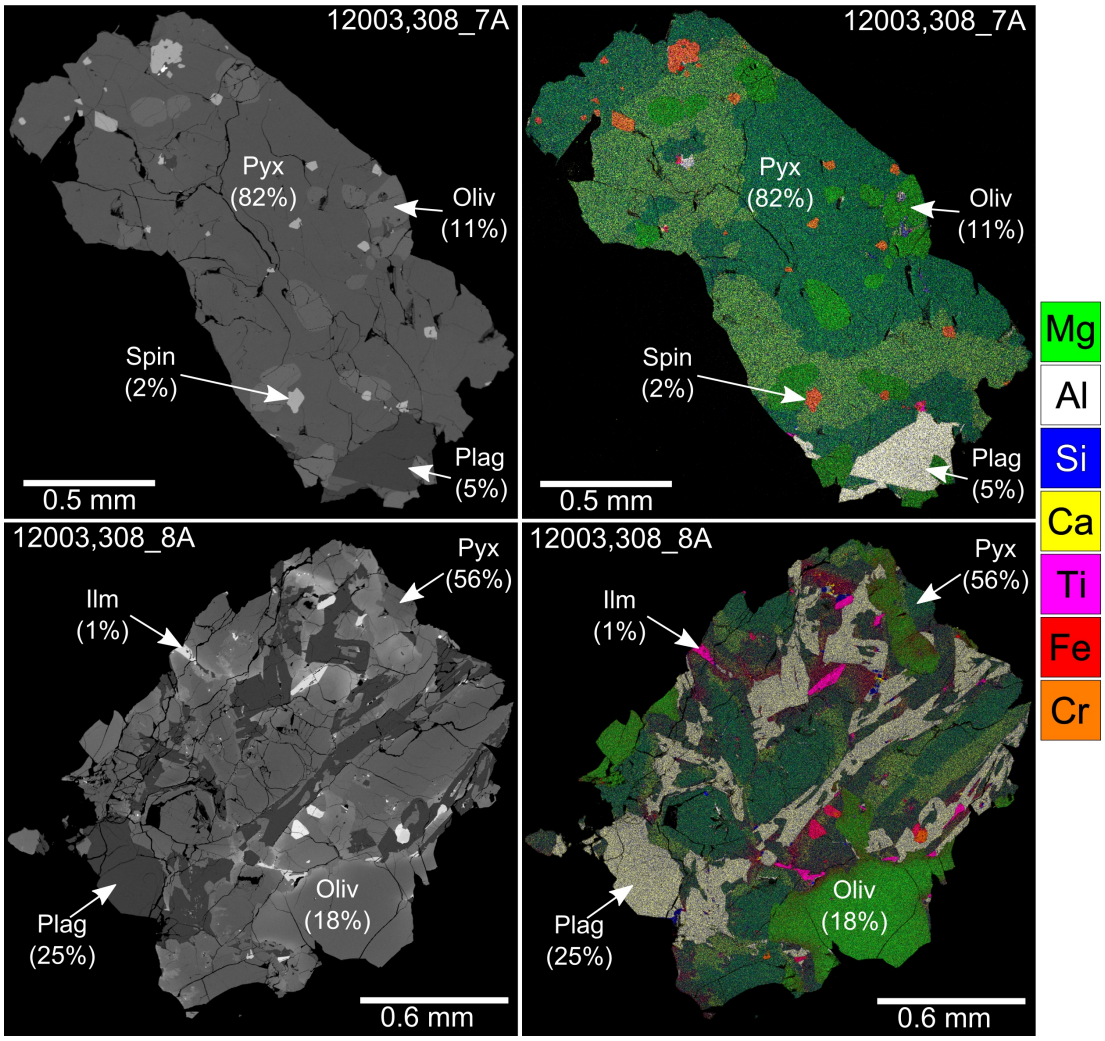

Figure 6.3: Backscattered electron (BSE) images and false colour element maps of samples 12003,308_7-8A. The colours of the element maps represent distribution and concentration of the following elements: Si = blue, Al = white, Mg = green, Fe = red, Ca = yellow, Ti = pink and Cr = orange. Examples of the major phases within the samples have been indicated along with their modal abundances. Pyx = pyroxene; Plag = plagioclase; Oliv = olivine; Sil = silica; Ilm = ilmenite; Spin = spinel.

observations. For the purpose of this discussion a preliminary grouping has been defined based on the textural similarities between the samples, their modal mineralogies and bulk compositions (Tables 6.1; 6.2).

Groups 1 and 2 consist of four porphyritic-ophitic samples (12003,308_1A;_2A;_4A;_8A), similar to those observed within other basaltic lunar samples, including many other Apollo 12 basalts (e.g. 12012, 12014 and 12038; *Reid* 1971; *Rhodes et al.* 1977; *Beaty et al.* 1979). Group 1 is comprised solely of the finest grained (∼0.01-0.40 mm) of these samples (,308_1A). It is a subophitic basalt containing prominently zoned pyroxene and laths of plagioclase (Fig. 6.1). The remaining three samples are coarser grained (∼0.10-0.70 mm) and have more ophitic textures. These Group 2 samples also contain significant amounts (17-19% by modal

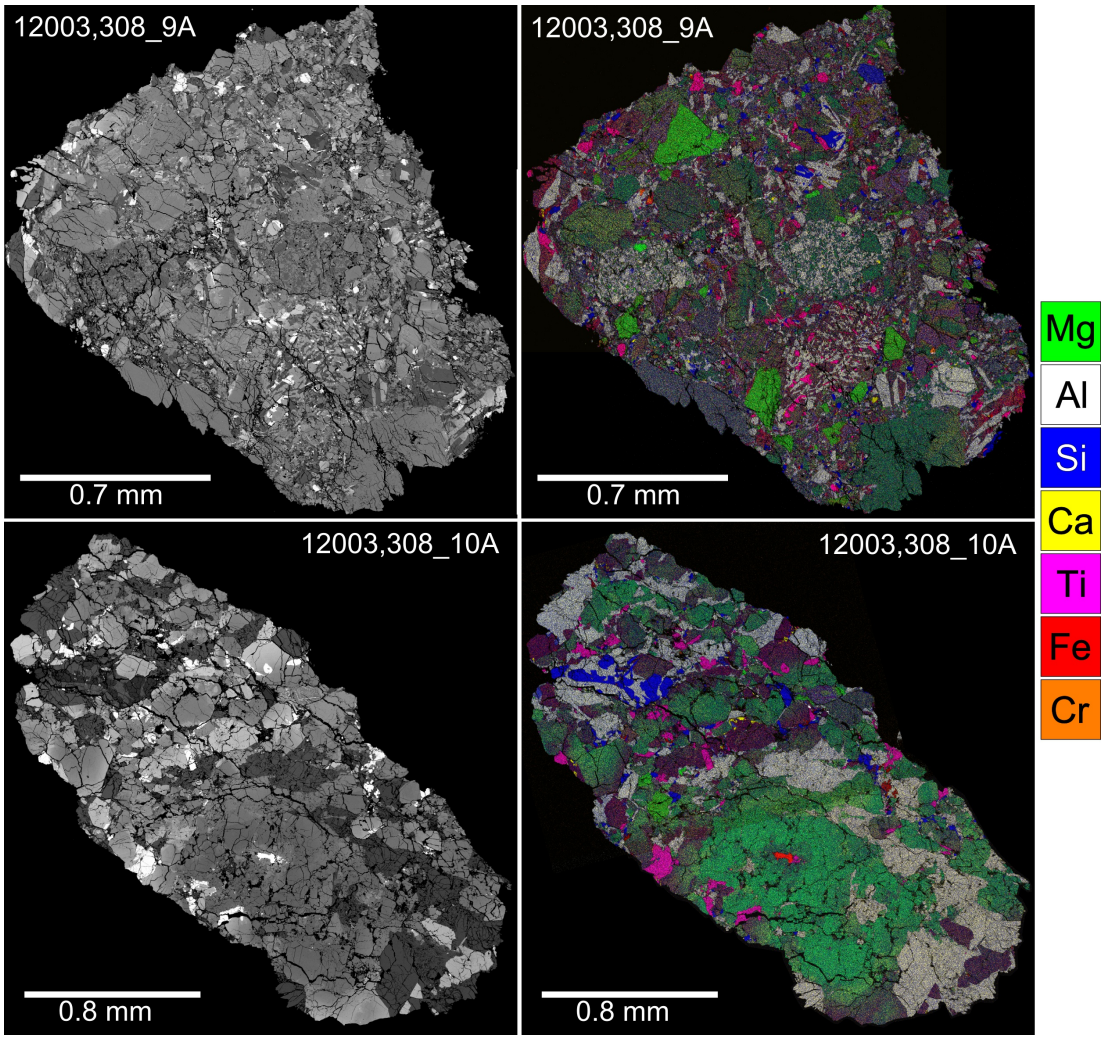

Figure 6.4: Backscattered electron (BSE) images and false colour element maps of samples 12003,308_9-10A. The colours of the element maps represent distribution and concentration of the following elements: Si = blue, Al = white, Mg = green, Fe = red, Ca = yellow, Ti = pink and Cr = orange.

abundance) of olivine which is absent from ,308_1A (Table 6.1; Figs. 6.1; 6.2; 6.3).

The samples of Groups 3 and 4 have coarser grain sizes (~0.25-0.80 mm) than those of Groups 1 and 2, and contain mafic phases showing little to no major element zonation. Group 3 is represented by 12003,308_3A. This sample has a cumulate texture and is composed mostly of rounded grains of olivine, pyroxene and plagioclase (Fig. 6.1). The Group 4 samples (12003,308_5A and ,308_7A) are almost entirely composed of mafic minerals (93-95% by modal abundance) and contain little plagioclase (1-5%; Figs. 6.2; 6.3).

In addition to the seven samples identified as representing primary igneous lithologies, three non-igneous samples were identified. These include two breccias (12003,308_9A; and _10A) and a granulitic impactite sample (12003,308_6A; Figs. 6.2; 6.4).

Table 6.1: Modal mineralogies of the 10 12003,308 A-splits. Summaries of the modal mineralogies for the Apollo 12 ilmenite, pigeonite and olivine basalt suites (*Papike and Vaniman*, 1978a) and averages of the modal mineralogies reported by *Neal et al.* (1994a) are presented for comparison.

Sample	Pyx.	LCP	HCP	Oliv.	Plag.	Sil.	Ilm.	Spin.	Tr.	FeNi	Phos.	Glass/Meso.
12003,308_1A	51.1	-	-	-	39.1	5.9	3.7	0.1	0.1	-	-	-
12003,308_2A	51.9	-	-	16.6	26.7	0.8	2.7	0.9	0.1	-	-	0.2
12003,308_3A	-	31.1	3.0	37.5	25.9	-	0.6	1.8	0.1	-	-	0.1
12003,308_4A	60.3	-	-	19.0	17.8	0.2	1.4	1.1	0.1	-	-	0.1
12003,308_5A	-	71.8	13.1	9.8	0.8	-	1.6	2.9	-	-	-	-
12003,308_6A	-	37.1	10.4	-	50.0	-	2.2	-	-	-	0.3	-
12003,308_7A	-	49.1	32.9	10.6	4.8	-	-	2.4	-	-	-	0.1
12003,308_8A	56.2	-	-	17.6	24.5	0.2	1.0	0.5	-	-	-	-
12003,308_9A	67.7	-	-	4.6	24.4	1.0	2.0	-	-	0.1	0.1	-
12003,308_10A	67.6	-	-	0.6	27.2	1.9	2.4	-	-	0.2	0.1	-

Average modal mineralogies of Apollo 12 basaltic suites (*Papike and Vaniman*, 1978a)

	Pyx.	Oliv.	Plag.	Opaques
Ilmenite	61.1	3.6	25.9	9.3
Pigeonite	68.4	1.4	21.1	9.1
Olivine	53.5	20.2	19.2	7.1

Average of Apollo 12 modal mineralogies reported by *Neal et al.* (1994a)

	Pyx.	Oliv.	Plag.	Sil.	Ilm.	Spin.	Tr.	FeNi	Glass/Meso.
Ilmenite	54.6	9.6	24.9	0.7	4.4	2.0	0.2	0.1	4.4
Pigeonite	58.8	1.5	31.4	2.0	2.7	1.1	0.4	0.1	1.8
Olivine	43.8	24.6	20.9	0.2	1.1	2.3	0.2	0.1	6.3
Feldspathic	48.8	0.1	43.8	2.7	3.5	0.2	0.1	0.1	0.7

Pyx. = pyroxene; LCP = low-Ca pyroxene; HCP = high-Ca pyroxene; Oliv. = olivine; Plag = plagioclase; Ilm = ilmenite; Sil = silica; Spin = spinel; Tr = troilite; FeNi = FeNi metal grains; Phos = phosphates; Meso. = mesostasis. Opaques include ilmenite, spinel, troilite and FeNi metal.

6.2.1 Petrography and mineral chemistry

Group 1 (12003,308_1A)

12003,308_1A is a porphyritic basalt with a subophitic matrix (Fig. 6.1). The most common phase in the sample is pyroxene (51% by modal abundance) followed by plagioclase (39%). The sample has a higher abundance of plagioclase than any of the other igneous 12003,308 samples (39%; Table 6.1).

The pyroxene within the sample is zoned between more magnesian cores to the Fe-rich rims ($Wo_{10-38}En_{0-56}Fs_{22-85}$; Fig. 6.1; Fig. 6.5). Two ∼0.2-0.3 mm phenocrysts of pyroxene are also present which have less Fe-rich rims ($Wo_{13-38}En_{8-56}Fs_{22-62}$) than the groundmass pyroxene throughout the sample. The grainsize of ,308_1A only allowed for one of the pyroxene phenocrysts to be analysed by LA-ICP-MS. This was found to have a composition with lower light-rare earth element (LREE) concentrations compared with heavy-rare earth element (HREE) concentrations (La_{cn}/Lu_{cn} = 0.1-0.5; where $_{cn}$ implies chondrite normalised values using the CI concentrations reported by *Anders and Grevesse* 1989). The chondrite normalised rare earth element (REE) patterns become flatter towards the rim of the crystal, as the concentrations of LREE increase more than

Table 6.2: Major and minor element bulk chemistries of the 10 12003,308 A-splits. Normalised compositions are reported as oxide wt% values. Errors are 1σ standard deviations of the specified number of raster beam analyses.

	12003,308_1A	12003,308_2A	12003,308_3A	12003,308_4A	12003,308_5A
SiO_2	45.80 ± 0.25	44.48 ± 0.09	42.44 ± 0.08	45.54 ± 0.14	47.82 ± 0.07
TiO_2	4.77 ± 0.06	2.58 ± 0.07	1.22 ± 0.02	2.13 ± 0.04	2.43 ± 0.06
Al_2O_3	12.86 ± 0.04	10.12 ± 0.07	9.47 ± 0.14	7.19 ± 0.07	2.16 ± 0.03
Cr_2O_3	0.23 ± 0.02	0.71 ± 0.03	0.79 ± 0.03	0.72 ± 0.03	1.51 ± 0.03
FeO	19.85 ± 0.11	20.23 ± 0.13	21.73 ± 0.14	19.83 ± 0.14	18.48 ± 0.06
MnO	0.26 ± 0.04	0.29 ± 0.03	0.27 ± 0.02	0.30 ± 0.02	0.32 ± 0.02
MgO	4.34 ± 0.11	11.84 ± 0.08	17.03 ± 0.11	16.13 ± 0.09	20.91 ± 0.04
CaO	11.12 ± 0.13	9.13 ± 0.03	6.54 ± 0.06	7.68 ± 0.07	6.09 ± 0.03
Na_2O	0.40 ± 0.02	0.38 ± 0.01	0.37 ± 0.01	0.30 ± 0.01	0.23 ± 0.02
K_2O	0.09 ± 0.01	0.06 ± 0.01	0.03 ± 0.01	0.03 ± 0.01	b.d.
P_2O_5	0.27 ± 0.02	0.17 ± 0.03	0.10 ± 0.02	0.13 ± 0.02	0.04 ± 0.02
Total	100	100	100	100	100
Mg#	28.07	51.08	58.30	59.20	66.87
Na_2O+K_2O	0.48	0.44	0.40	0.33	0.23
No. of raster beam analyses	5	10	10	20	10

	12003,308_6A	12003,308_7A	12003,308_8A	12003,308_9A	12003,308_10A
SiO_2	47.88 ± 0.03	48.47 ± 0.06	46.22 ± 0.16	46.51 ± 0.05	47.19 ± 0.08
TiO_2	1.98 ± 0.04	1.23 ± 0.02	1.62 ± 0.04	3.38 ± 0.03	3.23 ± 0.05
Al_2O_3	16.67 ± 0.07	3.79 ± 0.03	9.00 ± 0.07	10.84 ± 0.04	9.37 ± 0.06
Cr_2O_3	0.28 ± 0.02	1.53 ± 0.03	0.58 ± 0.03	0.50 ± 0.02	0.39 ± 0.02
FeO	10.60 ± 0.05	16.24 ± 0.08	17.89 ± 0.06	17.21 ± 0.12	19.66 ± 0.09
MnO	0.16 ± 0.02	0.28 ± 0.03	0.26 ± 0.03	0.25 ± 0.02	0.29 ± 0.03
MgO	9.74 ± 0.03	19.41 ± 0.04	15.64 ± 0.06	10.26 ± 0.05	8.87 ± 0.05
CaO	11.00 ± 0.03	8.75 ± 0.04	8.31 ± 0.04	10.06 ± 0.03	10.35 ± 0.04
Na_2O	0.81 ± 0.01	0.23 ± 0.01	0.35 ± 0.01	0.45 ± 0.01	0.39 ± 0.01
K_2O	0.40 ± 0.01	b.d.	0.03 ± 0.01	0.16 ± 0.01	0.07 ± 0.01
P_2O_5	0.48 ± 0.02	0.05 ± 0.02	0.11 ± 0.02	0.39 ± 0.03	0.19 ± 0.03
Total	100	100	100	100	100
Mg#	62.12	68.07	60.93	51.54	44.59
Na_2O+K_2O	1.21	0.23	0.37	0.61	0.46
No. of raster beam analyses	10	10	10	10	20

Mg# = atomic Mg/[Fe+Mg]×100.

those of HREE (Fig. 6.6). It also has a negative Eu-anomaly which becomes slightly less pronounced towards the rim of the crystal (Eu/Eu* = 0.1-0.2; where Eu/Eu* is calculated as $Eu_{cn}/\sqrt{[Sm_{cn} \times Gd_{cn}]}$).

Elongated crystals of plagioclase (∼400×50 μm; An_{85-93}; Fig. 6.7) are common throughout the sample. A general alignment of many of these laths is also observed, however, this is not consistent in all cases. Many of the laths have an intrafasciculate texture with hollow cores containing pyroxene (Fig. 6.1). Other plagioclase grains occur in radiate plagioclase-pyroxene intergrowths. The plagioclase laths within ,308_1A were also too small to obtain many LA-ICP-MS analyses, however, two grains were analysed with single LA-ICP-MS spots. These had flatter chondrite normalised REE patterns than the pyroxenes and positive Eu-anomalies (La_{cn}/Lu_{cn} = 0.5-0.6; Fig. 6.8).

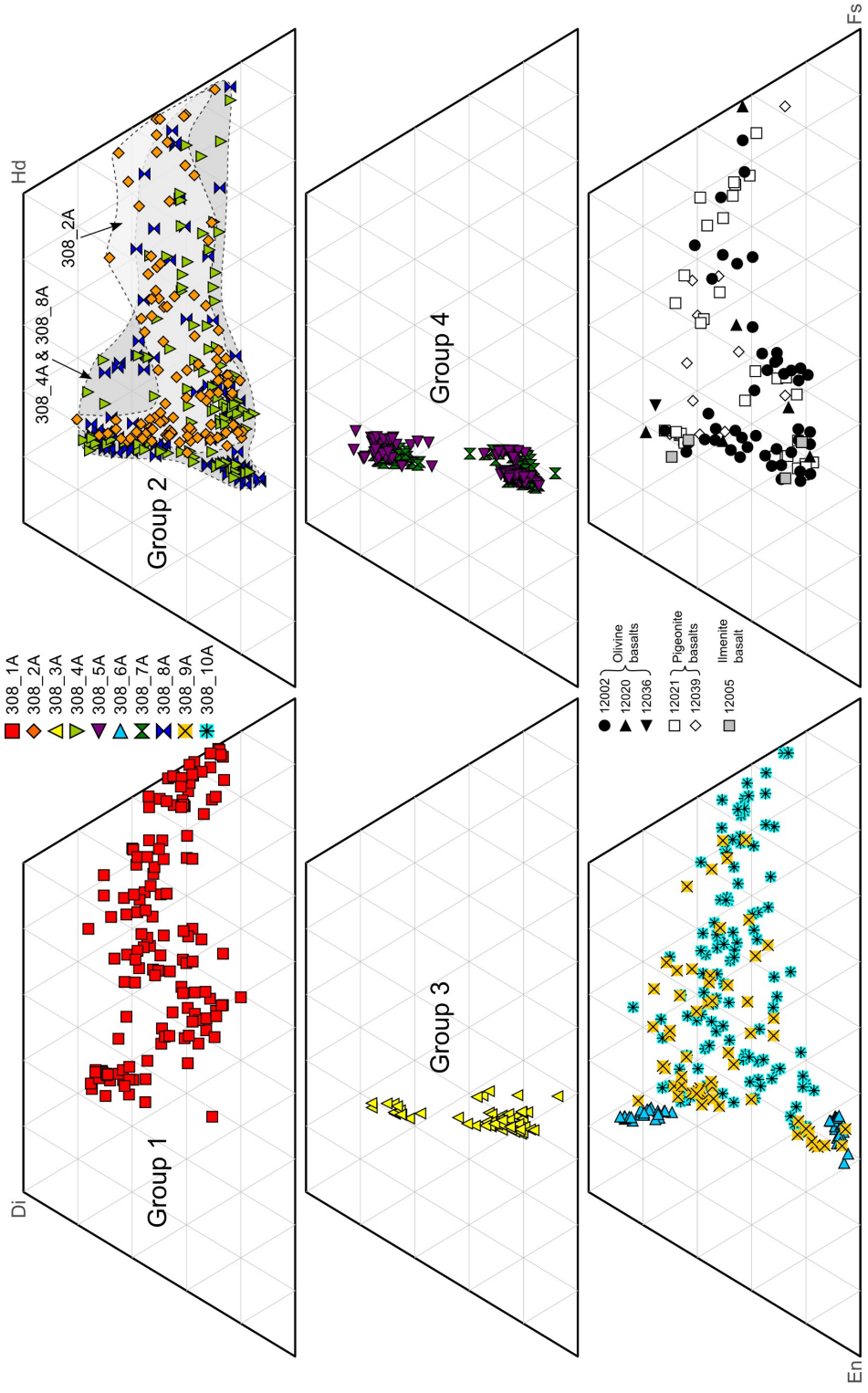

Figure 6.5: Compositions of pyroxene phases within samples 12003,308_1-10A. The 12003,308 pyroxene compositions are compared with those within other Apollo 12 samples (*Busche et al.* 1971; *Boyd and Smith* 1971; *Kushiro et al.* 1971; *Keil et al.* 1971; *Dence et al.* 1971; *Grove et al.* 1973; *Dungan and Brown* 1977; *Shearer et al.* 1989; *O'Sullivan, pers. comm.*). Di = diopside; Hd = hedenbergite; En = enstatite; Fs = ferrosilite.

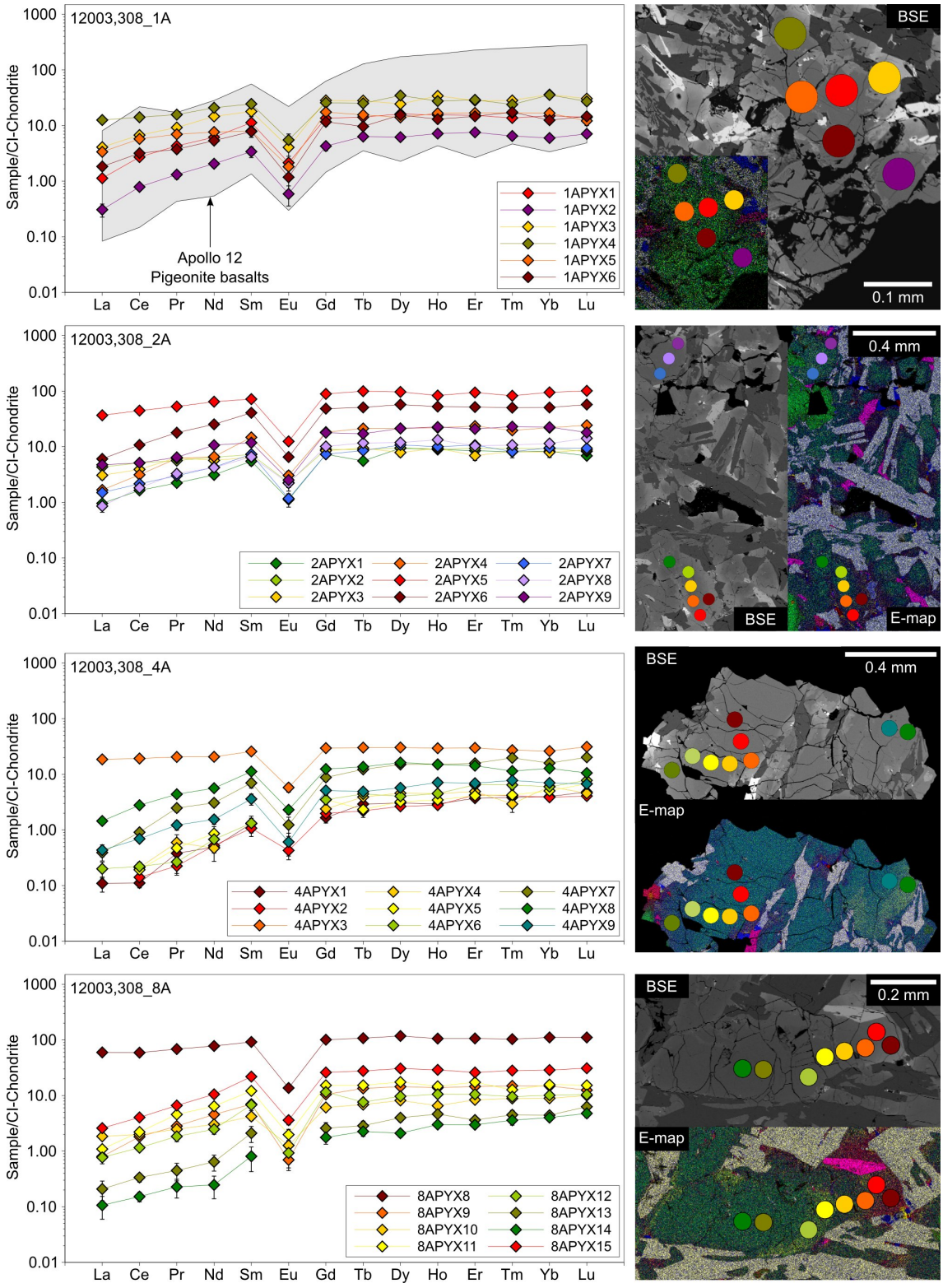

Figure 6.6: Chondrite normalised (*Anders and Grevesse*, 1989) REE patterns for pyroxenes within the 12003,308 Group 1 and 2 samples. The locations of the analyses are indicated in the accompanying backscattered electron (BSE) and false colour element maps with colour coded symbols. Error bars represent 1σ errors. Group 1 pyroxene analyses have been compared with the ranges of REE concentrations reported for pyroxenes in the pigeonite basalts 12021, 12039 and 12052 (*Shearer et al.* 1989; *O'Sullivan and Neal* 2010a; *O'Sullivan, pers. comm.* 2012).

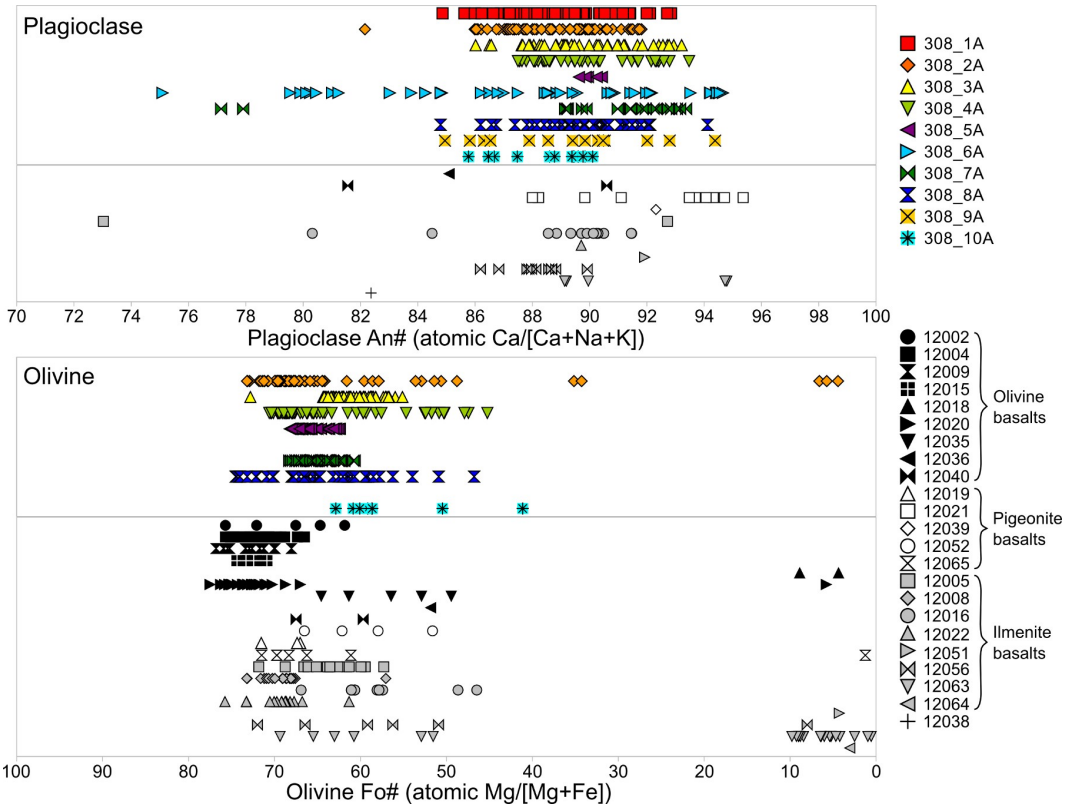

Figure 6.7: Ranges of plagioclase anorthite content (An: atomic Ca/[Ca+Na+K]×100) and olivine forsterite content (Fo: atomic Mg/[Mg+Fe]×100) within samples 12003,308_1-10A. The 12003,308 plagioclase and olivine compositions are compared with those within other Apollo 12 samples (*Bence et al.*, 1970; *Anderson and Smith*, 1971; *Brett et al.*, 1971a; *Brown et al.*, 1971; *El Goresy et al.*, 1971; *Hollister et al.*, 1971; *Keil et al.*, 1971; *Kushiro et al.*, 1971; *Newton et al.*, 1971; *Taylor et al.*, 1971a; *Weill et al.*, 1971; *Butler*, 1972; *Crawford*, 1973; *Dungan and Brown*, 1977; *Marvin and Walker*, 1985). Fa = fayalite; Ab = albite.

12003,308_1A also stands out as having significantly more crystalline silica than any of the other 12003,308 samples (6%; Table 6.1). This occurs as anhedral grains (∼10-75 μm) of an undetermined silica polymorph. These are commonly adjacent to the most Fe-rich areas of pyroxene grains (Fig. 6.1). The next most common minor mineral in this sample is ilmenite (4%). This also forms elongated laths (∼150×10 μm) which sometimes cross-cut and in other instances are cross-cut by the larger plagioclase grains. Relatively rare (0.1%) grains of ulvöspinel are also present in the sample (∼20 μm; $2Ti_{74-89}Al_{5-7}Cr_{6-19}$; Fig. 6.9).

Accessory minerals are common around the more evolved pyroxene rims and silica grains. These include small (<10 μm) grains of troilite and apatite (Tables 6.10; 6.11). The troilite (S = 38-39 wt%; Fe = 59-61 wt%) phases tend to occur alongside similarly sized grains of FeNi metal, however, these were not successfully analysed by EMP WDS.

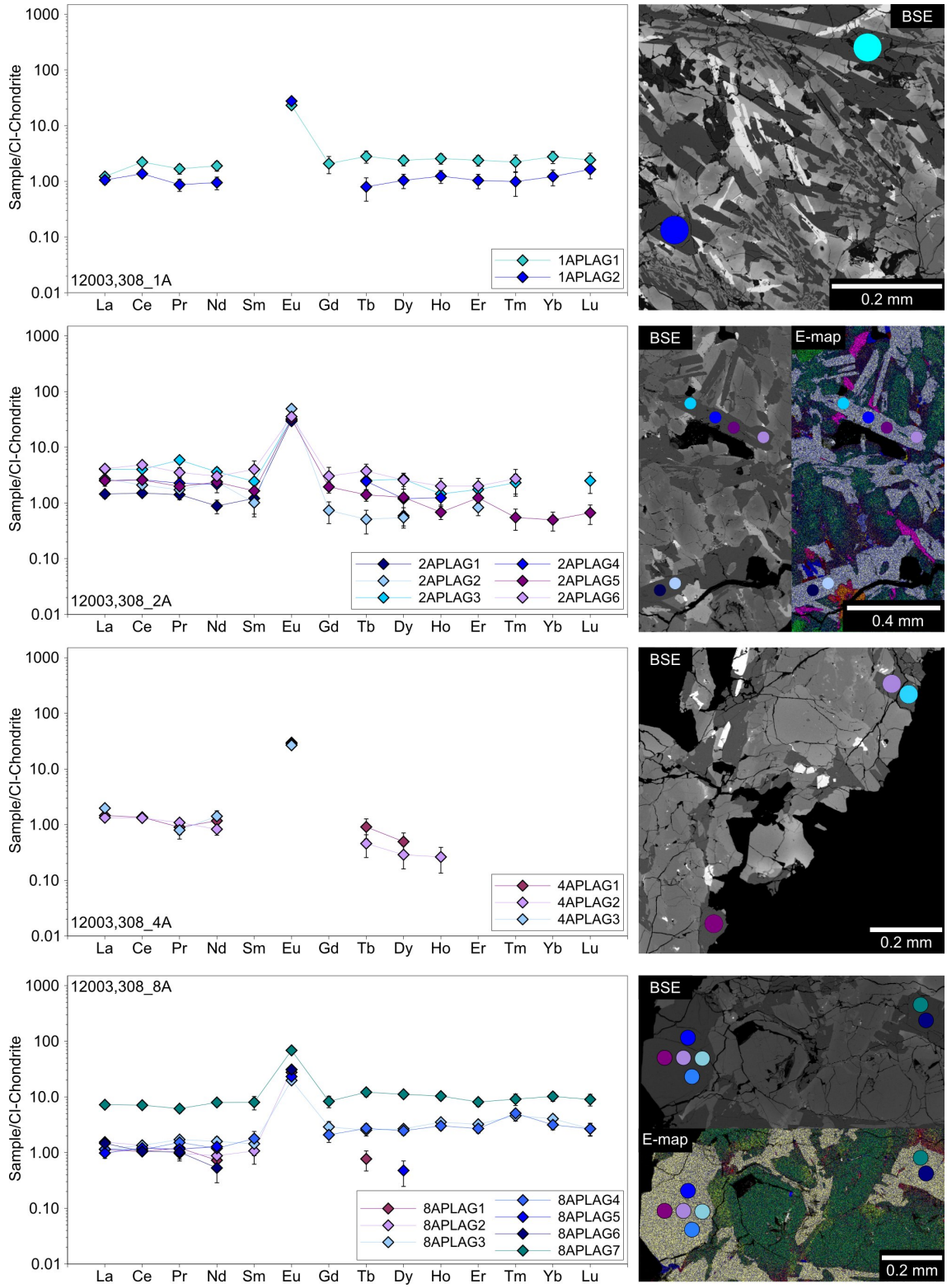

Figure 6.8: Chondrite normalised (*Anders and Grevesse*, 1989) REE patterns for plagioclase phases within the 12003,308 Group 1 and 2 samples. The locations of the analyses are indicated in the accompanying backscattered electron (BSE) and false colour element maps with colour coded symbols. Error bars represent 1σ errors.

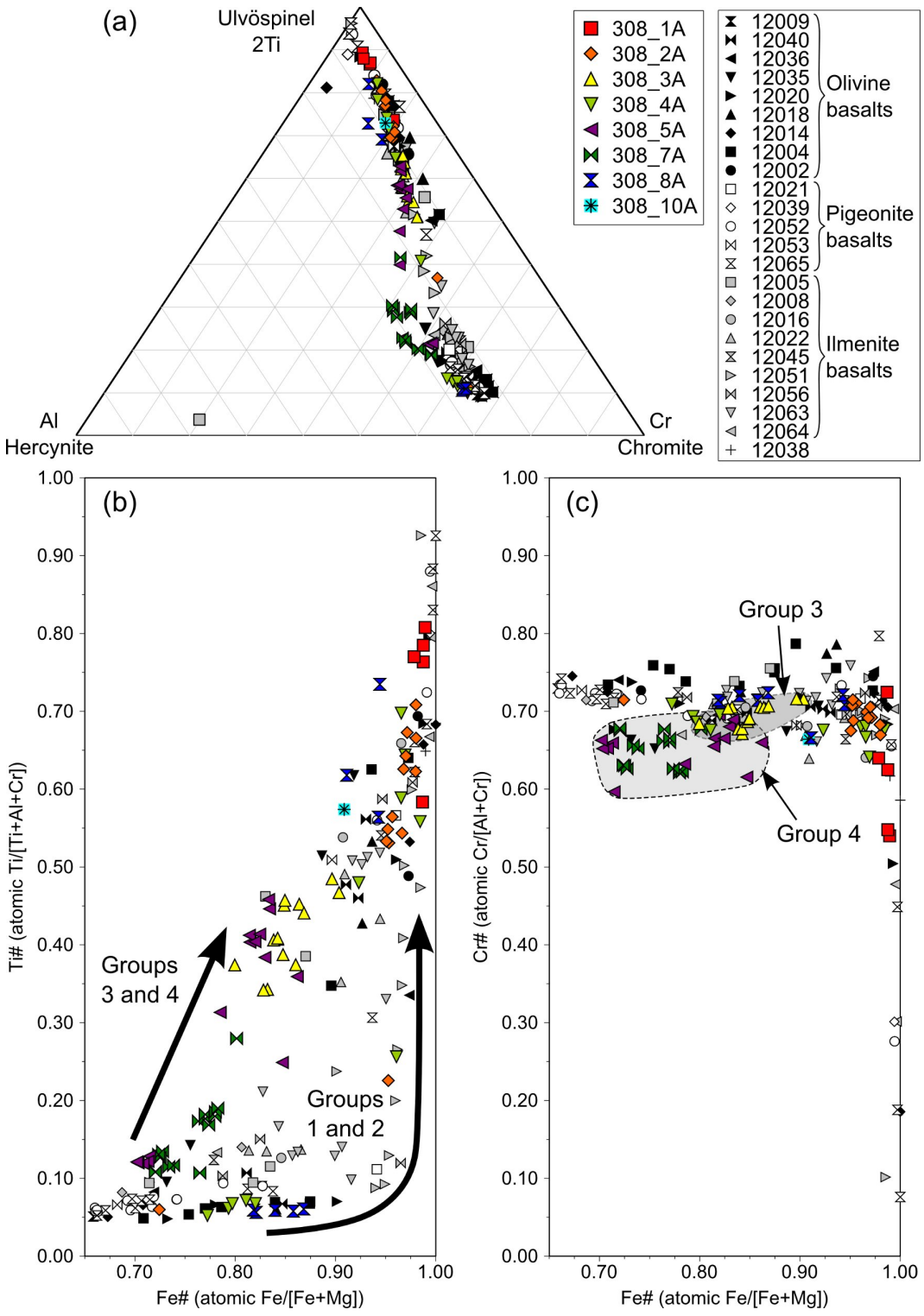

Figure 6.9: Compositions of spinel phases within samples 12003,308_1-10A. (a) 2Ti-Cr-Al in atomic %. (b) Ti# (atomic Ti/[Ti+Al+Cr]) vs Fe# (atomic Fe/[Fe+Mg]). Arrows indicate trends of compositional evolution from chromite to ulvöspinel. (c) Cr# (atomic Cr/[Al+Cr]) vs Fe# (atomic Fe/[Fe+Mg]). 12003,308 spinel compositions are compared with those reported in samples 12014, 12035, 12063 and 12065 (*Reid*, 1971; *Taylor et al.*, 1971a; *El Goresy et al.*, 1971).

Group 2 (12003,308_2A; 12003,308_4A; 12003,308_8A)

The Group 2 samples are characterised by having coarser grained (∼0.10-0.70 mm) more ophitic matrices than the Group 1 sample (,308_1A). 12003,308_2A is the finest grained of the Group 2 samples (∼0.10-0.50) and has the most subophitic texture. When compared with ,308_1A, all three samples have slightly higher modal abundances of pyroxene (52-60%) and lower modal abundances of plagioclase (18-27%; Table 6.1). Olivine is also present as a major component of these samples (17-19% by modal abundance) and occurs as 0.5-0.7 mm phenocrysts.

As in ,308_1A, the pyroxene phases of the Group 2 samples exhibit prominent compositional zonation ($Wo_{6-40}En_{1-66}Fs_{17-85}$; Figs. 6.1; 6.2; 6.3). Although the distribution of pyroxene compositions within these three samples is similar, ,308_2A appears to vary slightly from the other two samples (Fig. 6.5): for example, the low-Ca pyroxenes in this sample more Fe-rich than those of ,308_4A and ,308_8A. Similarly, when comparing the pyroxene Fe# (atomic Fe/[Mg+Fe]) with Ti# (atomic Ti/[Cr+Ti]) and the ratio of Al/Ti the resulting trends indicate that ,308_2A has more Fe-rich pyroxene compositions than the other Group 2 samples (Fig. 6.10;6.11). A wider range of olivine compositions is also noted within ,308_2A (Fo_{3-73}) compared with ,308_4A and ,308_8A (Fo_{45-74}; Fig. 6.7). The most Fe-rich olivines within ,308_2A occur as small (∼10-50 μm) fayalite grains adjacent to the more evolved pyroxene rims.

REE concentrations in the Group 2 pyroxenes follow a similar trend to that in ,308_1A (Fig. 6.6). The cores have lower LREE concentrations compared with the HREE, while the more evolved rims exhibit flatter chondrite normalised REE patterns (La_{cn}/Lu_{cn} = 0.01-0.6). The negative Eu-anomalies observed within the pyroxenes of the Group 2 samples do not appear to vary systematically between the cores and rims of the phases (Eu/Eu* = 0.1-0.3).

The Group 2 plagioclase grains are less elongate and more tabular than those in ,308_1A (∼350×100 μm; An_{82-94}). However, the plagioclase in ,308_2A and ,308_8A do have similar intrafasciculate textures to the Group 1 plagioclases, and radiating plagioclase-pyroxene intergrowths are also present in ,308_2A (Figs. 6.1; 6.3). They have variable chondrite normalised REE patterns (La_{cn}/Lu_{cn} = 0.4-3.8; Eu/Eu* = 8.4-40; Fig. 6.8). Those in 12003,308_2A and ,308_4A appear to have slightly higher concentrations of LREE than HREE (La_{cn}/Lu_{cn} = 1.6-3.8), whereas in ,308_8A the opposite trend is observed (La_{cn}/Lu_{cn} = 0.4-0.8).

The Group 2 samples contain less ilmenite (1-3% by modal abundance) and less silica (≤1%) than the Group 1 sample ,308_1A (Table 6.1). Spinel is more common in the

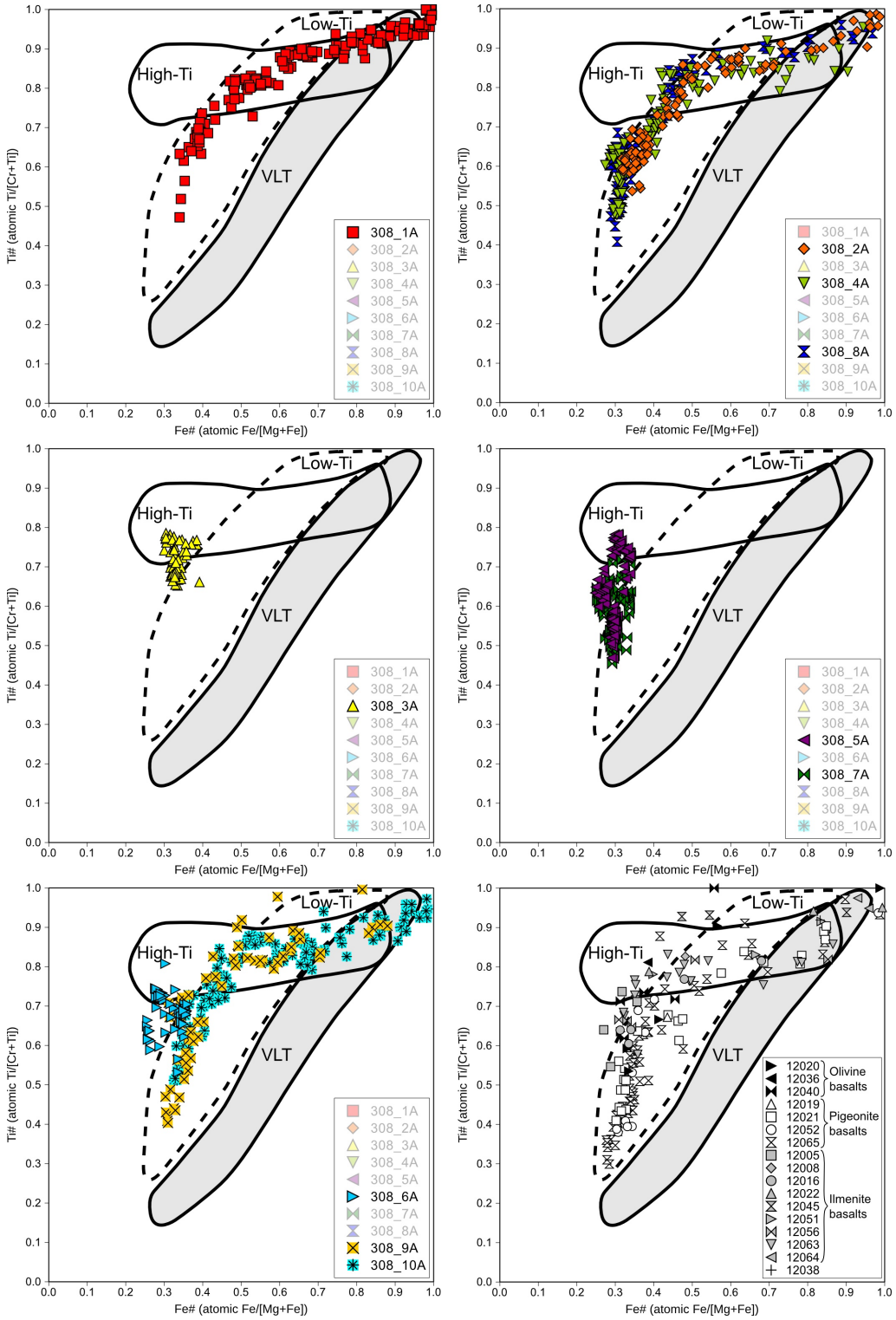

Figure 6.10: Fe# (atomic Fe/[Mg+Fe] vs Ti# (atomic Ti/[Ti+Cr]) for pyroxene phases within samples 12003,308_1-10A. Compositions are compared with those reported for pyroxenes in other Apollo 12 samples (*Bence et al.*, 1970; *Anderson and Smith*, 1971; *Boyd and Smith*, 1971; *Brown et al.*, 1971; *Dence et al.*, 1971; *Hollister et al.*, 1971; *Keil et al.*, 1971; *Kushiro et al.*, 1971; *Newton et al.*, 1971; *Weill et al.*, 1971). High-Ti, Low-Ti and VLT fields are adapted from *Nielsen and Drake* (1978); *Arai et al.* (1996) and *Robinson and Treiman* (2010).

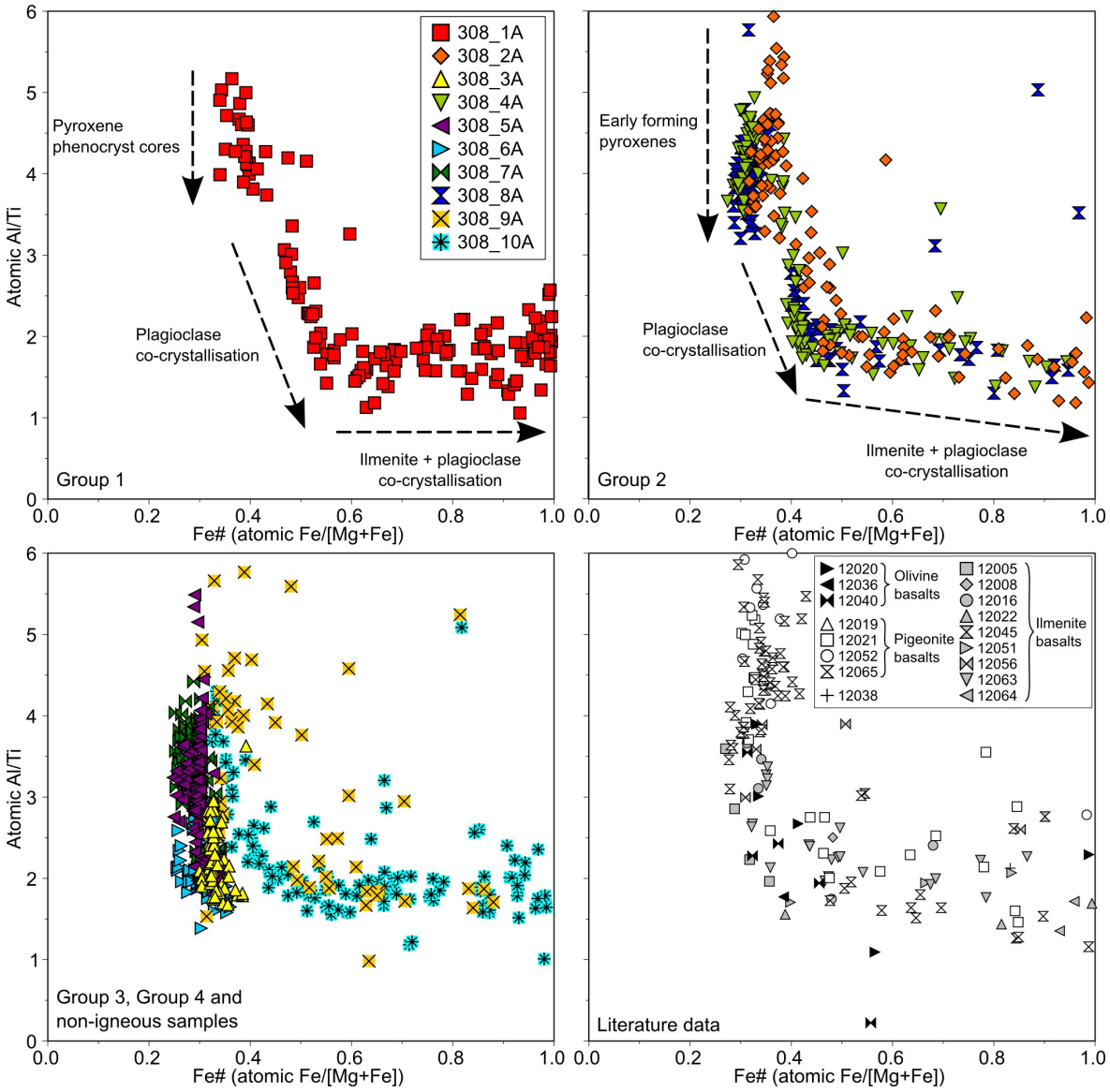

Figure 6.11: Atomic Al/Ti vs Fe# (atomic Fe/[Mg+Fe]) for pyroxene phases within the 12003,308 samples. Compositions are compared with those reported for pyroxenes in other Apollo 12 samples (*Bence et al.*, 1970; *Anderson and Smith*, 1971; *Boyd and Smith*, 1971; *Brown et al.*, 1971; *Dence et al.*, 1971; *Hollister et al.*, 1971; *Keil et al.*, 1971; *Kushiro et al.*, 1971; *Newton et al.*, 1971; *Weill et al.*, 1971).

Group 2 samples (∼1%). The spinel phases occur as subhedral to euhedral grains between ∼30-180 μm in size. Many of these grains exhibit chromite cores with ulvöspinel rims ($2Ti_{10-85}Al_{6-28}Cr_{11-64}$; Fig. 6.9; Table 6.8). Most of the spinel grains are adjacent to the pyroxene and olivine phases, although two ∼20-30 μm microphenocrysts of Cr-rich spinel are entirely enclosed within the larger olivine phenocrysts of ,308_2A.

Accessory minerals such as FeNi metal, troilite and apatite are present throughout the Group 2 samples (Tables 6.10; 6.11). These are most common in the Fe-rich pyroxene rims and often occur adjacent to silica grains and within fine grained (<1

μm) mesostasis areas (Figs. 6.1; 6.2; 6.3). EMP WDS measurements of the FeNi metal grains were successfully performed for 12003,308_2A and ,308_4A (Table 6.11). Although these samples were observed to have a similar range in Co contents (1.2-1.5 wt%), the Ni content was found to be significantly higher in ,308_2A (4.5-5.4 wt%) than in ,308_4A (2.4 wt%). Several (3-4) troilite grains were also successfully analysed in each sample (S = 36-39 wt%; Fe = 60-63 wt%).

Group 3 (12003,308_3A)

12003,308_3A is distinguished from any of the other ,308 samples by its modal mineralogy and texture. This sample has a coarse grained (∼0.25-0.80 mm) cumulate texture with mineral grains that are much more rounded than any of the Group 1 or 2 samples (Fig. 6.1). The most abundant phase is olivine (38% by modal abundance), followed by pyroxene (34%) and then plagioclase (26%).

The compositions of olivine grains within ,308_3A (Fo_{55-73}) also distinguish it from the other ,308 samples. The texture is most similar to those of the Group 4 samples, however, the olivine grains of that group are typically more forsteritic than those of ,308_3A (Fig. 6.7). The concentrations of minor elements in olivines such as V, Co and Ni are also lower than in a majority of the other ,308 samples (Table 6.6; Fig. 6.12).

Unlike that of the Group 1 and 2 samples, the pyroxene in ,308_3A shows much less compositional zoning and appears more equilibrated. A majority of the pyroxene (31% of the entire sample) occurs as low-Ca pigeonite ($Wo_{4-22}En_{51-62}Fs_{25-38}$). However, several distinct regions of more Ca-rich augite (3%; $Wo_{29-38}En_{43-49}Fs_{19-23}$) are also present.

The concentration of trace elements within the ,308_3A pyroxenes does not appear to vary systematically between the cores and rims of the mineral grains (Fig. 6.13). The augite phases generally have higher concentrations of REE (∼2-11 ×CI abundances) than the pigeonites (∼0.5-11 times CI abundances; Fig. 6.13). Both phases have negative Eu anomalies and lower concentrations of LREE than HREE (Eu/Eu* = 0.1-0.7; La_{cn}/Lu_{cn} = 0.01-0.05).

The plagioclase within the ,308_3A has a similar compositional range to that of the Group 1 and 2 samples (An_{86-93}; Fig. 6.7). There is no significant variation in the abundance of trace elements throughout the plagioclase grains (Fig. 6.14). They have higher concentrations of LREE than HREE (La_{cn}/Lu_{cn} = 5.3-9.2) and have chondrite normalised REE patterns with large positive Eu anomalies (Eu/Eu* = 37-105).

Spinel is present as a minor phase in ,308_3A (2% by modal abundance). The

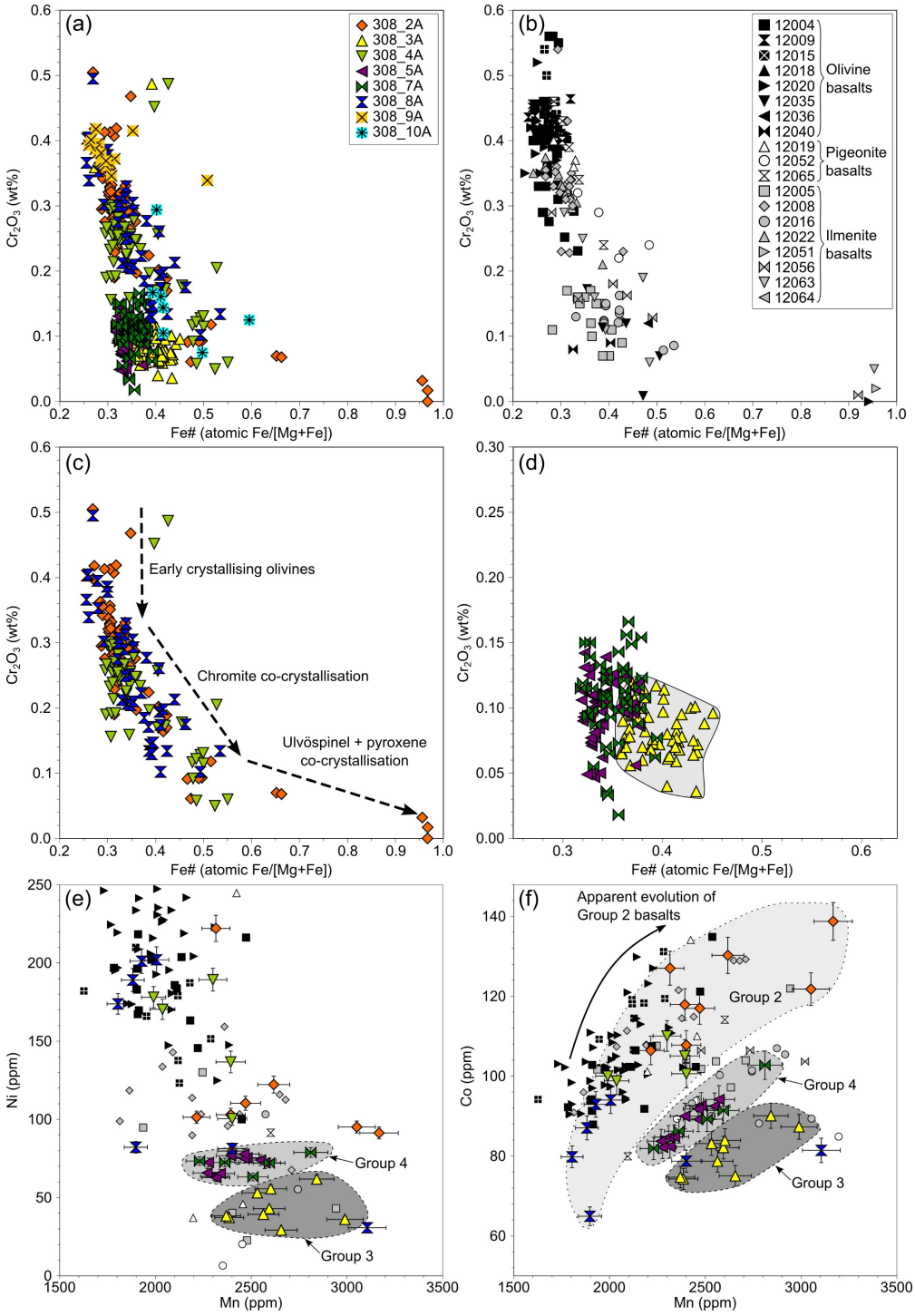

Figure 6.12: Concentrations of Cr_2O_3 vs Fe# (atomic Fe/[Fe+Mg]) in olivine phases within (a) the 12003,308 samples, (b) other Apollo 12 basalts, (c) the Group 2 samples and (d) the Group 3 and 4 samples. Note the reduced scale in (d) to account for the more limited compositional variations of the Group 3 and 4 olivines. Concentrations of (e) Ni and (f) Co vs Mn, for olivine phases within samples 12003,308_2-8A. Mn acts as an indicator of igneous fractionation because it behaves incompatibly in olivine (*Karner et al.*, 2003). Data are compared with those for olivines in other Apollo 12 basalts (*Bence et al.* 1970; *Brett et al.* 1971a; *Brown et al.* 1971; *El Goresy et al.* 1971; *Hollister et al.* 1971; *Keil et al.* 1971; *Kushiro et al.* 1971; *Newton et al.* 1971; *Weill et al.* 1971; *Butler* 1972; *Dungan and Brown* 1977; *Fagan et al.* 2012; *O'Sullivan, pers. comm.* 2012). Error bars represent 1σ errors.

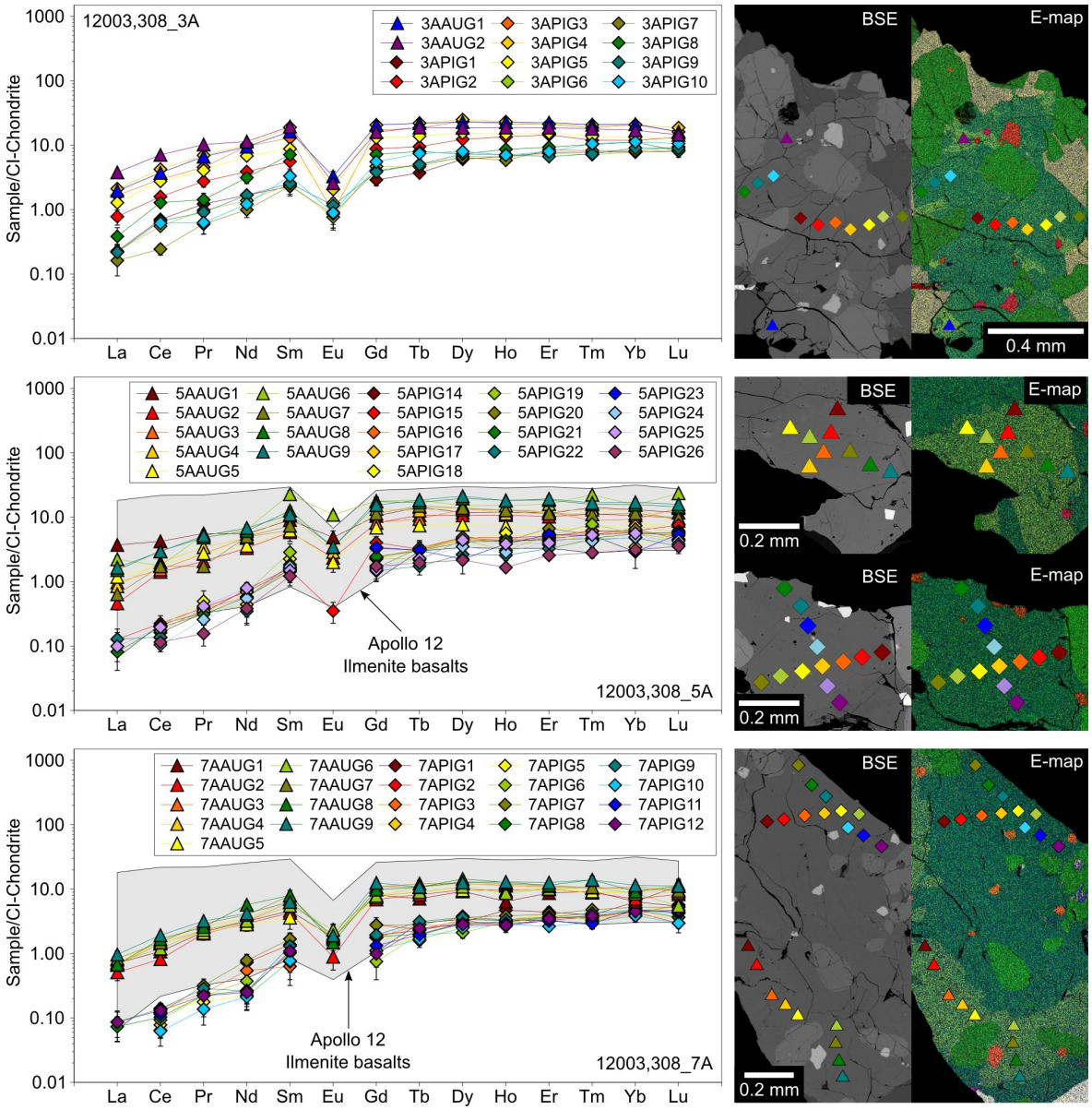

Figure 6.13: Chondrite normalised (*Anders and Grevesse*, 1989) REE patterns for pyroxenes within the 12003,308 Group 3 and 4 samples. The locations of the analyses are indicated in the accompanying backscattered electron (BSE) and false colour element maps with colour coded symbols. Error bars represent 1σ errors. The Group 4 pyroxene analyses have been compared with the ranges of REE concentrations reported for pyroxenes in the ilmenite basalts 12016, 12054, and 12056 (*O'Sullivan and Neal* 2010b; *O'Sullivan, pers. comm.* 2012).

spinel forms subhedral grains which range between ~50-100 μm in size. The range of spinel compositions is less variable then the Group 2 samples and individual grains are generally more homogeneous, with the exception of patches of ilmenite exsolution ($2Ti_{51-65}Al_{10-15}Cr_{25-35}$; Figs. 6.1; 6.9). In addition to that identified within the spinels, a single 30×130 μm subhedral grain of ilmenite is identified within the ,308_3A.

Fewer accessory minerals are present in ,308_3A than either the Group 1 or Group 2 samples. The most significant of these are grains of troilite (~10-50 μm; S = 38 wt%;

Fe = 60-61 wt%; Table 6.11) and associated FeNi metal blebs which were too small (<10 μm) to be successfully analysed by EMP WDS. Several small (<10 μm) grains of K-feldspar were also identified, most notably in a region of mesostasis adjacent to an olivine grain (Fig. 6.1; Table 6.9).

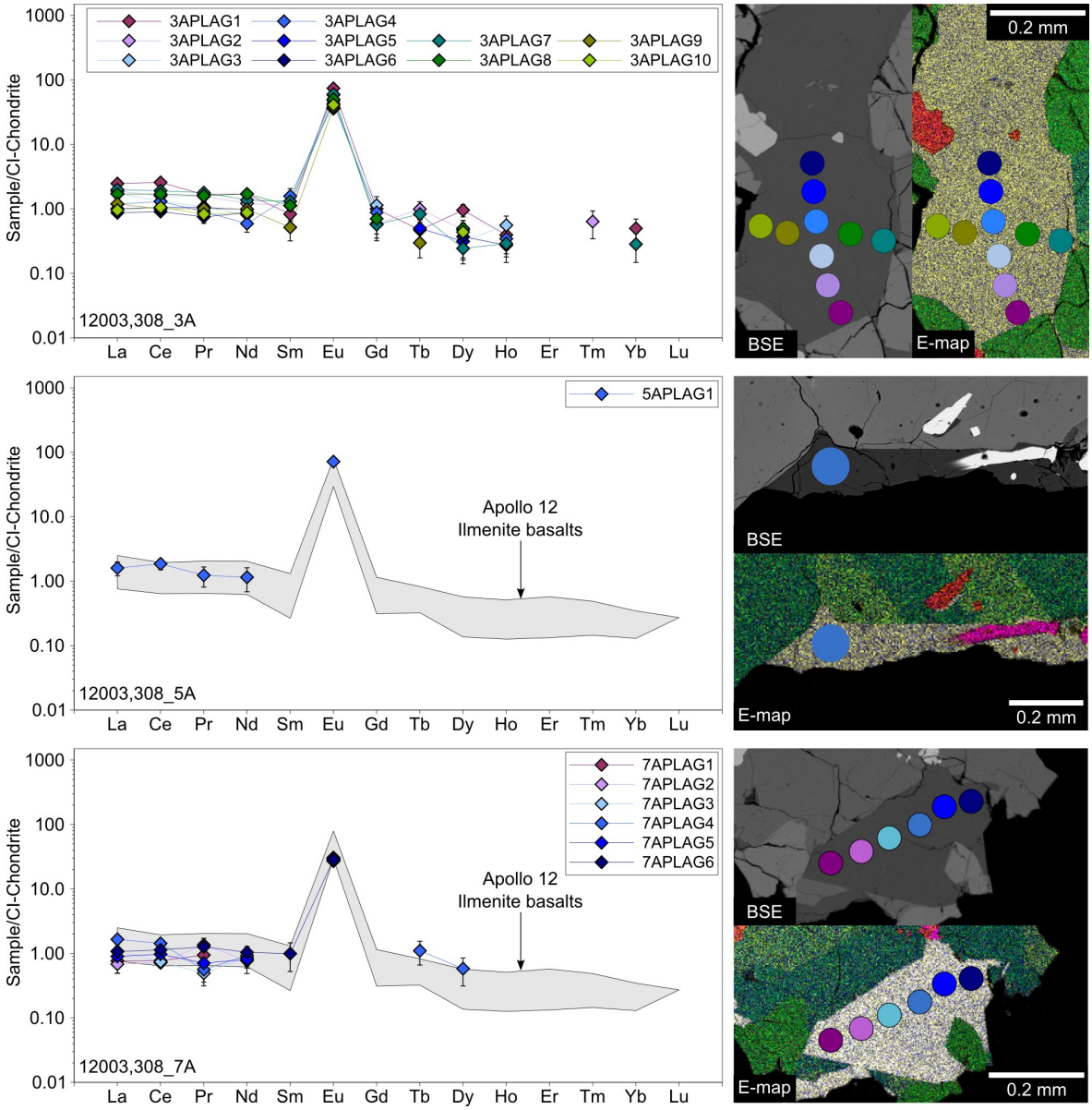

Figure 6.14: Chondrite normalised (*Anders and Grevesse*, 1989) REE patterns for plagioclase phases within the 12003,308 Group 3 and 4 samples. The locations of the analyses are indicated in the accompanying backscattered electron (BSE) and false colour element maps with colour coded symbols. Error bars represent 1σ errors. The Group 4 plagioclase analyses have been compared with the ranges of REE concentrations reported for plagioclase in the ilmenite basalts 12016 and 12056 (*O'Sullivan, pers. comm.* 2012).

Group 4 (12003,308_5A; 12003,308_7A)

The Group 4 samples are largely dominated by pyroxene (82-85%) and, to a lesser extent, olivine (10-11%). They contain significantly less plagioclase (1-5%) than any of the other eight ,308 samples (Table 6.1). They have a similar grain size (∼0.25-0.80 mm) to ,308_3A and also exhibit a cumulate-like texture.

The pyroxene in the Group 4 samples is clearly differentiated into low- and high-Ca phases. The low-Ca pigeonite ($Wo_{4-20}En_{55-66}Fs_{25-31}$) is the most abundant phase in both samples, accounting for 72% (by modal abundance) of ,308_5A and 49% of ,308_7A. The Ca-rich augite ($Wo_{27-41}En_{41-53}Fs_{15-23}$) is less abundant: 13% in ,308_5A and 33% in ,308_7A.

As with the pyroxenes of ,308_3A, the Group 4 augites have higher REE concentrations (∼0.5-11 ×CI abundances) than the pigeonites (∼0.1-6.0 ×CI abundances; 6.13). However, the Group 4 pigeonites show much less variation in REE concentrations than those in ,308_3A, with REE patterns that are clearly distinct from those of the Group 4 augites (Fig. 6.13). Both the augites and pigeonites in the Group 4 samples have trace element concentrations with low LREE compared with HREE, and have negative Eu-anomalies (La_{cn}/Lu_{cn} = 0.01-0.3; Eu/Eu* = 0.1-0.7).

Olivine occurs as rounded medium-large (∼65-550 μm) grains entirely enclosed by the pyroxene phases of these samples. The compositions of these grains are relatively homogeneous (Fo_{62-68}) when compared with the Group 2 olivines, and more magnesian than those in the Group 3 sample ,308_3A (Fig. 6.7). The concentrations of trace elements such V, Co and Ni tend to be higher in olivine grains of the Group 4 samples compared with those of ,308_3A and are much less variable than those of the Group 2 samples (Table 6.6; Fig. 6.12).

Subhedral-euhedral spinel grains (∼30-100 μm) are relatively common (2-3%) within the Group 4 samples. As in ,308_3A the individual grains tend to be quite compositionally homogeneous. However, they are commonly more Cr-rich than the spinels in that sample, particularly in ,308_7A ($2Ti_{21-63}Al_{23-32}Cr_{38-55}$; Fig. 6.9). A wider range of spinel compositions is found in ,308_5A ($2Ti_{19-44}Al_{12-31}Cr_{26-52}$). There are few intermediate compositions observed in this sample, with grains at either the Ti-rich or Cr-rich end of this range (Fig. 6.9). The Ti-rich spinels appear to be clustered on one side of the sample around a large (∼220 μm) ilmenite grain, and contain smaller exsolved anhedral ilmenite grains (Fig. 6.2). The ilmenite in ,308_5A is noted to have a higher Mg content than any of the other ,308 samples (MgO >5 wt%; Table 6.7).

Small (<10 μm) merrillite grains were identified in both samples (Table 6.10). Similarly sized troilite grains (S = 39 wt%; Fe = 62 wt%) and associated FeNi metal grains

were also identified within one of the more Ti-rich spinels in ,308_5A (Ni = 1.8-12 wt%; Co = 1.8-2.4 wt%; Table 6.11). FeNi metal grains are observed to occur independently of troilite and spinel in both samples but were not successfully analysed by EMP WDS.

Non-igneous samples (12003,308_6A; 12003,308_9A; 12003,308_10A)

12003,308_6A has a texture similar to several of the granulitic impactites described by *Cushing et al.* (1999). The fragment exhibits a poikilitic-granoblastic (*Cushing et al.*, 1999) texture unlike any of the other ,308 samples. It is composed of nearly equal amounts of plagioclase (50%) and pyroxene (47%), with minor amounts of ilmenite (2%) and the phosphate phase merrillite (<1%). As in the Group 3 and 4 samples, the pyroxene in ,308_6A is divided into high-Ca ($Wo_{32-44}En_{41-46}Fs_{14-23}$) and low-Ca ($Wo_{2-6}En_{61-69}Fs_{28-35}$) phases. However, a wider compositional gap occurs between these than in any of the Group 3 or 4 samples (Fig. 6.5). LA-ICP-MS analyses of the plagioclase and pyroxene within ,308_6A reveal that they have significantly higher concentrations of REE than those found in any of the other ,308 samples (up to ∼100 ×CI abundances; Fig. 6.15;6.16).

The two brecciated samples (12003,308_9A;_10A) are both composed predominantly of pyroxene (68%) and plagioclase (24-27%). Although both samples have similar modal mineralogies and bulk compositions, they exhibit very different textures (Tables 6.1; 6.2; Fig. 6.4). 12003,308_9A is a clast-supported lithic breccia with a variable clast grainsize (∼10-400 μm). The clasts include fragments of impact melt, crystalline igneous materials and individual large (>100 μm) mineral grains. 12003,308_10A is more coarsely grained (∼0.1-1.0 mm) than ,308_9A and is composed of a less varied range of lithic fragments. A wide range of pyroxene compositions are observed throughout both samples ($Wo_{3-42}En_{1-66}Fs_{18-85}$).

6.3 Discussion

6.3.1 Igneous samples

Crystallisation history and equilibrium parent magma composition

Group 1 (12003,308_1A)

The presence of two large pyroxene phenocrysts in the Group 1 sample (,308_1A) suggests that pyroxene was one of the first phases to crystallise (Fig. 6.1). Plagioclase laths commonly cross-cut the groundmass pyroxene phases. This indicates that they

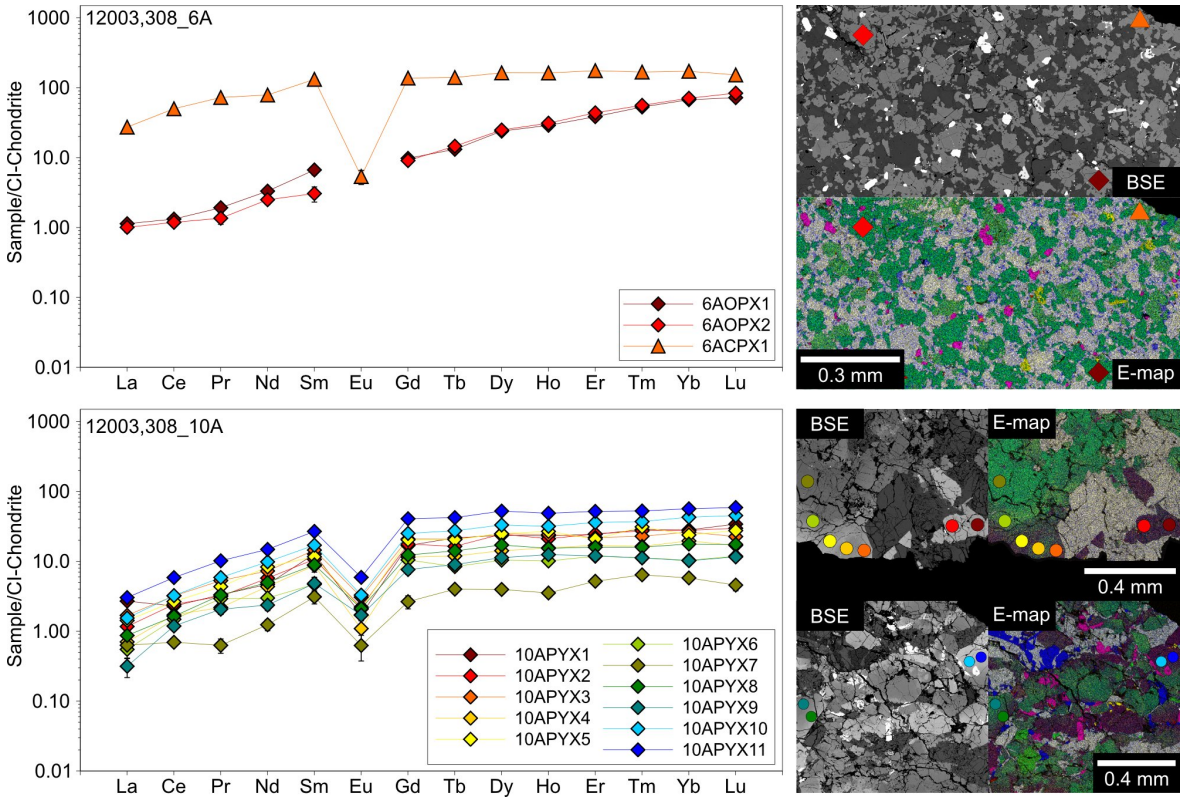

Figure 6.15: Chondrite normalised (*Anders and Grevesse*, 1989) REE patterns for pyroxenes within the non-igneous 12003,308 samples. The locations of the analyses are indicated in the accompanying backscattered electron (BSE) and false colour element maps with colour coded symbols. Error bars represent 1σ errors.

began to crystallise after the pyroxene phenocrysts but during the formation of the pyroxene groundmass. The radiating plagioclase-pyroxene intergrowths in ,308_1A provide further evidence of the co-crystallisation of the two phases (*Drever et al.*, 1973). The presence of ilmenite laths which both cross-cut and are cross-cut by plagioclase indicates co-crystallisation of ilmenite with plagioclase.

The rates at which the pyroxene ratios of Al/Ti and Ti# change with increasing Fe# can provide an indication of co-crystallisation of pyroxene with phases such as plagioclase, spinel and ilmenite. For the pyroxenes in ,308_1A there is not a clear indication of when plagioclase began to crystallise, however, there may be a very subtle change in the Al/Ti ratios at Fe# ∼0.45 indicating the partitioning of Al into another phase (Fig. 6.11). A more obvious change occurs in the Ti# between Fe# of ∼0.35-0.40 and indicates that Ti is being partitioned into another phase (Fig. 6.10). As such, this is interpreted as a transition in the co-crystallising spinel phases from early formed chromite to Ti-richer ulvöspinel. A second change occurs between Fe# ∼0.55-0.60, indicating further partitioning of Ti into another co-crystallising phase, most likely ilmenite. The ratio of Al/Ti in pyroxene provides further evidence of the

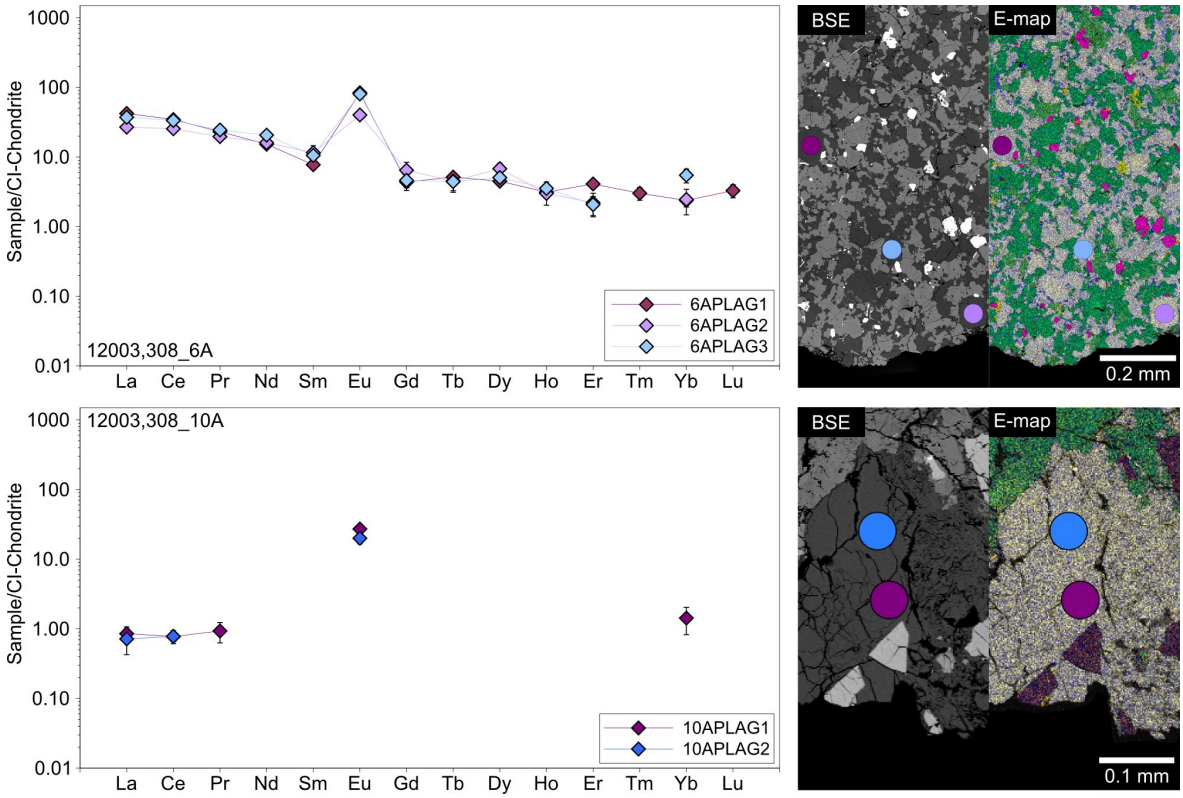

Figure 6.16: Chondrite normalised (*Anders and Grevesse*, 1989) REE patterns for plagioclase phases within the non-igneous 12003,308 samples. The locations of the analyses are indicated in the accompanying backscattered electron (BSE) and false colour element maps with colour coded symbols. Error bars represent 1σ errors.

co-crystallisation of ilmenite beginning between Fe# ~0.55-0.60 (Fig. 6.11). Evaluation of textural relationships between minerals as well as major and minor element concentrations indicate a crystallisation sequence of chromite → pyroxene → ulvöspinel → plagioclase → ilmenite.

The equilibrium parent melt REE composition of the Group 1 sample was reconstructed from a LA-ICP-MS analysis of one of the pyroxene phenocryst cores using the Wo_{12} partition coefficients of *McKay et al.* (1986b) and *Schnare et al.* (2008). This calculation indicates that the ,308_1A parent melt had REE abundances between 5.7-40 ×CI. The CI-normalised REE profile of the reconstructed melt has higher abundances of LREE than HREE and a negative Eu-anomaly (La_{cn}/Lu_{cn} = 2.8; Eu/Eu* = 0.4; Fig. 6.17). The pyroxene core analysis used for the reconstruction had a slightly higher Ca content (Wo_{15}) than that for which the partition coefficients were derived. Clinopyroxene REE partition coefficients decrease with increasing Ca content (*McKay et al.*, 1986b; *Shearer et al.*, 1989; *Treiman*, 1996) and, as such, it should be noted that this may lead to artificially high REE concentrations in the reconstructed parent melt for ,308_1A. Limited distribution coefficients for lunar conditions are currently available,

making the Wo_{12} coefficients of *McKay et al.* (1986b) the most suitable option (*Schnare et al.*, 2008).

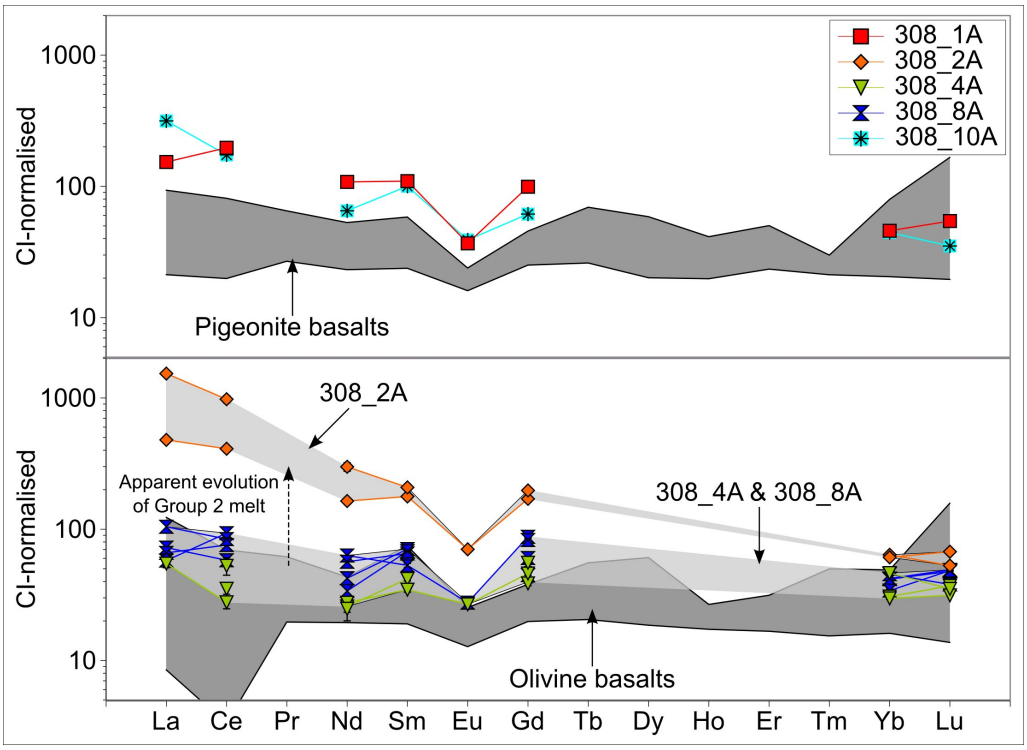

Figure 6.17: Chondrite normalised (*Anders and Grevesse*, 1989) REE concentrations of 12003,308 Group 1 and Group 2 parental melts. The parental melt compositions have been reconstructed from LA-ICP-MS analyses of low-Ca pyroxenes ($Wo_{\sim 12}$) using partition coefficients from *McKay et al.* (1986b) and *Schnare et al.* (2008). The melt compositions have been compared with the bulk compositions of Apollo 12 pigeonite and olivine basalts (*Gast and Hubbard*, 1970; *Bouchet et al.*, 1971; *Brunfelt et al.*, 1971; *Compston et al.*, 1971; *Goles et al.*, 1971; *Haskin et al.*, 1971; *Hubbard et al.*, 1971; *Kharkar and Turekian*, 1971; *Maxwell and Wiik*, 1971; *Morrison et al.*, 1971; *Schnetzler and Philpotts*, 1971; *Taylor et al.*, 1971b; *Wakita et al.*, 1971; *Wänke et al.*, 1971; *Taylor and Bence*, 1975; *Nyquist et al.*, 1977; *Rhodes et al.*, 1977; *Nyquist et al.*, 1979; *Nyquist et al.*, 1981; *Unruh et al.*, 1984; *Warren et al.*, 1986; *Dickinson et al.*, 1989; *Neal et al.*, 1994a; *Snyder et al.*, 1997; *Neal*, 2001).

Group 2 (12003,308_2A; 12003,308_4A; 12003,308_8A

The olivine phenocrysts of the Group 2 samples are interpreted as the first phases to crystallise in the samples. Rare occurrences of chromite, which are completely enclosed in two of the ,308_2A olivine phenocrysts indicate that chromite began to crystallise before or while the olivine phenocrysts were still precipitating. The Group 2 plagioclase grains do not appear to cross-cut the pyroxenes as they do in the Group 1 sample (,308_1A). However, the presence of the radiating plagioclase-pyroxene texture in ,308_2A indicates the co-crystallisation of the two phases at least in this sample.

The variation of Cr concentrations in the Group 2 olivines is illustrated in Fig. 6.12. Early crystallising olivines (Fo_{75-65}) commonly have concentrations of Cr_2O_3 in

excess of 0.25 wt%. The Cr content begins to rapidly decrease as the olivines evolve beyond Fo values of 70-65. This may be due to the co-crystallisation of chromite. Few analyses were successfully made of Group 2 olivines with $Fo_{<45}$. However, the most evolved olivines analysed in ,308_2A indicate a further change in the variation of Cr concentrations at $Fo_{\sim 50-40}$. The Cr content in these olivines decreases less rapidly, possibly indicating a transition in the co-crystallising spinel phase from chromite to ulvöspinel. The continuing reduction of Cr in these olivines is interpreted as evidence of partitioning of Cr into another co-crystallising phase; possibly pyroxene. Mn behaves incompatibly in olivine and provides an indicator of igneous fractionation (*Karner et al.*, 2003). The Mn concentrations in Group 2 olivines increase from ,308_8A to ,308_4A with ,308_2A being the most Mn-rich (Fig. 6.12). This is interpreted as evidence of a fractionation sequence between the three samples, with ,308_2A representing the most evolved of the Group 2 basalts.

The Group 2 pyroxene compositions are consistent with the texturally inferred crystallisation sequence. The variation in Ti# with Fe# changes at Fe# ∼0.30-0.35, indicating a transition in the co-crystallising spinel phase from chromite to ulvöspinel (Fig. 6.10). This is followed by a second change at Fe# ∼0.45 which is interpreted as the co-crystallisation of ilmenite. The crystallisation of ilmenite at this point is also seen in the evolving Al/Ti ratio of the Group 2 pyroxenes (Fig. 6.11). The decreasing Al/Ti ratio indicates the appearance of plagioclase on the liquidus at Fe# ∼0.35. Relationships between the Group 2 mineral textures and minor element concentrations indicate a crystallisation sequence of olivine → chromite → pyroxene → ulvöspinel → plagioclase → ilmenite.

The more Fe-rich compositions of the ,308_2A pyroxenes also indicate a fractionation sequence within the Group 2 samples (Figs. 6.5; 6.10; 6.11). Further evidence of this systematic variation within the Group 2 pyroxenes may be apparent in the ratio of Ti/V (Fig. 6.18). This ratio appears to increase more rapidly with Fe# in the ,308_4A and ,308_8A pyroxenes, although this could be due to an inadequate number of pyroxene analyses.

Parent melt REE concentrations reconstructed from analyses of the Group 2 pyroxene cores also indicate that ,308_2A crystallised from a more evolved parent than the other two Group 2 samples (Fig. 6.17). The parent melts of ,308_4A and ,308_8A have REE concentrations between 3.4-40 ×CI abundances. The two ,308_4A parent melt reconstructions with the lowest REE concentrations were calculated from pyroxene cores with Wo_{8-9}. As such, the actual range of parent melt REE concentrations is likely to be closer to the remaining values calculated for Wo_{10-12} pyroxenes in ,308_4A and ,308_8A

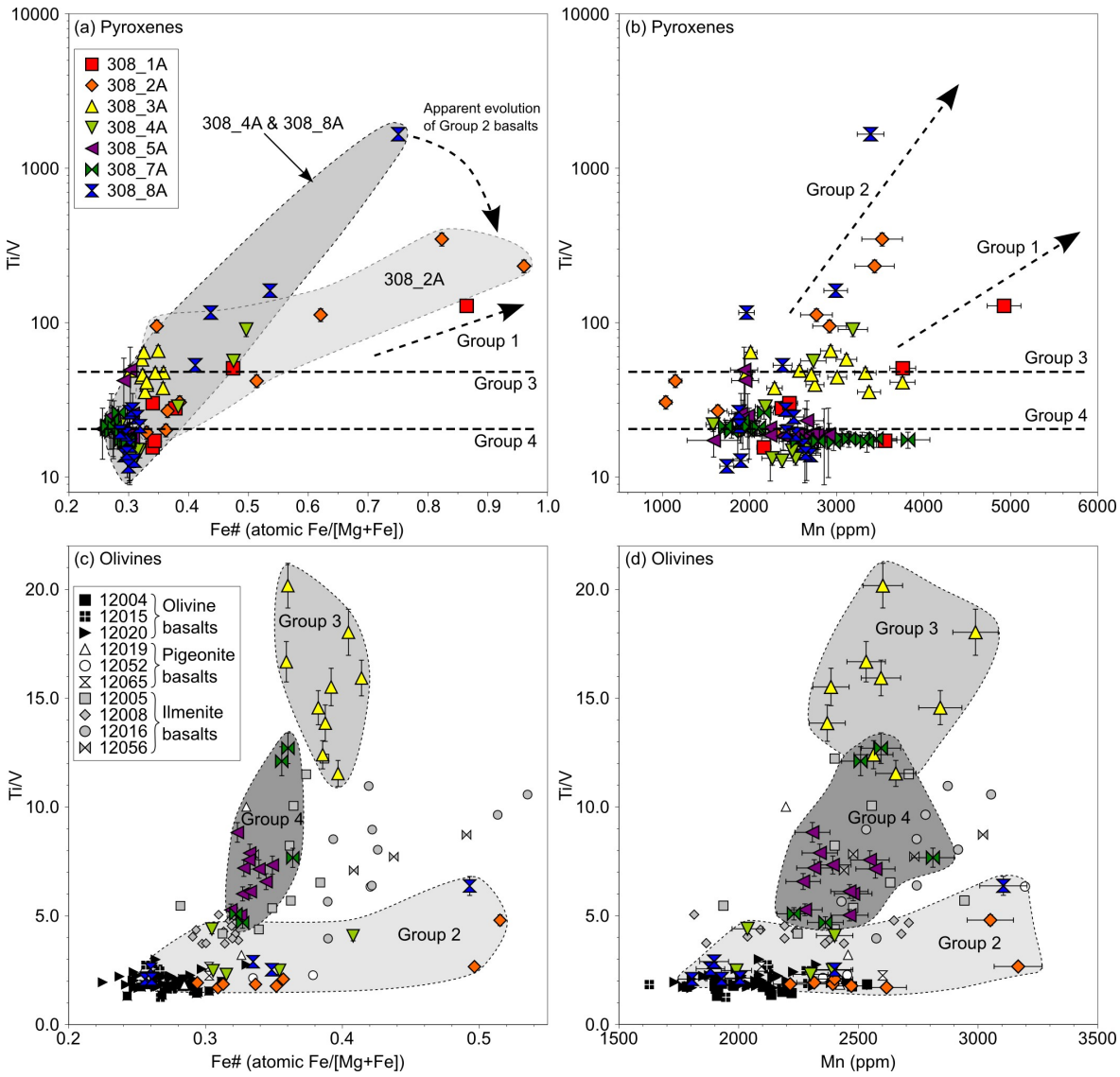

Figure 6.18: Ti/V ratios in 12003,308 mafic phases. Data are compared with those of *Fagan et al.* (2012) and *O'Sullivan, pers. comm.* (2012). Error bars represent 1σ errors.

(i.e. 5.2-40 ×CI abundances). The CI-normalised REE patterns of the ,308_4A and ,308_8A parent melts are almost flat with negative Eu-anomalies (La_{cn}/Lu_{cn} = 1.3-2.2; Eu/Eu* = 0.4-0.7). The ,308_2A parent melt (calculated from two pyroxene cores with Wo_{11-16}) is estimated to have higher REE concentrations (6.6-260 ×CI abundances) than the other Group 2 melts. All of the Group 2 reconstructed parent melts have similar HREE concentrations, but the ,308_2A parent melt has significantly higher LREE concentrations (La_{cn}/Lu_{cn} = 9.1-22; Eu/Eu* = 0.4). The concentration of LREE in the Group 2 parent melt would increase as the melt evolved due to the crystallisation of mafic minerals that preferentially include HREE over LREE (*Haskin and Warren*, 1991). It is also possible that the higher REE concentrations calculated for the ,308_2A parent melt could be the result of not sampling the most primitive pyroxene core com-

positions.

Group 3 (12003,308_3A)

Mineral phases in the Group 3 sample are compositionally equilibrated, and, therefore, crystallisation sequences are hard to infer from major and minor element concentrations in pyroxenes, olivines and plagioclases. The subhedral spinel grains are often entirely enclosed within olivine, plagioclase or pyroxene (Fig. 6.1). As such the spinels are interpreted to be amongst the first phases to crystallise. Two olivine grains within ,308_3A are completely enclosed by pyroxene, indicating that olivine began to crystallise prior to pyroxene. The sequence of later stage crystallisation products is less clear.

Group 4 (12003,308_5A; 12003,308_7A)

Mineral phases in Group 4 samples are also equilibrated, and, therefore, crystallisation sequences are hard to infer from major and minor element concentrations in pyroxenes, olivines and plagioclases. The Group 4 olivines are completely enclosed within pyroxene (Figs. 6.2; 6.3). Unlike those in the Group 2 and 3 samples, none of the Group 4 spinels are enclosed within olivine but only within the larger pyroxene phases. Thus, olivine is interpretated to be the first phase to crystallise, followed by spinel. The relative timings of plagioclase and pyroxene crystallisation are less clear.

Intergroup comparisons

Although the Group 1 and Group 2 samples have some compositional and textural similarities there are clear distinctions between them. These include the finer grain size of the Group 1 sample, the absence of olivine and the increased amount of minor phases such as ilmenite and silica (Figs. 6.1; 6.2; 6.3; Table 6.1). Their pyroxene mineral chemistries also reveal some apparent distinctions between the samples. A larger proportion of the Group 1 pyroxenes appear to be more Fe-rich than in the Group 2 samples (Figs. 6.5; 6.10). It also appears that co-crystallising phases such as ulvöspinel, plagioclase and ilmenite appear on the liquidus earlier in the evolution of the Group 2 pyroxenes.

The narrower compositional range of the Group 3 and 4 pyroxenes when compared with those in the other 12003,308 samples may be due to either (i) equilibrium crystallisation in a closed system or (ii) sub-solidus equilibration (Figs. 6.5; 6.10; 6.11). However, the lack of exsolution features typically associated with subsolidus equilibration supports the first of these explanations (Fig. 6.1;6.2;6.3; *Peckett and Brown* 1973;

Lally et al. 1975; *Jolliff et al.* 1999; *McCallum et al.* 2006). The compositional equilibration in these samples also makes it unclear whether the mineral compositions analysed are representative of the most primitive compositions. For this reason, equilibrium parent melt compositions were not reconstructed for the Group 3 or 4 samples.

Many of the Group 4 pyroxenes have higher Al concentrations (up to ∼3.5 wt% Al_2O_3) than the Group 3 pyroxenes (Al_2O_3 <3.0 wt%; Fig. 6.11). This may be explained by the crystallisation of the Group 4 samples as cumulates in a more mafic system which produced less plagioclase, resulting in more Al being partitioned into the Group 4 pyroxenes. This would also suggest that the low modal abundance of plagioclase identified in the Group 4 samples may be indicative of the parent rocks from which these samples originated, and not an artefact of unrepresentative sampling. Alternatively, later crystallisation of spinel in the Group 4 samples, as indicated by their absence in the Group 4 olivines, may have resulted in more Al being present in the melt as the first pyroxenes crystallised. The Group 3 pyroxenes have lower Cr and Al concentrations (Al_2O_3 <3.0 wt%; Cr_2O_3 <0.7 wt%) than those in the other 12003,308 samples (Al_2O_3 <6.0 wt%; Cr_2O_3 <1.1 wt%; Figs. 6.10; 6.11). This may indicate that the ,308_3A crystallised from a separate melt with lower concentrations of such elements than any of the other 12003,308 parent melts.

As with the pyroxenes, the olivine compositions within the Group 2 samples span a wider range than those in the Group 3 and 4 samples. This also suggests the Group 2 samples formed via a process of fractional crystallisation, unlike the Group 3 and 4 samples. The Group 3 olivines have lower concentrations of minor and trace elements such as Cr, Ni and Co than a majority of those in the Group 2 and 4 samples (Fig. 6.12c;6.12d; Table 6.6). The olivines in the Group 4 samples have a similarly narrow compositional range when compared with the Group 3 olivines, but have slightly more primitive compositions (Fo_{62-68}). Several of the Group 4 olivines have higher concentrations of trace elements such as Ni and Co (Figs. 6.7; 6.12). These observations are interpreted as further evidence that all three groups originated from separate parent melts.

Comparison with Apollo 12 basalts

All ten of the 12003,308 samples have low-Ti compositions (i.e. where bulk TiO_2 = 1-6 wt%; *Neal and Taylor* 1992) consistent with other Apollo 12 basaltic compositions (Fig. 6.19; *Papike and Vaniman* 1978b). The compositions of the pyroxenes within the 12003,308 samples are also largely consistent with those of low-Ti mare basalts (Fig. 6.10; *Nielsen and Drake* 1978; *Arai et al.* 1996).

Previous studies of Apollo 12 basalts have resulted in their subdivision according to several different classification schemes relying on whole-rock characteristics (i.e. modal mineralogy and bulk composition; *James and Wright* 1972; *Rhodes et al.* 1977; *Neal et al.* 1994a). As such, some tentative comparisons of the 12003,308 bulk compositions and modal mineralogies have been made with those of other Apollo 12 basalts in addition to observed similarities in mineral chemistries. *James and Wright* (1972) defined a classification scheme based largely on the modal mineralogies of samples (Chapter 4). Average modal mineralogies for the three main Apollo 12 basaltic groups, as reported by *Papike and Vaniman* (1978a), are included in Table 6.1.

The whole-rock chemistry classification scheme proposed by *Neal et al.* (1994a) is based upon the bulk Mg# (atomic Mg/[Mg+Fe]) and Rb/Sr ratio of the Apollo 12 basalts; where olivine basalts have Mg# >46 and Rb/Sr >0.008, pigeonite basalts have Mg# <46 and Rb/Sr >0.008 and ilmenite basalts have Rb/Sr <0.008 and Mg# spanning the range of both the olivine and pigeonite suites. The sole feldspathic basalt 12038, falls within the ilmenite basalt classification. While Mg# values have been measured for the 12003,308 samples (Table 6.2), it has not been possible to perform bulk trace element analyses that would provide a measure of their Rb/Sr ratios. The Group 2, 3 and 4 samples all have Mg# >46 and, thus, fall within the range of either olivine or ilmenite basalts. 12003,308_1A (Group 1) has a much lower Mg# (28.1) and is within the range of either the feldspathic, pigeonite or ilmenite basalts, according to the *Neal et al.* (1994a) scheme.

Group 1

The Group 1 sample has the highest bulk Ti-content of the 12003,308 samples (TiO_2 = 4.8 wt%; Fig. 6.19), attributable to its relatively high ilmenite content (3.7% by mode). Of the seven 12003,308 igneous samples ,308_1A also has the highest Al-content (Al_2O_3 = 12.9 wt%), exceeding the typical Al range for most Apollo 12 basalts (Al_2O_3 <11 wt%; *Neal and Taylor* 1992; *Neal et al.* 1994a; Fig. 6.19). The high modal abundance of silica in ,308_1A (5.9%) is also unusual for the Apollo 12 basalts (*James and Wright*, 1972; *Neal et al.*, 1994a). A larger proportion of the Group 1 pyroxenes appear to be more evolved than in most other Apollo 12 basalts (Figs. 6.5; 6.10; *Bence et al.* 1970; *Anderson and Smith* 1971; *Boyd and Smith* 1971; *Brown et al.* 1971; *Dence et al.* 1971; *Hollister et al.* 1971; *Keil et al.* 1971; *Kushiro et al.* 1971; *Newton et al.* 1971; *Weill et al.* 1971).

Group 1 lacks olivine in the chip analysed, and so is not likely to be a member of the Apollo 12 olivine basalt suite. However, similarities can be seen between the Group 1

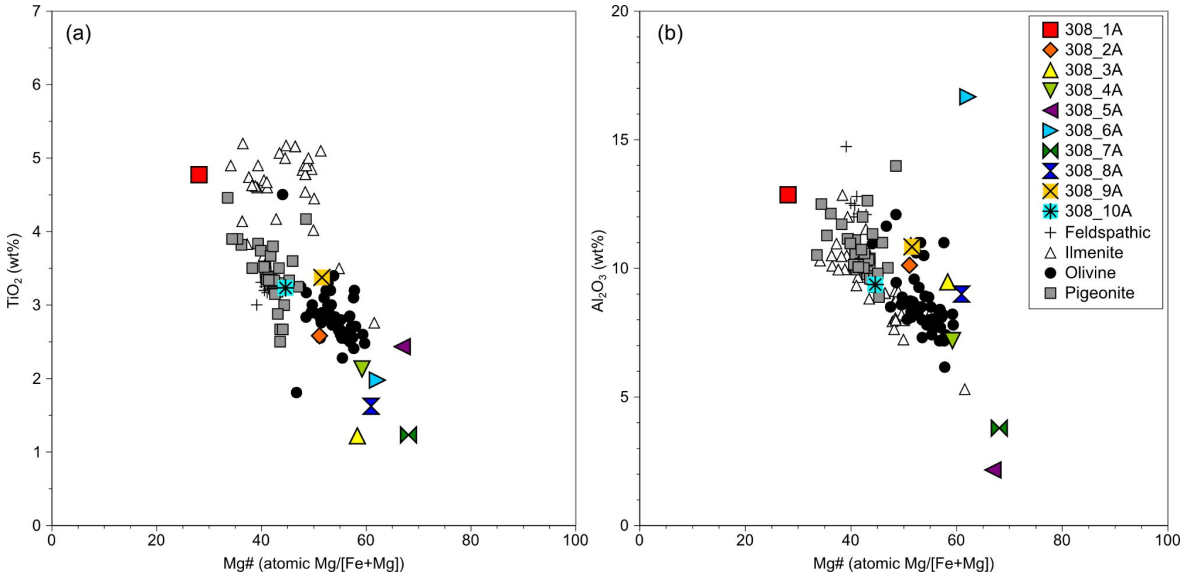

Figure 6.19: Bulk compositions of the 12003,308 samples compared with previously analysed Apollo 12 samples. (a) TiO_2 vs. Mg# (atomic Mg/[Fe+Mg]×100); (b) Al_2O_3 vs. Mg# (atomic Mg/[Fe+Mg]×100). 12003,308 data are compared with those of *Lunar Sample Preliminary Examination Team* (1970b); *Bouchet et al.* (1971); *Brunfelt et al.* (1971); *Cuttitta et al.* (1971); *Compston et al.* (1971); *Engel et al.* (1971); *Goles et al.* (1971); *Klein et al.* (1971); *Kushiro and Haramura* (1971); *Maxwell and Wiik* (1971); *Morrison et al.* (1971); *Smales et al.* (1971); *Wakita and Schmitt* (1971); *Wänke et al.* (1971); *Willis et al.* (1971, 1972); *Papike et al.* (1976); *Rhodes et al.* (1977); *Baldridge et al.* (1979); *Beaty et al.* (1979); *Warren et al.* (1986); *Neal et al.* (1994a).

sample and the feldspathic, ilmenite and pigeonite basaltic suites. The plagioclase-rich nature of the Group 1 sample 12003,308_1A and its lack of olivine is comparable to the feldspathic basalt 12038 (*Neal et al.*, 1994a). While a majority of the Apollo 12 ilmenite basalts are reported to have similarly high TiO_2 contents (*James and Wright*, 1972; *Rhodes et al.*, 1977; *Neal et al.*, 1994a; *Meyer*, 2005), the absence of olivine and the large amounts of silica in ,308_1A are less common features of the ilmenite basalt suite. Several of the ilmenite basalts do have similar modal mineralogies to the Group 1 sample (e.g. 12047, 12061, 12062 and 12064; *Klein et al.* 1971; *McGee et al.* 1977; *Dungan and Brown* 1977; *Neal et al.* 1994a).

Low modal abundances of olivine and high abundances of silica are common in the pigeonite basalts (e.g. samples 12007, 12021, 12031, 12039, 12043 and 12065; *McGee et al.* 1977; *Baldridge et al.* 1979; *Neal et al.* 1994a). Most of these samples tend to be coarser grained than ,308_1A. The pigeonite basalt 12021 bears the closest textural resemblance to the Group 1 sample. For example, ,308_1A has both the intrafasciculate and radiate textures of 12021 described by *Drever et al.* (1972, 1973), which they suggest are the result of rapid cooling (Fig. 6.1).

Compositional zoning of pyroxene in the Group 1 sample is consistent with that observed in 12021 (*Boyd and Smith*, 1971; *Weill et al.*, 1971) and 12031 (*Beaty et al.* 1979;

Fig. 6.5). REE concentrations of pyroxene in the Group 1 sample are also consistent with those observed in 12021 (*Shearer et al.* 1989; *O'Sullivan, pers. comm.* 2012). Plagioclase and spinel compositions reported for 12021 are also broadly similar with those of the Group 1 sample (Fig. 6.7; *Weill et al.* 1971; *Crawford* 1973). The reconstructed parent melt REE concentrations of the Group 1 sample are slightly higher than the bulk REE concentrations of the Apollo 12 pigeonite basalts (Fig. 6.17). However, this may reflect the limitations of the melt reconstruction discussed in Section 6.3.1.

Although a crystallisation sequence has not been presented for 12021, the crystallisation sequences presented by *Baldridge et al.* (1979) for various pigeonite basalts are consistent with that inferred for ,308_1A from the pyroxene chemistries (chromite → pyroxene → ulvöspinel → plagioclase → ilmenite). The Group 1 sample (,308_1A) is, therefore provisionally interpreted to be a small fragment of the same lava flow that sourced the Apollo 12 pigeonite basalts.

Group 2

The Group 2 samples have modal mineralogies which are similar to those of the Apollo 12 olivine basalts (*Grove et al.*, 1973; *Neal et al.*, 1994a). The bulk chemistries of these samples are also largely within the range of most of the olivine basalts, although the Ti content of ,308_8A (TiO_2 = 1.6 wt%) is slightly lower than that of the olivine basalts (TiO_2 = 1.8-4.5 wt%; *Bouchet et al.* 1971; *Beaty et al.* 1979; *Neal et al.* 1994a; Fig. 6.19). As noted earlier, this may be a sampling effect. Texturally the Group 2 samples resemble the medium-grained porphyritic olivine basalt 12002 (*Grove et al.*, 1973; *Meyer*, 2005). *Grove et al.* (1973) describe 12002 as containing phenocrysts of olivine and pyroxene, ilmenite laths and "complexly zoned spinels with chromite cores overgrown by rims of chromian ulvöspinel". These features are observed in all three Group 2 samples. Many of the Group 2 plagioclase crystals exhibit an intrafasciculate texture which is also observed in 12002 (*Drever et al.*, 1972; *Grove et al.*, 1973; *Meyer*, 2005).

Major and minor element compositions of pyroxene and olivine within the Group 2 samples are consistent with those of 12002 and other olivine basalts (Fig. 6.5; *Grove et al.* 1973). The ratios of Ti/V for many of the Group 2 olivines are similar to those of Apollo 12 olivine basalts (Fig. 6.18; *Fagan et al.* 2012). Several olivine analyses in each of the Group 2 samples have higher Ti/V ratios than previously observed in Apollo 12 olivine basalts, however, mineral trace element data is currently only available for three basalts from the olivine suite. The spinel compositions in the Group 2 samples are also comparable to those described in 12002 and a number of other variolitic and subophitic

basalts within the Apollo 12 olivine and ilmenite suites (e.g. 12014, 12063 and 12065; *Reid* 1971; *Taylor et al.* 1971a; *El Goresy et al.* 1971; Fig. 6.9).

Reconstructions of the parent melt REE concentrations for ,308_4A and ,308_8A are largely within the range of bulk REE concentrations reported for Apollo 12 olivine basalts (Fig. 6.17). The ,308_2A parent is calculated to have higher REE concentrations than the Apollo 12 olivine basalts, consistent with the hypothesis that it represents a more evolved member of the Group 2 samples (Fig. 6.17).

The Group 2 olivine and pyroxene chemistries have been used to infer the following crystallisation sequence: olivine → chromite → pyroxene → ulvöspinel → plagioclase → ilmenite. This is in good agreement with the sequence of 12002 which *Walker et al.* (1976a) derived from phase-equilibria and cooling rate studies. As such, the Group 2 samples are inferred to be fragments of the same lava flow that sourced the Apollo 12 olivine basalts.

Group 3

The modal mineralogy of the Group 3 sample ,308_3A is unlike most Apollo 12 basaltic samples. It is most similar to those reported by *Brett et al.* (1971a) and *Papike et al.* (1976) for the olivine basalt 12035. 12035, and ,308_3A also have (i) similar bulk compositions (Table 6.2; *Compston et al.* 1971); (ii) similar olivine compositions (Figs. 6.7; 6.12; *Butler* 1972); and (iii) similar spinel compositions (Fig. 6.9; *Reid* 1971). *Reid* (1971) described this sample as a gabbro (see also *James and Wright* 1972) with a cumulate texture and interpreted the spinel compositions and textural characteristics as being consistent with materials which crystallised early and accumulated towards the bottom of a lava flow, while the other finer grained olvine basalts represented the near-surface layers of the flow. Similar pyroxene, olivine and spinel compositions are also observed in the ilmenite basalt 12005 (Figs. 6.5; 6.12; 6.9; *Dungan and Brown* 1977). 12005 is one of the only Apollo 12 samples identified as containing similarly equilibrated pigeonite and augite phases (*Dungan and Brown*, 1977; *Meyer*, 2005).

The ratios of Ti/V for the Group 3 olivines are significantly higher than any other Apollo 12 basalts (Fig. 6.18; *Fagan et al.* 2012; *O'Sullivan, pers. comm.* 2012). Limited olivine trace element data is currently available for comparison. However, when combined with the sample's unusual modal mineralogy, this may indicate that the ,308_3A represents a fragment of a previously unrecognised low-Ti lava flow.

Group 4

The Group 4 samples also have modal mineralogies unlike any of the main Apollo 12 basaltic groups (Table 6.1; *Papike and Vaniman* 1978a). Several samples (e.g. 12008, 12009, 12015) in the Apollo 12 sample collection, which are classed as olivine vitrophyres, do have similarly low modal abundances of plagioclase, but also contain significantly more olivine and less pyroxene than the Group 4 samples (*Brett et al.*, 1971a; *Papike et al.*, 1976; *Baldridge et al.*, 1979; *Neal et al.*, 1994a). The textures of these olivine vitrophyres, with their fine grained matrices and skeletal, dendritic and euhedral olivine phenocrysts, are quite unlike the coarse grained Group 4 samples with their rounded olivine grains (*James and Wright* 1972; *Rhodes et al.* 1977; *Baldridge et al.* 1979; Figs. 6.2; 6.3). The ilmenite basalt 12005 is also reported to have very low abundances of plagioclase and although it too contains more olivine and less pyroxene than the Group 4 samples, the cumulate texture described by *Rhodes et al.* (1977) and *Dungan and Brown* (1977) is more similar to that of ,308_5A and ,308_7A. 12005 has the highest Mg content of any previously studied Apollo 12 basalt (MgO = 19.97 wt%; *Rhodes et al.* 1977; *Meyer* 2005). This is very close to the values measured for ,308_5A (MgO = 19.91 wt%) and ,308_7A (MgO = 18.57 wt%; Table 6.2)

12005 also has a very similar range of olivine and pyroxene compositions to the Group 4 samples (Fig. 6.7; *Dungan and Brown* 1977). For example, in addition to their unusually narrow compositional range, many of the clinopyroxene phases within 308_5A and 308_7A are less Fe-rich than most clinopyroxene phases in the other 12003,308 samples or other Apollo 12 basalts (Fig. 6.5). *Dungan and Brown* (1977) also report the compositions of spinels in 12005, which fall along the same trend as the Group 4 spinels on a plot of Ti# against Fe# (Fig. 6.9a). As with the Group 4 spinels, those in 12005 commonly exhibit ilmenite exsolution (*Dungan and Brown*, 1977). The high Mg content of the ilmenite in ,308_5A also correlates with the ilmenite analyses reported by *Dungan and Brown* (1977) for 12005. *Dungan and Brown* (1977) also report the compositions of metal grains in 12005 (Ni = ∼6-18 wt%; Co ∼2 wt%), which are comparable with those in ,308_5A FeNi metal grains (Ni = 1.8-12 wt%; Co = 1.8-2.4 wt%; Table 6.11).

The Ti/V ratios of the Group 4 olivines are also consistent with those of other Apollo 12 ilmenite basalts (Fig. 6.18; *Fagan et al.* 2012; *O'Sullivan, pers. comm.* 2012). They are in particularly good agreement with those of 12005. Based on these observations, the Group 4 samples are interpreted to be fragments of the ilmenite basalt suite.

6.3.2 Non-igneous samples

Breccias

The modal mineralogies and bulk compositions of the two brecciated samples (12003,308_9A and ,308_10A) are very similar, indicating that they may both contain material from similar bedrock sources (e.g. low-Ti lava flows). The bulk composition of ,308_9A is closer to that of the Apollo 12 olivine basalts, whereas ,308_10A has a slightly higher Mg# more similar to the Apollo 12 pigeonite basalts (Fig. 6.19). ,308_9A appears to contain a more diverse range of materials from individual mineral grains, to clasts with textures similar to the 12003,308 Group 2 samples (olivine basalts) and others with impact melt-like textures. ,308_10A is composed of a less varied range of materials which resemble some of the most coarsely grained pigeonite basalts (e.g. 12007 and 12039; *Bunch et al.* 1972; *Baldridge et al.* 1979).

When the Fe# and Al/Ti ratios of the pyroxenes within these samples are compared to those of the other ,308 fines, the ,308_10A pyroxenes form a trend similar to that observed in the Group 2 samples (Fig. 6.11). The ,308_9A pyroxene compositions are less well constrained. This may indicate that they originate from impact mixing of more than one lava flow implying that the sample is a polymict lithic breccia. ,308_10A is more likely to be a monomict breccia generated from pigeonite basalt. Assuming that ,308_10A is a monomict breccia, the parent melt REE composition was reconstructed from a pyroxene core analysis using the Wo_{12} partition coefficients of *McKay et al.* (1986b). The CI-normalised REE profile has higher abundances LREE than HREE and a negative Eu-anomaly (La_{cn}/Lu_{cn} = 9.0; Eu/Eu* = 0.5; 5.7-55 ×CI abundances) and is very similar to that of the Group 1 sample (,308_1A; Fig. 6.17).

Granulitic impactite

12003,308_6A has a poikilitic-granoblastic texture similar to that described by *Cushing et al.* (1999) in several of the granulitic impactite samples collected from the Apollo 17 landing site and at least one lunar meteorite (e.g. 72559, 78527, Northwest Africa 3163; *Nehru et al.* 1978; *Meyer* 2005; *Irving et al.* 2006). The sample has a relatively fine grain size (∼50 μm) compared to its overall size (∼1.6×1.4 mm). The modal mineralogy and bulk composition obtained are, therefore, considered to be representative of the parent rock from which the sample originated. It is the most aluminous (Al_2O_3 = 16.7 wt%) of the 12003,308 samples (Al_2O_3 = 2.2-12.9 wt%) and significantly more aluminous than most of the materials collected by the Apollo 12 mission. As such, it is not likely to represent metamorphosed lava flows sampled at the Apollo 12 site. High REE contents

Table 6.3: Summary of the igneous samples identified in 12003,308.

Sample	Group	Texture	Similar samples		
			Number	Basaltic suite	References
,308_1A	1	Porphyritic	12021; 12039	Pigeonite	*Weill et al.* 1971; *Rhodes et al.* 1977
,308_2A	2	Ophitic	12002	Olivine	*Grove et al.* 1973; *Neal et al.* 1994a
,308_3A	3	Gabbroic	12035; 12005	Olivine; Ilmenite	*Reid* 1971; *Dungan and Brown* 1977
,308_4A	2	Ophitic	12002	Olivine	*Grove et al.* 1973; *Neal et al.* 1994a
,308_5A	4	Cumulate	12005	Ilmenite	*Rhodes et al.* 1977; *Dungan and Brown* 1977
,308_7A	4	Cumulate	12005	Ilmenite	*Rhodes et al.* 1977; *Dungan and Brown* 1977
,308_8A	2	Ophitic	12002	Olivine	*Grove et al.* 1973; *Neal et al.* 1994a

in the plagioclase (between ∼10-50 ×CI abundances; 6.16) and clinopyroxene (∼100 ×CI abundances; Fig. 6.15) phases in this sample as well as the high modal abundance of merrillites imply that it has high concentrations of incompatible trace elements (i.e. KREEP). Previous studies have attempted to identify the provenance of the KREEP component found at the Apollo 12 site (e.g. *Meyer et al.* 1971; *Wasson and Baedecker* 1972; *Barra et al.* 2006; *Korotev et al.* 2011). These suggest the most likely sources to be the Copernicus, Reinhold or Lansberg craters (*Korotev et al.*, 2011).

6.4 Summary

Based on these results, four individual groups of igneous samples have been identified within 12003,308. These have been compared with other similar samples from the Apollo 12 basaltic suite (Table 6.3).

- The Group 1 sample (12003,308_1A) has a porphyritic texture with a subophitic matrix. It appears to be a more evolved basaltic rock, with a higher concentration of Fe-rich pyroxene compositions and more silica, than other Apollo 12 samples (Table 6.1). It is most similar to the pigeonite basalts 12021 and 12039 (*Weill et al.*, 1971; *Drever et al.*, 1972; *Rhodes et al.*, 1977).

- The Group 2 samples have ophitic textures which are the most similar of the 12003,308 samples to the majority of previously studied Apollo 12 basalts (Fig. 6.5; Table 6.1). They are particularly similar to the olivine basalt 12002 (*Grove et al.*, 1973; *Neal et al.*, 1994a). The minor and trace element mineral chemistry of the Group 2 samples provide evidence of a fractionation sequence within the parent melt, with ,308_2A representing the most evolved member of the group.

- The Group 3 sample (12003,308_3A) has a relatively coarse grained cumulate texture. Its modal mineralogy, bulk composition and range of mineral chemistries

are broadly similar to the olivine basalts 12035 and 12036, as well as the ilmenite basalt 12005 (Figs. 6.7; 6.9; *Reid* 1971; *James and Wright* 1972). However, of all the 12003,308 basalts, it is the least similar to any previously reported Apollo 12 samples.

- The Group 4 samples have the coarsest grainsize and are composed predominantly of olivine and pyroxene. They are most similar to the ilmenite basalt 12005, which is itself unlike most other Apollo 12 ilmenite basalt samples and has been suggested that it might belong to a separate basaltic group altogether (*Meyer*, 2005).

In summary, the 12003,308 basalt samples appear to have originated from four separate lava flows. Three of these are interpreted as fragments of the already established olivine, pigeonite and ilmenite basaltic suites. The fourth (Group 3; i.e. sample ,308_3A) may represent a previously unrecognised basaltic suite.

Table 6.4: Major, minor and trace element abundances for representative pyroxene phases within 12003,308_1-10A. Errors for major and minor elements are 1σ standard deviations calculated from repeat measurements of the BCR-2 USGS basaltic glass reference material. Errors for the trace elements are 1σ standard deviations calculated by the Glitter software.

Table 6.4

	021210_24 ,308_1A_p7 Undiff. Pyx.	101210_6 ,308_2A_p2 Undiff. Pyx.	101210_146 ,308_3A_p10 Aug.	121110_141 ,308_3A_p29 Pig.	130411_97 ,308_4A_p9 Undiff. Pyx.
Major and minor elements measured by WDS EMPA (wt%)					
SiO_2	45.7 ± 0.3	50.5 ± 0.7	49.1 ± 0.3	50.2 ± 0.2	51.6 ± 0.2
TiO_2	2.13 ± 0.06	0.98 ± 0.02	1.86 ± 0.02	1.22 ± 0.02	0.64 ± 0.01
Al_2O_3	5.18 ± 0.22	2.75 ± 0.06	2.37 ± 0.05	1.51 ± 0.06	1.51 ± 0.03
Cr_2O_3	1.17 ± 0.03	0.52 ± 0.02	0.51 ± 0.02	0.50 ± 0.02	0.61 ± 0.02
FeO	13.0 ± 0.2	20.7 ± 0.1	12.9 ± 0.1	18.2 ± 0.2	17.3 ± 0.1
MnO	0.27 ± 0.02	0.33 ± 0.02	0.25 ± 0.01	0.29 ± 0.02	0.31 ± 0.02
MgO	14.1 ± 0.4	18.5 ± 0.6	15.1 ± 0.4	19.4 ± 0.5	21.8 ± 0.9
CaO	15.9 ± 0.05	5.37 ± 0.02	15.9 ± 0.1	6.70 ± 0.06	4.33 ± 0.03
Na_2O	0.06 ± 0.01	0.02 ± 0.01	0.07 ± 0.01	0.03 ± 0.01	0.03 ± 0.01
Total	97.5	99.7	98.0	98.1	98.1
Mg#	66.0	61.5	67.5	65.6	69.2
Wo	34.8	11.4	33.8	14.0	8.98
En	43.0	54.5	44.7	56.4	63.0
Fs	22.2	34.1	21.5	29.6	28.1
Minor and trace elements measured by LA-ICP-MS (ppm; wt% for Al_2O_3, TiO_2, Cr_2O_3 and MnO)					
Mg	140173 ± 5123	51436 ± 1900	140975 ± 4915	224094 ± 7990	178538 ± 6223
Al	28493 ± 1261	12469 ± 579	12768 ± 480	9754 ± 374	9560 ± 437
Al_2O_3	5.38 ± 0.24	2.36 ± 0.11	2.41 ± 0.09	1.84 ± 0.07	1.81 ± 0.08
K	17.9 ± 2.8	146 ± 28	2.92 ± 0.86	4.61 ± 0.94	b.d.
Ca	113880 ± 4071	38401 ± 1534	113394 ± 3800	47864 ± 1681	30918 ± 1062
Sc	130 ± 5	48.8 ± 2.4	107 ± 4	71.2 ± 3.0	61.0 ± 3.3
Ti	14399 ± 949	4913 ± 377	12416 ± 792	8314 ± 534	4433 ± 277
TiO_2	2.40 ± 0.16	0.82 ± 0.06	2.07 ± 0.13	1.39 ± 0.09	0.74 ± 0.05
V	478 ± 29	161 ± 10	193 ± 8	175 ± 8	347 ± 26
Cr	8319 ± 467	2385 ± 153	3811 ± 203	3648 ± 196	5041 ± 457
Cr_2O_3	1.22 ± 0.07	0.35 ± 0.02	0.56 ± 0.03	0.53 ± 0.03	0.74 ± 0.07
Mn	2457 ± 93	1036 ± 70	2011 ± 73	3330 ± 123	2373 ± 125
MnO	0.32 ± 0.01	0.13 ± 0.01	0.26 ± 0.01	0.43 ± 0.02	0.31 ± 0.02
Co	25.2 ± 1.5	14.0 ± 1.0	27.2 ± 1.3	47.9 ± 2.3	39.8 ± 2.3
Ni	2.41 ± 0.55	4.35 ± 0.66	11.7 ± 1.0	26.8 ± 1.7	12.7 ± 1.3
Cu	1.01 ± 0.23	0.82 ± 0.21	0.27 ± 0.09	b.d.	b.d.
Zn	13.1 ± 1.6	11.7 ± 1.9	0.97 ± 0.24	1.50 ± 0.29	2.40 ± 0.33
Ga	2.14 ± 0.25	1.07 ± 0.15	1.64 ± 0.16	0.96 ± 0.10	0.48 ± 0.06
Ge	b.d.	b.d.	b.d.	b.d.	0.22 ± 0.09
Rb	b.d.	0.21 ± 0.07	b.d.	b.d.	b.d.
Sr	7.31 ± 0.45	7.97 ± 0.50	14.1 ± 0.6	3.87 ± 0.21	0.43 ± 0.04
Y	24.3 ± 1.2	10.6 ± 0.7	29.9 ± 1.3	10.4 ± 0.5	4.55 ± 0.27
Zr	33.3 ± 1.8	16.6 ± 1.8	16.4 ± 0.8	3.75 ± 0.26	2.13 ± 0.30
Nb	0.60 ± 0.11	0.65 ± 0.12	b.d.	b.d.	b.d.
Ag	b.d.	0.17 ± 0.07	b.d.	b.d.	b.d.
Cs	1.92 ± 0.17	b.d.	b.d.	b.d.	b.d.
Ba	6.36 ± 0.81	9.07 ± 1.14	b.d.	b.d.	b.d.
La	0.79 ± 0.10	0.72 ± 0.12	0.46 ± 0.06	0.05 ± 0.02	b.d.
Ce	3.47 ± 0.24	2.36 ± 0.25	2.25 ± 0.14	0.40 ± 0.04	0.09 ± 0.01
Pr	0.62 ± 0.08	0.57 ± 0.08	0.59 ± 0.05	0.08 ± 0.02	0.02 ± 0.01
Nd	3.46 ± 0.45	2.57 ± 0.43	4.29 ± 0.37	0.76 ± 0.12	0.24 ± 0.05
Sm	1.17 ± 0.27	0.95 ± 0.27	2.40 ± 0.28	0.38 ± 0.09	0.16 ± 0.05
Eu	0.10 ± 0.04	b.d.	0.18 ± 0.04	0.07 ± 0.02	0.02 ± 0.01
Gd	3.43 ± 0.49	1.67 ± 0.38	4.06 ± 0.38	0.76 ± 0.13	0.39 ± 0.07
Tb	0.57 ± 0.07	0.34 ± 0.06	0.80 ± 0.06	0.18 ± 0.03	0.08 ± 0.01
Dy	3.40 ± 0.38	1.91 ± 0.30	5.56 ± 0.37	1.78 ± 0.17	0.64 ± 0.07
Ho	0.93 ± 0.10	0.52 ± 0.08	1.26 ± 0.09	0.40 ± 0.04	0.16 ± 0.02
Er	2.68 ± 0.29	1.10 ± 0.20	3.56 ± 0.25	1.06 ± 0.11	0.68 ± 0.07
Tm	0.41 ± 0.06	0.20 ± 0.05	0.50 ± 0.05	0.18 ± 0.02	0.10 ± 0.01
Yb	2.72 ± 0.34	1.29 ± 0.25	3.45 ± 0.28	1.47 ± 0.15	0.63 ± 0.07
Lu	0.30 ± 0.05	0.21 ± 0.05	0.39 ± 0.04	0.22 ± 0.03	0.10 ± 0.01
Hf	2.01 ± 0.25	0.75 ± 0.17	1.05 ± 0.12	0.21 ± 0.05	0.13 ± 0.03
Ta	b.d.	0.08 ± 0.03	b.d.	b.d.	b.d.
Pb	0.08 ± 0.04	0.12 ± 0.05	b.d.	b.d.	b.d.
Th	0.10 ± 0.03	0.15 ± 0.05	b.d.	b.d.	b.d.
U	b.d.	0.04 ± 0.02	b.d.	b.d.	b.d.

Table 6.4 (continued)

	221010_294 ,308_5A_p58 Aug.	171110_335 ,308_5A_p58 Pig.	101210_272 ,308_6A_p34 CPX	101210_9 ,308_6A_p1 OPX	160411_75 ,308_7A_p59 Aug.
Major and minor elements measured by WDS EMPA (wt%)					
SiO_2	51.5 ± 1.1	51.8 ± 0.5	51.3 ± 0.3	53.4 ± 0.8	49.5 ± 0.3
TiO_2	1.15 ± 0.03	0.84 ± 0.02	2.08 ± 0.06	0.55 ± 0.01	1.62 ± 0.05
Al_2O_3	2.35 ± 0.08	1.69 ± 0.04	1.84 ± 0.03	0.64 ± 0.01	3.11 ± 0.07
Cr_2O_3	0.73 ± 0.02	0.65 ± 0.02	0.47 ± 0.02	0.26 ± 0.02	0.83 ± 0.02
FeO	11.2 ± 0.1	16.2 ± 0.1	12.4 ± 0.1	20.0 ± 0.1	10.3 ± 0.1
MnO	0.24 ± 0.02	0.31 ± 0.03	0.24 ± 0.03	0.30 ± 0.02	0.23 ± 0.01
MgO	18.2 ± 0.9	21.2 ± 0.7	16.0 ± 0.3	24.0 ± 0.7	15.9 ± 0.3
CaO	16.3 ± 0.1	5.38 ± 0.04	16.9 ± 0.0	1.87 ± 0.01	16.7 ± 0.4
Na_2O	0.06 ± 0.01	b.d.	0.19 ± 0.01	<0.01	0.07 ± 0.01
Total	101.6	98.0	101.3	101.1	98.3
Mg#	74.4	69.9	69.7	68.2	73.5
Wo	32.4	11.3	34.6	3.68	35.7
En	50.3	62.0	45.6	65.7	47.3
Fs	17.3	26.7	19.8	30.7	17.1
Minor and trace elements measured by LA-ICP-MS (ppm; wt% for Al_2O_3, TiO_2, Cr_2O_3 and MnO)					
Mg	164801 ± 7875	207171 ± 11816	149501 ± 5356	235545 ± 9488	149728 ± 5565
Al	14689 ± 790	8304 ± 548	9780 ± 377	3873 ± 165	17261 ± 720
Al_2O_3	2.78 ± 0.15	1.57 ± 0.10	1.85 ± 0.07	0.73 ± 0.03	3.26 ± 0.14
K	b.d.	b.d.	60.5 ± 5.5	23.9 ± 2.3	b.d.
Ca	116282 ± 3785	38429 ± 1318	120484 ± 4276	13386 ± 589	119612 ± 3851
Sc	94.0 ± 6.3	59.5 ± 5.1	98.9 ± 5.2	33.0 ± 1.9	110 ± 4
Ti	9002 ± 3145	5328 ± 2595	11293 ± 735	3841 ± 260	9835 ± 583
TiO_2	1.50 ± 0.52	0.89 ± 0.43	1.88 ± 0.12	0.64 ± 0.04	1.64 ± 0.10
V	439 ± 43	288 ± 36	129 ± 6	62.9 ± 3.2	459 ± 33
Cr	5602 ± 1502	4786 ± 1743	3422 b.d. 253	1975 ± 150	5568 ± 383
Cr_2O_3	0.82 ± 0.22	0.70 ± 0.25	0.50 ± 0.04	0.29 ± 0.02	0.81 ± 0.06
Mn	1995 ± 149	2634 ± 251	2213 ± 101	2958 ± 145	1721 ± 82
MnO	0.26 ± 0.02	0.34 ± 0.03	0.29 ± 0.01	0.38 ± 0.02	0.22 ± 0.01
Co	29.9 ± 2.6	41.5 ± 4.6	12.4 ± 0.8	18.7 ± 1.0	23.6 ± 1.3
Ni	20.9 ± 3.4	24.6 ± 5.3	5.15 ± 0.80	8.59 ± 0.74	16.9 ± 1.3
Cu	1.95 ± 0.26	b.d.	b.d.	b.d.	b.d.
Zn	5.21 ± 1.30	1.07 ± 0.41	3.57 ± 0.79	7.11 ± 1.08	1.02 ± 0.16
Ga	1.99 ± 0.20	0.57 ± 0.09	1.38 ± 0.20	0.65 ± 0.09	1.03 ± 0.10
Ge	2.09 ± 0.40	b.d.	b.d.	0.71 ± 0.23	b.d.
Rb	0.84 ± 0.11	b.d.	b.d.	0.08 ± 0.03	b.d.
Sr	7.49 ± 0.43	0.65 ± 0.07	7.11 ± 0.49	0.14 ± 0.03	7.73 ± 0.38
Y	13.5 ± 1.1	5.31 ± 0.58	232 ± 13	46.1 ± 2.7	15.7 ± 0.8
Zr	6.73 ± 0.66	1.85 ± 0.25	289 ± 13	62.1 ± 3.1	8.19 ± 0.43
Nb	0.54 ± 0.08	b.d.	10.3 ± 0.7	0.45 ± 0.06	0.03 ± 0.01
Ag	1.02 ± 0.17	b.d.	b.d.	b.d.	b.d.
Cs	0.39 ± 0.06	b.d.	b.d.	b.d.	b.d.
Ba	3.89 ± 0.68	b.d.	3.21 ± 0.58	0.23 ± 0.10	b.d.
La	0.52 ± 0.06	b.d.	6.41 ± 0.41	0.24 ± 0.04	0.20 ± 0.02
Ce	1.07 ± 0.10	0.10 ± 0.02	30.2 ± 1.8	0.72 ± 0.07	0.89 ± 0.06
Pr	0.47 ± 0.05	0.04 ± 0.02	6.46 ± 0.41	0.12 ± 0.02	0.26 ± 0.02
Nd	2.91 ± 0.37	0.26 ± 0.11	35.6 ± 2.4	1.13 ± 0.17	1.80 ± 0.16
Sm	3.34 ± 0.48	0.26 ± 0.12	19.4 ± 1.5	0.45 ± 0.11	1.17 ± 0.12
Eu	0.61 ± 0.07	b.d.	0.30 ± 0.07	b.d.	0.09 ± 0.02
Gd	3.51 ± 0.52	0.52 ± 0.15	27.0 ± 1.9	1.78 ± 0.23	2.16 ± 0.19
Tb	0.67 ± 0.07	0.09 ± 0.02	5.08 ± 0.33	0.53 ± 0.05	0.39 ± 0.03
Dy	3.65 ± 0.44	0.95 ± 0.17	39.6 ± 2.3	6.03 ± 0.43	3.18 ± 0.22
Ho	0.85 ± 0.08	0.21 ± 0.03	9.04 ± 0.56	1.73 ± 0.13	0.67 ± 0.05
Er	2.54 ± 0.29	0.84 ± 0.14	27.9 ± 1.5	6.95 ± 0.43	1.78 ± 0.12
Tm	0.54 ± 0.06	0.09 ± 0.02	4.05 ± 0.27	1.36 ± 0.10	0.26 ± 0.02
Yb	2.51 ± 0.29	1.01 ± 0.16	27.9 ± 1.5	11.5 ± 0.7	1.63 ± 0.13
Lu	0.57 ± 0.06	0.14 ± 0.03	3.70 ± 0.27	2.03 ± 0.14	0.23 ± 0.02
Hf	1.45 ± 0.17	0.12 ± 0.05	6.26 ± 0.51	2.12 ± 0.19	0.52 ± 0.06
Ta	0.32 ± 0.04	b.d.	0.34 ± 0.06	0.02 ± 0.01	b.d.
Pb	0.30 ± 0.07	b.d.	0.33 ± 0.07	0.08 ± 0.02	b.d.
Th	0.31 ± 0.04	b.d.	0.46 ± 0.07	0.21 ± 0.03	b.d.
U	0.23 ± 0.04	b.d.	0.32 ± 0.05	0.07 ± 0.01	b.d.

Table 6.4 (continued)

	081010_173 ,308_7A_p43 Pig.	110411_47 ,308_8A_p15 Undiff. Pyx.	291010_201 ,308_9A_p28 Undiff. Pyx.	291010_323 ,308_10A_p10 Undiff. Pyx.
Major and minor elements measured by WDS EMPA (wt%)				
SiO_2	51.9 ± 0.4	51.3 ± 0.5	46.6 ± 0.5	51.1 ± 0.4
TiO_2	0.74 ± 0.02	0.69 ± 0.02	1.77 ± 0.04	0.78 ± 0.01
Al_2O_3	1.44 ± 0.04	1.69 ± 0.05	8.47 ± 0.12	1.84 ± 0.04
Cr_2O_3	0.66 ± 0.02	0.71 ± 0.02	0.36 ± 0.02	0.71 ± 0.02
FeO	17.1 ± 0.1	17.6 ± 0.1	18.2 ± 0.1	18.3 ± 0.1
MnO	0.29 ± 0.03	0.33 ± 0.01	0.23 ± 0.03	0.34 ± 0.02
MgO	22.7 ± 0.5	22.0 ± 0.4	13.7 ± 0.3	21.3 ± 0.6
CaO	5.03 ± 0.03	4.80 ± 0.05	10.1 ± 0.0	4.65 ± 0.02
Na_2O	<0.01	<0.01	0.06 ± 0.01	<0.01
Total	99.7	99.1	99.4	99.0
Mg#	70.3	69.1	57.3	67.6
Wo	10.1	9.77	23.3	9.57
En	63.2	62.3	43.9	61.1
Fs	26.7	27.9	32.7	29.3
Minor and trace elements measured by LA-ICP-MS (ppm; wt% for Al_2O_3, TiO_2, Cr_2O_3 and MnO)				
Mg	251686 ± 10194	131695 ± 4561	n.m.	171324 ± 5899
Al	8841 ± 368	9091 ± 398	n.m.	10977 ± 459
Al_2O_3	1.67 ± 0.07	1.72 ± 0.08	n.m.	2.07 ± 0.09
K	b.d.	b.d.	n.m.	7.94 ± 1.16
Ca	35935 ± 1257	34320 ± 1230	n.m.	33262 ± 1142
Sc	60.6 ± 2.5	58.4 ± 2.8	n.m.	66.3 ± 2.8
Ti	5553 ± 526	4246 ± 233	n.m.	5697 ± 243
TiO_2	0.93 ± 0.09	0.71 ± 0.04	n.m.	0.95 ± 0.04
V	310 ± 20	331 ± 17	n.m.	374 ± 21
Cr	5256 ± 556	4604 ± 419	n.m.	5909 ± 355
Cr_2O_3	0.77 ± 0.08	0.67 ± 0.06	n.m.	0.86 ± 0.05
Mn	3060 ± 193	1897 ± 88	n.m.	2544 ± 99
MnO	0.40 ± 0.02	0.24 ± 0.01	n.m.	0.33 ± 0.01
Co	49.9 ± 2.8	31.6 ± 1.3	n.m.	44.4 ± 2.3
Ni	32.6 ± 2.4	9.19 ± 0.74	n.m.	3.79 ± 0.36
Cu	b.d.	0.20 ± 0.09	n.m.	0.20 ± 0.08
Zn	1.34 ± 0.25	3.85 ± 0.47	n.m.	4.94 ± 0.48
Ga	0.71 ± 0.08	0.42 ± 0.06	n.m.	0.65 ± 0.07
Ge	b.d.	b.d.	n.m.	b.d.
Rb	b.d.	b.d.	n.m.	b.d.
Sr	0.56 ± 0.06	0.65 ± 0.07	n.m.	2.75 ± 0.14
Y	4.64 ± 0.26	5.82 ± 0.36	n.m.	6.10 ± 0.32
Zr	1.69 ± 0.15	3.25 ± 0.31	n.m.	3.52 ± 0.25
Nb	b.d.	b.d.	n.m.	0.13 ± 0.03
Ag	b.d.	b.d.	n.m.	b.d.
Cs	b.d.	b.d.	n.m.	b.d.
Ba	b.d.	b.d.	n.m.	0.99 ± 0.18
La	b.d.	0.05 ± 0.02	n.m.	0.15 ± 0.03
Ce	0.09 ± 0.02	0.20 ± 0.04	n.m.	0.42 ± 0.04
Pr	0.02 ± 0.01	0.04 ± 0.01	n.m.	0.06 ± 0.01
Nd	0.25 ± 0.06	0.29 ± 0.09	n.m.	0.56 ± 0.10
Sm	0.09 ± 0.05	0.31 ± 0.10	n.m.	0.46 ± 0.10
Eu	b.d.	b.d.	n.m.	0.04 ± 0.01
Gd	0.35 ± 0.08	0.51 ± 0.13	n.m.	0.52 ± 0.11
Tb	0.10 ± 0.02	0.10 ± 0.02	n.m.	0.15 ± 0.02
Dy	0.64 ± 0.09	0.97 ± 0.15	n.m.	0.96 ± 0.11
Ho	0.18 ± 0.02	0.26 ± 0.04	n.m.	0.20 ± 0.03
Er	0.60 ± 0.07	0.58 ± 0.09	n.m.	0.82 ± 0.09
Tm	0.08 ± 0.02	0.11 ± 0.02	n.m.	0.16 ± 0.02
Yb	0.66 ± 0.09	0.72 ± 0.12	n.m.	0.94 ± 0.12
Lu	0.14 ± 0.02	0.15 ± 0.03	n.m.	0.11 ± 0.02
Hf	0.09 ± 0.03	0.14 ± 0.05	n.m.	0.14 ± 0.04
Ta	b.d.	b.d.	n.m.	0.02 ± 0.01
Pb	b.d.	b.d.	n.m.	0.04 ± 0.02
Th	b.d.	b.d.	n.m.	0.02 ± 0.01
U	b.d.	b.d.	n.m.	b.d.

Undiff. Pyx. = undifferentiated pyroxene; Aug. = augite; Pig. = pigeonite; CPX = clinopyroxene; OPX = orthopyroxene. Values which were below instrument detection limits (b.d.) or not measured (n.m.) have been indicated.

Table 6.5: Major, minor and trace element abundances for representative plagioclase phases within 12003,308_1-10A. Errors for major and minor elements are 1σ standard deviations calculated from repeat measurements of the BCR-2 USGS basaltic glass reference material. Errors for the trace elements are 1σ standard deviations calculated by the Glitter software.

Table 6.5					
	261110_311 ,308_1A_p8	101210_285 ,308_2A_p65	121110_122 ,308_3A_p10	221010_5 ,308_4A_p1	261110_13 ,308_5A_p2
Major and minor elements measured by WDS EMPA (wt%)					
SiO_2	46.6 ± 0.3	45.9 ± 0.3	44.3 ± 0.2	46.9 ± 0.1	45.1 ± 0.2
TiO_2	0.10 ± 0.01	0.10 ± 0.01	0.08 ± 0.00	0.05 ± 0.01	0.23 ± 0.01
Al_2O_3	32.4 ± 0.4	33.3 ± 1.2	33.5 ± 1.3	33.7 ± 0.3	33.7 ± 0.5
FeO	0.91 ± 0.01	0.73 ± 0.01	0.36 ± 0.01	0.78 ± 0.01	0.62 ± 0.02
MnO	b.d.	0.02 ± 0.01	0.05 ± 0.01	<0.01	b.d.
MgO	0.30 ± 0.01	0.27 ± 0.01	0.19 ± 0.01	0.41 ± 0.01	0.21 ± 0.01
CaO	17.6 ± 0.01	18.4 ± 0.1	18.4 ± 0.2	17.9 ± 0.1	18.9 ± 0.2
K_2O	0.04 ± 0.01	0.03 ± 0.01	0.07 ± 0.01	0.05 ± 0.01	0.12 ± 0.01
Na_2O	1.17 ± 0.01	0.91 ± 0.01	1.19 ± 0.04	1.10 ± 0.02	1.05 ± 0.19
Total	99.2	99.7	98.2	100.8	99.9
An	89.1	91.7	89.2	89.7	90.3
Minor and trace elements measured by LA-ICP-MS (ppm; wt% for Al_2O_3 and K_2O)					
Mg	19287 ± 690	3226 ± 109	1458 ± 51	2281 ± 79	1654 ± 95
Al	176267 ± 7685	188251 ± 8280	199156 ± 7438	195127 ± 8865	205753 ± 14308
Al_2O_3	33.3 ± 1.5	35.6 ± 1.6	37.6 ± 1.4	36.9 ± 1.7	38.9 ± 2.7
K	296 ± 37	270 ± 51	509 ± 34	332 ± 39	953 ± 395
K_2O	0.04 ± 0.01	0.03 ± 0.01	0.06 ± 0.01	0.04 ± 0.01	0.11 ± 0.05
Ca	125873 ± 4290	131727 ± 4475	131712 ± 4333	127939 ± 4316	134743 ± 4882
Sc	12.6 ± 0.7	2.49 ± 0.26	1.11 ± 0.13	1.17 ± 0.17	1.57 ± 0.29
Ti	2649 ± 175	1907 ± 144	473 ± 31	513 ± 34	1964 ± 333
V	30.9 ± 2.0	2.09 ± 0.21	1.82 ± 0.14	1.86 ± 0.21	3.63 ± 0.63
Cr	512 ± 30	8.34 ± 1.44	3.26 ± 0.97	5.53 ± 1.15	26.4 ± 6.4
Mn	371 ± 14	127 ± 9	46.5 ± 1.8	64.1 ± 3.5	43.7 ± 8.7
Co	5.19 ± 0.38	1.75 ± 0.19	0.27 ± 0.05	1.01 ± 0.13	0.29 ± 0.10
Ni	b.d.	b.d.	b.d.	b.d.	b.d.
Cu	1.69 ± 0.24	0.95 ± 0.24	0.21 ± 0.10	b.d.	0.39 ± 0.19
Zn	3.64 ± 0.60	3.35 ± 0.70	0.69 ± 0.21	1.71 ± 0.38	2.03 ± 0.82
Ga	6.69 ± 0.44	6.78 ± 0.46	10.3 ± 0.5	5.63 ± 0.44	9.68 ± 1.45
Rb	b.d.	b.d.	0.09 ± 0.03	b.d.	0.24 ± 0.09
Sr	228 ± 9	292 ± 12	528 ± 20	278 ± 12	590 ± 77
Y	2.93 ± 0.22	3.19 ± 0.28	0.31 ± 0.05	0.32 ± 0.06	0.49 ± 0.12
Zr	6.09 ± 0.46	12.5 ± 1.4	0.24 ± 0.06	0.70 ± 0.15	3.39 ± 0.50
Nb	0.10 ± 0.04	1.46 ± 0.18	b.d.	b.d.	0.25 ± 0.09
Cs	0.31 ± 0.05	b.d.	b.d.	b.d.	b.d.
Ba	19.8 ± 1.4	29.6 ± 2.4	44.1 ± 2.4	27.5 ± 1.7	44.5 ± 6.0
La	0.29 ± 0.05	0.95 ± 0.14	0.44 ± 0.05	0.34 ± 0.05	0.38 ± 0.09
Ce	1.34 ± 0.11	2.42 ± 0.24	0.97 ± 0.07	0.82 ± 0.08	1.12 ± 0.21
Pr	0.15 ± 0.03	0.53 ± 0.07	0.14 ± 0.02	0.08 ± 0.02	0.11 ± 0.04
Nd	0.86 ± 0.17	1.64 ± 0.32	0.55 ± 0.10	0.53 ± 0.13	0.52 ± 0.21
Sm	b.d.	0.36 ± 0.16	0.17 ± 0.07	b.d.	b.d.
Eu	1.30 ± 0.12	1.80 ± 0.18	3.28 ± 0.19	1.66 ± 0.14	4.00 ± 0.47
Gd	0.41 ± 0.14	b.d.	0.12 ± 0.05	b.d.	b.d.
Tb	0.10 ± 0.03	0.09 ± 0.03	0.04 ± 0.01	0.03 ± 0.01	b.d.
Dy	0.58 ± 0.12	0.65 ± 0.17	0.12 ± 0.05	0.12 ± 0.05	b.d.
Ho	0.14 ± 0.03	0.08 ± 0.03	b.d.	b.d.	b.d.
Er	0.38 ± 0.08	0.28 ± 0.09	b.d.	b.d.	b.d.
Tm	0.05 ± 0.02	0.06 ± 0.02	0.02 ± 0.01	b.d.	b.d.
Yb	0.45 ± 0.11	b.d.	b.d.	b.d.	b.d.
Lu	0.06 ± 0.02	0.06 ± 0.03	b.d.	b.d.	b.d.
Hf	0.21 ± 0.06	0.33 ± 0.10	b.d.	b.d.	b.d.
Pb	0.20 ± 0.04	0.12 ± 0.04	b.d.	b.d.	b.d.
Th	0.05 ± 0.02	0.11 ± 0.04	b.d.	b.d.	b.d.
U	0.14 ± 0.02	b.d.	b.d.	b.d.	b.d.

Table 6.5 (continued)

	261110_258 ,308_6A_p20	261110_11 ,308_7A_p3	261110_226 ,308_8A_p93	291010_298 ,308_9A_p115	291010_327 ,308_10A_p14
Major and minor elements measured by WDS EMPA (wt%)					
SiO_2	47.5 ± 0.3	45.4 ± 0.2	45.0 ± 0.3	47.5 ± 0.4	46.0 ± 0.4
TiO_2	0.04 ± 0.01	0.08 ± 0.01	0.08 ± 0.01	0.10 ± 0.01	0.06 ± 0.01
Al_2O_3	33.5 ± 0.6	33.4 ± 0.5	33.5 ± 0.6	31.9 ± 0.7	31.8 ± 0.7
FeO	0.23 ± 0.01	0.36 ± 0.01	0.60 ± 0.01	1.14 ± 0.01	0.74 ± 0.01
MnO	b.d.	b.d.	0.02 ± 0.01	0.02 ± 0.01	0.04 ± 0.01
MgO	0.05 ± 0.01	0.28 ± 0.01	0.27 ± 0.01	0.19 ± 0.01	0.22 ± 0.01
CaO	16.7 ± 0.1	18.2 ± 0.2	18.4 ± 0.1	17.9 ± 0.1	18.0 ± 0.1
K_2O	0.23 ± 0.01	0.03 ± 0.01	0.04 ± 0.01	0.06 ± 0.01	0.05 ± 0.01
Na_2O	2.22 ± 0.03	1.13 ± 0.21	0.86 ± 0.01	1.08 ± 0.02	1.09 ± 0.02
Total	100.5	98.9	98.8	99.9	98.0
An	79.5	89.7	92.0	89.8	89.8
Minor and trace elements measured by LA-ICP-MS (ppm; wt% for Al_2O_3 and K_2O)					
Mg	725 ± 25	2078 ± 79	2448 ± 87	n.m.	1747 ± 60
Al	193559 ± 7245	195860 ± 8293	193149 ± 8252	n.m.	191584 ± 7966
Al_2O_3	36.6 ± 1.4	37.0 ± 1.6	36.5 ± 1.6	n.m.	36.2 ± 1.5
K	1449 ± 123	228 ± 28	337 ± 33	n.m.	336 ± 38
K_2O	0.17 ± 0.01	0.03 ± 0.01	0.04 ± 0.01	n.m.	0.04 ± 0.01
Ca	119462 ± 3954	130376 ± 4401	131519 ± 4388	n.m.	128796 ± 4348
Sc	0.94 ± 0.12	1.38 ± 0.18	1.23 ± 0.15	n.m.	1.14 ± 0.16
Ti	194 ± 14	554 ± 35	537 ± 35	n.m.	462 ± 22
V	0.22 ± 0.05	3.65 ± 0.34	2.18 ± 0.20	n.m.	1.63 ± 0.17
Cr	b.d.	11.7 ± 1.6	7.60 ± 1.30	n.m.	2.86 ± 0.89
Mn	14.4 ± 0.7	51.1 ± 2.6	74.3 ± 3.3	n.m.	73.2 ± 3.0
Co	0.07 ± 0.04	0.32 ± 0.07	1.08 ± 0.13	n.m.	1.09 ± 0.14
Ni	0.25 ± 0.12	b.d.	b.d.	n.m.	0.69 ± 0.23
Cu	0.34 ± 0.11	b.d.	0.46 ± 0.13	n.m.	b.d.
Zn	0.57 ± 0.19	1.38 ± 0.33	0.73 ± 0.26	n.m.	0.93 ± 0.29
Ga	36.8 ± 1.9	5.80 ± 0.52	6.99 ± 0.44	n.m.	8.21 ± 0.54
Rb	0.82 ± 0.09	b.d.	0.05 ± 0.03	n.m.	b.d.
Sr	350 ± 17	309 ± 15	265 ± 12	n.m.	315 ± 11
Y	5.46 ± 0.34	0.16 ± 0.05	0.26 ± 0.05	n.m.	0.31 ± 0.07
Zr	0.85 ± 0.11	0.18 ± 0.07	b.d.	n.m.	b.d.
Nb	0.18 ± 0.04	b.d.	b.d.	n.m.	b.d.
Cs	b.d.	b.d.	b.d.	n.m.	0.62 ± 0.08
Ba	543 ± 32	15.1 ± 1.1	26.2 ± 2.1	n.m.	20.7 ± 1.6
La	9.91 ± 0.50	0.25 ± 0.05	0.27 ± 0.04	n.m.	0.20 ± 0.05
Ce	20.8 ± 1.2	0.45 ± 0.06	0.63 ± 0.06	n.m.	0.47 ± 0.07
Pr	2.06 ± 0.13	0.04 ± 0.02	0.11 ± 0.02	n.m.	0.08 ± 0.03
Nd	6.91 ± 0.53	0.39 ± 0.12	0.33 ± 0.10	n.m.	b.d.
Sm	1.14 ± 0.17	b.d.	b.d.	n.m.	b.d.
Eu	4.69 ± 0.29	1.59 ± 0.14	1.55 ± 0.13	n.m.	1.52 ± 0.16
Gd	0.86 ± 0.15	b.d.	b.d.	n.m.	b.d.
Tb	0.19 ± 0.03	b.d.	0.03 ± 0.01	n.m.	b.d.
Dy	1.09 ± 0.13	b.d.	b.d.	n.m.	b.d.
Ho	0.17 ± 0.03	b.d.	b.d.	n.m.	b.d.
Er	0.65 ± 0.08	b.d.	b.d.	n.m.	b.d.
Tm	0.07 ± 0.02	b.d.	b.d.	n.m.	b.d.
Yb	0.39 ± 0.08	b.d.	b.d.	n.m.	0.23 ± 0.10
Lu	0.08 ± 0.02	b.d.	b.d.	n.m.	b.d.
Hf	b.d.	b.d.	b.d.	n.m.	b.d.
Pb	0.46 ± 0.06	b.d.	b.d.	n.m.	b.d.
Th	0.16 ± 0.03	b.d.	b.d.	n.m.	b.d.
U	0.02 ± 0.01	b.d.	b.d.	n.m.	b.d.

Values which were below instrument detection limits (b.d.) or not measured (n.m.) have been indicated.

Table 6.6: Major, minor and trace element abundances for representative olivine grains within 12003,308_1-10A. Errors for major and minor elements are 1σ standard deviations calculated from repeat measurements of the BCR-2 USGS basaltic glass reference material. Errors for the trace elements are 1σ standard deviations calculated by the Glitter software.

Table 6.6				
	130411_277 ,308_2A_p53	101210_202 ,308_3A_p61	191110_13 ,308_4A_p2	171110_283 ,308_5A_p11
Major and minor elements measured by WDS EMPA (wt%)				
SiO_2	38.0 ± 0.3	36.6 ± 0.2	37.2 ± 0.3	37.1 ± 0.2
TiO_2	0.04 ± 0.00	0.06 ± 0.01	0.06 ± 0.01	0.06 ± 0.01
Al_2O_3	0.04 ± 0.00	b.d.	0.03 ± 0.01	<0.01
Cr_2O_3	0.28 ± 0.02	0.07 ± 0.01	0.29 ± 0.02	0.11 ± 0.01
FeO	26.4 ± 0.2	34.4 ± 0.3	27.6 ± 0.1	28.9 ± 0.2
MnO	0.30 ± 0.01	0.34 ± 0.02	0.26 ± 0.02	0.32 ± 0.02
MgO	35.5 ± 0.6	29.3 ± 0.5	35.2 ± 1.0	32.5 ± 1.0
CaO	0.28 ± 0.01	0.24 ± 0.01	0.27 ± 0.01	0.18 ± 0.01
Na_2O	<0.01	b.d.	b.d.	0.02 ± 0.01
P_2O_5	<0.01	<0.01	0.02 ± 0.01	<0.01
V_2O_3	0.04 ± 0.01	<0.01	b.d.	<0.01
Total	100.9	100.9	101.0	99.2
Mg#	70.6	60.3	69.4	66.7
Minor and trace elements measured by LA-ICP-MS (ppm; wt% for MgO, CaO and Cr_2O_3)				
Mg	228690 ± 7501	183031 ± 6644	209847 ± 7502	224004 ± 7550
MgO	37.9 ± 1.2	30.4 ± 1.1	34.8 ± 1.2	37.1 ± 1.3
Al	218 ± 7	54.0 ± 2.0	178 ± 7	103 ± 4
K	b.d.	b.d.	b.d.	1.77 ± 0.52
Ca	1985 ± 88	1181 ± 63	1634 ± 96	1279 ± 70
CaO	0.28 ± 0.01	0.17 ± 0.01	0.23 ± 0.01	0.18 ± 0.01
Sc	9.00 ± 0.36	7.22 ± 0.33	8.13 ± 0.35	8.11 ± 0.35
Ti	209 ± 8	281 ± 11	197 ± 8	274 ± 11
V	109 ± 4	24.4 ± 0.9	79.5 ± 2.7	44.9 ± 1.6
Cr	3090 ± 108	810 ± 29	2374 ± 86	785 ± 29
Cr_2O_3	0.45 ± 0.02	0.12 ± 0.01	0.35 ± 0.01	0.11 ± 0.01
Mn	2316 ± 73	2656 ± 84	1990 ± 63	2463 ± 78
Co	127 ± 4	75.0 ± 2.6	100 ± 3	91.8 ± 3.2
Ni	222 ± 8	29.3 ± 1.3	178 ± 7	75.1 ± 2.9
Cu	b.d.	b.d.	0.24 ± 0.08	0.16 ± 0.05
Zn	2.19 ± 0.19	1.98 ± 0.22	1.32 ± 0.19	1.96 ± 0.20
Ga	0.04 ± 0.02	0.10 ± 0.02	0.05 ± 0.02	0.05 ± 0.02
Ge	b.d.	0.44 ± 0.13	b.d.	b.d.
Rb	0.04 ± 0.01	b.d.	b.d.	b.d.
Sr	0.04 ± 0.01	0.03 ± 0.01	b.d.	b.d.
Y	0.23 ± 0.03	1.26 ± 0.09	0.20 ± 0.03	0.29 ± 0.03
Zr	0.07 ± 0.02	0.39 ± 0.05	0.07 ± 0.03	0.33 ± 0.05
Nb	b.d.	b.d.	b.d.	b.d.
Cs	b.d.	b.d.	b.d.	b.d.
Ba	b.d.	b.d.	b.d.	b.d.
La	b.d.	b.d.	b.d.	b.d.
Ce	b.d.	b.d.	0.02 ± 0.01	b.d.
Pr	b.d.	<0.01	b.d.	b.d.
Nd	b.d.	b.d.	b.d.	b.d.
Sm	b.d.	b.d.	b.d.	b.d.
Eu	b.d.	b.d.	b.d.	b.d.
Gd	b.d.	b.d.	b.d.	b.d.
Tb	b.d.	<0.01	b.d.	b.d.
Dy	0.03 ± 0.01	0.11 ± 0.02	0.03 ± 0.02	b.d.
Ho	b.d.	0.05 ± 0.01	b.d.	0.02 ± 0.00
Er	0.04 ± 0.01	0.17 ± 0.02	b.d.	0.06 ± 0.01
Tm	b.d.	0.03 ± 0.01	b.d.	<0.01
Yb	0.10 ± 0.03	0.37 ± 0.05	0.09 ± 0.03	0.11 ± 0.02
Lu	0.02 ± 0.01	0.08 ± 0.01	b.d.	0.03 ± 0.01

Table 6.6 (continued)

	291010_161 ,308_7A_p47	171110_21 ,308_8A_p16	291010_260 ,308_9A_p82	051110_120 ,308_10A_p94
Major and minor elements measured by WDS EMPA (wt%)				
SiO_2	37.1 ± 0.5	37.4 ± 0.1	37.2 ± 0.5	35.5 ± 0.2
TiO_2	0.11 ± 0.01	0.03 ± 0.01	0.08 ± 0.01	0.11 ± 0.01
Al_2O_3	b.d.	0.04 ± 0.01	0.03 ± 0.01	0.05 ± 0.01
Cr_2O_3	0.13 ± 0.01	0.34 ± 0.02	0.37 ± 0.02	0.29 ± 0.02
FeO	31.8 ± 0.2	23.4 ± 0.2	26.7 ± 0.2	34.1 ± 0.3
MnO	0.34 ± 0.04	0.25 ± 0.02	0.29 ± 0.02	0.40 ± 0.03
MgO	31.7 ± 0.8	37.3 ± 1.5	36.8 ± 1.0	28.5 ± 0.6
CaO	0.17 ± 0.01	0.27 ± 0.01	0.29 ± 0.01	0.42 ± 0.01
Na_2O	b.d.	0.02 ± 0.01	<0.01	b.d.
P_2O_5	0.07 ± 0.01	b.d.	0.02 ± 0.01	0.02 ± 0.01
V_2O_3	b.d.	b.d.	<0.01	0.03 ± 0.01
Total	101.5	99.0	101.7	99.4
Mg#	64.0	73.9	71.1	59.8
Minor and trace elements measured by LA-ICP-MS (ppm; wt% for MgO, CaO and Cr_2O_3)				
Mg	208995 ± 7005	246508 ± 9846	n.m.	n.m.
MgO	34.7 ± 1.2	40.9 ± 1.6	n.m.	n.m.
Al	207 ± 7	107 ± 4	n.m.	n.m.
K	13.1 ± 1.7	b.d.	n.m.	n.m.
Ca	1311 ± 80	1286 ± 90	n.m.	n.m.
CaO	0.18 ± 0.01	0.18 ± 0.01	n.m.	n.m.
Sc	9.21 ± 0.42	5.43 ± 0.27	n.m.	n.m.
Ti	491 ± 21	139 ± 6	n.m.	n.m.
V	38.6 ± 1.4	66.4 ± 2.4	n.m.	n.m.
Cr	912 ± 32	2347 ± 84	n.m.	n.m.
Cr_2O_3	0.13 ± 0.01	0.34 ± 0.01	n.m.	n.m.
Mn	2594 ± 82	1928 ± 61	n.m.	n.m.
Co	91.4 ± 3.2	92.9 ± 3.2	n.m.	n.m.
Ni	72.1 ± 2.8	201 ± 8	n.m.	n.m.
Cu	b.d.	b.d.	n.m.	n.m.
Zn	2.51 ± 0.28	7.89 ± 0.68	n.m.	n.m.
Ga	0.19 ± 0.04	b.d.	n.m.	n.m.
Ge	b.d.	0.47 ± 0.20	n.m.	n.m.
Rb	0.05 ± 0.02	b.d.	n.m.	n.m.
Sr	0.57 ± 0.05	0.03 ± 0.01	n.m.	n.m.
Y	0.85 ± 0.07	0.16 ± 0.03	n.m.	n.m.
Zr	1.40 ± 0.12	0.13 ± 0.04	n.m.	n.m.
Nb	0.03 ± 0.01	b.d.	n.m.	n.m.
Cs	b.d.	b.d.	n.m.	n.m.
Ba	1.42 ± 0.17	b.d.	n.m.	n.m.
La	0.06 ± 0.01	b.d.	n.m.	n.m.
Ce	0.14 ± 0.02	b.d.	n.m.	n.m.
Pr	0.02 ± 0.01	b.d.	n.m.	n.m.
Nd	0.10 ± 0.03	b.d.	n.m.	n.m.
Sm	0.08 ± 0.03	b.d.	n.m.	n.m.
Eu	b.d.	b.d.	n.m.	n.m.
Gd	0.06 ± 0.03	b.d.	n.m.	n.m.
Tb	b.d.	b.d.	n.m.	n.m.
Dy	0.10 ± 0.03	b.d.	n.m.	n.m.
Ho	0.02 ± 0.01	b.d.	n.m.	n.m.
Er	0.13 ± 0.03	b.d.	n.m.	n.m.
Tm	b.d.	b.d.	n.m.	n.m.
Yb	0.23 ± 0.04	b.d.	n.m.	n.m.
Lu	0.05 ± 0.01	<0.01	n.m.	n.m.

Values which were below instrument detection limits (b.d.) or not measured (n.m.) have been indicated.

Table 6.7: Major and minor element abundances (wt%) for representative ilmenite grains within 12003,308_1-10A. Errors for major and minor elements are 1σ standard deviations calculated from repeat measurements of the BCR-2 USGS basaltic glass reference material.

	130411_246 ,308_1A_p31	130411_55 ,308_2A_p37	151010_222 ,308_3A_p10	221010_162 ,308_4A_p136	221010_265 ,308_5A_p29
SiO_2	0.05 ± 0.01	0.27 ± 0.01	0.12 ± 0.01	b.d.	0.08 ± 0.01
TiO_2	53.3 ± 0.8	53.0 ± 1.4	52.6 ± 0.9	51.6 ± 1.1	54.2 ± 1.5
Al_2O_3	b.d.	b.d.	0.02 ± 0.01	0.14 ± 0.01	<0.01
Cr_2O_3	0.11 ± 0.02	0.51 ± 0.02	0.52 ± 0.02	0.41 ± 0.02	0.61 ± 0.02
FeO	47.4 ± 0.3	44.0 ± 0.4	42.2 ± 0.4	46.4 ± 0.6	40.6 ± 0.5
MnO	0.32 ± 0.01	0.38 ± 0.03	0.39 ± 0.02	0.31 ± 0.02	0.38 ± 0.03
MgO	0.04 ± 0.01	1.63 ± 0.03	4.40 ± 0.09	0.99 ± 0.01	5.58 ± 0.28
CaO	0.10 ± 0.01	0.25 ± 0.01	b.d.	0.10 ± 0.00	b.d.
Na_2O	0.03 ± 0.01	b.d.	b.d.	<0.01	b.d.
V_2O_3	0.15 ± 0.01	0.19 ± 0.09	0.26 ± 0.05	0.15 ± 0.02	0.21 ± 0.04
Total	101.4	100.2	100.5	100.1	101.6

	081010_97 ,308_6A_p51	110411_65 ,308_8A_p28	130411_80 ,308_9A_p15	160411_351 ,308_10A_p50
SiO_2	0.05 ± 0.01	0.06 ± 0.01	0.17 ± 0.01	0.12 ± 0.01
TiO_2	53.5 ± 0.8	51.5 ± 0.9	52.0 ± 1.1	53.0 ± 0.8
Al_2O_3	<0.01	b.d.	b.d.	b.d.
Cr_2O_3	0.25 ± 0.02	0.24 ± 0.02	0.10 ± 0.02	0.25 ± 0.02
FeO	42.6 ± 0.4	46.7 ± 0.3	47.2 ± 0.5	46.6 ± 0.4
MnO	0.38 ± 0.03	0.33 ± 0.02	0.35 ± 0.02	0.34 ± 0.02
MgO	4.50 ± 0.12	0.29 ± 0.01	0.09 ± 0.01	0.15 ± 0.01
CaO	0.15 ± 0.01	0.05 ± 0.01	0.18 ± 0.01	b.d.
Na_2O	b.d.	0.04 ± 0.01	b.d.	b.d.
V_2O_3	0.18 ± 0.03	b.d.	0.14 ± 0.01	0.12 ± 0.02
Total	101.6	99.1	100.2	100.6

Values which were below instrument detection limits (b.d.) have been indicated.

Table 6.8: Major and minor element abundances (wt%) for representative spinel phases within 12003,308_1-10A. Errors for major and minor elements are 1σ standard deviations calculated from repeat measurements of the BCR-2 USGS basaltic glass reference material.

	130411_262 ,308_1A_p47	130411_263 ,308_1A_p48	271011_149 ,308_2A_p7	130411_29 ,308_2A_p11	151010_247 ,308_3A_p30
SiO_2	0.13 ± 0.01	0.24 ± 0.01	0.06 ± 0.01	0.30 ± 0.01	0.08 ± 0.01
TiO_2	25.2 ± 0.4	31.3 ± 0.4	4.29 ± 0.08	29.4 ± 0.7	19.6 ± 0.4
Al_2O_3	3.17 ± 0.06	2.47 ± 0.05	12.3 ± 0.3	2.55 ± 0.07	7.13 ± 0.40
Cr_2O_3	12.4 ± 0.1	4.47 ± 0.05	45.8 ± 0.1	7.70 ± 0.06	25.3 ± 0.1
FeO	55.7 ± 0.4	60.6 ± 0.4	27.8 ± 0.1	58.0 ± 0.6	43.8 ± 0.4
MnO	0.31 ± 0.01	0.32 ± 0.01	0.33 ± 0.03	0.33 ± 0.02	0.33 ± 0.02
MgO	0.42 ± 0.01	0.43 ± 0.01	5.94 ± 0.12	0.66 ± 0.01	5.10 ± 0.12
CaO	0.02 ± 0.01	0.06 ± 0.01	0.02 ± 0.01	0.09 ± 0.01	b.d.
Na_2O	<0.01	b.d.	b.d.	0.03 ± 0.01	b.d.
V_2O_3	0.34 ± 0.02	0.20 ± 0.01	0.98 ± 0.11	0.27 ± 0.13	0.61 ± 0.08
Total	97.7	100.0	97.4	99.3	101.9

	121110_134 ,308_3A_p22	221010_147 ,308_4A_p121	221010_154 ,308_4A_p128	221010_270 ,308_5A_p34	221010_252 ,308_5A_p16
SiO_2	0.09 ± 0.01	0.15 ± 0.01	0.03 ± 0.01	0.08 ± 0.01	0.11 ± 0.01
TiO_2	24.2 ± 0.4	4.66 ± 0.10	30.4 ± 0.6	8.99 ± 0.24	21.6 ± 0.6
Al_2O_3	4.66 ± 0.18	12.5 ± 0.3	2.80 ± 0.08	15.7 ± 0.5	6.81 ± 0.22
Cr_2O_3	17.5 ± 0.1	42.5 ± 0.1	8.36 ± 0.06	34.6 ± 0.1	20.2 ± 0.1
FeO	49.4 ± 0.6	33.0 ± 0.4	57.0 ± 0.8	32.5 ± 0.4	45.1 ± 0.5
MnO	0.36 ± 0.02	0.34 ± 0.02	0.35 ± 0.02	0.35 ± 0.02	0.35 ± 0.02
MgO	3.20 ± 0.08	4.06 ± 0.06	1.14 ± 0.02	7.29 ± 0.37	5.75 ± 0.29
CaO	b.d.	0.03 ± 0.01	0.06 ± 0.01	b.d.	b.d.
Na_2O	b.d.	b.d.	0.02 ± 0.01	b.d.	<0.01
V_2O_3	0.43 ± 0.05	1.05 ± 0.17	0.26 ± 0.04	0.92 ± 0.15	0.50 ± 0.08
Total	99.9	98.2	100.4	100.4	100.4

	081010_176 ,308_7A_p46	291010_165 ,308_7A_p51	271011_172 ,308_8A_p5	261110_192 ,308_8A_p59	051110_26 ,308_10A_p5
SiO_2	0.10 ± 0.01	3.05 ± 0.04	0.08 ± 0.01	0.12 ± 0.01	0.86 ± 0.01
TiO_2	7.69 ± 0.22	11.2 ± 0.4	4.00 ± 0.08	30.6 ± 0.5	25.4 ± 0.5
Al_2O_3	13.1 ± 0.4	12.4 ± 0.2	12.4 ± 0.3	2.64 ± 0.05	4.04 ± 0.07
Cr_2O_3	40.6 ± 0.1	30.3 ± 0.1	45.4 ± 0.1	7.56 ± 0.06	11.9 ± 0.1
FeO	31.0 ± 0.2	35.2 ± 0.2	31.0 ± 0.2	55.0 ± 0.4	51.3 ± 0.4
MnO	0.32 ± 0.03	0.33 ± 0.04	0.32 ± 0.03	0.32 ± 0.03	0.35 ± 0.02
MgO	6.73 ± 0.13	5.58 ± 0.14	3.79 ± 0.07	0.81 ± 0.02	2.89 ± 0.05
CaO	b.d.	<0.01	0.02 ± 0.01	0.02 ± 0.01	0.15 ± 0.01
Na_2O	b.d.	0.05 ± 0.01	0.03 ± 0.01	b.d.	<0.01
V_2O_3	0.97 ± 0.14	0.77 ± 0.10	0.94 ± 0.10	0.26 ± 0.03	0.62 ± 0.10
Total	100.4	99.0	97.9	97.2	97.5

Values which were below instrument detection limits (b.d.) have been indicated.

Table 6.9: Major and minor element abundances for representative miscellaneous silicate phases within several of the 12003,308 A-splits measured by EMP WDS. Abundances are reported as oxide wt% values. Errors reported are 1σ standard deviations calculated from repeat measurements of the BCR-2 USGS basaltic glass reference material.

	130411_244 ,308_1A_p29 Silica	151010_161 ,308_2A_p129 Silica	291010_313 ,308_9A_p130 Silica	120411_9 ,308_1A_p6 K-Feldspar	130411_204 ,308_2A_p43 K-Feldspar	130411_14 ,308_3A_p1 K-Feldspar
SiO_2	96.8 ± 0.7	96.2 ± 0.6	96.8 ± 0.8	55.8 ± 0.5	63.5 ± 0.3	60.8 ± 0.3
TiO_2	0.35 ± 0.01	0.26 ± 0.01	0.41 ± 0.01	0.23 ± 0.01	0.13 ± 0.01	0.27 ± 0.01
Al_2O_3	0.69 ± 0.01	0.74 ± 0.01	0.82 ± 0.02	24.3 ± 0.3	22.2 ± 0.6	17.2 ± 0.3
Cr_2O_3	b.d.	b.d.	b.d.	b.d.	b.d.	b.d.
FeO	0.48 ± 0.01	0.46 ± 0.01	0.26 ± 0.01	1.71 ± 0.01	1.24 ± 0.01	1.21 ± 0.01
MnO	b.d.	0.02 ± 0.01	b.d.	0.02 ± 0.01	0.02 ± 0.01	0.03 ± 0.01
MgO	b.d.	<0.01	<0.01	<0.01	b.d.	0.13 ± 0.01
CaO	0.26 ± 0.01	0.32 ± 0.01	0.30 ± 0.01	6.80 ± 0.10	0.99 ± 0.01	1.32 ± 0.01
K_2O	0.06 ± 0.01	0.03 ± 0.01	<0.01	7.31 ± 0.19	7.66 ± 0.09	9.78 ± 0.18
Na_2O	0.10 ± 0.01	0.15 ± 0.01	0.13 ± 0.01	0.64 ± 0.01	0.26 ± 0.01	0.37 ± 0.01
P_2O_5	<0.01	b.d.	<0.01	0.07 ± 0.01	0.13 ± 0.01	0.22 ± 0.01
BaO	0.03 ± 0.01	n.m.	n.m.	2.84 ± 0.09	6.24 ± 0.13	8.51 ± 0.15
Total	98.8	98.2	98.7	99.7	102.4	99.9

	110411_32 ,308_6A_p27 K-Feldspar	17112010_32 ,308_2A_p7 High-K glass	17112010_38 ,308_3A_p1 High-K glass	13042011_104 ,308_4A_p11 High-K glass	13042011_195 ,308_8A_p2 High-K glass	13042011_67 ,308_9A_p2 High-K glass
SiO_2	58.0 ± 0.5	79.1 ± 0.4	70.3 ± 0.4	74.7 ± 0.4	78.7 ± 0.4	76.0 ± 0.5
TiO_2	0.36 ± 0.01	0.51 ± 0.01	0.55 ± 0.01	0.72 ± 0.01	0.88 ± 0.02	0.27 ± 0.01
Al_2O_3	14.4 ± 0.4	9.15 ± 0.23	14.3 ± 0.4	11.5 ± 0.2	9.42 ± 0.24	11.6 ± 0.4
Cr_2O_3	0.11 ± 0.01	0.01 ± 0.01	0.02 ± 0.01	<0.01	<0.01	<0.01
FeO	3.79 ± 0.03	3.03 ± 0.03	1.39 ± 0.01	2.07 ± 0.01	4.46 ± 0.03	0.35 ± 0.01
MnO	0.07 ± 0.01	0.04 ± 0.01	0.02 ± 0.01	<0.01	<0.01	b.d.
MgO	4.64 ± 0.09	<0.01	0.18 ± 0.01	0.03 ± 0.01	<0.01	<0.01
CaO	12.0 ± 0.1	1.04 ± 0.01	2.63 ± 0.02	1.41 ± 0.01	0.95 ± 0.01	0.49 ± 0.01
K_2O	7.13 ± 0.23	6.83 ± 0.06	7.08 ± 0.06	5.98 ± 0.04	4.90 ± 0.06	8.53 ± 0.44
Na_2O	1.17 ± 0.03	0.17 ± 0.01	1.29 ± 0.03	0.58 ± 0.01	0.22 ± 0.01	0.87 ± 0.22
P_2O_5	0.02 ± 0.01	0.11 ± 0.01	0.15 ± 0.01	0.30 ± 0.02	0.15 ± 0.01	0.02 ± 0.01
BaO	0.39 ± 0.06	± 0.01	± 0.01	1.06 ± 0.07	0.38 ± 0.06	1.64 ± 0.08
Total	102.0	100.0	97.9	98.3	100.0	99.8

Values which were below instrument detection limits (b.d.) have been indicated.

Table 6.10: Major and minor element abundances for representative phosphate mineral grains within several of the 12003,308 A-splits measured by EMP WDS. Abundances are reported as oxide wt% values. Errors are 1σ standard deviations calculated from repeat measurements of the BCR-2 USGS basaltic glass reference material. n.b. F values have not been corrected for electron beam damage.

	131110_13 ,308_1A_p4 Apatite	131110_4 ,308_2A_p1 Apatite	131110_18 ,308_5A_p2 Merrillite	131110_24 ,308_6A_p3 Merrillite	131110_22 ,308_7A_p3 Merrillite
CaO	52.7 ± 0.1	52.6 ± 0.1	46.0 ± 0.1	43.5 ± 0.1	45.7 ± 0.1
P_2O_5	41.8 ± 0.2	39.1 ± 0.2	45.4 ± 0.2	45.4 ± 0.2	45.4 ± 0.2
FeO	2.15 ± 0.03	1.91 ± 0.03	1.88 ± 0.03	0.89 ± 0.02	1.51 ± 0.03
MgO	<0.01	b.d.	3.46 ± 0.03	3.17 ± 0.03	3.24 ± 0.03
Na_2O	b.d.	b.d.	1.23 ± 0.04	0.62 ± 0.03	1.05 ± 0.03
K_2O	0.02 ± 0.01	0.15 ± 0.01	0.06 ± 0.01	0.05 ± 0.01	0.22 ± 0.01
SiO_2	0.54 ± 0.02	1.66 ± 0.03	0.50 ± 0.02	0.18 ± 0.01	0.57 ± 0.02
TiO_2	0.52 ± 0.03	b.d.	0.08 ± 0.02	b.d.	b.d.
Al_2O_3	0.11 ± 0.02	0.20 ± 0.02	0.06 ± 0.02	b.d.	0.13 ± 0.02
Y_2O_3	0.25 ± 0.03	0.86 ± 0.04	0.48 ± 0.03	1.67 ± 0.05	0.19 ± 0.02
La_2O_3	b.d.	0.08 ± 0.03	0.29 ± 0.04	0.74 ± 0.05	0.49 ± 0.04
Ce_2O_3	0.13 ± 0.03	0.32 ± 0.03	0.77 ± 0.04	2.10 ± 0.06	1.19 ± 0.05
Nd_2O_3	0.11 ± 0.03	0.27 ± 0.03	0.44 ± 0.04	1.12 ± 0.04	0.53 ± 0.04
Cl	0.07 ± 0.01	0.14 ± 0.01	<0.01	<0.01	b.d.
F	2.76 ± 0.09	2.31 ± 0.08	0.47 ± 0.04	0.40 ± 0.04	0.45 ± 0.04
Total	101.1	99.6	101.1	99.8	100.7

Values which were below instrument detection limits (b.d.) have been indicated.

Table 6.11: Major and minor element abundances for representative metal and sulfide grains within 12003,308_1-10A measured by EMP WDS. Abundances are reported as element wt% values. Errors reported are 1σ standard deviations calculated from repeat measurements of the BCR-2 USGS basaltic glass reference material.

	12110_12 ,308_2A_p2 FeNi metal	121110_38 ,308_4A_p7 FeNi metal	121110_41 ,308_5A_p3 FeNi metal	121110_52 ,308_6A_p4 FeNi metal	281011_70 ,308_9A_p2 FeNi metal	190411_15 ,308_10A_p3 FeNi metal
Si	0.13 ± 0.01	0.05 ± 0.01	0.07 ± 0.01	0.06 ± 0.01	0.32 ± 0.01	0.09 ± 0.01
Ti	0.03 ± 0.01	0.07 ± 0.01	0.21 ± 0.01	0.03 ± 0.01	0.14 ± 0.01	0.05 ± 0.01
Cr	0.05 ± 0.01	b.d.	0.04 ± 0.01	0.03 ± 0.01	0.08 ± 0.01	0.02 ± 0.01
Fe	93.3 ± 0.1	93.9 ± 0.2	88.2 ± 0.2	92.1 ± 0.1	95.4 ± 0.2	97.7 ± 0.2
Cu	0.05 ± 0.02	b.d.	0.05 ± 0.02	b.d.	0.09 ± 0.02	0.04 ± 0.02
Mn	b.d.	0.02 ± 0.01	b.d.	b.d.	0.03 ± 0.01	b.d.
Mg	b.d.	<0.01	0.02 ± 0.01	0.02 ± 0.01	0.15 ± 0.01	b.d.
Ni	4.57 ± 0.03	2.40 ± 0.02	8.40 ± 0.04	5.46 ± 0.03	2.60 ± 0.02	0.15 ± 0.01
Co	1.34 ± 0.02	1.51 ± 0.02	2.15 ± 0.03	0.81 ± 0.02	1.13 ± 0.01	1.15 ± 0.01
S	b.d.	0.09 ± 0.01	<0.01	<0.01	0.02 ± 0.00	b.d.
Total	99.5	98.0	99.2	98.5	100.0	99.2

	121110_10 ,308_1A_p10 Troilite	121110_20 ,308_2A_p10 Troilite	121110_24 ,308_3A_p4 Troilite	121110_32 ,308_4A_p1 Troilite	121110_46 ,308_5A_p8 Troilite
Si	0.09 ± 0.01	0.11 ± 0.01	0.04 ± 0.01	0.07 ± 0.01	0.07 ± 0.01
Ti	0.26 ± 0.02	<0.01	b.d.	0.50 ± 0.02	0.43 ± 0.02
Cr	<0.01	<0.01	0.03 ± 0.01	0.06 ± 0.01	0.65 ± 0.02
Fe	60.7 ± 0.1	61.5 ± 0.1	60.7 ± 0.1	61.5 ± 0.1	61.7 ± 0.1
Cu	b.d.	0.08 ± 0.02	b.d.	b.d.	b.d.
Mg	0.02 ± 0.01	b.d.	b.d.	<0.01	0.02 ± 0.01
Ni	b.d.	b.d.	b.d.	b.d.	b.d.
S	37.9 ± 0.1	38.4 ± 0.1	37.8 ± 0.1	38.1 ± 0.1	38.6 ± 0.1
Total	99.0	100.1	98.6	100.2	101.5

	121110_49 ,308_6A_p1 Troilite	121110_59 ,308_8A_p5 Troilite	190411_3 ,308_9A_p3 Troilite	190411_19 ,308_10A_p7 Troilite
Si	0.41 ± 0.01	0.40 ± 0.01	0.07 ± 0.01	0.08 ± 0.01
Ti	b.d.	0.06 ± 0.01	0.04 ± 0.01	0.06 ± 0.01
Cr	0.05 ± 0.01	0.03 ± 0.01	b.d.	<0.01
Fe	60.4 ± 0.1	60.2 ± 0.1	62.3 ± 0.1	61.9 ± 0.1
Cu	b.d.	b.d.	0.03 ± 0.02	b.d.
Mg	0.02 ± 0.01	0.11 ± 0.01	b.d.	b.d.
Ni	0.05 ± 0.01	b.d.	b.d.	b.d.
S	36.6 ± 0.1	37.9 ± 0.1	37.7 ± 0.1	38.5 ± 0.1
Total	97.6	98.6	100.1	100.4

Values which were below instrument detection limits (b.d.) have been indicated.

Chapter 7

12003 Chips

7.1 Introduction

In addition to the ten 12003,308 samples (discussed in Chapter 6) six further samples were selected for study from the 12003 soil. These six samples, comprising of a total of ten individual ∼2-4 mm chips with a combined mass of 0.68 g, were allocated the identifiers 12003,310;,311;,312;,314;,316;,317 by the Lunar Sample Laboratory at the NASA Johnson Space Center. As with the ,308 samples, each chip was then split (see Chapter 2) into two sub-sections, in order to obtain one sample to use for petrologic analysis and a second sample which could be retained for radiometric dating. This chapter will focus entirely on the petrologic examination of these samples.

7.2 Results

7.2.1 12003,310

The four samples from 12003,310 selected for petrographic analysis are ,310_1C; ,310_2D; ,310_3A; ,310_4A (∼1.5-2.5 mm). These are subophitic to porphyritic basalts composed predominantly of pyroxene (47-60% by mode) and plagioclase (21-33%; Figs. 7.1; 7.2; Table 7.1). The ,310 pyroxenes (∼0.1-0.5 mm) are zoned between more magnesian cores to the Fe-rich rims ($Wo_{8-40}En_{1-61}Fs_{18-86}$; Fig. 7.3). The pyroxenes in ,310_1C have higher abundances of HREE than LREE and CI-normalised REE patterns with negative Eu-anomalies (Fig. 7.4; $La_{cn}/Lu_{cn} = 0.1$; $Eu/Eu^* = 0.1$; where $_{cn}$ implies chondrite normalised values using the CI concentrations reported by *Anders and Grevesse* 1989 and Eu/Eu* is calculated as $Eu_{cn}/\sqrt{[Sm_{cn} \times Gd_{cn}]}$). The REE abundances in the ,310_1C pyroxenes are between 0.9-29 ×CI values, with the highest abundances located

Table 7.1: Modal mineralogies of the 10 12003 chips. The 12003,312 values marked with an asterisk were obtained from a section of the fine grained sample matrix (i.e. excluding mafic phenocrysts). Summaries of the modal mineralogies for the Apollo 12 ilmenite, pigeonite and olivine basalt suites (*Papike and Vaniman*, 1978a) and averages of the modal mineralogies reported by *Neal et al.* (1994a) are presented for comparison.

Sample	Pyx.	LCP	HCP	Oliv.	Plag.	Sil.	Ilm.	Spin.	Tr.	FeNi	Phos.	Glass/Meso.
12003,310_1C	47.1	-	-	16.8	30.6	0.8	3.6	0.7	0.1	<0.1	<0.1	0.3
12003,310_2D	48.8	-	-	26.4	20.9	0.1	1.3	2.1	<0.1	<0.1	<0.1	0.2
12003,310_3A	60.1	-	-	4.1	32.5	0.9	2.0	0.2	0.1	-	<0.1	0.2
12003,310_4A	49.4	-	-	22.4	23.3	0.5	2.2	2.0	0.1	-	<0.1	0.2
12003,311_1C	41.7	-	-	19.0	35.7	<0.1	1.7	1.7	<0.1	0.1	<0.1	0.0
12003,311_2C	43.2	-	-	17.7	38.0	<0.1	0.4	0.5	<0.1	<0.1	<0.1	0.1
12003,312_C	73.2	-	-	1.1	21.2	1.9	2.3	0.3	-	<0.1	-	-
12003,312_C*	44.7	-	-	-	49.6	1.9	3.9	-	-	-	-	-
12003,314_D	38.5	-	-	-	54.7	4.2	1.0	1.3	0.1	<0.1	0.1	0.1
12003,316_C	-	15.3	2.2	44.3	36.8	-	0.5	0.9	<0.1	<0.1	<0.1	0.1
12003,317_D	56.6	-	-	-	33.9	5.0	4.1	-	0.1	<0.1	0.1	0.2

Average modal mineralogies of Apollo 12 basaltic suites (*Papike and Vaniman*, 1978a)

	Pyx.	Oliv.	Plag.	Opaques
Ilmenite	61.1	3.6	25.9	9.3
Pigeonite	68.4	1.4	21.1	9.1
Olivine	53.5	20.2	19.2	7.1

Average of Apollo 12 modal mineralogies reported by *Neal et al.* (1994a)

	Pyx.	Oliv.	Plag.	Sil.	Ilm.	Spin.	Tr.	FeNi	Glass/Meso.
Ilmenite	54.6	9.6	24.9	0.7	4.4	2.0	0.2	0.1	4.4
Pigeonite	58.8	1.5	31.4	2.0	2.7	1.1	0.4	0.1	1.8
Olivine	43.8	24.6	20.9	0.2	1.1	2.3	0.2	0.1	6.3
Feldspathic	48.8	0.1	43.8	2.7	3.5	0.2	0.1	0.1	0.7

Pyx. = pyroxene; LCP = low-Ca pyroxene; HCP = high-Ca pyroxene; Oliv. = olivine; Plag = plagioclase; Ilm = ilmenite; Sil = silica; Spin = spinel; Tr = troilite; FeNi = FeNi metal grains; Phos = phosphates; Meso. = mesostasis. Opaques include ilmenite, spinel, troilite and FeNi metal.

Table 7.2: Major and minor element bulk chemistries of the 10 12003 chips. Normalised compositions are reported as oxide wt% values. The 12003,312 measurement marked with an asterisk was obtained from a section of the fine grained sample matrix (i.e. excluding mafic phenocrysts). Errors are 1σ standard deviations of the specified number of raster beam analyses.

	12003,310_1C	12003,310_2D	12003,310_3A	12003,310_4A	12003,311_1C	12003,311_2C
SiO_2	42.8 ± 0.1	42.7 ± 0.1	46.2 ± 0.1	42.6 ± 0.1	43.1 ± 0.1	45.1 ± 0.3
TiO_2	3.75 ± 0.04	2.16 ± 0.02	2.72 ± 0.02	2.74 ± 0.03	2.48 ± 0.04	0.98 ± 0.04
Al_2O_3	9.50 ± 0.04	7.40 ± 0.05	11.0 ± 0.1	7.58 ± 0.05	11.5 ± 0.1	12.2 ± 0.1
Cr_2O_3	0.65 ± 0.03	1.37 ± 0.03	0.50 ± 0.02	1.43 ± 0.04	0.67 ± 0.01	0.30 ± 0.02
FeO	21.1 ± 0.1	22.2 ± 0.1	18.6 ± 0.1	22.2 ± 0.1	19.3 ± 0.1	17.8 ± 0.2
MnO	0.26 ± 0.01	0.29 ± 0.03	0.28 ± 0.02	0.30 ± 0.03	0.26 ± 0.03	0.25 ± 0.03
MgO	11.6 ± 0.1	15.6 ± 0.1	8.9 ± 0.1	14.9 ± 0.1	12.8 ± 0.1	12.8 ± 0.1
CaO	8.53 ± 0.04	7.25 ± 0.03	10.8 ± 0.1	7.48 ± 0.05	9.10 ± 0.03	9.40 ± 0.04
Na_2O	1.28 ± 0.03	0.72 ± 0.03	0.65 ± 0.01	0.48 ± 0.02	0.52 ± 0.01	0.80 ± 0.01
K_2O	0.07 ± 0.01	0.05 ± 0.01	0.08 ± 0.01	0.05 ± 0.01	0.02 ± 0.01	0.05 ± 0.01
P_2O_5	0.46 ± 0.02	0.31 ± 0.01	0.31 ± 0.03	0.25 ± 0.03	0.27 ± 0.02	0.36 ± 0.02
Total	100	100	100	100	100	100
Mg#	49.4	55.6	46.0	54.5	54.3	56.1
Na+K	1.35	0.77	0.73	0.53	0.55	0.84
No. of raster beam analyses	10	10	10	10	10	10

	12003,312_C	12003,312_C*	12003,314_D	12003,316_C	12003,317_D
SiO_2	45.9 ± 0.1	44.9 ± 0.1	47.3 ± 0.2	40.5 ± 0.1	45.3 ± 0.2
TiO_2	3.43 ± 0.03	4.67 ± 0.05	1.98 ± 0.06	0.91 ± 0.02	3.91 ± 0.11
Al_2O_3	10.05 ± 0.04	13.1 ± 0.1	16.7 ± 0.1	11.7 ± 0.1	11.1 ± 0.1
Cr_2O_3	0.58 ± 0.02	0.04 ± 0.04	0.26 ± 0.03	0.60 ± 0.02	0.26 ± 0.03
FeO	20.0 ± 0.1	22.9 ± 0.1	14.6 ± 0.2	20.5 ± 0.1	19.7 ± 0.1
MnO	0.27 ± 0.02	0.28 ± 0.03	0.18 ± 0.02	0.25 ± 0.02	0.27 ± 0.03
MgO	7.79 ± 0.04	2.52 ± 0.01	4.71 ± 0.06	17.3 ± 0.1	5.51 ± 0.04
CaO	10.5 ± 0.1	10.3 ± 0.1	12.7 ± 0.1	6.73 ± 0.05	11.3 ± 0.1
Na_2O	1.08 ± 0.02	0.77 ± 0.01	1.16 ± 0.02	1.11 ± 0.02	2.06 ± 0.02
K_2O	0.07 ± 0.01	0.11 ± 0.01	0.06 ± 0.01	0.03 ± 0.01	0.08 ± 0.01
P_2O_5	0.39 ± 0.02	0.37 ± 0.02	0.43 ± 0.02	0.35 ± 0.03	0.55 ± 0.02
Total	100	100	100	100	100
Mg#	41.0	16.4	36.6	60.1	33.3
Na+K	1.15	0.88	1.22	1.14	2.15
No. of raster beam analyses	25	5	10	10	15

Mg# = atomic Mg/[Fe+Mg]×100.

near the edges of the grains (Fig. 7.4; Table 7.4).

Elongate crystals (∼500×80 μm) of plagioclase are common throughout the ,310 samples (An_{87-93}; Fig. 7.5; Table 7.5). Many of these have intrafasciculate textures. The plagioclase and pyroxene phases occasionally form radiating intergrowths, which are most apparent in ,310_3A (Fig. 7.2). The ,310_1C plagioclase grains have a similar range of REE abundances as the pyroxenes (0.7-33 ×CI abundances; Fig. 7.6).

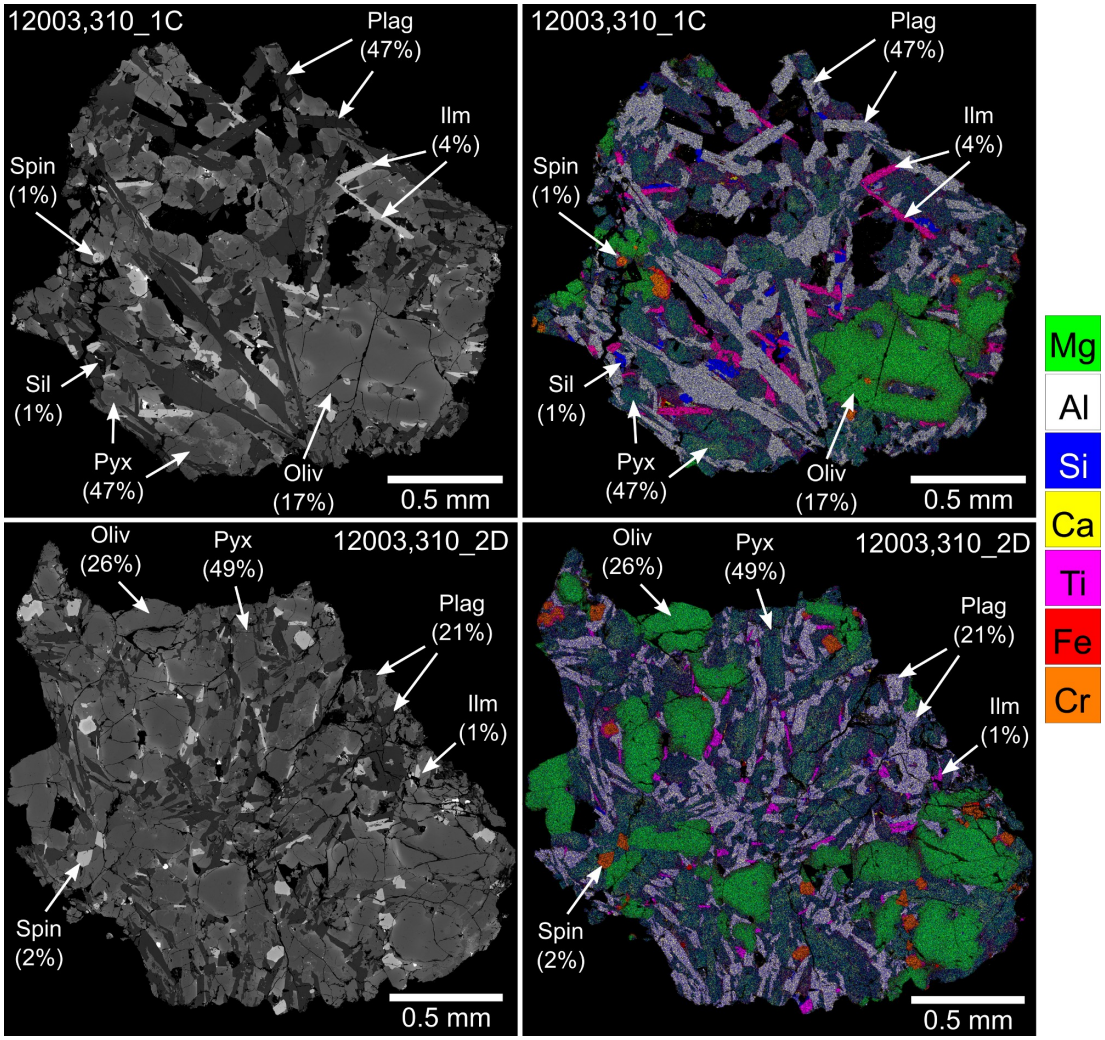

Figure 7.1: Backscattered electron (BSE) images and false colour element maps of samples 12003,310_1C and ,310_2D. The colours of the element maps represent distribution and concentration of the following elements: Si = blue, Al = white, Mg = green, Fe = red, Ca = yellow, Ti = pink and Cr = orange. Examples of the major phases within the samples have been indicated along with their modal abundances. Pyx = pyroxene; Plag = plagioclase; Oliv = olivine; Sil = silica; Ilm = ilmenite; Spin = spinel.

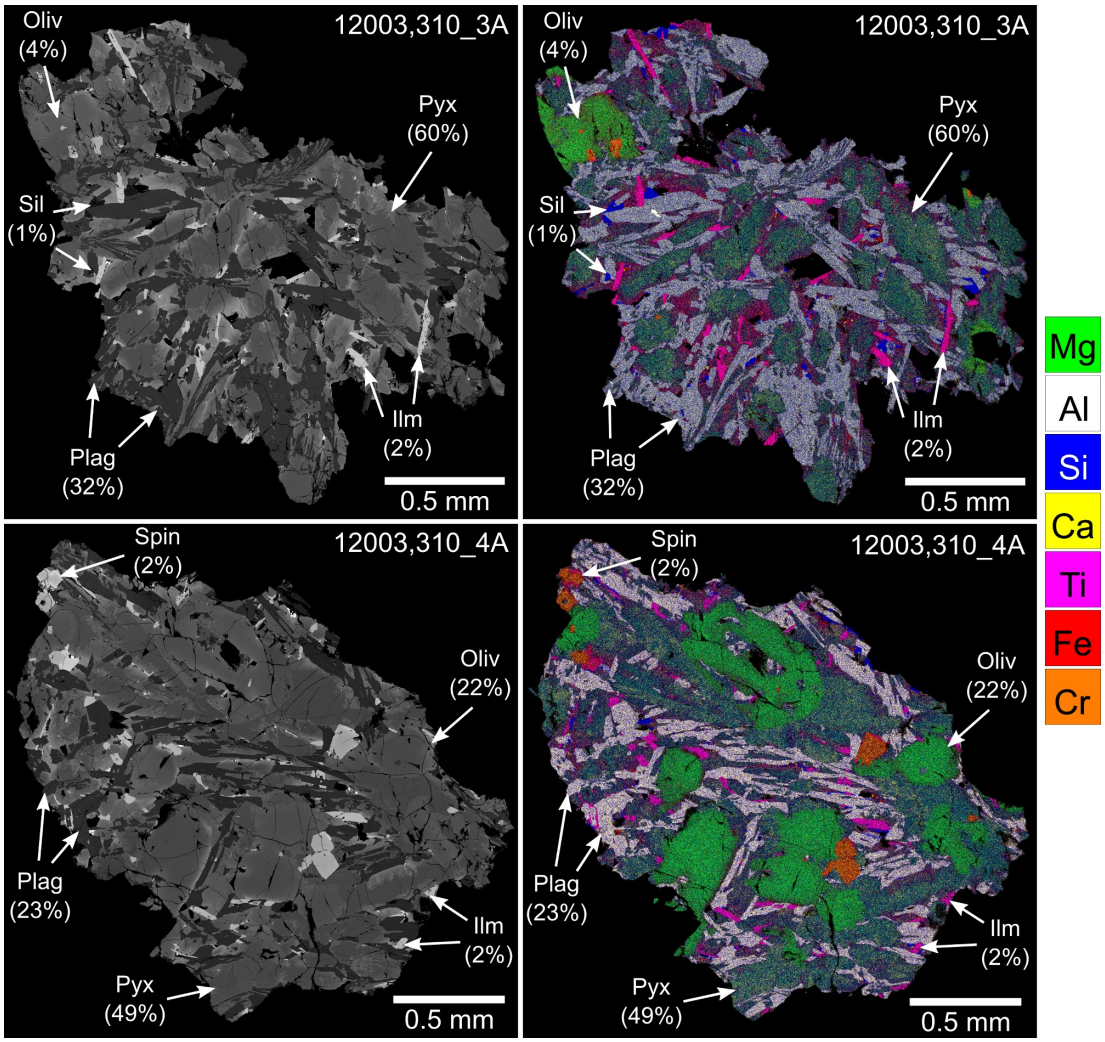

Figure 7.2: Backscattered electron (BSE) images and false colour element maps of samples 12003,310_3A and ,310_4A. The colours of the element maps represent distribution and concentration of the following elements: Si = blue, Al = white, Mg = green, Fe = red, Ca = yellow, Ti = pink and Cr = orange. Examples of the major phases within the samples have been indicated along with their modal abundances. Pyx = pyroxene; Plag = plagioclase; Oliv = olivine; Sil = silica; Ilm = ilmenite; Spin = spinel.

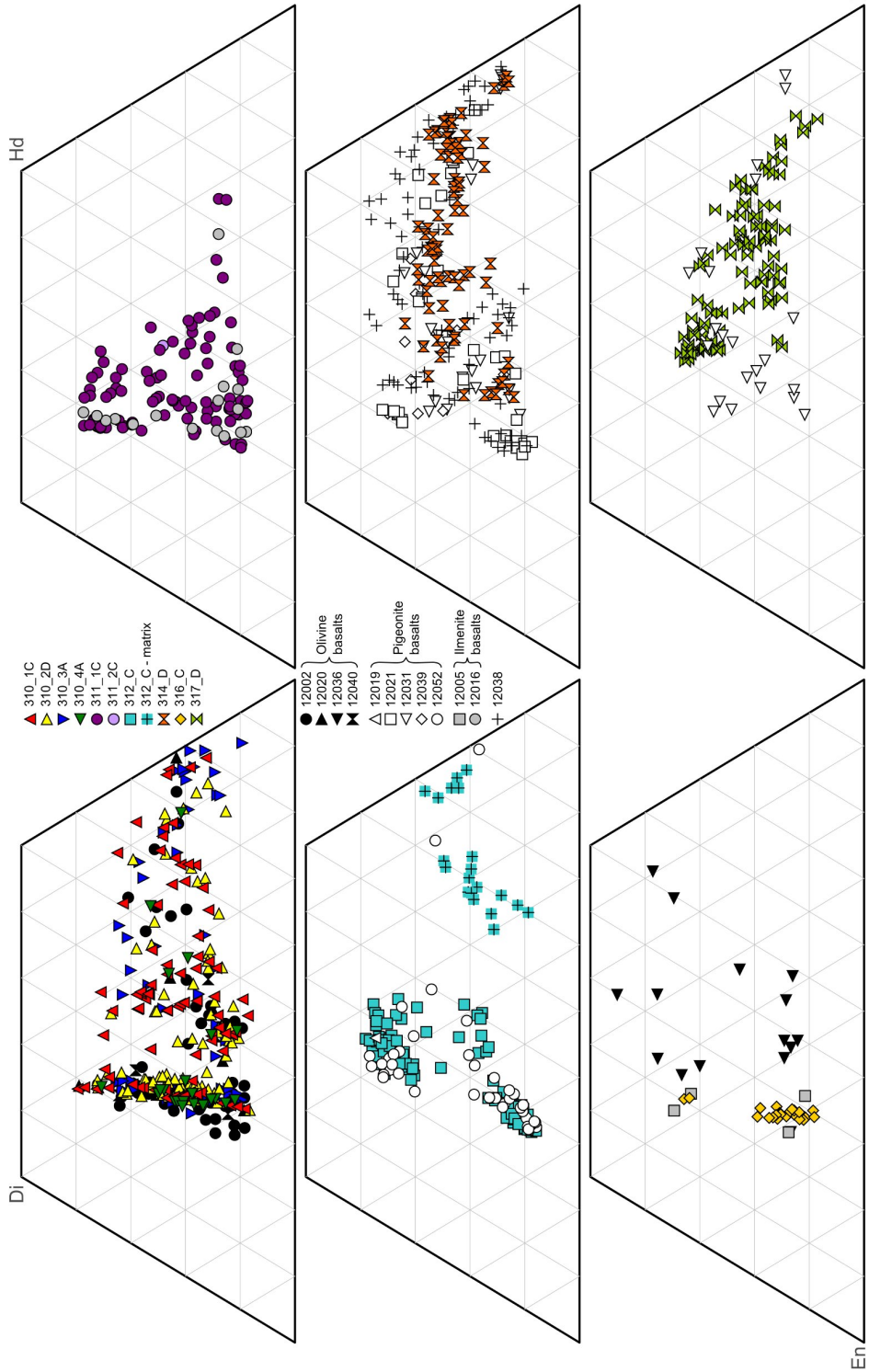

Figure 7.3: Compositions of pyroxene phases within samples 12003,310;,311;,312;,314;,316;,317. The 12003 pyroxene compositions are compared with those within other Apollo 12 samples (*Bence et al.* 1970, 1971; *Brown et al.* 1971; *Busche et al.* 1971; *Keil et al.* 1971; *Kushiro et al.* 1971; *Newton et al.* 1971; *Grove et al.* 1973; *Dungan and Brown* 1977; *Beaty et al.* 1979;*O'Sullivan, pers. comm.* 2012). Di = diopside; Hd = hedenbergite; En = enstatite; Fs = ferrosilite.

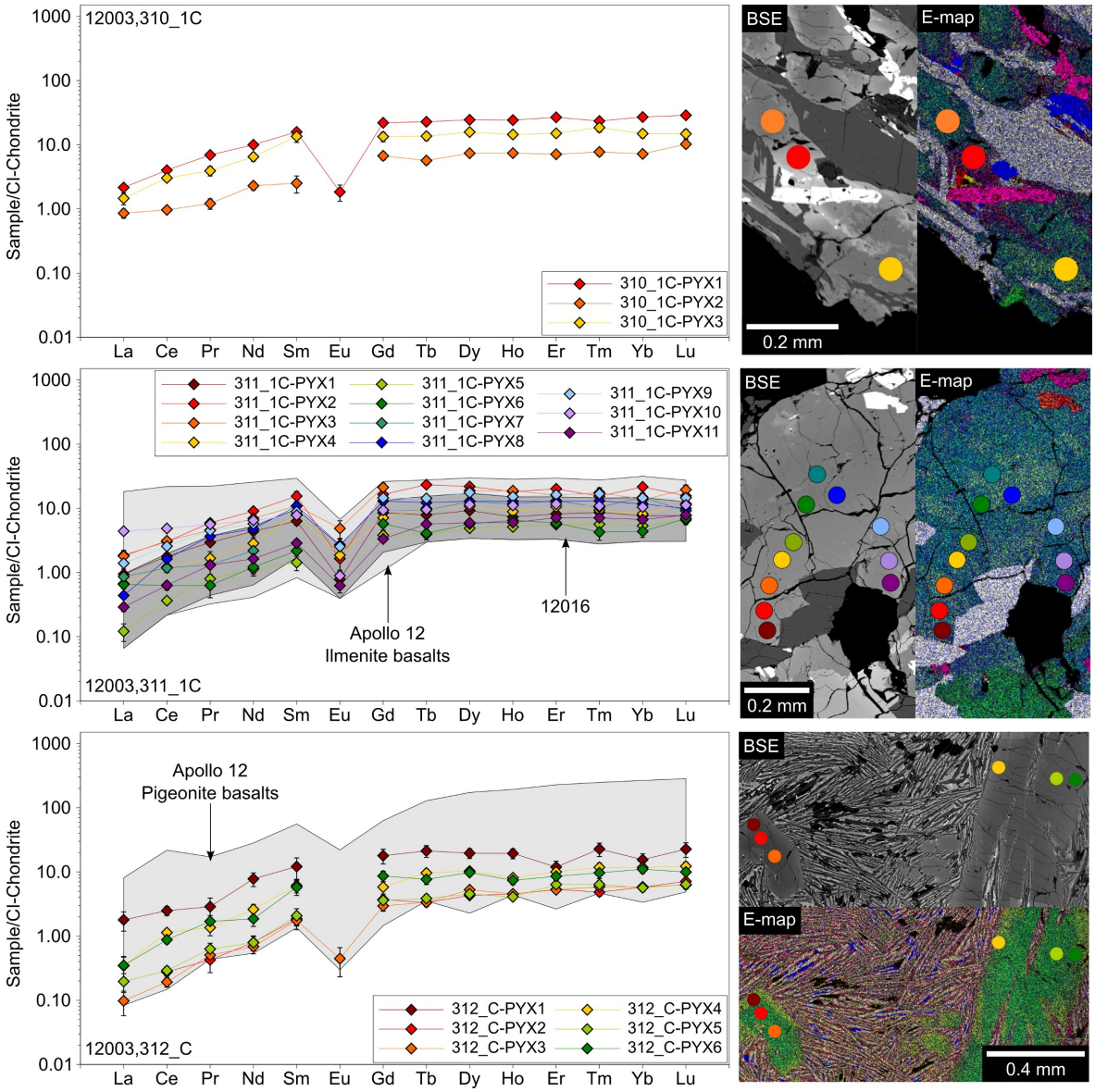

Figure 7.4: Chondrite normalised (*Anders and Grevesse*, 1989) REE patterns for pyroxenes within 12003,310_1C;,311_1C;,312_C. The locations of the analyses are indicated in the accompanying backscattered electron (BSE) and false colour element maps with colour coded symbols. Error bars represent 1σ errors. 12003 data are compared with the ranges of REE concentrations reported for pyroxenes in the ilmenite basalts 12016, 12054 and 12056, and pigeonite basalts 12021, 12039 and 12052 (*Shearer et al.* 1989; *O'Sullivan and Neal* 2010a; *O'Sullivan, pers. comm.* 2012).

All four ,310 samples contain large (~0.2-0.7 mm) phenocrysts of olivine, although, the amount of olivine in each sample varies considerably (4-26% by modal abundance; Table 7.1). The olivine phenocrysts show similar degrees of zoning in all four samples from Mg-rich cores to more Fe-rich rims (Fo_{39-73}; Figs. 7.1; 7.5; Table 7.6).

Subhedral microphenocrysts of spinel (~10-110 μm) are present in all four samples (1-2% by mode). A majority of the spinel phenocrysts are adjacent to and only partially enclosed by olivine. However, several small (~10-30 μm) grains are completely enclosed

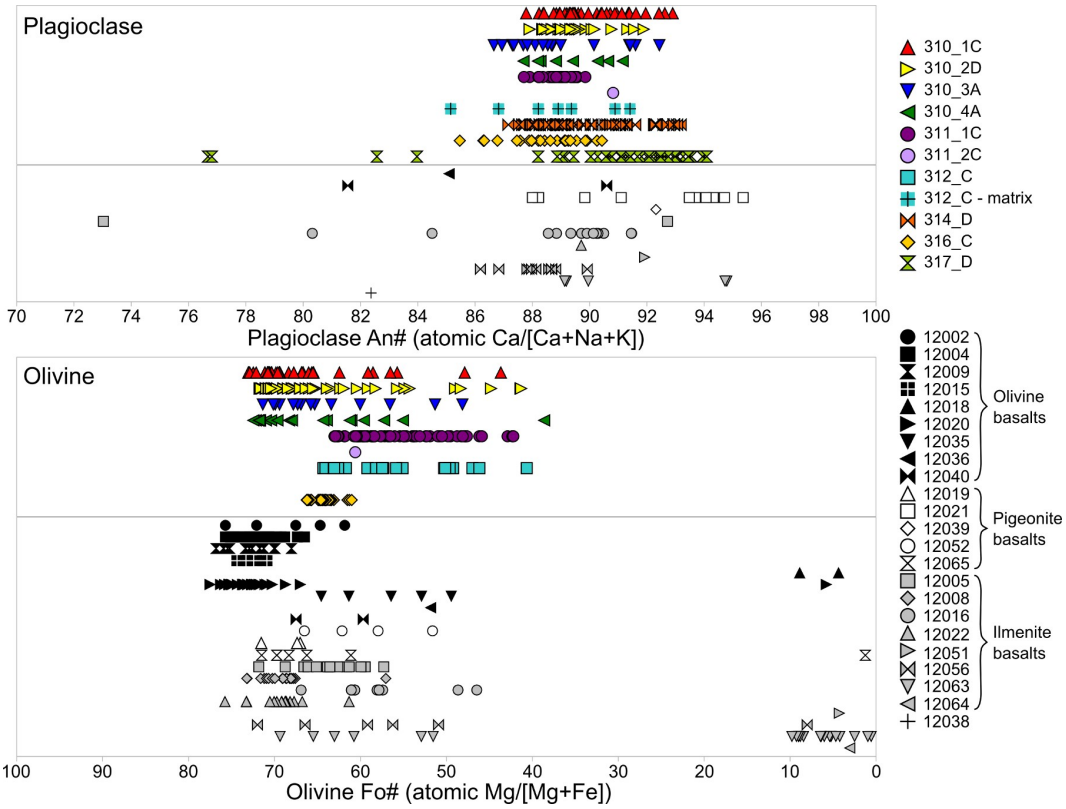

Figure 7.5: Ranges of plagioclase anorthite content (An: atomic Ca/[Ca+Na+K]×100) and olivine forsterite content (Fo: atomic Mg/[Mg+Fe]×100) within samples 12003,310;,311;,312;,314;,316;,317. The 12003 plagioclase and olivine compositions are compared with those within other Apollo 12 samples (*Bence et al.* 1970; *Anderson and Smith* 1971; *Brett et al.* 1971a; *Brown et al.* 1971; *El Goresy et al.* 1971; *Hollister et al.* 1971; *Keil et al.* 1971; *Kushiro et al.* 1971; *Newton et al.* 1971; *Taylor et al.* 1971a; *Weill et al.* 1971; *Butler* 1972; *Crawford* 1973; *Dungan and Brown* 1977; *Marvin and Walker* 1985; *O'Sullivan, pers. comm.* 2012).

within the larger olivine phenocrysts. The spinel grains are commonly grouped together to form glomerophyric clusters. The spinel crystals have mostly chromite compositions ($2Ti_{10-14}Al_{24-29}Cr_{60-66}$; Fig. 7.7; Table 7.8), however, many of the larger crystals and glomerophyric clusters have ulvöspinel rims ($2Ti_{57-86}Al_{6-13}Cr_{8-32}$; Figs. 7.1; 7.2; 7.7; Table 7.8). Where the spinel grains are adjacent to olivine, the ulvöspinel rims occur around the edges which are not in contact with olivine (typically adjacent to pyroxene; Figs. 7.1; 7.2).

The other minor phases in the ,310 samples are ilmenite (1-4%) and a silica polymorph (1%). The ilmenite forms both anhedral interstitial grains and subhedral laths which are typically associated with the Fe-rich pyroxene rims (∼10-200 μm; Fig. 7.1;7.2; Table 7.7). The ilmenite laths both cross-cut and in other instances are cross-cut by the larger plagioclase laths. The silica occurs as anhedral grains which are also associated with the more Fe-rich pyroxene rims (Table 7.9).

The four ,310 samples also contain small (<10 μm) grains of accessory minerals in

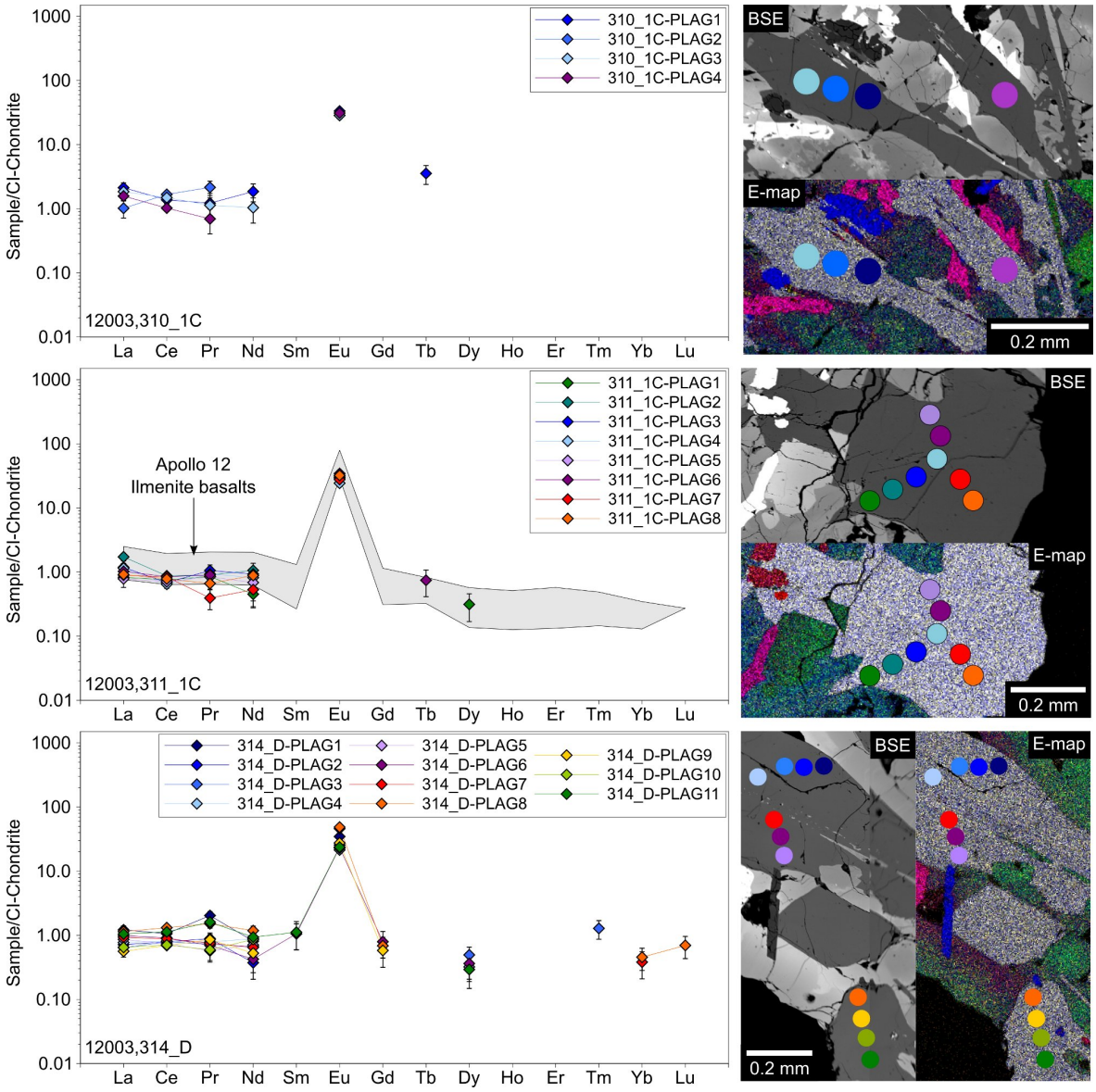

Figure 7.6: Chondrite normalised (*Anders and Grevesse*, 1989) REE patterns for plagioclases within 12003,310_1C;,311_1C;,314_D. The locations of the analyses are indicated in the accompanying backscattered electron (BSE) and false colour element maps with colour coded symbols. Error bars represent 1σ errors. Plagioclase analyses in ,311_1C have been compared with the ranges of REE concentrations reported for plagioclase in the ilmenite basalts 12016 and 12056 (*O'Sullivan, pers. comm.* 2012).

areas of mesostasis, typically associated with the most Fe-rich pyroxene compositions. These include undetermined phosphate phases, high-K glass, FeNi metal and sulfide grains (Tables 7.9; 7.10). The ,310 metal grains have variable concentrations of Ni (0.4-9.6 wt%) and Co (0.5-1.5 wt%). The sulfides in the ,310 samples have troilite compositions (S = 37 wt%; Fe = 63-64 wt%).

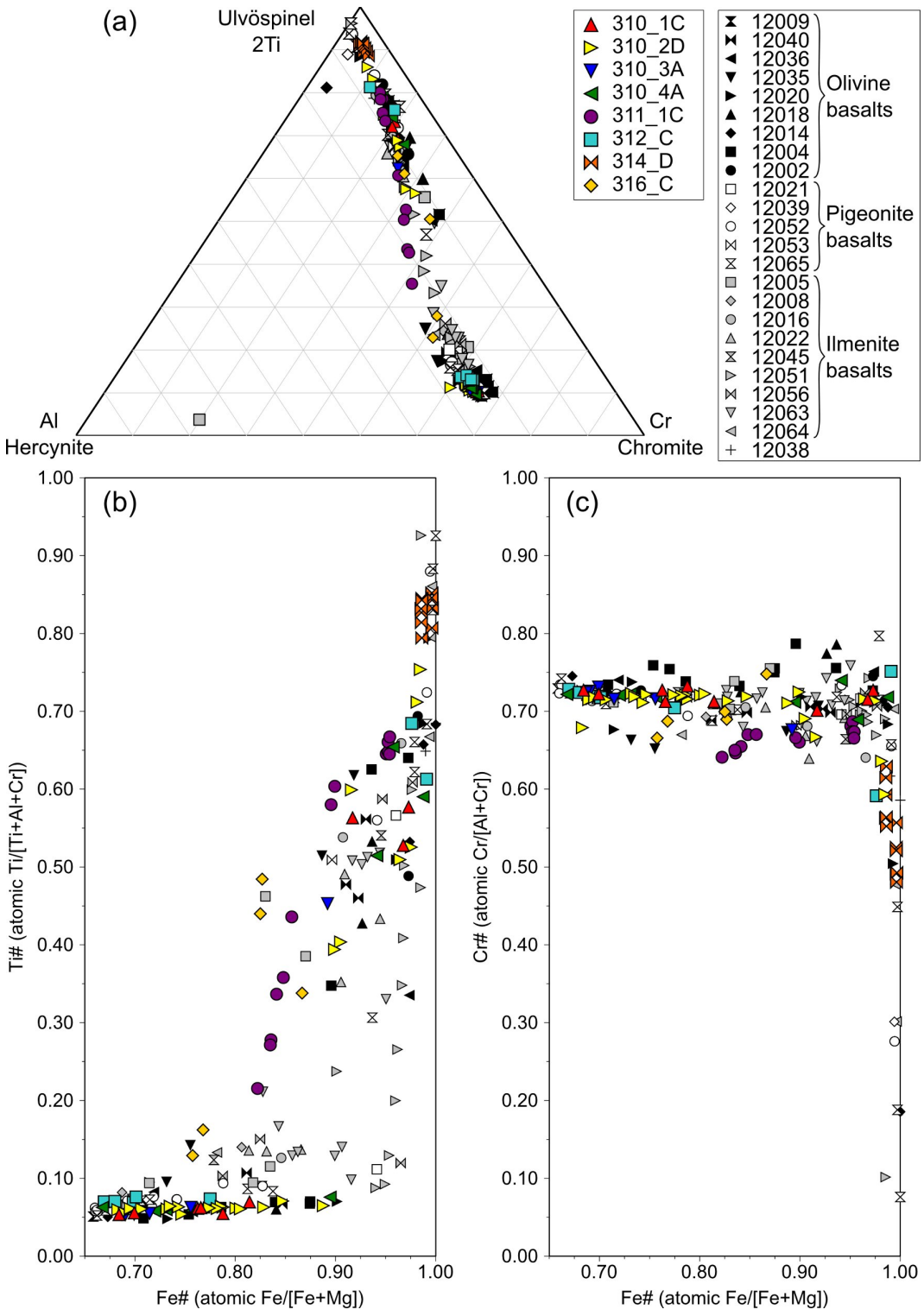

Figure 7.7: Compositions of spinel phases within the 12003 chips. (a) 2TI-Cr-Al in atomic %. (b) Ti# (atomic Ti/[Ti+Al+Cr]) vs Fe# (atomic Fe/[Fe+Mg]). (c) Cr# (atomic Cr/[Al+Cr]) vs Fe# (atomic Fe/[Fe+Mg]). 12003 spinel compositions are compared with those reported in other Apollo 12 samples (*Gibb et al.*, 1970; *Haggerty and Meyer*, 1970; *Brett et al.*, 1971a; *Brown et al.*, 1971; *Cameron*, 1971; *Champness et al.*, 1971; *El Goresy et al.*, 1971; *Keil et al.*, 1971; *Kushiro et al.*, 1971; *Reid*, 1971; *Simpson and Bowie*, 1971; *Taylor et al.*, 1971a; *Weill et al.*, 1971; *Dungan and Brown*, 1977).

7.2.2 12003,311

The two samples from the ,311 parent (,311_1C; ,311_2C) have coarse grained (∼0.2-0.6 mm) cumulate textures (Fig. 7.8). The minerals in these samples appear less compositionally fractionated than those in the ,310 samples. Pyroxene is the most abundant phase in the ,311 samples (42-43% by mode). This most commonly occurs as anhedral grains surrounding subhedral olivine (18-19%) phenocrysts and intergrown with plagioclase (36-38%). The samples also contain several anhedral-subhedral pyroxene grains which are fully enclosed in plagioclase.

The ,311 pyroxenes have a similar range of Ca abundances as those in the ,310 samples but do not have Fe-rich rims and are generally less heterogeneous ($Wo_{9-39}En_{22-62}Fs_{17-64}$; Fig. 7.3). The pyroxenes exhibit patchy zoning between the high- and low-Ca phases (Fig. 7.8). Several of the pyroxenes in also contain 1-10 μm thick lamellae (Fig. 7.9). These have two orientations, which intersect at ∼40°, and are occasionally slightly curved (Fig. 7.9c). The pyroxene grains in ,311_1C have REE abundances between 0.1-23 ×CI abundances, with higher HREE than LREE concentrations (La_{cn}/Lu_{cn} = 0.02-0.40; Eu/Eu* = 0.1-0.3; Fig. 7.4; Table 7.4). The plagioclase in the ,311 samples forms anhedral interstitial grains. These have a slightly more narrow compositional range than that of the ,310 samples (An_{88-91}; Fig. 7.5; Table 7.5). The ,311_1C plagioclases have REE abundances between 0.3-34 ×CI values (Fig. 7.6).

Subhedral spinel grains are present in both of the ,311 samples. The individual grains are largely compositionally homogeneous, however the compositions vary between the grains ($2Ti_{36-80}Al_{7-23}Cr_{13-41}$; Fig. 7.7; Table 7.8), and several of the more Ti-rich spinels include exsolved ilmenite and Fe metal. Ilmenite also occurs in both samples as independent anhedral grains (∼20-250 μm; Fig. 7.8; Table 7.7).

Accessory minerals identified in the ,311 samples include K-feldspar (Table 7.9), unidentified phosphate species, FeNi metal and sulfide grains (∼5-20 μm). These are commonly associated with the larger ilmenite grains (Fig. 7.8). The ,311_1C metal grains have less variable compositions than those in the ,310 samples (Ni = 2.8-4.7 wt%; 1.0-1.2 wt%; Table 7.10). The sulfides in the ,311_1C sample have troilite compositions (S = 38 wt%; Fe = 63-64 wt%; Table 7.10).

7.2.3 12003,312

12003,312_C has a porphyritic texture with large (up to ∼1.6 mm) mafic phenocrysts in a fine grained (∼5-80 μm) variolitic matrix (Fig. 7.8). The matrix is composed of thin plagioclase laths (∼60×5 μm; 50% by mode; An_{85-91}; Fig. 7.5; Table 7.5); interstitial

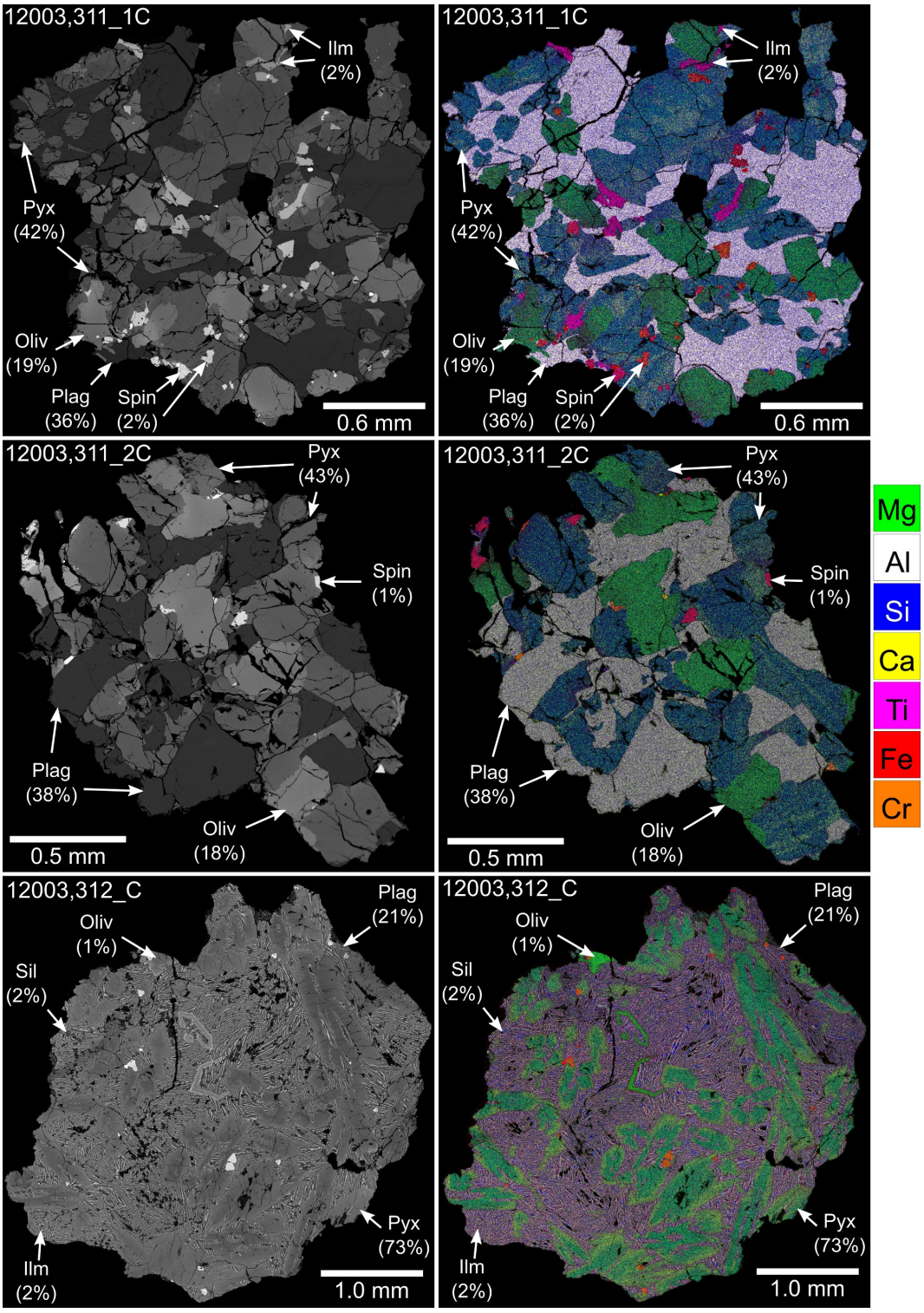

Figure 7.8: Backscattered electron (BSE) images and false colour element maps of samples 12003,311_1C; ,311_2C; and ,312_C. The colours of the element maps represent distribution and concentration of the following elements: Si = blue, Al = white, Mg = green, Fe = red, Ca = yellow, Ti = pink and Cr = orange. Examples of the major phases within the samples have been indicated along with their modal abundances. Pyx = pyroxene; Plag = plagioclase; Oliv = olivine; Sil = silica; Ilm = ilmenite; Spin = spinel.

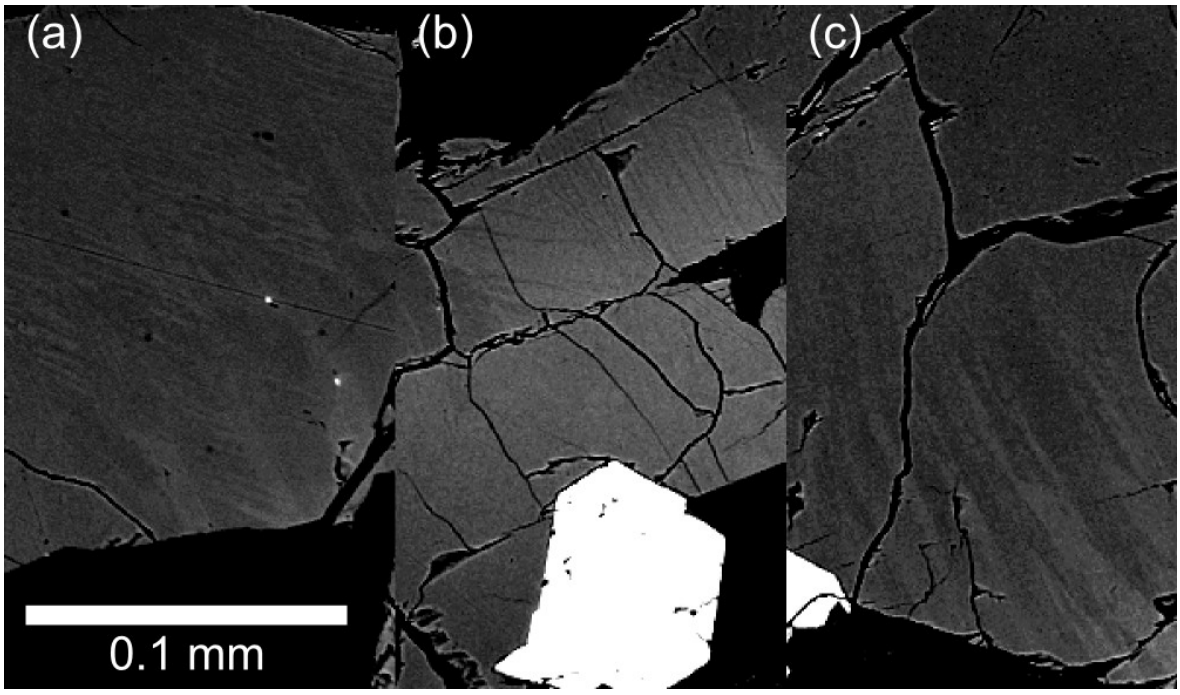

Figure 7.9: BSE (contrast and brightness enhanced) images of lamellae in 12003,311_1C.

pyroxene grains (∼50×10 μm; 45% by mode; $Wo_{9-28}En_{3-30}Fs_{55-76}$); small ilmenite needles (∼15×2 μm; 4% by mode; Table 7.7); and occasional interstitial grains of a silica polymorph (∼10-30 μm; 2% by mode). The matrix has bulk REE abundances between 24-93 ×CI values, with slightly higher LREE than HREE and chondrite normalised REE patterns with a negative Eu-anomaly (La_{cn}/Lu_{cn} = 1.2-1.7; Eu/Eu* = 0.4-0.6).

A majority of the phenocrysts are elongated (∼0.3-1.6 mm) zoned pyroxenes. These have significantly more magnesian compositions ($Wo_{8-39}En_{30-64}Fs_{23-41}$) than those in the ,312_C matrix (Fig. 7.3). The phenocrysts also have a wider range of Ti# (atomic Ti/[Cr+Ti]) and higher concentrations of Al than the matrix pyroxenes (Figs. 7.10; 7.11). REE abundances in the pyroxene phenocrysts are between 0.1-23 ×CI abundances, with the highest abundances in the phenocryst rims (Fig. 7.4; Table 7.4). They have significantly higher HREE than LREE, and chondrite normalised REE patterns with negative Eu-anomalies (La_{cn}/Lu_{cn} = 0.02-0.08; Eu/Eu* = 0.2; Fig. 7.4). The sample also contains several olivine phenocrysts, including two skeletal olivine grains (∼0.2-0.5 mm; Fig. 7.8). These exhibit prominent compositional zoning (Fo_{41-64}; Fig. 7.8;7.5).

Subhedral to euhedral spinel crystals (30-90 μm) are also present throughout the sample. These occur as isolated grains in the fine grained matrix as well as adjacent to and partially enclosed in the larger pyroxene and olivine phenocrysts. The spinel grains have distinct chromite cores and ulvöspinel rims ($2Ti_{13-81}Al_{6-26}Cr_{11-63}$; Fig. 7.7;

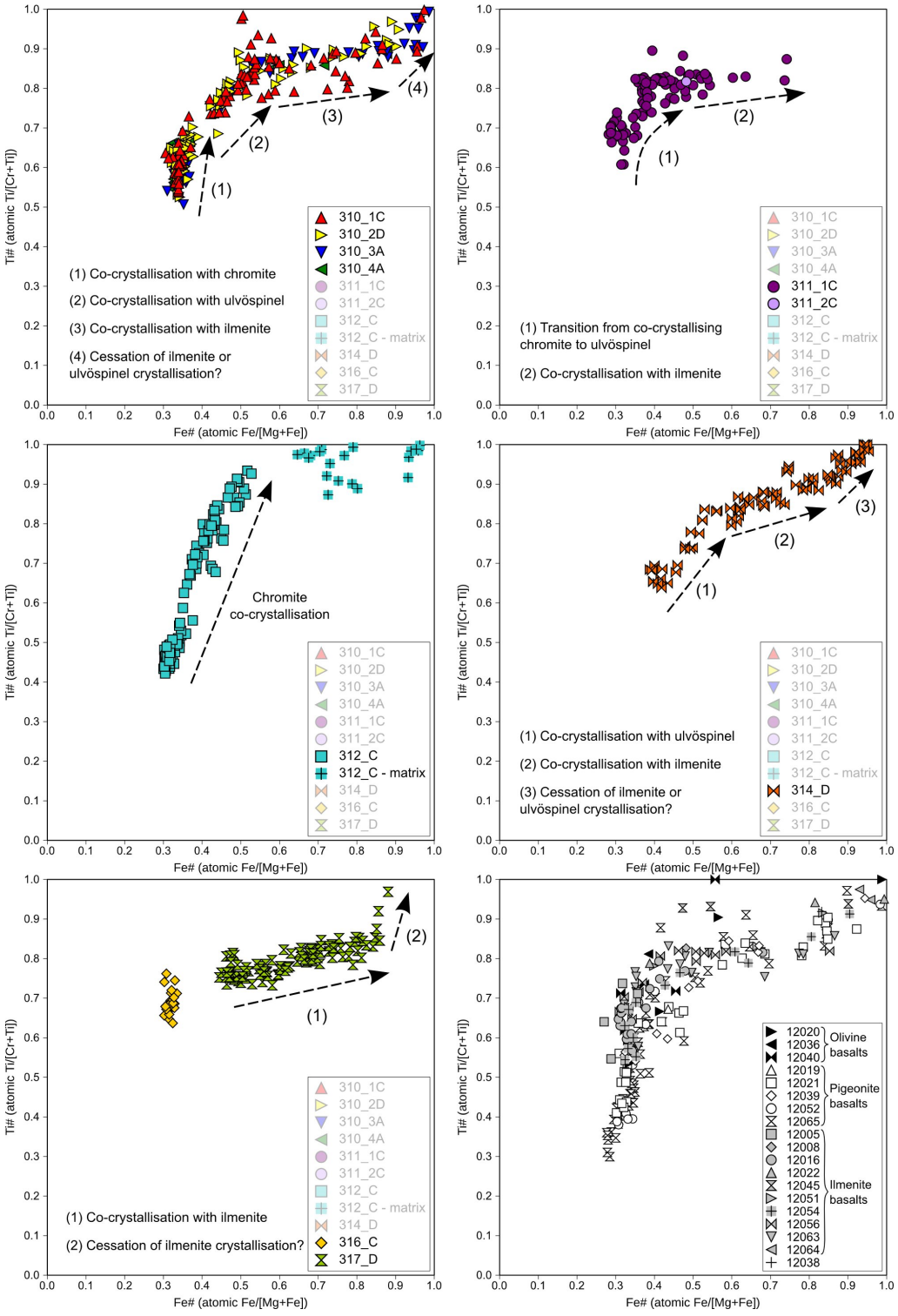

Figure 7.10: Ti# (atomic Ti/[Ti+Cr]) vs Fe# (atomic Fe/[Mg+Fe]) for pyroxene phases within 12003,310;,311;,312;,314;,316;,317. Compositions are compared with those reported for pyroxenes in other Apollo 12 samples (*Bence et al.*, 1970; *Anderson and Smith*, 1971; *Boyd and Smith*, 1971; *Brown et al.*, 1971; *Dence et al.*, 1971; *Hollister et al.*, 1971; *Keil et al.*, 1971; *Kushiro et al.*, 1971; *Newton et al.*, 1971; *Weill et al.*, 1971).

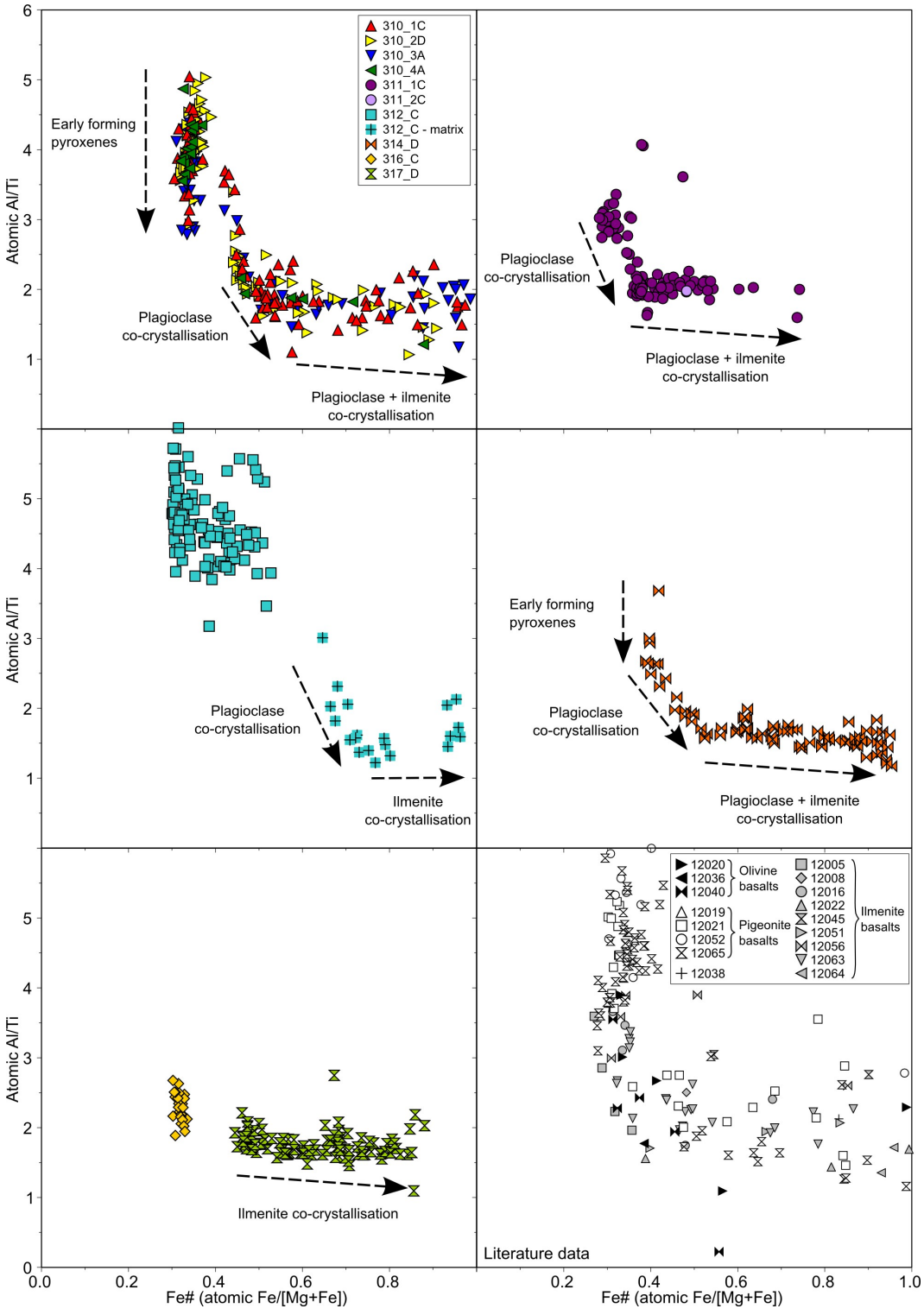

Figure 7.11: Atomic Al/Ti vs Fe# (atomic Fe/[Mg+Fe]) for pyroxene phases within 12003,310;,311;,312;,314;,316;,317. Compositions are compared with those reported for pyroxenes in other Apollo 12 samples (*Bence et al.*, 1970; *Anderson and Smith*, 1971; *Boyd and Smith*, 1971; *Brown et al.*, 1971; *Dence et al.*, 1971; *Hollister et al.*, 1971; *Keil et al.*, 1971; *Kushiro et al.*, 1971; *Newton et al.*, 1971; *Weill et al.*, 1971).

Table 7.8). The sample contains a single glomerophyric spinel cluster which appears to be associated with a small (30 μm) grain of FeNi metal. Several other smaller (10-20 μm) independent FeNi metal grains are present in the ,312_C matrix. These have Ni concentrations of 3.7-4.1 wt% and Co concentrations of 1.4 wt% (Table 7.10).

7.2.4 12003,314

12003,314_D is a coarse grained (0.2-1.1 mm) subophitic sample composed mostly of plagioclase (55% by mode) and pyroxene (39%) which form graphic intergrowths (Fig. 7.12). The plagioclase in ,314_D forms large (∼0.1-1.3 mm) elongated crystals (An_{87-93}; Fig. 7.5; Table 7.5). These have REE abundances between 0.3-49 ×CI values and nearly flat chondrite normalised REE patterns with positive Eu-anomalies (La_{cn}/Lu_{cn} = 2; Eu/Eu* = 26; Fig. 7.6).

The pyroxenes in ,314_D exhibit prominent zoning from more magnesian to more Fe-rich compositions ($Wo_{12-32}En_{4-53}Fs_{30-83}$; Fig. 7.3; Table 7.4). The core to rim relationship of this zoning is difficult to infer due to the plagioclase intergrowths. The pyroxenes have REE abundances between 0.3-111 ×CI values and chondrite normalised REE patterns with higher HREE than LREE and negative Eu-anomalies (La_{cn}/Lu_{cn} = 0.03-0.53; Eu/Eu* = 0.1-0.4; Fig. 7.13). The REE abundances of the ,314_D pyroxenes increase significantly in the more Fe-rich areas and the chondrite normalised REE patterns become slightly flatter (Fig. 7.13).

The minor phases in ,314_D include silica, spinel and ilmenite (Fig. 7.12; Table 7.1). These form intergrowths with plagioclase and pyroxene on a smaller scale (<50 μm) than that of the two major phases. Large (0.1-0.6 mm) crystals of a silica polymorph are common throughout the sample (4% by modal abundance). These are often fractured and embayed. Spinel is the next most abundant phase in ,314_D (1%) and forms subhedral ulvöspinel crystals (∼0.1-0.3 mm; $2Ti_{89-92}Al_{4-5}Cr_{4-7}$; Fig. 7.7; Table 7.8). The largest of these also contains small (∼10-30 μm) exsolved grains of ilmenite. Ilmenite is also present (1% by modal abundance) as separate subhedral crystals (∼0.03-0.30 mm; Fig. 7.12; Table 7.7).

12003,314_D contains several regions of mesostasis containing pyroxferroite, K-feldspar, high-K glass (Table 7.9), phosphate, sulfide and Fe metal grains. The ,314_D sulfides have troilite compositions (S = 38 wt%; Fe = 64 wt%; Table 7.10). The Fe metal in ,314_D occurs as small (∼5 μm) exsolved grains in the troilite phases. These have very low concentrations of Ni (<0.1 wt%; Table 7.10).

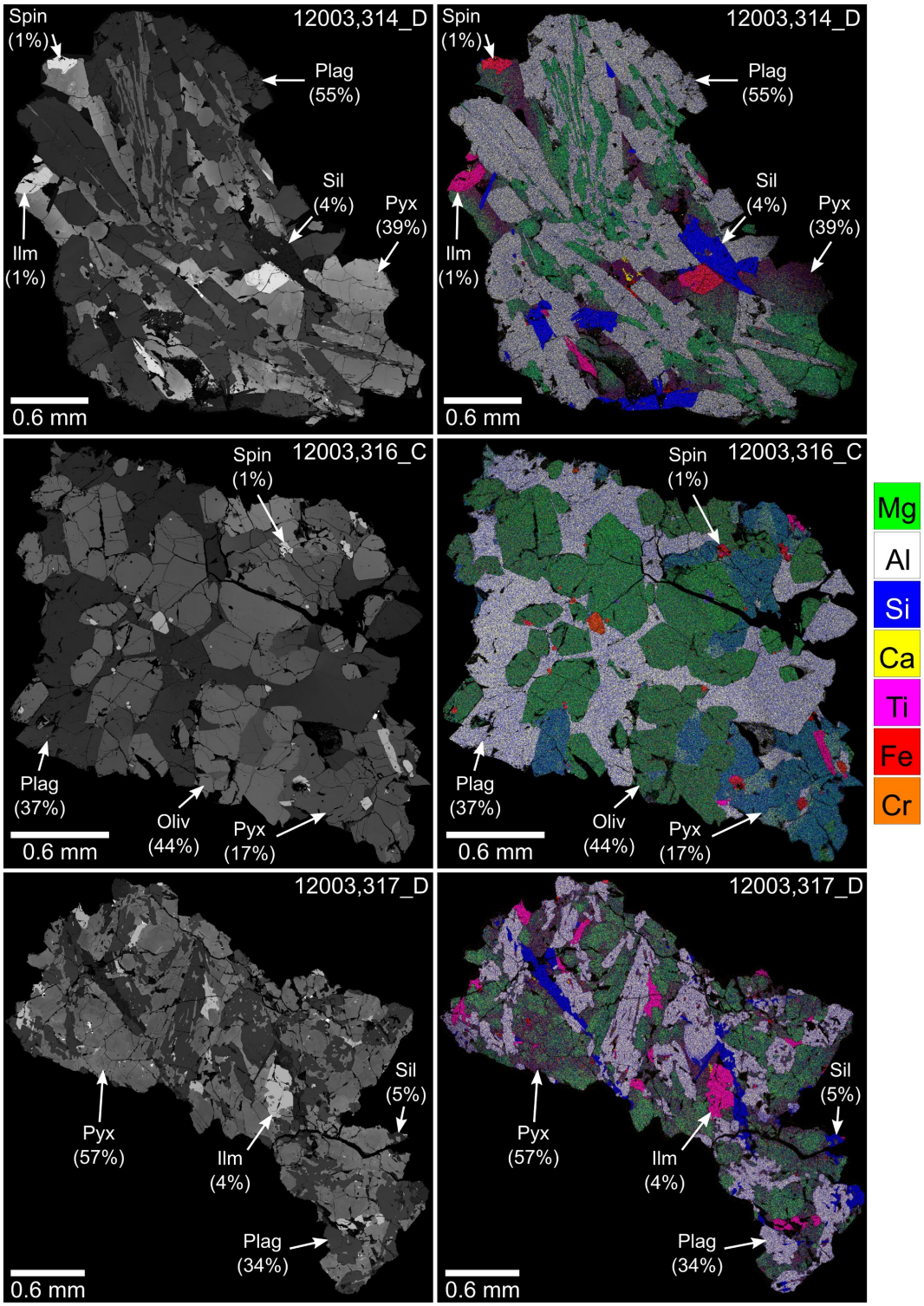

Figure 7.12: Backscattered electron (BSE) images and false colour element maps of samples 12003,314_D; ,316_C; and ,317_D. The colours of the element maps represent distribution and concentration of the following elements: Si = blue, Al = white, Mg = green, Fe = red, Ca = yellow, Ti = pink and Cr = orange. Examples of the major phases within the samples have been indicated along with their modal abundances. Pyx = pyroxene; Plag = plagioclase; Oliv = olivine; Sil = silica; Ilm = ilmenite; Spin = spinel.

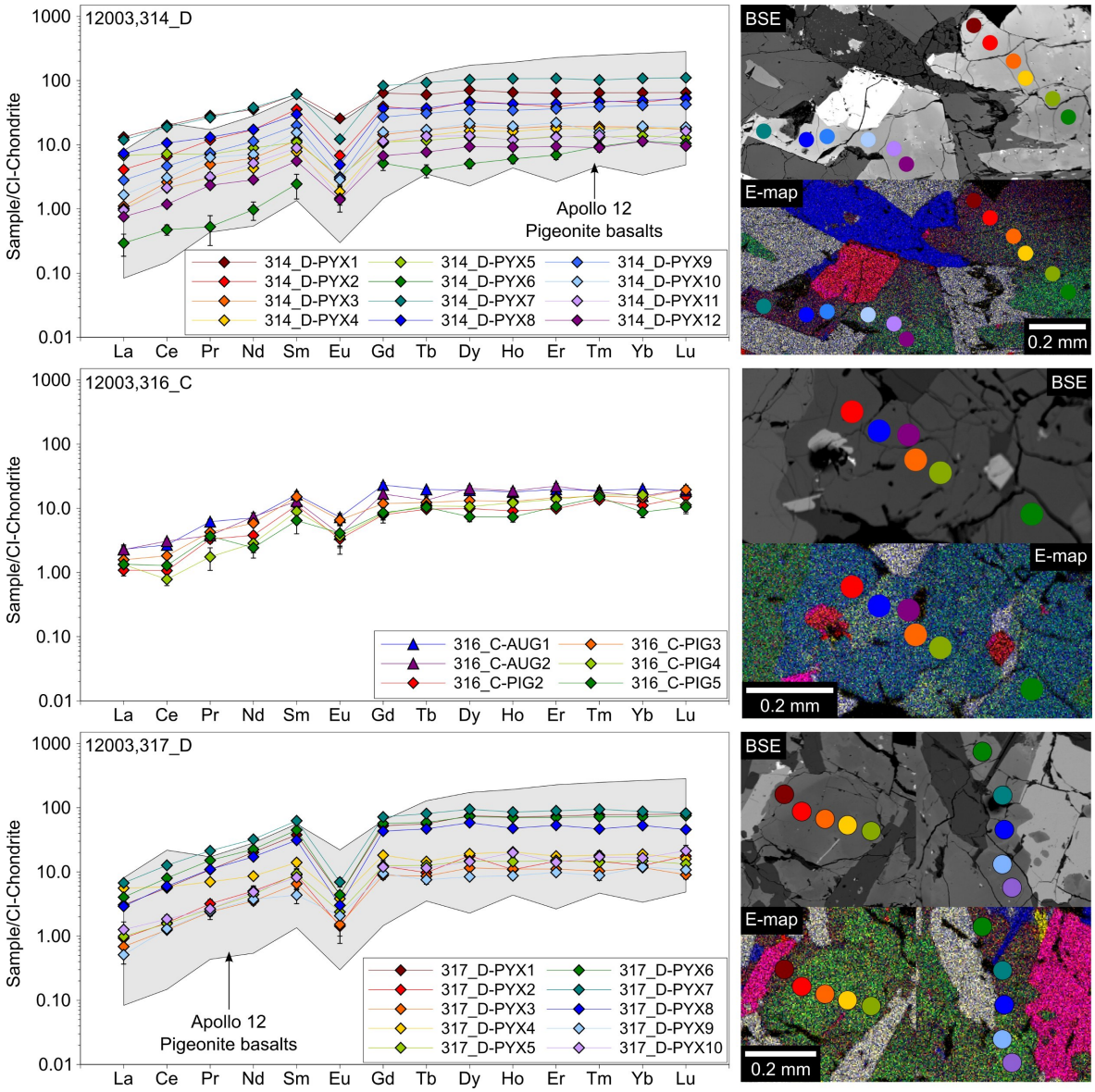

Figure 7.13: Chondrite normalised (*Anders and Grevesse*, 1989) REE patterns for pyroxenes within 12003,314_D;,316_C;,317_D. The locations of the analyses are indicated in the accompanying backscattered electron (BSE) and false colour element maps with colour coded symbols. Error bars represent 1σ errors. 12003 data are compared with the ranges of REE concentrations reported for pyroxenes in the pigeonite basalts 12021, 12039 and 12052 (*Shearer et al.* 1989; *O'Sullivan and Neal* 2010a; *O'Sullivan, pers. comm.* 2012).

7.2.5 12003,316

12003,316_C is a coarse grained (~0.1-0.8 mm) sample with a cumulate texture dominated by subhedral to euhedral crystals of olivine (44% by modal abundance) and anhedral interstitial plagioclase (37%) and pyroxene crystals (17%; Fig. 7.12; Table 7.1). The samples is fairly equilibrated, with less compositional mineral zoning than the other 12003 samples discussed in this chapter. The ,316_C olivines are relatively compositionally homogeneous (Fo_{61-66}; Fig. 7.5). The plagioclase grains in ,316_C vary

between An_{86-90} and have REE element abundances of between 0.6-36 ×CI values with higher HREE than LREE and positive Eu-anomalies (La_{cn}/Lu_{cn} = 0.2-0.4; Eu/Eu* = 4-10; Fig. 7.14; Table 7.5).

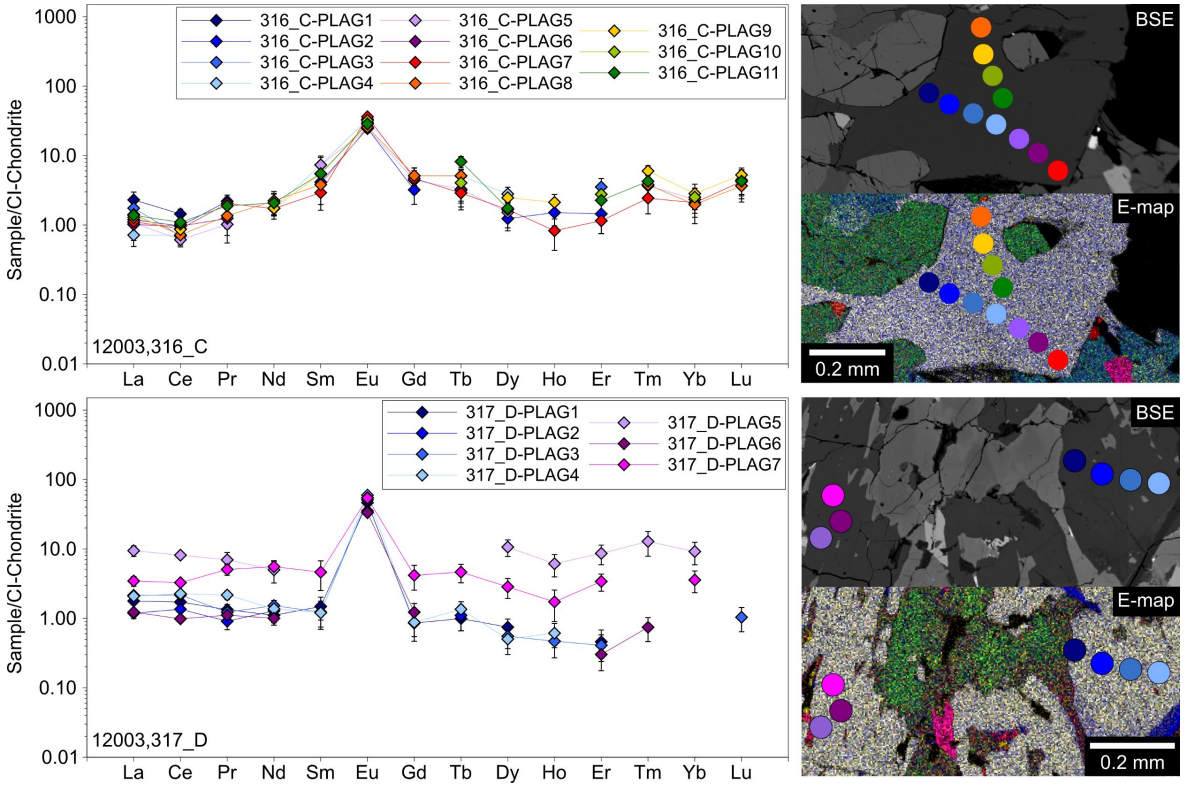

Figure 7.14: Chondrite normalised (*Anders and Grevesse*, 1989) REE patterns for plagioclases within 12003,316_C;,317_D. The locations of the analyses are indicated in the accompanying backscattered electron (BSE) and false colour element maps with colour coded symbols. Error bars represent 1σ errors.

The ,316_C pyroxenes are divided into high-Ca augite ($Wo_{32-33}En_{47}Fs_{20-21}$; Table 7.4) and low-Ca pigeonite ($Wo_{9-20}En_{55-61}Fs_{24-30}$; Table 7.4) phases. The pigeonite is significantly more abundant (15%) than the augite (2%). Despite the contrasting Ca abundances of the augite and pigeonite phases, both have REE abundances between 0.8-24 ×CI values with higher HREE than LREE and negative Eu-anomalies (La_{cn}/Lu_{cn} = 0.1-0.2; Eu/Eu* = 0.3-0.6; Fig. 7.13).

The most abundant minor phase in ,316_C is spinel (1% by mode) which forms subhedral microphenocrysts (∼20-100 μm; Fig. 7.12). As with the spinel grains in the ,311 samples, the compositions of those in ,316_C vary between different grains ($2Ti_{23-65}Al_{11-26}Cr_{24-51}$; Fig. 7.7; Table 7.8) but individual grains are largely homogeneous. The more Cr-rich spinels occur adjacent to, or enclosed near the edges of the olivine grains. The more Ti-rich phases, however, are more commonly associated with pyroxene (Fig. 7.12). There are also exsolved ilmenite grains (∼5-15 μm) within some

of the more Ti-rich spinels. The sample also contains several (0.5% by mode) separate subhedral to anhedral ilmenite grains (∼40 μm; Fig. 7.12; Table 7.7).

Accessory minerals in ,316_C include sulfide and FeNi metal. These occur as ∼5-30 μm grains located in interstitial sites adjacent to pyroxene. The metal grains in ,316_C have higher Ni concentrations (12 wt%) than those in any of the other 12003 samples (Table 7.10). None of the ,316_C sulfides were successfully analysed.

7.2.6 12003,317

12003,317_D has a more granular texture than the other 12003 samples and is composed mostly of pyroxene (57% by mode) and plagioclase (34%; Fig. 7.12). The plagioclase phases occasionally occur as elongated subhedral grains with intrafasciculate textures, but more commonly as anhedral grains with irregular resorbed edges. The ,317_D plagioclase phases have a wider compositional range than those in the other 12003 samples (An_{77-94}; Fig. 7.5; Table 7.5). They have REE abundances between 0.3-59 ×CI values and nearly flat chondrite normalised REE patterns with positive Eu-anomalies (La_{cn}/Lu_{cn} = 2; Eu/Eu* = 12-58; Fig. 7.14).

The pyroxene in ,317_D encloses plagioclase and exhibits irregular patchy zoning between more magnesian to more Fe-rich compositions ($Wo_{9-34}En_{10-44}Fs_{30-79}$; Fig. 7.3; Table 7.4). They have a relatively narrow Ti# range and low concentrations of Al (Al_2O_3 <2.0 wt%) when compared with the other 12003 samples (Figs. 7.10; 7.11). Unlike in the other 12003 samples, the most primitive (magnesian) pyroxene compositions in ,317_D are also the most Ca-rich. The compositional zoning of the pyroxenes is also apparent in the REE abundances which increase towards the more Fe-rich regions (0.1-6 ×CI abundances; La_{cn}/Lu_{cn} = 0.04-0.4; Eu/Eu* = 0.1-0.3; Fig. 7.13).

The most abundant minor phase in ,317_D is a silica polymorph (5% by mode; Table 7.9). This is present as medium to large (∼70-600 μm) grains which tend to be adjacent to and intergrown with the plagioclase phases. Several smaller grains are completely enclosed in plagioclase (Fig. 7.12). Anhedral ilmenite grains are also common (4%) and typically occur at the boundaries between the plagioclase and pyroxene phases.

Mesostasis areas are often associated with the most Fe-rich pyroxene compositions (Fig. 7.12). These contain pyroxferroite, high-K glass (Table 7.9) and phosphate phases. The Fe-rich pyroxenes also contain exsolved Fe metal grains (Ni = 0.2-0.3 wt%; Co = 1.2 wt%; Table 7.10).

7.3 Discussion

7.3.1 Crystallisation history and equilibrium parent magma composition

12003,310

The olivine and chromite phenocrysts of the ,310 samples were the first phases to crystallise. The presence of small chromite grains completely enclosed in olivine, but located towards the olivine rims, indicates that the olivine began to crystallise first and subsequently co-crystallised with chromite. The ulvöspinel rims of the chromite grains rarely occur adjacent to olivine, but commonly at the boundary with pyroxene. This implies that ulvöspinel began to crystallise towards the end of olivine crystallisation, and during the crystallisation of pyroxene. The presence of the radiating plagioclase-pyroxene texture in ,310 samples indicate that plagioclase also co-crystallised with pyroxene. The association of the minor and accessory phases (i.e. ilmenite, silica, phosphates and sulfides) with the more evolved pyroxene rims suggests that these were amongst the last to crystallise. However, the cross-cutting of the ilmenite and plagioclase laths is interpreted as evidence that plagioclase continued to crystallise after ilmenite had appeared on the liquidus.

The variation of Cr in the ,310 olivine phenocrysts provides an indication of the co-crystallising phases (Fig. 7.15). Early crystallising olivines (Fo_{75-65}) commonly have concentrations of Cr_2O_3 in excess of 0.25 wt%. The Cr content begins to rapidly decrease as the olivines evolve beyond Fo values of 70-65. This may be due to the beginning of chromite crystallisation. The Cr content in the most evolved olivine phases ($Fo_{\sim 55-35}$) decreases less rapidly. This is interpreted as evidence of a transition from chromite to ulvöspinel. However, the decrease in Cr in the more evolved olivines indicates continued, albeit less significant, partitioning of Cr into another phase; possibly pyroxene.

The Ti# in the ,310 pyroxenes increases very rapidly between Fe# ∼0.30-0.35 (Fig. 7.10). Between Fe# ∼0.35-0.50 there is a change in this trend suggesting the partitioning of Ti into another phase or increasing Cr in the pyroxenes. As such, this is interpreted as evidence of spinels evolving from chromite to ulvöspinel. As the pyroxenes evolve beyond Fe# ∼0.50 the Ti# increases less rapidly. This indicates further partitioning of Ti into another co-crystallising phase; most likely ilmenite. A final change in the Ti# vs Fe# trend appears to occur in the most evolved ,310 pyroxene phases (from Fe# ∼0.85) particularly in ,310_2D and ,310_3A. The Ti# begins to in-

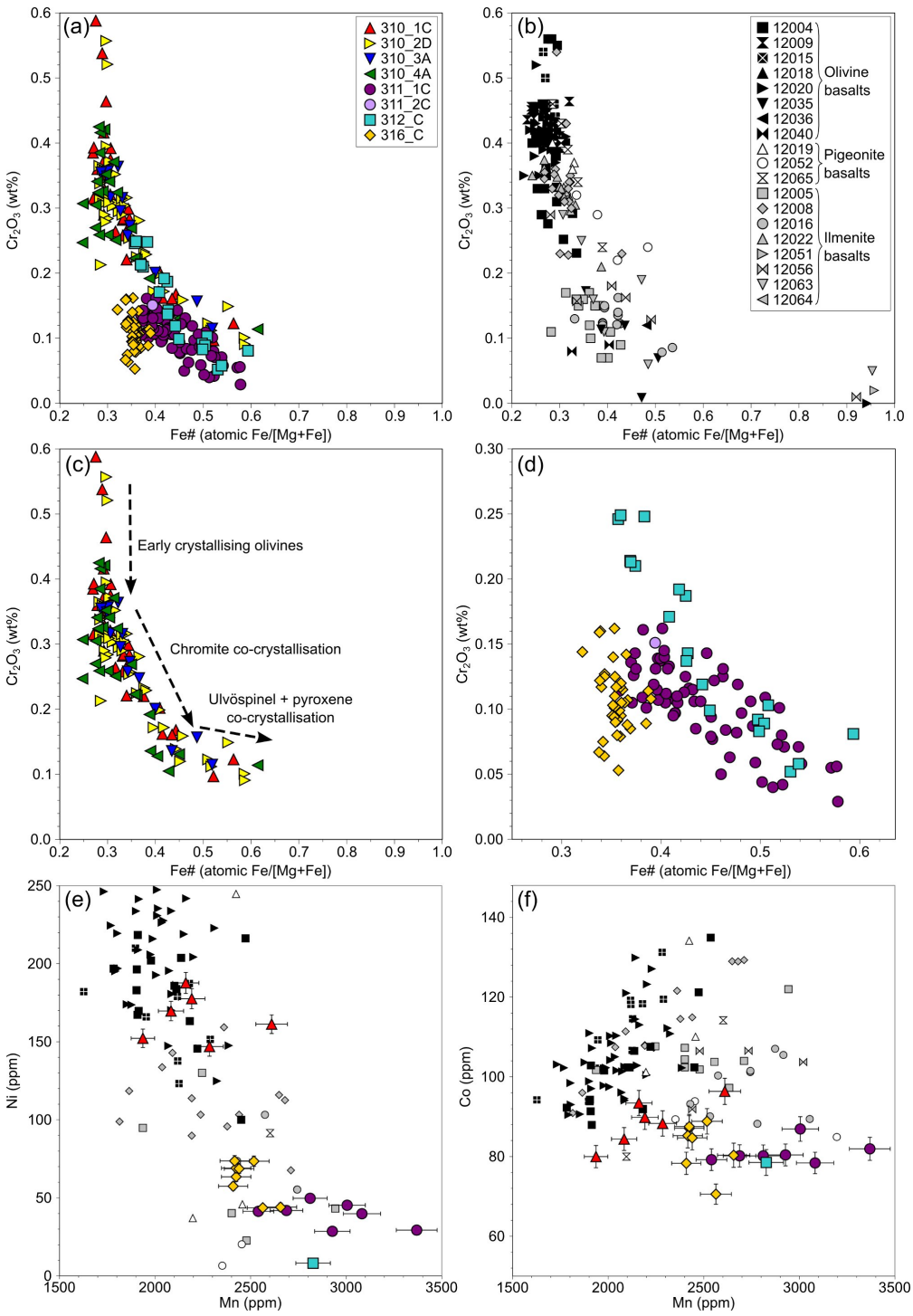

Figure 7.15: (a-d) Concentrations of Cr_2O_3 vs Fe# in olivine phases within the 12003 chips and other Apollo 12 basalts. Note the reduced scale in (d) to account for the more limited compositional variations of the olivines in ,311;,312; and ,316. Concentrations of (e) Ni and (f) Co vs Mn, for olivine phases within samples 12003,310_1C;,311_1C;,312_C; and ,316_C. Manganese acts as an indicator of igneous fractionation because it behaves incompatibly in olivine (*Karner et al.*, 2003). Data are compared with those for olivines in other Apollo 12 basalts (*Bence et al.* 1970; *Brett et al.* 1971a; *Brown et al.* 1971; *El Goresy et al.* 1971; *Hollister et al.* 1971; *Keil et al.* 1971; *Kushiro et al.* 1971; *Newton et al.* 1971; *Weill et al.* 1971; *Butler* 1972; *Dungan and Brown* 1977; *Fagan et al.* 2012; *O'Sullivan, pers. comm.* 2012). Error bars represent 1σ errors.

crease more rapidly again, indicating either an increase of Ti or a decrease of Cr in the pyroxenes. This could be due to further chromite crystallisation, however the lack of chromite phases associated with Fe-rich pyroxenes in the ,310 samples makes this seem unlikely. It could also indicate the cessation of ilmenite or ulvöspinel crystallisation. The appearance of ilmenite on the liquidus at pyroxene Fe# ∼0.50 is supported by the trend in pyroxene Al/Ti ratios (Fig. 7.11). The decreasing Al/Ti ratio in the ,310 pyroxenes between Fe# ∼0.40-0.45 provides an indication of plagioclase co-crystallisation. To summarise, relationships between the ,310 mineral textures and minor element concentrations indicate the following crystallisation sequence: olivine → chromite → pyroxene → ulvöspinel → plagioclase → ilmenite.

The equilibrium parent melt REE composition of the ,310 samples was reconstructed from a LA-ICP-MS analysis of one of the ,310_1C pyroxene cores using the Wo_{12} partition coefficients of *McKay et al.* (1986b) and *Schnare et al.* (2008). This calculation indicates that the ,310 parent melt had REE abundances between 55-428 ×CI. The CI-normalised REE profile of the reconstructed melt has higher abundances of LREE than HREE (La_{cn}/Lu_{cn} = 5.5; Fig. 7.16). The pyroxene core analysis used for the reconstruction had a significantly higher Ca content (Wo_{18}) than that for which the partition coefficients were derived. REE partition coefficients for clinopyroxene decrease with increasing Ca content and, therefore, this may have led to artificially high REE concentrations in the ,310 reconstructed parent melt.

12003,311

The olivine phenocrysts are interpreted as the first phases to crystallise in the ,311 samples. As in the ,310 samples, the presence of small chromite grains enclosed towards the edges of the olivine phenocrysts indicates that chromite appeared on the liquidus while olivine was still crystallising. However, the association of ulvöspinel grains with pyroxene suggests that olivine crystallisation ceased prior to the appearance of ulvöspinel on the liquidus. The interstitial natures of pyroxene and plagioclase in the ,311 samples indicates that they began to crystallise after olivine. The occurrence of pyroxene grains completely enclosed in plagioclase may also suggest that they crystallised prior to plagioclase crystallisation.

The Cr content in the ,311 olivines decreases with decreasing Fo values (Fig. 7.15). This indicates the partitioning of Cr into another phase and, therefore, supports the co-crystallisation of olivine and chromite inferred from textural observations. Unlike the ,310 samples, the olivine Cr compositions do not provide a clear indication that olivine began to crystallise prior to chromite.

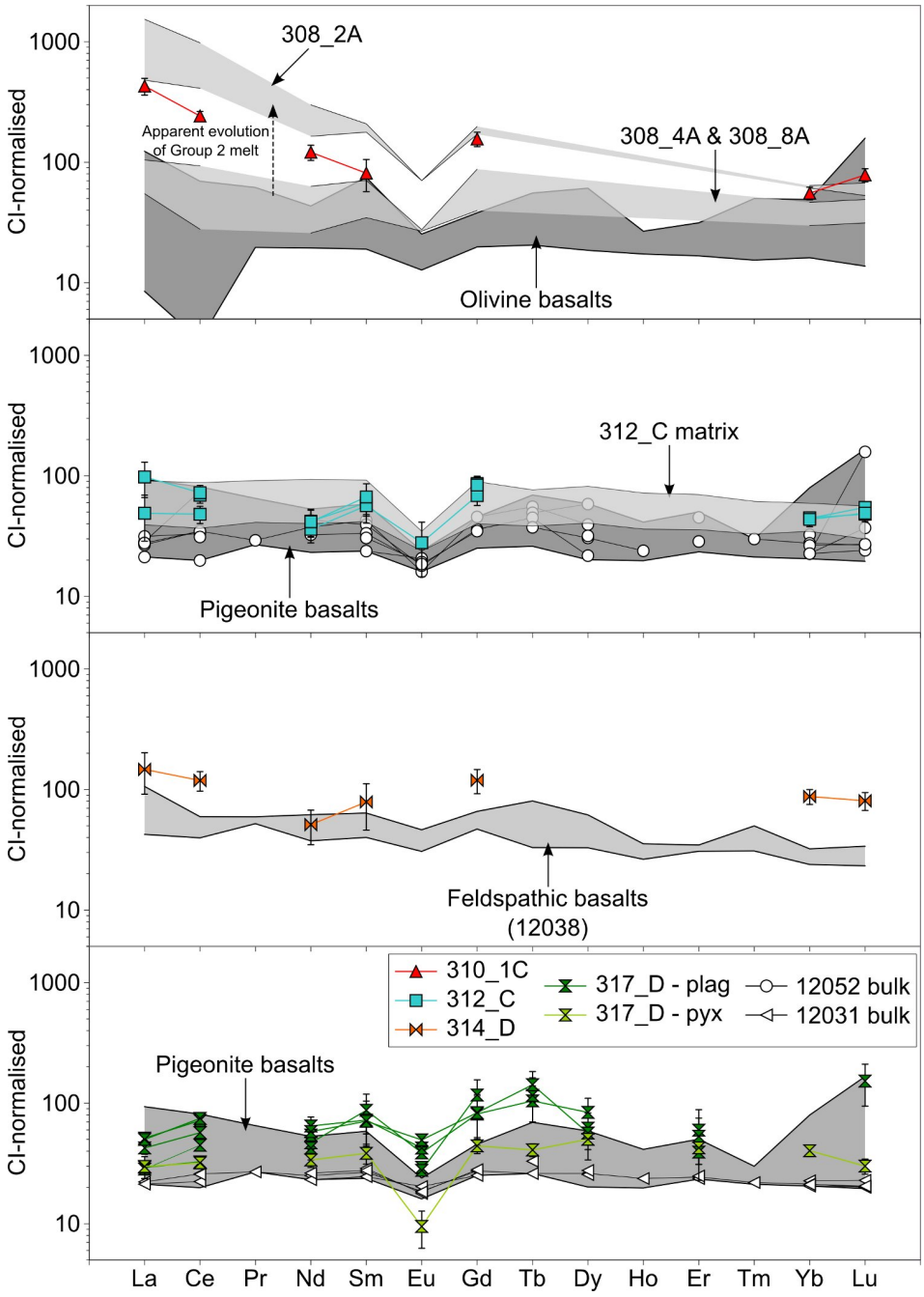

Figure 7.16: Chondrite normalised (*Anders and Grevesse*, 1989) REE concentrations of the reconstructed 12003 chip parental melts. The parental melt compositions have been reconstructed from LA-ICP-MS analyses of pyroxene (and plagioclase in the case of ,317_D) cores using partition coefficients from *McKay et al.* (1986b) and *Schnare et al.* (2008). The reconstructed parent melt REE concentrations of the Group 2 12003,308 samples are indicated for comparison with that of ,310_1C. The 12003 melt compositions have also been compared with the bulk compositions of Apollo 12 olivine, pigeonite and feldspathic basalts (*Gast and Hubbard*, 1970; *Bouchet et al.*, 1971; *Brunfelt et al.*, 1971; *Compston et al.*, 1971; *Goles et al.*, 1971; *Haskin et al.*, 1971; *Hubbard et al.*, 1971; *Kharkar and Turekian*, 1971; *Maxwell and Wiik*, 1971; *Morrison et al.*, 1971; *Schnetzler and Philpotts*, 1971; *Taylor et al.*, 1971b; *Wakita et al.*, 1971; *Wänke et al.*, 1971; *Taylor and Bence*, 1975; *Nyquist et al.*, 1977; *Rhodes et al.*, 1977; *Nyquist et al.*, 1979; *Nyquist et al.*, 1981; *Unruh et al.*, 1984; *Warren et al.*, 1986; *Dickinson et al.*, 1989; *Neal et al.*, 1994a; *Snyder et al.*, 1997; *Neal*, 2001).

The rate at which Ti# in the ,311 pyroxenes increases declines between Fe# ∼0.25-0.40. This is interpretated as a more gradual transition from co-crystallising chromite to ulvöspinel than is seen in the ,310 samples. Further evidence of this can be seen in the trend of Ti# vs Fe# in the ,311_1C spinels which has a more constant gradient than that of the ,310 spinels (Fig. 7.7). Beyond Fe# 0.40 the Ti# in the ,311 pyroxenes increases much more slowly, indicating further partitioning of Ti into another phase; most likely ilmenite. This is also supported by the Al/Ti ratio vs Fe# in the pyroxenes which decreases much less significantly for pyroxenes with Fe# >0.40 (Fig. 7.11). The rapidly decreasing Al/Ti ratio for pyroxenes with Fe# <0.40, is interpreted as evidence of plagioclase co-crystallising with pyroxene, however, there is no clear indication that pyroxene began to crystallise before plagioclase.

Based on these observations, the following crystallisation sequence is inferred for the ,311 samples: olivine + spinel → pyroxene + plagioclase → ilmenite. Note, however, that chromite and ulvöspinel are not specifically identified in this sequence due to the gradual transition towards more Ti-rich spinel compositions.

The lamellae in ,311_1C are interpreted as either shock lamellae or exsolution lamellae resulting from partial sub-solidus equilibration. In either case, the re-mobilisation of elements in the pyroxenes makes it unclear whether the pyroxenes analysed are truly representative of the most primitive pyroxene compositions. As such, it has not been possible to reconstruct the parent melt REE concentrations of the ,311 samples.

12003,312

The mafic phenocrysts are interpreted as the first phases to crystallise in ,312_C, under different cooling conditions from the rest of the sample. However, the order in which these formed is difficult to determine on the basis of textural characteristics. None of the spinel phenocrysts are entirely enclosed within olivine or pyroxene. In addition to this, there is no apparent association between the olivine and pyroxene phenocrysts. The ulvöspinel rims of the spinel grains are most prominent at the boundaries with the fine grained matrix, and are significantly thinned (if present at all) when adjacent to the olivine and pyroxene phenocrysts. This is interpreted as evidence that crystallisation of the olivine and pyroxene phenocrysts was largely complete when ulvöspinel began to crystallise. The fine grained matrix indicates a subsequent period of significantly more rapid crystallisation. The interstitial nature of the matrix pyroxene suggests that it formed after the plagioclase laths.

The Cr content of the olivine phenocrysts and the Ti# of the pyroxene phenocrysts in ,312_C, indicate decreasing amounts of Cr with increasing Fe# in these phases (Figs.

7.10; 7.15). As such, this suggests the partitioning of Cr into another phase and supports the co-crystallisation of chromite with the early olivine and pyroxene phenocrysts. The more constant Ti# in the ,312_C groundmass pyroxenes indicate that chromite crystallisation had finished prior to the formation of the groundmass phases. The Al/Ti ratios of the groundmass pyroxenes indicate decreasing Al in the pyroxenes and, therefore, co-crystallisation of plagioclase between Fe# ∼0.65-0.75 (Fig. 7.11). The trend in Al/Ti ratios changes for pyroxenes with Fe# >0.75, indicating the co-crystallisation of ilmenite.

There is no clear indication in the textural characteristics or mineral chemistries to suggest that either the olivine, pyroxene or chromite phenocrysts began to crystallise first. Equally, it is difficult to determine a clear crystallisation sequence for all of the individual phases in the ,312_C matrix. The following crystallisation is proposed for ,312_C: olivine phenocrysts + pyroxene phenocrysts + chromite phenocrysts → ulvöspinel → groundmass plagioclase → groundmass pyroxene → ilmenite.

The equilibrium parent melt REE composition of ,312_C was reconstructed from three analyses of pyroxene phenocryst cores (Wo_{9-11}). The resulting chondrite normalised REE parent melt profile is good agreement with that of the ,312_C matrix ,312 (28-98 ×CI-abundances; La_{cn}/Lu_{cn} = 1.0-2.0; Eu/Eu* = 0.4; Fig. 7.16). This implies that there was very little change in the REE composition of the parent melt between the formation of the phenocrysts and the groundmass phases.

12003,314

The intergrown texture of plagioclase and pyroxene in ,314_D indicates co-crystallisation of the two phases (Fig. 7.12). Furthermore, the association and intergrowth of these with the minor phases in ,314_D is interpreted as evidence that both pyroxene and plagioclase were still crystallising when silica, spinel and ilmenite appeared on the liquidus.

The rate at which Ti# increases with Fe# for ,314_D pyroxenes between Fe# ∼0.45-0.55, is similar to that identified in other samples during the co-crystallisation of pyroxene and ulvöspinel (Fig. 7.10). This rate then decreases between Fe# ∼0.55-0.85. This is interpretated as evidence for the partitioning of Ti into co-crystallising ilmenite. A final change occurs in the Ti# vs Fe# trend at Fe# ∼0.85, with the Ti# beginning to increase more rapidly again. This may indicate the end of either ulvöspinel or ilmenite crystallisation, resulting in increasing pyroxene Ti content.

The Al/Ti ratios of the ,314_D pyroxenes provide an indication that pyroxene may have begun to crystallise prior to plagioclase, although a lack of analyses of these

most magnesian pyroxenes (Fe# ∼0.40) makes this somewhat ambiguous (Fig. 7.11). The downward trend of the Al/Ti ratio between Fe# ∼0.40-0.55 is more distinct, and is interpreted as evidence of co-crystallisation of the two major phases. The pyroxene Al/Ti ratios (as with the Ti#) also indicate the co-crystallisation of ilmenite starting at ∼0.55. In summary, the crystallisation sequence for ,314_D is interpreted as: pyroxene → plagioclase → ulvöspinel → ilmenite.

The ,314 parent melt REE composition was reconstructed from an analysis of a pyroxene grain with Wo_{16} (Fig. 7.16). Reconstructed REE abundances in the ,314 parent melt are between 51-147 ×CI values. The chondrite normalised REE profile for the melt is nearly flat (La_{cn}/Lu_{cn} = 1.8). As with the reconstructed ,310_1C parent melt, the ,314 melt may be slightly elevated as it was reconstructed from a pyroxene analysis with a relatively high Wo number compared to that of the partition coefficients used (Wo_{12}; *McKay et al.* 1986b; *Schnare et al.* 2008).

12003,316

Compositional equilibration in the phases of ,316_C mean that crystallisation sequences are hard to infer from major and minor element concentrations in pyroxenes, olivines and plagioclases (Figs. 7.10; 7.11; 7.15). The lack of exsolution features in the pyroxenes suggests that sub-solidus equilibration has not occurred in ,316_C, and that the equilibration in the ,316 minerals is the result of equilibrium crystallisation in a closed system. Nevertheless reconstruction of parental melt REE concentrations from phases in ,316_C are considered to be unreliable as it is impossible to ensure that the measured compositions are truly representative of the most primitive mineral compositions. As such, it has not been possible to reconstruct the REE concentrations of the ,316 parent melt. Several observations can be made on the basis of textural features within ,316_C (Fig. 7.12).

As in other 12003 samples, olivine and spinel appear to be the first phases to crystallise in ,316. The inclusion of small chromite grains near the edges of olivine phenocrysts indicates that these phases began to co-crystallise after olivine had appeared on the liquidus. Plagioclase and pyroxene both appear to have begun crystallising after olivine and spinel. It is difficult to determine the relative crystallisation sequences of these two phases based on textural characteristics.

12003,317

The plagioclase in ,317_D is commonly enclosed by pyroxene, which also fills interstitial areas in the plagioclase. As such, plagioclase appears to have begun crystallising at

the same time as or possibly before pyroxene. Pyroxene Ti# and Al/Ti ratios in ,314_D indicate co-crystallisation with ilmenite (Figs. 7.10; 7.11). Unlike in many of the other 12003 samples, there is no clear indication that pyroxene co-crystallised with plagioclase, or that it began to crystallise prior to plagioclase or ilmenite.

Due to the Ca-rich nature of the more primitive pyroxene compositions in the sample, the ,317_D parent melt was reconstructed from a pyroxene with Wo_{29} using the Wo_{32} partition coefficients of *McKay et al.* (1986b). The reconstructed ,317_D parent melt has REE abundances between 9.5-50 ×CI values and a nearly flat CI-normalised REE profile with a negative Eu-anomaly (La_{cn}/Lu_{cn} = 1.0; Eu/Eu* = 0.2; Fig. 7.16). The ,317_D parent melt was also reconstructed from five plagioclase analyses (Fig. 7.16). The resulting parent melt has similar, but slightly higher REE abundances than those reconstructed from the ,317_D pyroxene (28-153 ×CI abundances; La_{cn}/Lu_{cn} = 0.3; Eu/Eu* = 0.5-0.6; Fig. 7.16). This is interpreted as evidence that pyroxene began to crystallise at the same time as, or just before plagioclase.

Based on the textural observations as well as major, minor and trace element mineral compositions, the following crystallisation sequence is inferred for ,317_D: plagioclase + pyroxene → ilmenite → silica.

7.3.2 Intersample comparisons

Of the six specific sets of samples discussed in this chapter, ,311 and ,316 are the most texturally similar (cumulate-like), suggesting similarly slow crystallisation conditions (Figs. 7.8; 7.12). However, significant differences between the bulk compositions, modal mineralogies and mineral chemistries of these samples suggest that they are most likely from separate parent melts. Conversely, while the textures of ,312_C and ,317_D are very different, both samples have similar bulk compositions (Fig. 7.17; Table 7.2). The reconstructed REE concentrations of ,317_D are also similar to those of ,312_C and the measured REE concentrations of the ,312_C matrix (Fig. 7.16). These samples may, therefore, have crystallised from the same parent melt but under different cooling conditions.

The most unusual of these samples is ,314_D. The coarse grain size of the sample - when compared with the overall sample size - may mean that the modal mineralogy and bulk composition may not be truly representative of the parent basalt (Fig. 7.12). However, the sample is much more aluminous than any other basaltic 12003 sample (Tables 7.1; 7.2). The Ti-rich nature of the spinels, large (0.1-0.6 mm) silica grains and comparatively large phosphate grains (up to ∼50 μm), also distinguish the ,314_D from

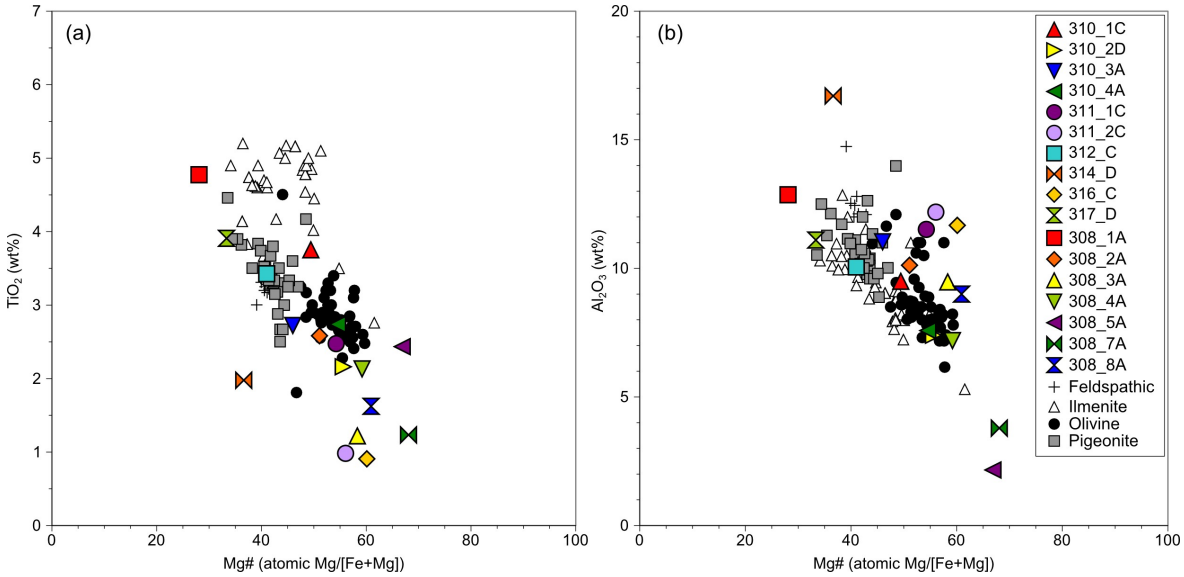

Figure 7.17: Bulk compositions of the basaltic 12003,308;,310;,311;,312;,314;,316;,317 samples compared with previously analysed Apollo 12 samples. (a) TiO_2 vs. Mg# (atomic Mg/[Fe+Mg]×100); (b) Al_2O_3 vs. Mg# (atomic Mg/[Fe+Mg]×100). 12003 data are compared with those of *Lunar Sample Preliminary Examination Team* (1970b); *Bouchet et al.* (1971); *Brunfelt et al.* (1971); *Cuttitta et al.* (1971); *Compston et al.* (1971); *Engel et al.* (1971); *Goles et al.* (1971); *Klein et al.* (1971); *Kushiro and Haramura* (1971); *Maxwell and Wiik* (1971); *Morrison et al.* (1971); *Smales et al.* (1971); *Wakita and Schmitt* (1971); *Wänke et al.* (1971); *Willis et al.* (1971, 1972); *Papike et al.* (1976); *Rhodes et al.* (1977); *Baldridge et al.* (1979); *Beaty et al.* (1979); *Warren et al.* (1986); *Neal et al.* (1994a).

the other 12003 samples.

Several similarities are noted between the 12003 chips discussed in this chapter and the 12003,308 samples discussed in Chapter 6:

- The ,310 samples, for example, are texturally and compositionally akin to those of the Group 2 ,308 samples. The major, minor and trace element concentrations of pyroxene, plagioclase, olivine and spinel for all of these samples are also comparable. The reconstructed REE concentrations of the ,310_1C parent melt place it between ,308_2A and 308_8A in the fractionation sequence identified for the Group 2 samples (Fig. 7.16).

- The cumulate texture of ,316_C bears a close resemblance to that of the Group 3 sample ,308_3A (see Chapter 6). The bulk compositions and mineral chemistries of these samples are also similar, with both samples containing compositionally equilibrated phases, including distinct augites and pigeonites, and similarly homogeneous spinel phenocrysts exhibiting ilmenite exsolution. The Ti/V ratios in the mafic phases of ,316_C are also in agreement with those of the ,308_3A sample (Fig. 7.18). As such, ,316_C is interpreted as having originated from the same parent melt as the Group 3 sample ,308_3A.

- Many of the olivines in ,311_1C also have similarly high ratios of Ti/V as ,308_3A (Fig. 7.18). However, both the pyroxenes and olivines in the ,311 samples are more compositionally varied than those of either ,316_C or ,308_3A. One possible explanation for this is that all three samples originated from the same lava flow, and ,311 underwent significantly less sub-solidus equilibration. Alternatively ,311 may be unrelated to ,308_3A and ,316_C.

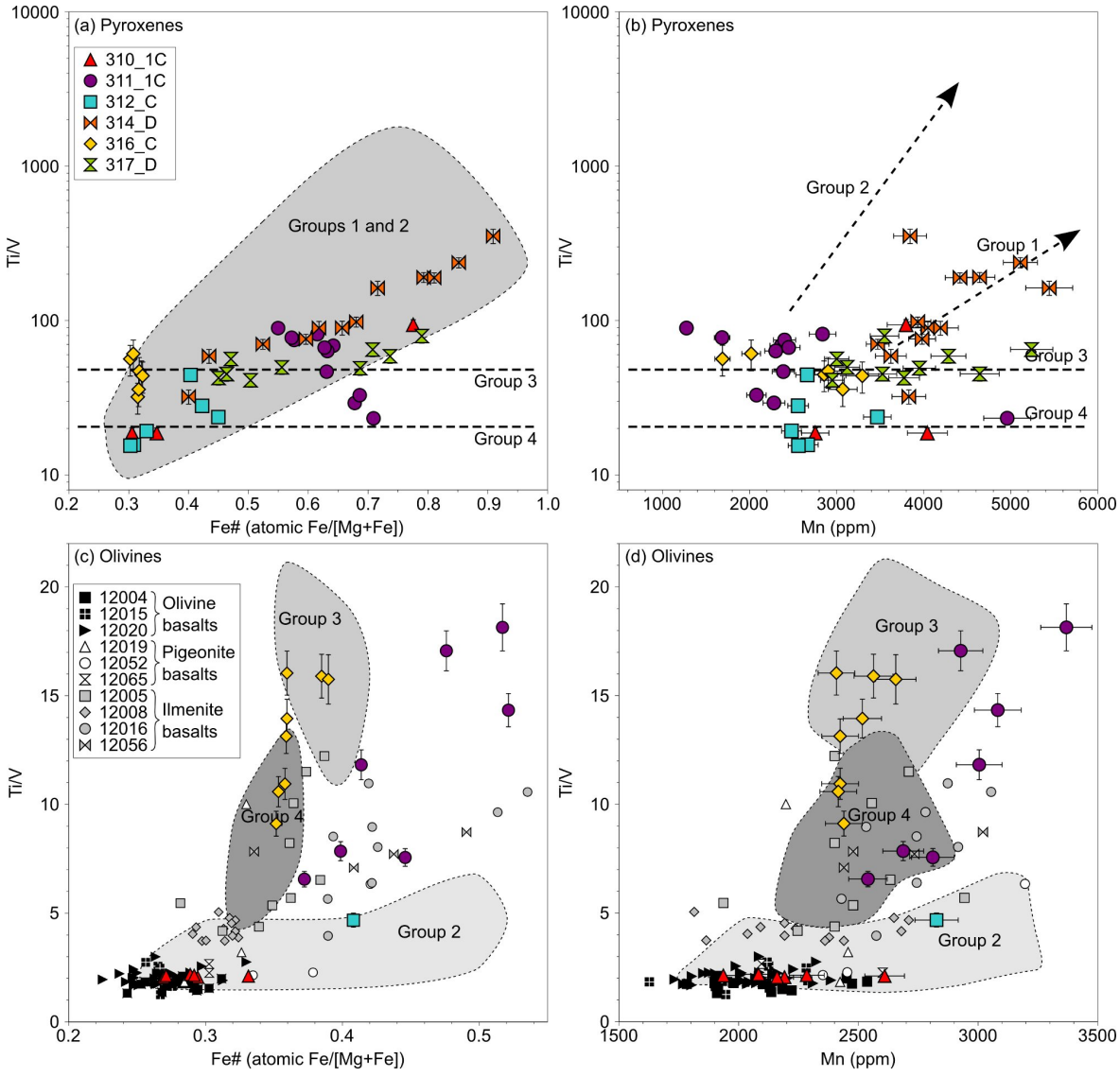

Figure 7.18: Ti/V ratios in mafic phases of the 12003 chips. The fields and trends of the 12003,308 groups (see Chapter 6) are indicated for comparison. Olivine data are also compared with those of *Fagan et al.* (2012) and *O'Sullivan, pers. comm.* 2012. Error bars represent 1σ errors.

7.3.3 Comparison with other Apollo 12 basalts

12003,310

The textures of the ,310 samples are most similar to porphyritic-subophitic Apollo 12 olivine basalts (e.g. 12002; *Grove et al.* 1973; *Neal et al.* 1994a). Although the modal mineralogies, and in particular the olivine content, of the four samples vary significantly, they are most similar to those reported for ilmenite and olivine basalts (Table 7.1). However, the samples have lower bulk concentrations of TiO_2 and higher Mg# than most ilmenite basalts and are more similar to the bulk compositions of Apollo 12 olivine basalts (Fig. 7.17; *Neal et al.* 1994a). The major and minor element compositions of pyroxene, olivine and spinel in the ,310 samples are in good agreement with those of other olivine basalts (e.g. 12002, 12004, 12018 and 12020; Figs. 7.3; 7.5;7.7). Trace element abundances for olivines in ,310_1C are also consistent with those from several olivine basalts, including 12004 and 12020 (Figs. 7.15; 7.18; *Fagan et al.* 2012).

The reconstructed REE concentrations of the ,310_1C parent melt, and in particular the LREE concentrations, are higher than the bulk REE concentrations reported for any other Apollo 12 olivine basalt samples (Fig. 7.16). This may be evidence of fractionation of the parent melt. It could also reflect a limitation of the LA-ICP-MS technique, for which the size of the analysed area may have been too large (55 μm) in comparison to the scale of compositional zoning in the pyroxenes.

12003,311

The textures of the ,311 samples reflect those in the equigranular ilmenite basalt 12016 (Fig. 7.8; *Dungan and Brown* 1977). The modal mineralogies of the two ,311 samples are also comparable with those reported for 12016 (Table 7.1; *Neal et al.* 1994a; *Dungan and Brown* 1977). Despite these similarities, the ,311 samples have less ilmenite, lower bulk concentrations of TiO_2 and higher bulk Mg# than any of the ilmenite basalts (Fig. 7.17; Table 7.2). The composition of ,311_1C is closer to that of many olivine basalts, while ,311_2C has significantly lower TiO_2 than any other Apollo 12 basalt. Given the comparatively coarse grained textures and small sizes of these samples, this may be attributed to unrepresentative sampling of the parent rock.

The major and minor element concentrations of the ,311 pyroxene, olivine and spinel phases are in very good agreement with those from the ilmenite basalt 12016 (Figs. 7.3; 7.5; 7.7). Similarly, the ,311 pyroxene and plagioclase REE abundances are comparable with those of 12016 (Figs. 7.4; 7.6). However, the trace element concentrations in the olivines in ,311_1C differ from those of 12016. All of the olivines analysed in ,311_1C

samples have lower concentrations of trace elements such as Ni and Co than 12016 (Fig. 7.15). The most evolved olivines in ,311_1C (i.e. with the highest Fa numbers and Mn concentrations) also have significantly higher Ti/V ratios then any reported for 12016 or any other Apollo 12 basalt (Fig. 7.18). This may indicate that the ,311 samples represent a previously unrecognised basaltic group. However, given the limited amount of available olivine trace element data for Apollo 12 basalts, these Ti/V ratios could be common of more evolved olivines in ilmenite basalts.

12003,312

Several other porphyritic pigeonite basalts exist with similar textures to ,312_C (e.g. 12019, 12052, 12053, 12055; *Meyer* 2005). The modal mineralogy of ,312_C is also in good agreement with those reported for Apollo 12 pigeonite basalts, including the porphyritic samples 12019, 12052 and 12053 (Table 7.1; *Papike et al.* 1976; *Papike and Vaniman* 1978a; *Baldridge et al.* 1979; *Neal et al.* 1994a). The bulk composition of ,312_C is most similar to those reported for pigeonite basalts (Fig. 7.17; Table 7.2).

The pyroxene compositions in the ,312_C phenocrysts are consistent with those reported for 12052 by *Bence et al.* (1970, 1971) and *O'Sullivan, pers. comm.* 2012 (Figs. 7.3; 7.4). The range of olivine compositions in ,312_C (Fo_{41-64}) is slightly wider than that reported in 12052 (Fo_{52-67}; Fig. 7.5; *Bence et al.* 1970; *Fagan et al.* 2012), although, only four 12052 olivine analyses are available for comparison. Spinel compositions were reported for 12052 by *Gibb et al.* (1970) and *Haggerty and Meyer* (1970). These are in very good agreement with those measured in ,312_C (Fig. 7.7). Based on these observations, these samples may have originated from the same parent melt.

12003,314

12003,314_D is texturally similar to the pigeonite basalts 12007, 12031 and 12039 and the feldspathic basalt 12038. Like ,314_D, 12038 has high abundances of plagioclase, and correspondingly high concentrations of Al_2O_3 when compared to other Apollo 12 basalts (Figs. 7.12; 7.17; Tables 7.1; 7.2; *Neal et al.* 1994a). The modal abundance of ilmenite in ,314_D is lower than that in 12038 and most pigeonite basalts (Table 7.1). As such, the bulk TiO_2 concentration of ,314_D is also lower that reported for either 12038 or any pigeonite basalts (Fig. 7.17). However, as previously stated, the coarse grainsize of ,314_D means that the sample's bulk composition and modal mineralogy should be viewed with caution.

The major and minor element concentrations in the ,314_D pyroxenes are within the range of those reported for 12038 (*Keil et al.*, 1971; *Beaty et al.*, 1979) and the pigeonite basalts 12021, 12031 and 12039 (Fig. 7.3; *Weill et al.* 1971; *Beaty et al.* 1979; *Shearer et al.* 1989;*O'Sullivan, pers. comm.* 2012). Pyroxene trace element data is currently unavailable for 12038, although the REE abundances of the ,314_D pyroxenes are broadly within the range of those in the Apollo 12 pigeonite basalts (Fig. 7.13). Both *Simpson and Bowie* (1971) and *Keil et al.* (1971) report the presence of ulvöspinel in 12038. As in ,314_D, this is described as containing exsolved ilmenite (*Simpson and Bowie*, 1971). The Fe# and Cr# of the 12038 and ,314_D ulvöspinels are very similar, however, those in ,314_D have higher Ti# (Fig. 7.7; Table 7.8).

The reconstructed parent melt REE concentrations of ,314_D are generally higher than the bulk REE concentrations reported for 12038 or the Apollo 12 pigeonite basalts (Fig. 7.16). As discussed in Section 7.3.1, the ,314_D parent melt was not reconstructed from pyroxene compositions with ideal compositions for the available partition coefficients (i.e. Wo_{12}). On balance, ,314_D is interpreted as most likely being a feldspathic basalt. If this interpretation is correct, it almost certainly crystallised from a separate lava flow to any of the other 12003 samples and is notable as being one of only two currently recognised feldspathic basalts in the Apollo 12 sample collection (*Neal et al.*, 1994a; *Meyer*, 2005). *Neal et al.* (1994a) speculated that 12038 may represent an exotic sample introduced to the Apollo 12 site by impact mixing or, alternatively, that feldspathic basalt flows were poorly sampled by the Apollo 12 mission. Identification of further feldspathic basalts would strengthen the case for feldspathic basalt flows being local to the Apollo 12 site.

12003,316

Like that of the Group 3 sample (,308_3A), the texture of ,316_C is similar to that described for the olivine basalts 12035 and 12036 (*Keil et al.*, 1971; *James and Wright*, 1972; *Meyer*, 2005). The mineralogical mode of ,316_C is unusual, with significantly more olivine and less pyroxene than any other Apollo 12 basalt (Table 7.1; *Neal et al.* 1994a). The only sample with similar abundances of olivine and pyroxene is the porphyritic ilmenite basalt 12008, however, this is the only apparent similarity between these samples (*Dungan and Brown*, 1977; *Neal et al.*, 1994a). The bulk Mg# of ,316_C is in good agreement with those reported for olivine basalts (Fig. 7.17; Table 7.2). Despite this, the sample has a lower bulk Ti content than any other Apollo 12 basalt ($TiO_2 = 0.9$ wt%; Fig. 7.17; Table 7.2), placing it in the category of very-low Ti basalts (i.e. where bulk $TiO_2 < 1$ wt%; *Neal and Taylor* 1992). Conversely, the Fe# and Ti#

of the ,316_C pyroxenes are more similar to those of low-Ti and high-Ti mare basalts (Fig. 7.10; *Nielsen and Drake* 1978; *Arai et al.* 1996; *Robinson and Treiman* 2010). As with ,311_1C and ,314_D, the coarse grainsize of ,316_C in comparison with the overall sample size may be resulting in unrepresentative measurements of modal mineralogy and bulk sample composition.

The compositionally equilibrated phases in ,316_C are unusual compared with most Apollo 12 basalts. The ilmenite basalt 12005 is one of the few Apollo 12 samples reported to have similarly equilibrated augites and pigeonites (Fig. 7.3), although the 12005 olivines have a slightly wider compositional range (Fo_{57-67}) than those in ,316_C (Fo_{61-66}; Fig. 7.5; *Dungan and Brown* 1977). However, the Ti/V ratios of the olivines in ,316_C are significantly higher than those that are reported for any other Apollo 12 basalt, including 12005 (Fig. 7.18; *Fagan et al.* 2012). Spinel compositions in ,316_C are similar to those reported for other Apollo 12 samples with coarse grained and cumulate textures, including the ilmenite basalt 12005 and the olivine basalt 12035 (*Reid*, 1971; *Dungan and Brown*, 1977), but are less varied than those reported in 12036 (Fig. 7.7; *Busche et al.* 1972). The Ni content of ,316_C metal grains (12 wt%) is also comparable with those reported for 12005 (∼6-18 wt%; *Dungan and Brown* 1977) and 12035 (∼1-19 wt%; *Brett et al.* 1971a).

The unusual nature of ,316_C when compared to most other Apollo 12 samples suggest that it, like ,308_3A, may represent a cumulate of a previously unrecognised basaltic suite.

12003,317

The texture of ,317_D is similar to the more granular texture described by *Beaty et al.* (1979) in the pigeonite basalt 12031. The abundances of minor phases within the two samples are very similar, however 12031 has more plagioclase and less pyroxene than ,317_D. It is Fe-richer (Mg# = 33.3) than 12031 (Mg# = 43.1; *Rhodes et al.* 1977), however, the bulk composition of ,317_D is in general most similar to that of the pigeonite basalts (Fig. 7.17).

12031 is reported to have a wide range of plagioclase compositions (An_{48-98}; *Beaty et al.* 1979). The range of plagioclase compositions measured within ,317_D, therefore, are well within this range (Fig. 7.5). The most primitive pyroxene compositions of 12031 are significantly more magnesian than those in ,317_D (Fig. 7.3). As such, if the two samples do originate from similar sources, then ,317_D may represent the product of a later stage of crystallisation than 12031. This is also consistent with the difference in bulk Mg# between the two samples. Concentrations of REE in the ,317_D are within

Table 7.3: Summary of the six 12003 chips.

Sample	Texture	Similar samples		
		Number	Basaltic suite	References
12003,310	Ophitic	12002	Olivine	*Grove et al.* 1973; *Neal et al.* 1994a
12003,311	Equigranular microgabbro	12016	Ilmenite	*Dungan and Brown* 1977
12003,312	Porphyritic	12052	Pigeonite	*Bence et al.* 1971
12003,314	Subophitic-intergranular	12038	Feldspathic	*Beaty et al.* 1979
12003,316	Gabbroic/Cumulate	12035; 12005	Olivine; Ilmenite	*Reid* 1971; *Dungan and Brown* 1977
12003,317	Granular	12031	Pigeonite	*Beaty et al.* 1979

the range of other Apollo 12 pigeonite basalts (Fig. 7.13).

The reconstructed parent melt REE concentrations of ,317_D are similar to, although slightly higher than, the bulk REE concentrations of 12031 (Fig. 7.16). This is interpreted further evidence that ,317_D crystallised from a more evolved melt than 12031.

7.4 Summary

Based on these results, the following conclusions (Table 7.3) are drawn for the 12003 chips:

- The 12003,310 samples have ophitic textures similar to those seen throughout the Apollo 12 basalts. Their compositions and mineral chemistries most closely resemble those of porphyritic-ophitic olivine basalts such as 12002, 12004 and 12020 (*Brett et al.*, 1971b; *Klein et al.*, 1971; *Kushiro et al.*, 1971; *Grove et al.*, 1973). The ,310 samples are interpreted as originating from the same parent melt as the Group 2 ,308 samples.

- The 12003,311 samples are equigranular microgabbros with textural and compositional similarities to the ilmenite basalt 12016 (*Dungan and Brown*, 1977). The Ti/V ratios in the ,311_1C olivines are unusually high compared with available data for Apollo 12 basalts. It is currently unclear whether this is simply a reflection of the limited amount of mineral trace element data reported for Apollo 12 basalts.

- 12003,312 is a porphyritic basalt with a fine-grained variolitic matrix. It is very similar to several porphyritic pigeonite basalts, including 12019, 12052, 12053 and 12055 (*Bence et al.*, 1971; *Meyer*, 2005).

- 12003,314 is a coarse grained subophitic-intergranular sample. It is texturally and

compositionally similar to the feldspathic basalt 12038 (*Beaty et al.*, 1979), and may represent a slightly more evolved product of the same parent melt.

- 12003,316 has a gabbroic-cumulate texture, similar to those reported for 12035 and 12036. However, the modal mineralogy, bulk composition and mineral chemistries in this sample are unlike most other Apollo 12 basalts. The Group 3 12003,308 sample (,308_3A) and ,316 are interpreted as originating from the same parent melt, which has not been previously identified in the Apollo 12 sample collection.

- 12003,317 has an unusual granular texture compared with the other 12003 samples. This is most similar to one of the two main textures described in the pigeonite basalt 12031 by *Beaty et al.* (1979). The bulk composition of ,317 is most similar to those of the pigeonite basalts and the range of mineral chemistries are similar to those in 12031 (Figs. 7.17;7.3). Despite having very different textures, ,317 and ,312 may have originated from the same parent melt.

In summary the 12003 chips appear to have crystallised from between 4-6 separate lava flows. These samples include a possible new member of the Apollo 12 feldspathic basaltic suite (12003,314), and at least one sample (12003,316) which may represent a previously unrecognised basaltic suite.

Table 7.4: Major, minor and trace element abundances for representative pyroxene phases within 12003,310; ,311; ,312; ,314; ,316; ,317. Errors for major and minor elements are 1σ standard deviations calculated from repeat measurements of the BCR-2 USGS basaltic glass reference material. Errors for the trace elements are 1σ standard deviations calculated by the Glitter software.

Table 7.4

	170811_347 ,310_1C_p91 Pyx. Rim	170811_352 ,310_1C_p96 Pyx. Core	170811_496 ,310_2D_p27 Pyx. Rim	071011_152 ,310_2D_p137 Pyx. Core	071011_174 ,310_3A_p15 Pyx. Rim
Major and minor elements measured by WDS EMPA (wt%)					
SiO_2	46.7 ± 0.3	49.8 ± 0.3	45.6 ± 0.3	50.3 ± 0.4	44.6 ± 0.3
TiO_2	1.08 ± 0.03	1.14 ± 0.03	0.87 ± 0.02	0.78 ± 0.02	0.94 ± 0.02
Al_2O_3	1.27 ± 0.02	2.69 ± 0.05	1.01 ± 0.01	1.46 ± 0.02	1.12 ± 0.03
Cr_2O_3	0.25 ± 0.02	0.67 ± 0.02	0.09 ± 0.01	0.67 ± 0.02	b.d.
FeO	35.2 ± 0.2	17.6 ± 0.1	40.9 ± 0.2	18.4 ± 0.1	44.0 ± 0.2
MnO	0.46 ± 0.04	0.32 ± 0.02	0.50 ± 0.04	0.34 ± 0.03	0.49 ± 0.03
MgO	5.72 ± 0.07	18.5 ± 0.2	2.48 ± 0.06	19.8 ± 0.4	0.35 ± 0.01
CaO	8.59 ± 0.04	8.65 ± 0.04	7.78 ± 0.04	5.93 ± 0.07	8.24 ± 0.33
Na_2O	0.05 ± 0.01	0.06 ± 0.01	0.03 ± 0.01	<0.01	b.d.
Total	99.3	99.4	99.3	97.8	99.8
Mg#	22.5	65.3	9.75	65.8	1.40
Wo	19.5	18.0	18.0	12.4	19.1
En	18.1	53.6	8.00	57.6	1.13
Fs	62.4	28.5	74.0	30.0	79.7
Minor and trace elements measured by LA-ICP-MS (ppm; wt% for Al_2O_3, TiO_2, Cr_2O_3 and MnO)					
Mg	80344 ± 3249	252356 ± 10158	n.m.	n.m.	n.m.
Al	7357 ± 280	14613 ± 554	n.m.	n.m.	n.m.
Al_2O_3	1.39 ± 0.05	2.76 ± 0.10	n.m.	n.m.	n.m.
K	7.47 ± 1.38	6.48 ± 1.37	n.m.	n.m.	n.m.
Ca	61364 ± 2066	61786 ± 2053	n.m.	n.m.	n.m.
Sc	78.4 ± 3.9	86.2 ± 4.2	n.m.	n.m.	n.m.
Ti	6595 ± 381	7082 ± 408	n.m.	n.m.	n.m.
TiO_2	1.10 ± 0.06	1.18 ± 0.07	n.m.	n.m.	n.m.
V	70.3 ± 3.9	379.7 ± 20.5	n.m.	n.m.	n.m.
Cr	1645 ± 128	5402 ± 420	n.m.	n.m.	n.m.
Cr_2O_3	0.24 ± 0.02	0.79 ± 0.06	n.m.	n.m.	n.m.
Mn	3796 ± 216	4042 ± 230	n.m.	n.m.	n.m.
MnO	0.49 ± 0.03	0.52 ± 0.03	n.m.	n.m.	n.m.
Co	38.2 ± 2.5	44.5 ± 2.9	n.m.	n.m.	n.m.
Ni	6.28 ± 0.57	15.3 ± 1.1	n.m.	n.m.	n.m.
Cu	b.d.	0.30 ± 0.12	n.m.	n.m.	n.m.
Zn	12.6 ± 1.4	2.73 ± 0.43	n.m.	n.m.	n.m.
Ga	1.09 ± 0.10	0.73 ± 0.07	n.m.	n.m.	n.m.
Ge	0.52 ± 0.16	0.56 ± 0.16	n.m.	n.m.	n.m.
Rb	b.d.	b.d.	n.m.	n.m.	n.m.
Sr	5.38 ± 0.32	3.29 ± 0.21	n.m.	n.m.	n.m.
Y	33.3 ± 1.6	10.0 ± 0.5	n.m.	n.m.	n.m.
Zr	26.8 ± 1.2	6.89 ± 0.37	n.m.	n.m.	n.m.
Nb	0.10 ± 0.03	0.15 ± 0.03	n.m.	n.m.	n.m.
Ag	b.d.	b.d.	n.m.	n.m.	n.m.
Cs	b.d.	b.d.	n.m.	n.m.	n.m.
Ba	0.47 ± 0.16	0.81 ± 0.19	n.m.	n.m.	n.m.
La	0.51 ± 0.06	0.20 ± 0.03	n.m.	n.m.	n.m.
Ce	2.42 ± 0.16	0.58 ± 0.05	n.m.	n.m.	n.m.
Pr	0.62 ± 0.05	0.11 ± 0.02	n.m.	n.m.	n.m.
Nd	4.52 ± 0.39	1.04 ± 0.15	n.m.	n.m.	n.m.
Sm	2.33 ± 0.29	0.37 ± 0.11	n.m.	n.m.	n.m.
Eu	0.10 ± 0.03	b.d.	n.m.	n.m.	n.m.
Gd	4.32 ± 0.39	1.32 ± 0.18	n.m.	n.m.	n.m.
Tb	0.83 ± 0.06	0.21 ± 0.03	n.m.	n.m.	n.m.
Dy	5.94 ± 0.43	1.79 ± 0.18	n.m.	n.m.	n.m.
Ho	1.35 ± 0.09	0.41 ± 0.04	n.m.	n.m.	n.m.
Er	4.25 ± 0.30	1.13 ± 0.12	n.m.	n.m.	n.m.
Tm	0.57 ± 0.05	0.19 ± 0.03	n.m.	n.m.	n.m.
Yb	4.39 ± 0.33	1.17 ± 0.14	n.m.	n.m.	n.m.
Lu	0.70 ± 0.06	0.25 ± 0.03	n.m.	n.m.	n.m.
Hf	1.24 ± 0.13	0.36 ± 0.07	n.m.	n.m.	n.m.
Ta	b.d.	b.d.	n.m.	n.m.	n.m.
Pb	b.d.	b.d.	n.m.	n.m.	n.m.
Th	b.d.	b.d.	n.m.	n.m.	n.m.
U	b.d.	b.d.	n.m.	n.m.	n.m.

Table 7.4 (continued)

	071011_290 ,310_3A_p121 Pyx. Core	141011_27 ,310_4A_p17 Pyx. Rim	141011_47 ,310_4A_p37 Pyx. Core	090811_249 ,311_1C_p74 Pyx. Rim	090811_263 ,311_1C_p88 Pyx. Core
Major and minor elements measured by WDS EMPA (wt%)					
SiO_2	50.5 ± 0.1	45.2 ± 0.3	50.2 ± 0.4	48.2 ± 0.3	50.6 ± 0.3
TiO_2	0.94 ± 0.02	0.75 ± 0.02	0.87 ± 0.02	1.97 ± 0.04	0.97 ± 0.02
Al_2O_3	2.54 ± 0.04	0.58 ± 0.01	2.02 ± 0.03	2.65 ± 0.05	1.69 ± 0.03
Cr_2O_3	0.80 ± 0.02	0.09 ± 0.01	0.66 ± 0.02	0.42 ± 0.02	0.51 ± 0.02
FeO	18.9 ± 0.1	38.4 ± 0.2	17.1 ± 0.1	15.6 ± 0.1	17.4 ± 0.1
MnO	0.36 ± 0.03	0.47 ± 0.06	0.33 ± 0.04	0.27 ± 0.01	0.32 ± 0.02
MgO	20.6 ± 0.3	3.00 ± 0.04	19.5 ± 0.3	14.0 ± 0.3	20.5 ± 0.4
CaO	5.15 ± 0.81	8.97 ± 0.06	8.16 ± 0.05	15.4 ± 0.1	6.15 ± 0.06
Na_2O	0.04 ± 0.01	0.02 ± 0.01	0.02 ± 0.01	0.07 ± 0.01	<0.01
Total	99.8	97.5	98.8	98.6	98.1
Mg#	66.0	12.2	67.1	61.5	67.8
Wo	10.6	20.8	16.8	32.7	12.7
En	59.0	9.67	55.8	41.4	59.1
Fs	30.4	69.5	27.4	25.9	28.1
Minor and trace elements measured by LA-ICP-MS (ppm; wt% for Al_2O_3, TiO_2, Cr_2O_3 and MnO)					
Mg	n.m.	n.m.	n.m.	159768 ± 10354	160784 ± 10535
Al	n.m.	n.m.	n.m.	13011 ± 559	8241 ± 363
Al_2O_3	n.m.	n.m.	n.m.	2.46 ± 0.11	1.56 ± 0.07
K	n.m.	n.m.	n.m.	b.d.	5.42 ± 1.48
Ca	n.m.	n.m.	n.m.	109928 ± 3980	43933 ± 1700
Sc	n.m.	n.m.	n.m.	119 ± 6	51.3 ± 2.6
Ti	n.m.	n.m.	n.m.	12587 ± 922	5896 ± 436
TiO_2	n.m.	n.m.	n.m.	2.10 ± 0.15	0.98 ± 0.07
V	n.m.	n.m.	n.m.	154 ± 8	202 ± 11
Cr	n.m.	n.m.	n.m.	3264 ± 294	3074 ± 278
Cr_2O_3	n.m.	n.m.	n.m.	0.48 ± 0.04	0.45 ± 0.04
Mn	n.m.	n.m.	n.m.	2837 ± 153	2279 ± 125
MnO	n.m.	n.m.	n.m.	0.37 ± 0.02	0.29 ± 0.02
Co	n.m.	n.m.	n.m.	34.4 ± 2.1	28.6 ± 1.7
Ni	n.m.	n.m.	n.m.	10.1 ± 1.3	10.2 ± 1.1
Cu	n.m.	n.m.	n.m.	b.d.	0.42 ± 0.19
Zn	n.m.	n.m.	n.m.	5.64 ± 1.08	4.92 ± 0.83
Ga	n.m.	n.m.	n.m.	1.02 ± 0.18	0.40 ± 0.09
Ge	n.m.	n.m.	n.m.	b.d.	b.d.
Rb	n.m.	n.m.	n.m.	b.d.	b.d.
Sr	n.m.	n.m.	n.m.	11.2 ± 0.7	2.62 ± 0.21
Y	n.m.	n.m.	n.m.	26.7 ± 1.4	7.40 ± 0.45
Zr	n.m.	n.m.	n.m.	16.0 ± 1.3	3.60 ± 0.37
Nb	n.m.	n.m.	n.m.	b.d.	0.14 ± 0.04
Ag	n.m.	n.m.	n.m.	b.d.	b.d.
Cs	n.m.	n.m.	n.m.	b.d.	b.d.
Ba	n.m.	n.m.	n.m.	b.d.	b.d.
La	n.m.	n.m.	n.m.	0.44 ± 0.08	0.15 ± 0.04
Ce	n.m.	n.m.	n.m.	1.83 ± 0.17	0.38 ± 0.06
Pr	n.m.	n.m.	n.m.	0.53 ± 0.08	0.06 ± 0.02
Nd	n.m.	n.m.	n.m.	4.10 ± 0.54	0.55 ± 0.15
Sm	n.m.	n.m.	n.m.	2.28 ± 0.41	0.32 ± 0.13
Eu	n.m.	n.m.	n.m.	0.09 ± 0.04	b.d.
Gd	n.m.	n.m.	n.m.	3.24 ± 0.50	1.13 ± 0.23
Tb	n.m.	n.m.	n.m.	0.85 ± 0.10	0.15 ± 0.03
Dy	n.m.	n.m.	n.m.	5.31 ± 0.52	1.39 ± 0.20
Ho	n.m.	n.m.	n.m.	1.01 ± 0.11	0.36 ± 0.05
Er	n.m.	n.m.	n.m.	3.20 ± 0.34	0.94 ± 0.14
Tm	n.m.	n.m.	n.m.	0.37 ± 0.06	0.10 ± 0.03
Yb	n.m.	n.m.	n.m.	3.51 ± 0.42	0.71 ± 0.14
Lu	n.m.	n.m.	n.m.	0.38 ± 0.06	0.17 ± 0.03
Hf	n.m.	n.m.	n.m.	1.33 ± 0.21	0.16 ± 0.06
Ta	n.m.	n.m.	n.m.	b.d.	b.d.
Pb	n.m.	n.m.	n.m.	b.d.	b.d.
Th	n.m.	n.m.	n.m.	b.d.	b.d.
U	n.m.	n.m.	n.m.	b.d.	b.d.

Table 7.4 (continued)

	090811_49 ,312_C_p44 Pyx. Core	090811_52 ,312_C_p47 Pyx. Rim	090811_486 ,314_D_p54 Pyx. Rim	090811_505 ,314_D_p73 Pyx. Core
Major and minor elements measured by WDS EMPA (wt%)				
SiO_2	50.0 ± 0.2	47.8 ± 0.2	46.6 ± 0.4	50.7 ± 0.5
TiO_2	0.90 ± 0.02	1.55 ± 0.04	0.88 ± 0.02	1.12 ± 0.02
Al_2O_3	2.45 ± 0.01	3.87 ± 0.02	0.86 ± 0.02	1.78 ± 0.05
Cr_2O_3	0.94 ± 0.02	0.65 ± 0.02	0.04 ± 0.01	0.47 ± 0.02
FeO	17.7 ± 0.1	19.9 ± 0.1	38.2 ± 0.3	20.9 ± 0.2
MnO	0.33 ± 0.04	0.34 ± 0.04	0.49 ± 0.05	0.36 ± 0.04
MgO	20.1 ± 0.2	15.3 ± 0.2	2.14 ± 0.01	17.6 ± 0.1
CaO	5.07 ± 0.04	8.34 ± 0.07	10.6 ± 0.1	7.84 ± 0.08
Na_2O	0.03 ± 0.01	0.04 ± 0.01	0.04 ± 0.01	0.02 ± 0.01
Total	97.5	97.8	99.8	100.9
Mg#	67.0	57.7	9.10	60.0
Wo	10.8	18.5	24.4	16.1
En	59.8	47.1	6.88	50.3
Fs	29.4	34.5	68.7	33.6
Minor and trace elements measured by LA-ICP-MS (ppm; wt% for Al_2O_3, TiO_2, Cr_2O_3 and MnO)				
Mg	174106 ± 6356	148631 ± 5582	16539 ± 708	201300 ± 8907
Al	13515 ± 517	21641 ± 850	13111 ± 569	10051 ± 450
Al_2O_3	2.55 ± 0.10	4.09 ± 0.16	2.48 ± 0.11	1.90 ± 0.09
K	b.d.	b.d.	172 ± 17	7.93 ± 2.79
Ca	36257 ± 1300	59585 ± 2262	75522 ± 2619	56054 ± 2138
Sc	64.6 ± 2.9	94.7 ± 4.4	68.7 ± 3.3	79.9 ± 4.0
Ti	5545 ± 412	9374 ± 702	5746 ± 487	7483 ± 640
TiO_2	0.92 ± 0.07	1.56 ± 0.12	0.96 ± 0.08	1.25 ± 0.11
V	288 ± 14	335 ± 17	16.3 ± 1.0	233 ± 14
Cr	4770 ± 366	4713 ± 365	273 ± 26	4101 ± 393
Cr_2O_3	0.70 ± 0.05	0.69 ± 0.05	0.04 ± 0.01	0.60 ± 0.06
Mn	2480 ± 113	2557 ± 118	3843 ± 190	3829 ± 194
MnO	0.32 ± 0.01	0.33 ± 0.02	0.50 ± 0.02	0.49 ± 0.03
Co	29.2 ± 1.7	28.0 ± 1.7	17.4 ± 1.2	39.6 ± 2.6
Ni	2.69 ± 0.34	2.57 ± 0.50	b.d.	1.66 ± 0.44
Cu	b.d.	b.d.	0.84 ± 0.20	b.d.
Zn	1.04 ± 0.27	4.64 ± 0.83	37.6 ± 4.4	12.6 ± 1.9
Ga	0.71 ± 0.09	1.22 ± 0.18	3.47 ± 0.28	1.23 ± 0.18
Ge	b.d.	b.d.	b.d.	b.d.
Rb	b.d.	b.d.	b.d.	b.d.
Sr	0.92 ± 0.08	1.72 ± 0.17	111 ± 5	1.28 ± 0.14
Y	7.08 ± 0.34	13.0 ± 0.7	90.6 ± 4.9	8.31 ± 0.56
Zr	4.97 ± 0.34	12.5 ± 0.9	60.9 ± 8.0	3.79 ± 0.58
Nb	b.d.	b.d.	0.11 ± 0.03	b.d.
Ag	b.d.	b.d.	b.d.	b.d.
Cs	b.d.	b.d.	b.d.	b.d.
Ba	b.d.	b.d.	25.5 ± 1.9	b.d.
La	0.05 ± 0.02	0.08 ± 0.03	3.09 ± 0.19	0.07 ± 0.03
Ce	0.18 ± 0.03	0.53 ± 0.07	12.1 ± 0.6	0.29 ± 0.05
Pr	0.06 ± 0.01	0.15 ± 0.04	2.53 ± 0.16	0.05 ± 0.02
Nd	0.36 ± 0.09	0.84 ± 0.20	16.0 ± 1.0	0.44 ± 0.14
Sm	0.31 ± 0.09	0.85 ± 0.22	9.01 ± 0.69	0.36 ± 0.15
Eu	b.d.	b.d.	1.44 ± 0.12	b.d.
Gd	0.71 ± 0.13	1.70 ± 0.32	12.6 ± 0.8	1.01 ± 0.23
Tb	0.14 ± 0.02	0.28 ± 0.05	2.19 ± 0.14	0.14 ± 0.03
Dy	1.10 ± 0.13	2.37 ± 0.29	17.2 ± 1.0	1.23 ± 0.20
Ho	0.23 ± 0.03	0.41 ± 0.06	3.64 ± 0.19	0.33 ± 0.05
Er	1.01 ± 0.10	1.36 ± 0.19	10.1 ± 0.7	1.10 ± 0.17
Tm	0.15 ± 0.02	0.23 ± 0.04	1.56 ± 0.10	0.23 ± 0.04
Yb	0.92 ± 0.12	1.79 ± 0.25	10.5 ± 0.7	1.85 ± 0.26
Lu	0.16 ± 0.02	0.24 ± 0.04	1.58 ± 0.11	0.26 ± 0.04
Hf	0.26 ± 0.05	0.78 ± 0.14	2.75 ± 0.23	0.21 ± 0.07
Ta	b.d.	b.d.	0.04 ± 0.01	b.d.
Pb	b.d.	b.d.	0.38 ± 0.06	b.d.
Th	b.d.	b.d.	0.24 ± 0.03	b.d.
U	b.d.	b.d.	0.13 ± 0.02	b.d.

Table 7.4 (continued)

	090811_697 ,316_C_p50 Pigeonite	090811_708 ,316_C_p56 Augite	170811_17 ,317_D_p12 Pyx. Core	170811_245 ,317_D_p196 Pyx. Rim
Major and minor elements measured by WDS EMPA (wt%)				
SiO_2	52.1 ± 0.3	50.6 ± 0.4	48.7 ± 0.2	46.6 ± 0.1
TiO_2	1.05 ± 0.02	1.80 ± 0.03	1.25 ± 0.03	0.60 ± 0.01
Al_2O_3	1.47 ± 0.02	2.17 ± 0.19	1.40 ± 0.03	0.64 ± 0.01
Cr_2O_3	0.47 ± 0.02	0.54 ± 0.02	0.39 ± 0.02	0.16 ± 0.01
FeO	17.9 ± 0.1	12.8 ± 0.1	21.3 ± 0.1	38.0 ± 0.4
MnO	0.32 ± 0.02	0.26 ± 0.02	0.35 ± 0.03	0.51 ± 0.03
MgO	21.1 ± 0.3	16.2 ± 0.1	11.8 ± 0.2	5.67 ± 0.08
CaO	5.69 ± 0.03	15.3 ± 0.1	13.9 ± 0.1	6.85 ± 0.05
Na_2O	<0.01	0.09 ± 0.01	0.06 ± 0.01	<0.01
Total	100.0	99.8	99.0	99.0
Mg#	67.7	69.2	49.6	21.0
Wo	11.6	31.9	29.6	15.4
En	59.8	47.1	34.9	17.8
Fs	28.6	21.0	35.4	66.8
Minor and trace elements measured by LA-ICP-MS (ppm; wt% for Al_2O_3, TiO_2, Cr_2O_3 and MnO)				
Mg	235063 ± 9839	192517 ± 6887	124686 ± 4242	45312 ± 1530
Al	8449 ± 462	13435 ± 674	8046 ± 359	3209 ± 143
Al_2O_3	1.60 ± 0.09	2.54 ± 0.13	1.52 ± 0.07	0.61 ± 0.03
K	b.d.	b.d.	b.d.	b.d.
Ca	40652 ± 1942	109113 ± 3990	99172 ± 3268	48936 ± 1586
Sc	74.3 ± 4.4	104 ± 5	102 ± 5	72.6 ± 3.7
Ti	6842 ± 1492	11455 ± 2483	8189 ± 612	3663 ± 273
TiO_2	1.14 ± 0.25	1.91 ± 0.41	1.37 ± 0.10	0.61 ± 0.05
V	156 ± 11	188 ± 12	200 ± 13	46.2 ± 3.1
Cr	3222 ± 657	3666 ± 743	2734 ± 205	791 ± 59
Cr_2O_3	0.47 ± 0.10	0.54 ± 0.11	0.40 ± 0.03	0.12 ± 0.01
Mn	3295 ± 189	2017 ± 107	2950 ± 137	3550 ± 164
MnO	0.43 ± 0.02	0.26 ± 0.01	0.38 ± 0.02	0.46 ± 0.02
Co	43.9 ± 2.8	32.3 ± 1.9	30.0 ± 2.4	20.4 ± 1.6
Ni	19.6 ± 3.1	10.8 ± 1.8	1.23 ± 0.24	b.d.
Cu	b.d.	b.d.	0.32 ± 0.14	b.d.
Zn	10.0 ± 2.0	6.30 ± 1.34	3.47 ± 0.52	4.12 ± 0.44
Ga	1.20 ± 0.25	0.66 ± 0.21	0.86 ± 0.10	1.29 ± 0.09
Ge	2.08 ± 0.66	1.28 ± 0.48	0.71 ± 0.20	1.30 ± 0.15
Rb	b.d.	0.21 ± 0.09	b.d.	b.d.
Sr	1.41 ± 0.22	10.4 ± 0.7	6.22 ± 0.32	7.19 ± 0.32
Y	15.5 ± 1.2	27.4 ± 1.7	15.7 ± 1.0	94.0 ± 5.7
Zr	5.51 ± 0.73	13.3 ± 1.3	6.49 ± 0.51	33.7 ± 2.2
Nb	b.d.	b.d.	b.d.	0.06 ± 0.01
Ag	0.50 ± 0.16	0.32 ± 0.14	b.d.	b.d.
Cs	0.16 ± 0.06	b.d.	b.d.	b.d.
Ba	1.71 ± 0.57	b.d.	b.d.	b.d.
La	0.31 ± 0.09	0.53 ± 0.10	0.16 ± 0.03	0.95 ± 0.05
Ce	0.47 ± 0.10	1.86 ± 0.16	0.75 ± 0.06	4.83 ± 0.22
Pr	0.16 ± 0.06	0.34 ± 0.07	0.21 ± 0.03	1.35 ± 0.07
Nd	1.29 ± 0.37	3.34 ± 0.51	1.59 ± 0.21	10.2 ± 0.7
Sm	1.32 ± 0.44	1.90 ± 0.42	0.96 ± 0.18	6.60 ± 0.39
Eu	0.21 ± 0.10	0.22 ± 0.08	0.09 ± 0.03	0.25 ± 0.02
Gd	1.62 ± 0.46	3.29 ± 0.54	1.74 ± 0.24	11.2 ± 0.6
Tb	0.40 ± 0.07	0.49 ± 0.08	0.31 ± 0.04	2.14 ± 0.11
Dy	2.58 ± 0.39	4.96 ± 0.49	2.80 ± 0.25	17.7 ± 1.0
Ho	0.68 ± 0.10	1.04 ± 0.11	0.62 ± 0.06	3.90 ± 0.20
Er	2.20 ± 0.31	3.52 ± 0.37	1.76 ± 0.17	11.2 ± 0.6
Tm	0.39 ± 0.07	0.43 ± 0.07	0.25 ± 0.03	1.75 ± 0.09
Yb	2.63 ± 0.40	2.52 ± 0.34	1.90 ± 0.20	11.8 ± 0.6
Lu	0.28 ± 0.06	0.48 ± 0.07	0.22 ± 0.03	1.83 ± 0.10
Hf	0.68 ± 0.19	1.00 ± 0.19	0.35 ± 0.07	1.83 ± 0.13
Ta	0.19 ± 0.05	b.d.	b.d.	b.d.
Pb	0.15 ± 0.07	b.d.	b.d.	b.d.
Th	b.d.	b.d.	b.d.	0.01 ± 0.01
U	0.07 ± 0.03	b.d.	b.d.	b.d.

Pyx. = pyroxene; Aug. = augite; Pig. = pigeonite. Values which were below instrument detection limits (b.d.) or not measured (n.m.) have been indicated.

Table 7.5: Major, minor and trace element abundances for representative plagioclase phases within 12003,310; ,311; ,312; ,314; ,316; ,317. Errors for major and minor elements are 1σ standard deviations calculated from repeat measurements of the BCR-2 USGS basaltic glass reference material. Errors for the trace elements are 1σ standard deviations calculated by the Glitter software.

Table 7.5

	170811_258 ,310_1C_p7	071011_108 ,310_2D_p98	071011_199 ,310_3A_p40	040811_6 ,310_4A_p1	090811_187 ,311_1C_p17
Major and minor elements measured by WDS EMPA (wt%)					
SiO_2	47.6 ± 0.3	46.3 ± 0.4	46.7 ± 0.4	47.2 ± 0.4	45.7 ± 0.3
TiO_2	0.09 ± 0.01	0.11 ± 0.01	0.07 ± 0.01	0.12 ± 0.00	0.10 ± 0.00
Al_2O_3	32.4 ± 0.5	32.5 ± 0.9	31.1 ± 0.9	32.6 ± 0.3	34.3 ± 0.3
FeO	0.93 ± 0.01	1.01 ± 0.01	0.98 ± 0.01	0.85 ± 0.01	0.40 ± 0.01
MnO	<0.01	0.03 ± 0.01	<0.01	0.02 ± 0.01	0.02 ± 0.01
MgO	0.44 ± 0.01	0.30 ± 0.01	0.43 ± 0.01	0.31 ± 0.01	0.25 ± 0.01
CaO	17.6 ± 0.1	17.9 ± 0.2	17.7 ± 0.7	17.7 ± 0.1	18.3 ± 0.2
K_2O	0.05 ± 0.01	0.06 ± 0.01	0.04 ± 0.01	0.05 ± 0.00	0.03 ± 0.01
Na_2O	1.25 ± 0.03	1.11 ± 0.03	1.24 ± 0.03	1.20 ± 0.03	1.23 ± 0.03
Total	100.4	99.4	98.3	100.1	100.3
An#	88.4	89.6	88.5	88.8	89.0
Minor and trace elements measured by LA-ICP-MS (ppm; wt% for Al_2O_3, K_2O and TiO_2)					
Mg	3479 ± 140	n.m.	n.m.	n.m.	2020 ± 130
Al	190220 ± 7179	n.m.	n.m.	n.m.	192533 ± 8046
Al_2O_3	35.9 ± 1.4	n.m.	n.m.	n.m.	36.4 ± 1.5
K	333 ± 48	n.m.	n.m.	n.m.	259 ± 17
K_2O	0.04 ± 0.01	n.m.	n.m.	n.m.	0.03 ± 0.01
Ca	125644 ± 4135	n.m.	n.m.	n.m.	130633 ± 4355
Sc	1.11 ± 0.15	n.m.	n.m.	n.m.	0.57 ± 0.18
Ti	579 ± 34	n.m.	n.m.	n.m.	586 ± 44
TiO_2	0.10 ± 0.01	n.m.	n.m.	n.m.	0.10 ± 0.01
V	1.48 ± 0.14	n.m.	n.m.	n.m.	3.40 ± 0.26
Cr	4.16 ± 1.22	n.m.	n.m.	n.m.	6.54 ± 1.53
Mn	72.1 ± 4.2	n.m.	n.m.	n.m.	58.7 ± 3.2
Co	1.10 ± 0.13	n.m.	n.m.	n.m.	0.73 ± 0.11
Zn	b.d.	n.m.	n.m.	n.m.	b.d.
Ga	5.48 ± 0.31	n.m.	n.m.	n.m.	5.65 ± 0.36
Rb	b.d.	n.m.	n.m.	n.m.	b.d.
Sr	277 ± 14	n.m.	n.m.	n.m.	320 ± 13
Y	0.27 ± 0.06	n.m.	n.m.	n.m.	0.20 ± 0.04
Zr	b.d.	n.m.	n.m.	n.m.	b.d.
Cs	0.13 ± 0.03	n.m.	n.m.	n.m.	b.d.
Ba	26.1 ± 1.6	n.m.	n.m.	n.m.	14.3 ± 1.1
La	0.37 ± 0.05	n.m.	n.m.	n.m.	0.21 ± 0.04
Ce	0.62 ± 0.07	n.m.	n.m.	n.m.	0.51 ± 0.06
Pr	0.06 ± 0.03	n.m.	n.m.	n.m.	0.04 ± 0.01
Nd	b.d.	n.m.	n.m.	n.m.	0.24 ± 0.11
Sm	b.d.	n.m.	n.m.	n.m.	b.d.
Eu	1.74 ± 0.14	n.m.	n.m.	n.m.	1.55 ± 0.12
Gd	b.d.	n.m.	n.m.	n.m.	b.d.
Tb	b.d.	n.m.	n.m.	n.m.	b.d.
Dy	b.d.	n.m.	n.m.	n.m.	b.d.
Ho	b.d.	n.m.	n.m.	n.m.	b.d.
Er	b.d.	n.m.	n.m.	n.m.	b.d.
Tm	b.d.	n.m.	n.m.	n.m.	b.d.
Yb	b.d.	n.m.	n.m.	n.m.	b.d.
Lu	b.d.	n.m.	n.m.	n.m.	b.d.
Ta	b.d.	n.m.	n.m.	n.m.	0.11 ± 0.03
U	b.d.	n.m.	n.m.	n.m.	0.02 ± 0.01

Table 7.5 (continued)

	040811_23 ,312_C_p2	090811_440 ,314_D_p13	090811_653 ,316_C_p6	170811_39 ,317_D_p34
Major and minor elements measured by WDS EMPA (wt%)				
SiO_2	49.1 ± 0.3	45.1 ± 0.6	45.6 ± 0.2	44.1 ± 0.2
TiO_2	0.14 ± 0.00	0.06 ± 0.00	0.10 ± 0.01	0.04 ± 0.01
Al_2O_3	29.9 ± 0.4	34.8 ± 1.3	34.0 ± 0.5	36.5 ± 0.7
FeO	1.86 ± 0.02	0.50 ± 0.01	0.34 ± 0.01	0.46 ± 0.01
MnO	b.d.	<0.01	<0.01	0.03 ± 0.01
MgO	0.29 ± 0.01	0.24 ± 0.01	0.29 ± 0.01	0.08 ± 0.01
CaO	17.2 ± 0.1	18.4 ± 0.2	18.2 ± 0.1	18.0 ± 0.2
K_2O	0.09 ± 0.01	0.03 ± 0.01	0.03 ± 0.01	0.03 ± 0.01
Na_2O	1.13 ± 0.03	0.96 ± 0.02	1.24 ± 0.03	0.78 ± 0.01
Total	99.7	100.1	99.8	99.9
An#	88.9	91.3	88.9	92.5
Minor and trace elements measured by LA-ICP-MS (ppm; wt% for Al_2O_3, K_2O and TiO_2)				
Mg	n.m.	2024 ± 86	2153 ± 74	515 ± 40
Al	n.m.	186862 ± 7985	197035 ± 9382	196401 ± 7668
Al_2O_3	n.m.	35.3 ± 1.5	37.2 ± 1.8	37.1 ± 1.4
K	n.m.	230 ± 23	197 ± 25	284 ± 42
K_2O	n.m.	0.03 ± 0.01	0.02 ± 0.01	0.03 ± 0.01
Ca	n.m.	131727 ± 4356	129740 ± 4384	128417 ± 4239
Sc	n.m.	0.82 ± 0.12	1.40 ± 0.29	0.78 ± 0.12
Ti	n.m.	413 ± 36	598 ± 60	204 ± 15
TiO_2	n.m.	0.07 ± 0.01	0.10 ± 0.01	0.03 ± 0.00
V	n.m.	2.63 ± 0.22	3.47 ± 0.28	2.30 ± 0.19
Cr	n.m.	8.85 ± 1.36	9.54 ± 1.94	1.80 ± 0.78
Mn	n.m.	61.8 ± 3.1	48.0 ± 3.2	46.4 ± 2.4
Co	n.m.	0.37 ± 0.07	0.85 ± 0.14	0.15 ± 0.05
Zn	n.m.	1.19 ± 0.43	10.64 ± 1.39	2.63 ± 0.76
Ga	n.m.	5.47 ± 0.37	5.49 ± 0.43	10.50 ± 0.56
Rb	n.m.	b.d.	0.38 ± 0.07	b.d.
Sr	n.m.	231 ± 9	279 ± 11	393 ± 14
Y	n.m.	0.19 ± 0.04	0.44 ± 0.10	0.63 ± 0.07
Zr	n.m.	b.d.	b.d.	0.67 ± 0.10
Cs	n.m.	b.d.	b.d.	b.d.
Ba	n.m.	15.1 ± 1.2	15.0 ± 1.1	32.5 ± 2.2
La	n.m.	0.23 ± 0.04	0.17 ± 0.05	0.42 ± 0.05
Ce	n.m.	0.55 ± 0.05	0.43 ± 0.07	1.04 ± 0.08
Pr	n.m.	0.06 ± 0.02	b.d.	0.12 ± 0.02
Nd	n.m.	0.19 ± 0.07	0.79 ± 0.16	0.50 ± 0.11
Sm	n.m.	0.16 ± 0.07	1.08 ± 0.30	0.22 ± 0.08
Eu	n.m.	1.31 ± 0.11	1.87 ± 0.15	2.60 ± 0.15
Gd	n.m.	0.16 ± 0.07	1.00 ± 0.31	0.17 ± 0.08
Tb	n.m.	b.d.	0.19 ± 0.04	0.04 ± 0.01
Dy	n.m.	0.09 ± 0.04	0.68 ± 0.17	0.18 ± 0.06
Ho	n.m.	b.d.	b.d.	b.d.
Er	n.m.	b.d.	b.d.	0.07 ± 0.04
Tm	n.m.	b.d.	b.d.	b.d.
Yb	n.m.	b.d.	b.d.	b.d.
Lu	n.m.	b.d.	0.09 ± 0.02	b.d.
Ta	n.m.	b.d.	0.07 ± 0.03	b.d.
U	n.m.	b.d.	0.03 ± 0.01	b.d.

Values which were below instrument detection limits
(b.d.) or not measured (n.m.) have been indicated.

Table 7.6: Major, minor and trace element abundances for representative olivine phases within 12003,310; ,311; ,312; ,314; ,316; ,317. Errors for major and minor elements are 1σ standard deviations calculated from repeat measurements of the BCR-2 USGS basaltic glass reference material. Errors for the trace elements are 1σ standard deviations calculated by the Glitter software.

Table 7.6

	170811_262 ,310_1C_p11	170811_479 ,310_2D_p10	071011_171 ,310_3A_p12	141011_22 ,310_4A_p12
Major and minor elements measured by WDS EMPA (wt%)				
SiO_2	36.9 ± 0.2	36.9 ± 0.2	36.6 ± 0.3	36.1 ± 0.3
TiO_2	0.05 ± 0.01	0.07 ± 0.01	0.07 ± 0.01	0.03 ± 0.01
Al_2O_3	0.04 ± 0.01	0.03 ± 0.01	0.04 ± 0.01	0.06 ± 0.01
Cr_2O_3	0.32 ± 0.02	0.21 ± 0.02	0.36 ± 0.02	0.34 ± 0.02
FeO	25.6 ± 0.2	26.2 ± 0.1	27.2 ± 0.1	25.3 ± 0.1
MnO	0.27 ± 0.02	0.27 ± 0.02	0.30 ± 0.02	0.30 ± 0.04
MgO	35.3 ± 0.4	36.7 ± 0.8	35.5 ± 0.9	36.8 ± 0.5
CaO	0.28 ± 0.01	0.32 ± 0.01	0.26 ± 0.01	0.28 ± 0.01
Na_2O	<0.01	0.03 ± 0.01	b.d.	<0.01
P_2O_5	0.04 ± 0.01	0.02 ± 0.01	0.05 ± 0.01	<0.01
V_2O_3	<0.01	0.02 ± 0.01	0.02 ± 0.01	<0.01
Total	98.8	100.7	100.3	99.2
Mg#	71.1	71.4	69.9	72.2
Minor and trace elements measured by LA-ICP-MS (ppm; wt% for MgO and Cr_2O_3)				
Mg	243500 ± 7984	n.m.	n.m.	n.m.
MgO	40.4 ± 1.3	n.m.	n.m.	n.m.
Al	89.8 ± 3.2	n.m.	n.m.	n.m.
K	b.d.	n.m.	n.m.	n.m.
Ca	1278 ± 73	n.m.	n.m.	n.m.
Sc	5.66 ± 0.25	n.m.	n.m.	n.m.
Ti	143 ± 6	n.m.	n.m.	n.m.
V	65.7 ± 2.2	n.m.	n.m.	n.m.
Cr	2132 ± 79	n.m.	n.m.	n.m.
Cr_2O_3	0.31 ± 0.01	n.m.	n.m.	n.m.
Mn	2083 ± 66	n.m.	n.m.	n.m.
Co	84.4 ± 2.9	n.m.	n.m.	n.m.
Ni	170 ± 6	n.m.	n.m.	n.m.
Cu	b.d.	n.m.	n.m.	n.m.
Zn	4.88 ± 0.39	n.m.	n.m.	n.m.
Ga	b.d.	n.m.	n.m.	n.m.
Ge	b.d.	n.m.	n.m.	n.m.
Rb	b.d.	n.m.	n.m.	n.m.
Sr	b.d.	n.m.	n.m.	n.m.
Y	0.14 ± 0.03	n.m.	n.m.	n.m.
Zr	0.07 ± 0.03	n.m.	n.m.	n.m.
Nb	b.d.	n.m.	n.m.	n.m.
Cs	b.d.	n.m.	n.m.	n.m.
Ba	b.d.	n.m.	n.m.	n.m.
La	b.d.	n.m.	n.m.	n.m.
Ce	b.d.	n.m.	n.m.	n.m.
Pr	b.d.	n.m.	n.m.	n.m.
Nd	b.d.	n.m.	n.m.	n.m.
Sm	b.d.	n.m.	n.m.	n.m.
Eu	b.d.	n.m.	n.m.	n.m.
Gd	b.d.	n.m.	n.m.	n.m.
Tb	b.d.	n.m.	n.m.	n.m.
Dy	b.d.	n.m.	n.m.	n.m.
Ho	b.d.	n.m.	n.m.	n.m.
Er	0.04 ± 0.02	n.m.	n.m.	n.m.
Tm	b.d.	n.m.	n.m.	n.m.
Yb	b.d.	n.m.	n.m.	n.m.
Lu	0.02 ± 0.01	n.m.	n.m.	n.m.

Table 7.6 (continued)

	090811_213 ,311_1C_p43	090811_151 ,312_C_p136	090811_679 ,316_C_p32
Major and minor elements measured by WDS EMPA (wt%)			
SiO_2	34.6 ± 0.2	35.4 ± 0.2	36.5 ± 0.2
TiO_2	0.13 ± 0.01	0.08 ± 0.01	0.07 ± 0.01
Al_2O_3	<0.01	0.03 ± 0.01	<0.01
Cr_2O_3	0.08 ± 0.01	0.17 ± 0.02	0.14 ± 0.01
FeO	39.9 ± 0.3	34.4 ± 0.3	31.6 ± 0.2
MnO	0.38 ± 0.02	0.37 ± 0.02	0.32 ± 0.02
MgO	24.6 ± 0.2	28.0 ± 0.6	32.7 ± 0.5
CaO	0.30 ± 0.01	0.33 ± 0.01	0.26 ± 0.01
Na_2O	<0.01	<0.01	<0.01
P_2O_5	0.02 ± 0.01	0.03 ± 0.01	<0.01
V_2O_3	<0.01	<0.01	<0.01
Total	100.1	98.8	101.6
Mg#	52.4	59.2	64.8
Minor and trace elements measured by LA-ICP-MS (ppm; wt% for MgO and Cr_2O_3)			
Mg	158074 ± 5395	196663 ± 6995	205465 ± 7590
MgO	26.2 ± 0.9	32.6 ± 1.2	34.1 ± 1.3
Al	30.2 ± 1.1	107.5 ± 4.2	40.5 ± 1.6
K	b.d.	b.d.	b.d.
Ca	1261 ± 77	1590 ± 203	1762 ± 129
Sc	7.18 ± 0.31	9.12 ± 0.65	7.86 ± 0.41
Ti	325 ± 13	259 ± 14	246 ± 12
V	19.0 ± 0.7	55.2 ± 2.2	26.9 ± 1.0
Cr	563 ± 22	1124 ± 44	655 ± 26
Cr_2O_3	0.08 ± 0.01	0.16 ± 0.01	0.10 ± 0.01
Mn	2927 ± 93	2827 ± 90	2440 ± 77
Co	80.4 ± 2.7	78.5 ± 3.2	84.7 ± 3.0
Ni	28.6 ± 1.2	8.14 ± 1.23	68.7 ± 3.1
Cu	b.d.	b.d.	0.78 ± 0.20
Zn	2.81 ± 0.35	2.63 ± 0.90	10.4 ± 0.8
Ga	0.10 ± 0.03	b.d.	0.58 ± 0.10
Ge	b.d.	b.d.	2.98 ± 0.39
Rb	b.d.	b.d.	0.49 ± 0.08
Sr	b.d.	b.d.	0.26 ± 0.05
Y	1.60 ± 0.09	0.19 ± 0.07	0.84 ± 0.08
Zr	0.14 ± 0.05	b.d.	0.73 ± 0.13
Nb	b.d.	b.d.	0.25 ± 0.06
Cs	0.01 ± 0.00	b.d.	0.15 ± 0.03
Ba	b.d.	b.d.	0.81 ± 0.27
La	b.d.	b.d.	0.15 ± 0.04
Ce	0.01 ± 0.00	b.d.	0.17 ± 0.03
Pr	b.d.	b.d.	0.08 ± 0.03
Nd	b.d.	b.d.	0.71 ± 0.15
Sm	b.d.	b.d.	0.57 ± 0.18
Eu	b.d.	b.d.	0.18 ± 0.04
Gd	0.07 ± 0.02	b.d.	0.55 ± 0.16
Tb	b.d.	b.d.	0.13 ± 0.03
Dy	0.19 ± 0.03	b.d.	0.58 ± 0.10
Ho	0.05 ± 0.01	b.d.	0.16 ± 0.03
Er	0.24 ± 0.04	b.d.	0.32 ± 0.07
Tm	0.05 ± 0.01	b.d.	0.12 ± 0.02
Yb	0.40 ± 0.05	b.d.	0.54 ± 0.11
Lu	0.06 ± 0.01	b.d.	0.12 ± 0.02

Values which were below instrument detection limits (b.d.) or not measured (n.m.) have been indicated.

Table 7.7: Major and minor element abundances (wt%) for representative ilmenite phases within 12003,310; ,311; ,312; ,314; ,316; ,317. Errors for major and minor elements are 1σ standard deviations calculated from repeat measurements of the BCR-2 USGS basaltic glass reference material.

	170811_419 ,310_1C_p153	071011_95 ,310_2D_p85	271011_247 ,310_3A_p6	271011_116 ,310_4A_p71
SiO_2	<0.01	0.03 ± 0.01	0.02 ± 0.01	0.05 ± 0.01
TiO_2	54.5 ± 1.6	53.6 ± 1.0	53.4 ± 1.3	52.1 ± 1.6
Al_2O_3	b.d.	0.13 ± 0.01	0.13 ± 0.01	0.10 ± 0.01
Cr_2O_3	0.22 ± 0.02	0.25 ± 0.02	0.28 ± 0.02	0.45 ± 0.02
FeO	45.9 ± 0.3	46.1 ± 0.3	46.9 ± 0.3	44.8 ± 0.2
MnO	0.36 ± 0.02	0.29 ± 0.03	0.32 ± 0.03	0.32 ± 0.02
MgO	0.28 ± 0.01	1.12 ± 0.04	0.18 ± 0.01	0.44 ± 0.01
CaO	0.03 ± 0.01	0.08 ± 0.01	<0.01	0.20 ± 0.01
Na_2O	0.02 ± 0.01	0.06 ± 0.01	0.07 ± 0.01	b.d.
V_2O_3	0.12 ± 0.02	0.11 ± 0.01	0.14 ± 0.02	b.d.
Total	101.5	101.8	101.5	98.4

	090811_418 ,311_1C_p228	090811_613 ,314_D_p171	090811_750 ,316_C_p98	170811_154 ,317_D_p110
SiO_2	0.02 ± 0.01	0.02 ± 0.01	b.d.	b.d.
TiO_2	54.9 ± 1.0	53.9 ± 1.0	55.9 ± 0.9	54.6 ± 0.9
Al_2O_3	b.d.	b.d.	b.d.	b.d.
Cr_2O_3	0.42 ± 0.02	0.26 ± 0.02	0.47 ± 0.02	0.46 ± 0.02
FeO	43.0 ± 0.3	46.3 ± 0.3	38.8 ± 0.2	45.7 ± 0.3
MnO	0.34 ± 0.03	0.35 ± 0.02	0.34 ± 0.02	0.36 ± 0.02
MgO	2.79 ± 0.03	0.24 ± 0.01	5.44 ± 0.03	0.55 ± 0.01
CaO	b.d.	b.d.	<0.01	b.d.
Na_2O	b.d.	<0.01	b.d.	0.05 ± 0.01
V_2O_3	0.20 ± 0.04	0.15 ± 0.02	0.22 ± 0.03	0.18 ± 0.02
Total	101.7	101.2	101.2	101.8

Values which were below instrument detection limits (b.d.) have been indicated.

Table 7.8: Major and minor element abundances (wt%) for representative spinel phases within 12003,310; ,311; ,312; ,314; ,316; ,317. Errors for major and minor elements are 1σ standard deviations.

	170811_363 ,310_1C_p102	271011_219 ,310_1C_p5	071011_78 ,310_2D_p68	271011_181 ,310_2D_p7	071011_244 ,310_3A_p80
SiO_2	0.05 ± 0.01	0.10 ± 0.01	0.09 ± 0.01	0.09 ± 0.01	0.03 ± 0.01
TiO_2	26.2 ± 0.9	3.97 ± 0.10	30.6 ± 0.6	4.39 ± 0.08	23.4 ± 0.5
Al_2O_3	3.35 ± 0.04	12.3 ± 0.2	2.60 ± 0.08	12.0 ± 0.3	5.82 ± 0.10
Cr_2O_3	13.3 ± 0.1	48.7 ± 0.1	5.65 ± 0.05	46.7 ± 0.1	18.1 ± 0.1
FeO	54.7 ± 0.3	27.6 ± 0.2	59.7 ± 0.4	28.9 ± 0.1	46.9 ± 0.3
MnO	0.33 ± 0.03	0.35 ± 0.03	0.32 ± 0.03	0.34 ± 0.03	0.35 ± 0.03
MgO	0.85 ± 0.01	7.14 ± 0.23	0.53 ± 0.02	5.94 ± 0.12	3.18 ± 0.09
CaO	b.d.	b.d.	0.17 ± 0.01	<0.01	0.14 ± 0.02
Na_2O	b.d.	0.02 ± 0.01	0.05 ± 0.01	b.d.	0.04 ± 0.01
V_2O_3	0.41 ± 0.07	0.93 ± 0.15	0.25 ± 0.02	1.04 ± 0.11	0.63 ± 0.08
Total	99.2	101.0	99.9	99.5	98.6

	271011_222 ,310_3A_p2	271011_251 ,310_4A_p88	271011_213 ,310_4A_p81	090811_415 ,311_1C_p225	090811_403 ,311_1C_p213
SiO_2	0.11 ± 0.01	0.09 ± 0.01	0.09 ± 0.01	0.03 ± 0.01	0.05 ± 0.01
TiO_2	3.93 ± 0.10	29.0 ± 0.7	3.69 ± 0.04	29.1 ± 0.6	16.6 ± 0.3
Al_2O_3	12.2 ± 0.2	3.04 ± 0.06	12.2 ± 0.2	3.11 ± 0.02	9.75 ± 0.06
Cr_2O_3	48.0 ± 0.1	10.1 ± 0.1	47.8 ± 0.1	9.6 ± 0.1	26.6 ± 0.1
FeO	27.0 ± 0.2	55.8 ± 0.4	25.5 ± 0.2	55.6 ± 0.4	39.7 ± 0.3
MnO	0.33 ± 0.03	0.35 ± 0.03	0.32 ± 0.02	0.32 ± 0.03	0.30 ± 0.03
MgO	6.78 ± 0.22	1.38 ± 0.04	8.09 ± 0.14	1.56 ± 0.01	4.38 ± 0.04
CaO	b.d.	0.12 ± 0.01	b.d.	<0.01	b.d.
Na_2O	0.05 ± 0.01	0.03 ± 0.01	b.d.	<0.01	b.d.
V_2O_3	0.92 ± 0.15	0.34 ± 0.05	0.94 ± 0.18	0.32 ± 0.06	0.66 ± 0.13
Total	99.3	100.2	98.6	99.7	98.0

	271011_233 ,312_C_p4	271011_234 ,312_C_p5	090811_527 ,314_D_p95	271011_237 ,316_C_p5	271011_212 ,316_C_p3
SiO_2	0.09 ± 0.01	0.07 ± 0.01	0.05 ± 0.01	<0.01	0.04 ± 0.01
TiO_2	26.7 ± 0.6	5.08 ± 0.12	32.9 ± 0.6	23.8 ± 0.6	11.0 ± 0.1
Al_2O_3	2.68 ± 0.05	11.7 ± 0.2	2.03 ± 0.05	5.80 ± 0.12	11.4 ± 0.2
Cr_2O_3	12.1 ± 0.1	46.8 ± 0.1	2.8 ± 0.0	20.1 ± 0.1	37.3 ± 0.1
FeO	58.4 ± 0.4	27.1 ± 0.2	62.4 ± 0.5	45.2 ± 0.3	34.4 ± 0.2
MnO	0.29 ± 0.03	0.31 ± 0.03	0.29 ± 0.03	0.39 ± 0.03	0.36 ± 0.03
MgO	0.31 ± 0.01	7.52 ± 0.24	0.13 ± 0.01	5.37 ± 0.17	5.82 ± 0.10
CaO	0.15 ± 0.01	b.d.	b.d.	0.04 ± 0.01	b.d.
Na_2O	0.06 ± 0.01	b.d.	b.d.	0.05 ± 0.01	0.04 ± 0.01
V_2O_3	0.27 ± 0.04	1.12 ± 0.18	0.17 ± 0.02	0.54 ± 0.09	0.90 ± 0.17
Total	101.0	99.8	100.8	101.3	101.2

Values which were below instrument detection limits (b.d.) have been indicated.

Table 7.9: Major and minor element abundances (wt%) for miscellaneous silicate phases within 12003,310; ,311; ,314; ,317. Errors are 1σ standard deviations.

	170811_395 ,310_1C_p134 Silica	071011_240 ,310_3A_p76 Silica	090811_634 ,314_D_p192 Silica	090811_788 ,317_D_p31 Silica	271011_209 ,311_1C_p3 K-Feldspar
SiO_2	95.6 ± 0.4	94.9 ± 0.4	97.0 ± 0.5	97.5 ± 0.9	62.3 ± 0.6
TiO_2	0.36 ± 0.01	0.34 ± 0.01	0.18 ± 0.01	0.32 ± 0.01	0.36 ± 0.00
Al_2O_3	0.77 ± 0.01	1.24 ± 0.02	0.47 ± 0.01	0.39 ± 0.03	19.0 ± 0.4
Cr_2O_3	b.d.	b.d.	b.d.	b.d.	0.02 ± 0.01
FeO	0.32 ± 0.01	0.27 ± 0.01	0.28 ± 0.01	0.08 ± 0.01	0.88 ± 0.01
MnO	<0.01	<0.01	0.02 ± 0.01	0.02 ± 0.01	<0.01
MgO	<0.01	b.d.	b.d.	0.02 ± 0.01	0.06 ± 0.01
CaO	0.28 ± 0.01	0.45 ± 0.05	0.03 ± 0.01	0.03 ± 0.01	0.26 ± 0.01
K_2O	0.04 ± 0.01	0.06 ± 0.01	0.30 ± 0.01	0.23 ± 0.01	14.5 ± 0.1
Na_2O	0.17 ± 0.01	0.24 ± 0.01	0.04 ± 0.01	0.14 ± 0.01	0.47 ± 0.01
P_2O_5	b.d.	<0.01	<0.01	b.d.	0.06 ± 0.01
BaO	b.d.	b.d.	b.d.	b.d.	3.38 ± 0.14
Total	97.5	97.5	98.3	98.7	101.3

	271011_95 ,314_D_p5 K-Feldspar	271011_96 ,314_D_p6 K-Feldspar	27102011_72 ,310_1C_p1 High-K glass	27102011_92 ,314_D_p2 High-K glass	17082011_229 ,317_D_p180 High-K glass
SiO_2	65.5 ± 0.5	65.0 ± 0.5	76.9 ± 0.3	76.2 ± 0.6	78.2 ± 0.2
TiO_2	0.15 ± 0.01	0.11 ± 0.01	0.43 ± 0.01	0.41 ± 0.01	0.57 ± 0.01
Al_2O_3	17.7 ± 0.4	17.1 ± 0.4	11.6 ± 0.2	11.7 ± 0.3	12.1 ± 0.2
Cr_2O_3	b.d.	b.d.	b.d.	<0.01	<0.01
FeO	0.70 ± 0.01	0.58 ± 0.01	2.23 ± 0.01	1.25 ± 0.01	1.08 ± 0.01
MnO	0.03 ± 0.01	b.d.	0.02 ± 0.01	0.02 ± 0.01	b.d.
MgO	b.d.	b.d.	<0.01	<0.01	b.d.
CaO	0.28 ± 0.01	0.36 ± 0.01	0.92 ± 0.01	1.11 ± 0.01	0.66 ± 0.01
K_2O	15.3 ± 0.1	14.9 ± 0.1	6.86 ± 0.06	7.93 ± 0.06	7.81 ± 0.07
Na_2O	0.23 ± 0.01	0.14 ± 0.01	0.41 ± 0.02	0.32 ± 0.01	1.06 ± 0.02
P_2O_5	0.04 ± 0.01	0.04 ± 0.01	0.14 ± 0.01	0.18 ± 0.01	0.14 ± 0.01
BaO	b.d.	b.d.	0.43 ± 0.08	b.d.	b.d.
Total	99.9	98.3	99.9	99.2	101.6

Values which were below instrument detection limits (b.d.) have been indicated.

Table 7.10: Major and minor element abundances (wt%) of metal and sulfide grains within 12003,310; ,311; ,312; ,314; ,316; ,317. Errors for major and minor elements are 1σ standard deviations.

	281011_71 ,310_2D_p5 FeNi metal	281011_60 ,310_3A_p11 FeNi metal	281011_25 ,311_1C_p6 FeNi metal	281011_31 ,312_C_p4 FeNi metal	281011_35 ,314_D_p2 FeNi metal
Si	0.02 ± 0.01	0.03 ± 0.01	b.d.	0.03 ± 0.01	0.02 ± 0.01
Ti	0.13 ± 0.01	0.16 ± 0.01	0.22 ± 0.01	0.09 ± 0.01	b.d.
Cr	b.d.	<0.01	0.05 ± 0.01	0.06 ± 0.01	b.d.
Fe	93.5 ± 0.2	99.5 ± 0.2	96.9 ± 0.2	96.4 ± 0.2	99.3 ± 0.2
Cu	0.03 ± 0.02	0.08 ± 0.02	b.d.	b.d.	b.d.
Mn	b.d.	b.d.	b.d.	0.03 ± 0.01	b.d.
Mg	<0.01	b.d.	b.d.	0.02 ± 0.01	b.d.
Ni	5.68 ± 0.03	0.54 ± 0.02	3.18 ± 0.02	3.65 ± 0.03	0.05 ± 0.01
Co	1.32 ± 0.02	0.54 ± 0.01	1.09 ± 0.01	1.36 ± 0.02	0.99 ± 0.01
Si	0.02 ± 0.01	0.14 ± 0.01	b.d.	<0.01	0.75 ± 0.01
Total	100.7	101.0	101.4	101.6	101.1

	281011_42 ,316_C_p2 FeNi metal	281011_68 ,317_D_p8 FeNi metal	281011_14 ,310_1C_p6 Troilite	281011_73 ,310_2D_p7 Troilite
Si	0.02 ± 0.01	<0.01	0.02 ± 0.01	0.02 ± 0.01
Ti	b.d.	0.03 ± 0.01	0.51 ± 0.02	0.04 ± 0.01
Cr	0.02 ± 0.01	<0.01	0.02 ± 0.01	b.d.
Fe	88.4 ± 0.2	100.4 ± 0.2	63.7 ± 0.1	63.1 ± 0.1
Cu	0.12 ± 0.02	b.d.	b.d.	0.28 ± 0.02
Mn	b.d.	b.d.	b.d.	b.d.
Mg	b.d.	b.d.	b.d.	b.d.
Ni	11.9 ± 0.0	0.28 ± 0.01	<0.01	0.02 ± 0.01
Co	1.19 ± 0.01	1.21 ± 0.01	0.03 ± 0.01	<0.01
Si	0.03 ± 0.01	0.06 ± 0.01	37.3 ± 0.1	37.1 ± 0.1
Total	101.8	101.9	101.6	100.6

	281011_53 ,310_3A_p4 Troilite	281011_2 ,310_4A_p2 Troilite	281011_24 ,311_1C_p5 Troilite	281011_34 ,314_D_p1 Troilite
Si	0.02 ± 0.01	0.04 ± 0.01	0.02 ± 0.01	0.02 ± 0.01
Ti	0.03 ± 0.01	0.24 ± 0.01	b.d.	0.02 ± 0.01
Cr	b.d.	0.14 ± 0.01	b.d.	b.d.
Fe	63.9 ± 0.1	61.7 ± 0.1	63.3 ± 0.1	64.3 ± 0.1
Cu	0.07 ± 0.02	b.d.	0.04 ± 0.02	0.04 ± 0.02
Mn	b.d.	0.02 ± 0.01	b.d.	b.d.
Mg	b.d.	0.02 ± 0.01	b.d.	b.d.
Ni	b.d.	0.03 ± 0.01	b.d.	b.d.
Co	0.02 ± 0.01	0.02 ± 0.00	b.d.	b.d.
Si	37.4 ± 0.1	37.2 ± 0.1	37.8 ± 0.1	37.6 ± 0.1
Total	101.4	99.4	101.2	102.0

Values which were below instrument detection limits (b.d.) have been indicated.

Chapter 8

Summary

8.1 Lunar meteorite Northeast Africa 001

The analysis of the feldspathic regolith breccia NEA 001 has demonstrated the importance of lunar meteorites in improving our understanding of lunar geological diversity. Multiple lithologies have been identified in a single ∼12×9 mm section of the meteorite. These include feldspathic impact melt, ferroan noritic anorthosite, magnesian feldspathic clasts, and low-Ti and VLT basalts.

The largest of the VLT basalt clasts exhibits low-ITE concentrations, lower abundances of LREE than HREE, and a REE pattern with a positive Eu-anomaly. The low-ITE concentrations indicate that the clast originated from a parent melt that did not assimilate KREEP material. The positive Eu-anomalies and low-ITE concentrations are interpretated as evidence that the VLT material crystallised from a parent melt derived from early mantle cumulates that formed prior to the separation of plagioclase in the lunar magma ocean. This explanation has been previously suggested for the basaltic meteorite MIL 05035 (*Joy et al.*, 2008; *Liu et al.*, 2009). Compositional similarities are also noted between the VLT basaltic material in NEA 001 and the basaltic meteorite Kalahari 009 (*Sokol et al.*, 2008). It has been suggested that Kalahari 009 derives from a cryptomare source and may be a product of some of the earliest (∼4.35 Ga) lunar volcanism (*Terada et al.*, 2007; *Anand and Terada*, 2008).

The feldspathic impact lithologies in NEA 001 have more mafic bulk compositions than estimations for the composition of the upper feldspathic lunar crust (*Korotev et al.*, 2003) and are more Sc-rich than most of the Apollo 16 feldspathic impact melts (*Korotev*, 1994). This may indicate that the impact melts have incorporated more mafic lower crustal material (*Pieters et al.*, 1997; *Wieczorek and Zuber*, 2001). The impact melts have low-ITE concentrations when compared with those found in lower crustal

material sampled by Apollo mafic impact melts (*Jolliff et al.*, 1998). This suggests that they originated from a KREEP-poor region of the Moon.

The feldspathic nature of the sample, lack of a KREEP component, and the presence of magnesian feldspathic clasts (*Takeda et al.*, 2006), suggest that the meteorite has been sourced from the Outer-Feldspathic Highlands Terrane (*Jolliff et al.*, 2000), probably on the lunar farside. Previous studies investigating lateral mixing processes in the lunar regolith suggest that most foreign components in a given area will originate from within ∼1000 km (*Petro and Pieters*, 2007; *Zeigler et al.*, 2006), and based on this assessment the VLT basaltic clasts in NEA 001 would imply the presence of a buried near-surface reservoir of VLT deposits (i.e. VLT cryptomaria) within the farside crust.

8.2 Apollo 12 basaltic diversity

A total of sixteen separate samples have been studied from the 12003 soil. Analysis of these samples indicates that all three of the major Apollo 12 basaltic suites (olivine, ilmenite and pigeonite basalts) are represented in the soil collected at a single location near the Lunar Module landing site.

One sample (12003,314) has been identified as a possible addition to the feldspathic suite, currently consisting of only one other sample (12038). 12003,314_D has a subophitic-intergranular texture, similar to that of 12038 and several pigeonite basalts (e.g. 12007, 12031 and 12039). It has a higher modal abundance of plagioclase (55%) and bulk Al_2O_3 (16.5 wt%) than any other Apollo 12 basalt. The mineral chemistries of ,314_D are in good agreement with those reported in both 12038 and the pigeonite basalts. However, given the sample's bulk characteristics and textural similarity to 12038, it is interpreted as most likely being a feldspathic basalt. If correct, this has important implications for the diversity of Apollo 12 basalts as it would strengthen the argument that the feldspathic basalts are not exotic to the Apollo 12 site, but represent a poorly sampled basaltic flow local to the landing site (*Neal et al.*, 1994a).

Two samples (12003,308_3A and 12003,316) have been identified in the 12003 soil which may represent a previously unrecognised basaltic suite. These have gabbroic-cumulate textures, comparatively compositionally equilibrated minerals, and olivines with higher Ti/V ratios than are currently reported for any other Apollo 12 basalts. Both samples have relatively high abundances of olivine and low abundances of pyroxene relative to other Apollo 12 basalts, although these modal mineralogies are to be viewed with caution due to the comparatively coarse grain size (up to ∼0.8 mm) of the samples when compared with the overall surface areas studied (<4.2 mm^2).

The range of textures and mineral chemistries in the 12003 samples indicates a variety of crystallisation conditions. The compositional zoning identified in the phases of a majority of the samples is consistent with fractional crystallisation resulting, for example, in the concentration of REE towards the rims of phases. This is best illustrated with three samples (12003,308_2A; ,308_4A; and ,308_8A) which are proposed as products of a fractionating parent melt, with ,308_2A representing the most evolved of the three. The more coarse grained samples (12003,308_3A; ,308_5A; ,308_7A; and ,316) are interpreted as cumulates formed through slow equilibrium crystallisation towards the base of thick lava flows (*Reid*, 1971) or prior to eruption.

One granulitic impactite and two breccias were also identified in the 12003,308 samples (,308_6A; ,308_9A; and ,308_10A). The granulitic impactite (,308_6A) is more aluminous than most of the materials collected by the Apollo 12 mission, contains plagioclase and pyroxene with high REE contents, and has a high modal abundance of merrilite. These features indicate that the sample has high concentrations of KREEP and is exotic to the Apollo 12 site, possibly originating from the Copernicus, Reinhold or Lansberg Craters (*Meyer et al.*, 1971; *Wasson and Baedecker*, 1972; *Barra et al.*, 2006; *Korotev et al.*, 2011), and was introduced to the Apollo 12 area by lateral impact ejecta mixing processes. The diverse range of clast types and mineral compositions in the breccia ,308_9A indicate that it is a polymict breccia containing basaltic material originating from several different lava flows. Conversely, ,308_10A comprises a less varied range of materials, which are texturally and compositionally similar to several pigeonite basalts. Therefore, ,308_10A is interpreted as being a monomict breccia generated from pigeonite basalt.

Current interpretations of the differences between the samples' mineral chemistry, and the significance of these differences are limited by the availability of trace element mineral chemistry data for other Apollo 12 basalts. However, in addition to this project, there is also ongoing work by *O'Sullivan and Neal* (2008, 2010a,b), *O'Sullivan et al.* (2011) and *Fagan et al.* (2012) examining the petrogenesis of the Apollo 12 basaltic suites using trace element mineral chemistry. Studies such as these will hopefully begin to provide new datasets allowing for more incisive comparisons to be made.

8.3 Ongoing and future Work

The most significant ongoing work in the basaltic diversity project involves radioisotope dating of the B-splits (see Chapter 2) for each of the soil samples using the ^{40}Ar-^{39}Ar method (e.g. *Turner* 1970b, 1971). The primary goal of these analyses is to obtain

crystallisation ages for the basalts. This may provide further evidence of whether or not the samples originated from separate parent melts, assist in the identification of basaltic samples which are exotic to the Apollo 12 site, and help address the top-level science goal of investigating the duration of basaltic volcanism on the Moon. An initial analysis of the calibration sample 12038 (*Snape et al.*, 2011b) determined a crystallisation age of 3.14±0.04 Ga. This is within error of the Rb-Sr age (3.28±0.21 Ga) reported by *Compston et al.* (1971) and the Sm-Nd age (3.28±0.23 Ga) reported by *Nyquist et al.* (1981). The ^{40}Ar-^{39}Ar dating method can also provide information relating to the shock history of samples (e.g. *Fernandes et al.* 2003). Opportunities for additional radioisotope dating methods are also being investigated, including U-Pb dating of zircons and phosphate phases in the samples.

There are a number of additional ways in which the NEA 001 and Apollo 12 basaltic diversity studies could be continued. Several of these are discussed here:

- Identification of the same lithologies (e.g. comparatively Sc-rich feldspathic impact lithologies, and VLT basalt with low ITE concentrations) in other samples of NEA 001 would provide an opportunity to assess how representative the clasts in this sample are. This, in turn, would aid greatly in interpreting their significance with regard to the meteorite's provenance.

- In addition to 12003, several further Apollo 12 soil samples remain to be analysed as part of the Apollo 12 basaltic diversity project (e.g. 12023; *Alexander et al.* 2011). The locations at which these samples were collected are indicated in Fig. 8.1.

- *Biggar et al.* (1971) performed experiments to determine crystallisation sequences and liquidus temperatures for several Apollo 12 basalts, including 12022 and 12038. The major element bulk compositions obtained for 12022,304_C and 12038,263_A could be used to generate crystallisation sequences with the MELTS modelling code (*Ghiorso and Sack*, 1995; *Asimow and Ghiorso*, 1998). This would provide an opportunity to test the implementation of the MELTS code which was used to determine crystallisation sequences for NEA 001.

- The bulk compositions obtained for the 12003 chips could also be used to investigate liquidus temperatures and crystallisation sequences for these samples with the MELTS modelling code (*Ghiorso and Sack*, 1995; *Asimow and Ghiorso*, 1998). The results from this modelling could then be compared with the inferences based on the textures and mineral chemistries of the samples. Similar comparisons were

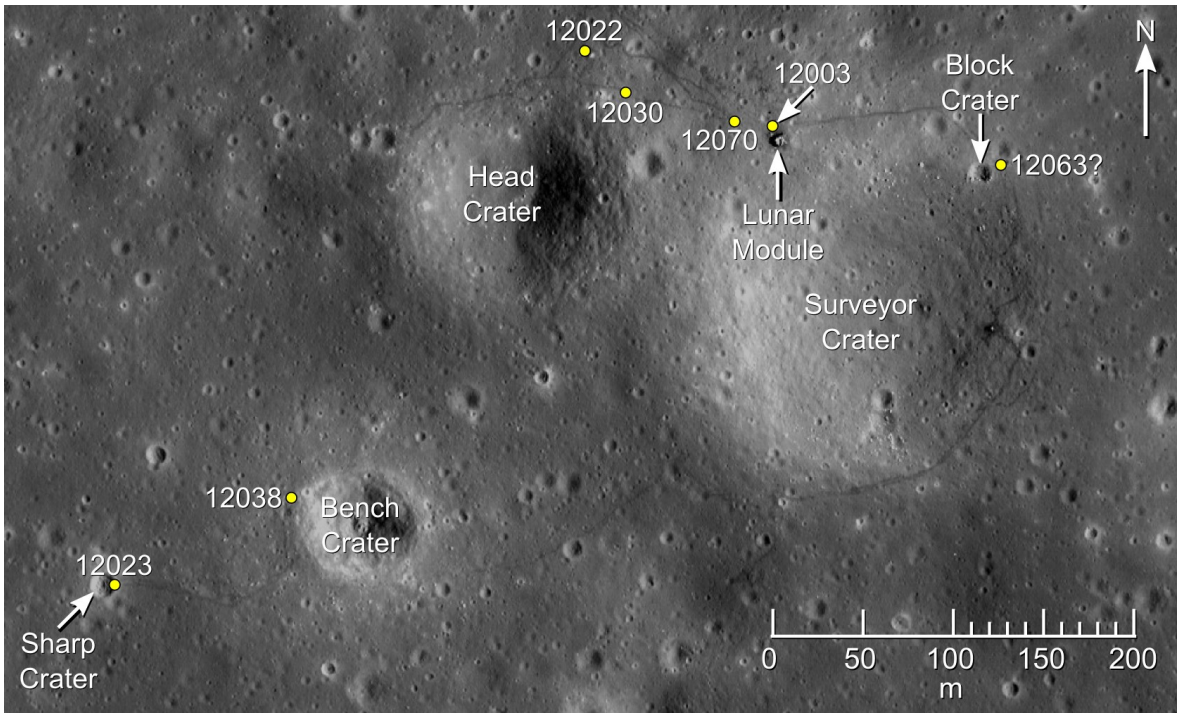

Figure 8.1: Map of the Apollo 12 landing site indicating the collection locations for the samples being analysed in the basaltic diversity project. Background image from the Lunar Reconnaissance Orbiter Narrow Angle Camera frame M175428601R (NASA/GSFC/Arizona State University). Sample locations have been based on maps of the landing site produced by the *Lunar Sample Preliminary Examination Team* (*LSPET* 1970a; 1970b) and additional information in the Apollo 12 Preliminary Science Report (*LSPET* 1970b).

made by *Joy et al.* (2006) between MELTS models and mineral chemistries of the LaPaz Icefield lunar meteorite.

- Radioisotope dating of the VLT basalt clasts in NEA 001 would be a valuable test of the hypothesis that these clasts represent products of some of the early lunar volcanism (*Terada et al.*, 2007).

- Crystal size distributions have been investigated in several other studies of Apollo basalts as a means to investigate crystallisation and melt evolution (*O'Sullivan and Neal*, 2008; *O'Sullivan et al.*, 2011, 2012). Such analyses could be performed on the 12003 samples using BSE images which have already been obtained and would not, therefore, require the collection of any additional data.

- The degree to which the 12003 samples have been shock metamorphosed by impact processes is currently unclear. Understanding this may help in the interpretation of exsolution features such as those noted in 12003,311. It has not been possible, for example, to determine whether plagioclase has been transformed into maskelynite (*Stöffler et al.*, 1991). Both Raman spectroscopy and electron backscatter

diffraction would be capable of revealing this.

- The LA-ICP-MS analyses of the 12003 mineral trace element abundances required measurements were made using 55 μm spots. The compositional zoning in the phases of several samples occurs on a smaller scale than this, making it hard to ensure that the areas analysed were homogeneous. Ion microprobe analyses of such phases may allow for trace element abundances to be obtained from smaller spot sizes.

- Improving resolution of remote sensing datasets may help to assess the range in basaltic composition and the effects of regolith mixing processes around the Apollo 12 site. For example, the Moon Mineralogy Mapper (M^3), which flew on the Indian Space Research Organization's Chandrayaan-1 mission, was able to make visible and near-infrared spectral measurements with an optimum resolution of 70 m/pixel (*Pieters et al.*, 2011). Such high levels of resolution may enable studies of the Apollo 12 site analogous to those performed on a larger scale by *Weider et al.* (2010), who used multispectral reflectance data from the Clementine mission to examine impact ejecta from craters penetrating lava flows, allowing them to infer thicknesses of individual flows.

Bibliography

Adler, I., Trombka, J. I., Yin, L. I., Gorenstein, P., Bjorkholm, P., and Gerard, J. (1973), Lunar composition from Apollo orbital measurements, *Naturwissenschaften*, *60*, 231–242, doi:10.1007/BF00625711.

Albee, A. L., Quick, J. E., and Chodos, A. A. (1977), Source and Magnitude of Errors in "Broad-Beam Analysis" (DBA) with the Electron Probe, in *Lunar and Planetary Science Conference*, vol. 8, pp. 7–9.

Alexander, E. C., Davis, P. K., Lewis, R. S., and Reynolds, J. H. (1972a), Rare Gas Analyses on Neutron Irradiated Lunar Samples, in *Lunar and Planetary Science Conference*, vol. 3, pp. 12–14.

Alexander, E. C., Jr., Davis, P. K., and Reynolds, J. H. (1972b), Rare-gas analyses on neutron irradiated Apollo 12 samples., in *Lunar and Planetary Science Conference*, vol. 3, edited by Metzger, A. E., Trombka, J. I., Peterson, L. E., Reedy, R. C., and Arnold, J. R., pp. 1787–1795.

Alexander, L., Snape, J. F., Crawford, I. A., Joy, K. H., and Burgess, R. (2011), A Study of the Mineralogy and Textures of Basalt Fines from Apollo 12 Regolith Sample 12023-,155, *Meteoritics and Planetary Science Supplement*, *74*, 5084.

Anand, M., and Terada, K. (2008), Timing and Duration of Mare Basalt Magmatism: Constraints from Lunar Samples, in *Lunar and Planetary Science Conference*, vol. 39, p. 2155.

Anand, M., Taylor, L. A., Misra, K. C., Demidova, S. I., and Nazarov, M. A. (2003), KREEPy lunar meteorite Dhofar 287A: A new lunar mare basalt, *Meteoritics and Planetary Science*, *38*, 485–499, doi:10.1111/j.1945-5100.2003.tb00022.x.

Anders, E., and Grevesse, N. (1989), Abundances of the elements - Meteoritic and solar, *Geochimica et Cosmochimica Acta*, *53*, 197–214, doi:10.1016/0016-7037(89)90286-X.

Anderson, A. T., Jr., and Smith, J. V. (1971), Nature, occurrence, and exotic origin of "gray mottled" (Luny Rock) basalts in Apollo 12 soils and breccias, in *Lunar and Planetary Science Conference*, vol. 2, pp. 431–438.

Antonenko, I. (1999), Global Estimates of Cryptomare Deposits: Implications for Lunar Volcanism, in *Lunar and Planetary Science Conference*, vol. 30, p. 1703.

Antonenko, I., Head, J. W., Mustard, J. F., and Ray Hawke, B. (1995), Criteria for the Detection of Lunar Cryptomaria, *Earth Moon and Planets*, *69*(2), 141–172, doi:10.1007/BF00613096.

Arai, T., and Warren, P. H. (1999), Lunar meteorite QUE 94281: Glass compositions and other evidence for launch pairing with Yamato-793274, *Meteoritics and Planetary Science*, *34*, 209–234, doi:10.1111/j.1945-5100.1999.tb01747.x.

Arai, T., Warren, P. H., and Takeda, H. (1996), Four Lunar Mare Meteorites: Crystallization Trends of Pyroxenes and Spinels, *Meteoritics and Planetary Science*, *31*, 877–892, doi:10.1111/j.1945-5100.1996.tb02121.x.

Arai, T., Takeda., H., and Miyamoto, M. (2006), Experimental petrology of ancient lunar mare basalt Asuka-881757: Spinel crystallization as a petrologic indicator, *Antarctic Meteorite Research*, *19*, 1–19.

Arai, T., Takeda, H., Yamaguchi, A., and Ohtake, M. (2008), A new model of lunar crust: asymmetry in crustal composition and evolution, *Earth, Planets, and Space*, *60*(4), 433–444.

Arai, T., Hawke, B. R., Giguere, T. A., Misawa, K., Miyamoto, M., and Kojima, H. (2010), Antarctic lunar meteorites Yamato-793169, Asuka-881757, MIL 05035, and MET 01210 (YAMM): Launch pairing and possible cryptomare origin, *Geochimica et Cosmochimica Acta*, *74*, 2231–2248, doi:10.1016/j.gca.2009.11.019.

Arnold, J. R. (1975), Monte Carlo simulation of turnover processes in the lunar regolith, in *Lunar and Planetary Science Conference*, vol. 6, pp. 2375–2395.

Arvidson, R., Drozd, R. J., Hohenberg, C. M., Morgan, C. J., and Poupeau, G. (1975), Horizontal transport of the regolith, modification of features, and erosion rates on the lunar surface, *Moon*, *13*, 67–79, doi:10.1007/BF00567508.

Asimow, P. D., and Ghiorso, M. S. (1998), Algorithmic modifications extending MELTS to calculate subsolidus phase relations, *American Mineralogist*, *83*, 1127–1132.

Baldridge, W. S., Beaty, D. W., Hill, S. M. R., and Albee, A. L. (1979), The petrology of the Apollo 12 pigeonite basalt suite, in *Lunar and Planetary Science Conference*, vol. 10, edited by Hinners, N. W., pp. 141–179.

Barra, F., Swindle, T. D., Korotev, R. L., Jolliff, B. L., Zeigler, R. A., and Olson, E. (2006), $^{40}Ar/^{39}Ar$ dating of Apollo 12 regolith: Implications for the age of Copernicus and the source of nonmare materials, *Geochimica et Cosmochimica Acta*, *70*(24), 6016–6031, doi:10.1016/j.gca.2006.09.013.

Barrat, J. A., Chaussidon, M., Bohn, M., Gillet, P., Göpel, C., and Lesourd, M. (2005), Lithium behavior during cooling of a dry basalt: An ion-microprobe study of the lunar meteorite Northwest Africa 479 (NWA 479), *Geochimica et Cosmochimica Acta*, *69*, 5597–5609, doi:10.1016/j.gca.2005.06.032.

Bart, G. D., Nickerson, R. D., Lawder, M. T., and Melosh, H. J. (2011), Global survey of lunar regolith depths from LROC images, *Icarus*, *215*, 485–490, doi:10.1016/j.icarus.2011.07.017.

Beaty, D. W., Hill, S. M. R., Albee, A. L., and Baldridge, W. S. (1979), Apollo 12 feldspathic basalts 12031, 12038 and 12072 - Petrology, comparison and interpretations, in *Lunar and Planetary Science Conference*, vol. 10, edited by Hinners, N. W., pp. 115–139.

Belton, M. J. S., Head, J. W., III, Pieters, C. M., Greeley, R., McEwen, A. S., Neukum, G., Klaasen, K. P., Anger, C. D., Carr, M. H., and Chapman, C. R. (1992), Lunar impact basins and crustal heterogeneity - New western limb and far side data from Galileo, *Science*, *255*, 570–576, doi:10.1126/science.255.5044.570.

Bence, A. E., Papike, J. J., and Prewitt, C. T. (1970), Apollo 12 clinopyroxenes: chemical trends, *Earth and Planetary Science Letters*, *8*, 393–399, doi:10.1016/0012-821X(70)90141-X.

Bence, A. E., Papike, J. J., and Lindsley, D. H. (1971), Crystallization histories of clinopyroxenes in two porphyritic rocks from Oceanus Procellarum, in *Lunar and Planetary Science Conference*, vol. 2, pp. 559–574.

Biggar, G. M., O'Hara, M. J., Peckett, A., and Humphries, D. J. (1971), Lunar lavas and the achondrites: Petrogenesis of protohypersthene basalts in the maria lava lakes, in *Lunar and Planetary Science Conference*, vol. 2, p. 617.

Binder, A. B. (1998), Lunar Prospector: Overview, *Science*, *281*, 1475–1476, doi: 10.1126/science.281.5382.1475.

Blanchard, D. P., and Budahn, J. R. (1979), Remnants from the ancient lunar crust - Clasts from consortium breccia 73255, in *Lunar and Planetary Science Conference*, vol. 10, edited by Hinners, N. W., pp. 803–816.

Bloss, F. D. (1952), Relationship between density and composition in mol percent for some solid solution series, *American Mineralogist*, *37*, 966–981.

Bogard, D. D., Garrison, D. H., Shih, C. Y., and Nyquist, L. E. (1994), 39 Ar- 40 Ar dating of two lunar granites: The age of Copernicus, *Geochimica et Cosmochimica Acta*, *58*, 3093–3100, doi:10.1016/0016-7037(94)90181-3.

Borg, L. E., Connelly, J. N., Boyet, M., and Carlson, R. W. (2011), Chronological evidence that the moon is either young or did not have a global magma ocean, *Nature*, *477*(7362), 70–72, doi:10.1038/nature10328.

Bouchet, M., Kaplan, G., Voudon, A., and Bertoletti, M.-J. (1971), Spark mass spectrometric analysis of major and minor elements in six lunar samples, in *Lunar and Planetary Science Conference*, vol. 2, pp. 1247–1252.

Boyce, J. W., Liu, Y., Rossman, G. R., Guan, Y., Eiler, J. M., Stolper, E. M., and Taylor, L. A. (2010), Lunar apatite with terrestrial volatile abundances, *Nature*, *466*, 466–469, doi:10.1038/nature09274.

Boyd, F. R., and Smith, D. (1971), Compositional zoning in pyroxenes from lunar rock 12021, Oceanus Procellarum., *Journal of Petrology*, *12*, 439–464.

Brett, R., Butler, P., Jr., Meyer, C., Jr., Reid, A. M., Takeda, H., and Williams, R. (1971a), Apollo 12 igneous rocks 12004, 12008, 12009, and 12022: A mineralogical and petrological study, in *Lunar and Planetary Science Conference*, vol. 2, pp. 301–317.

Brett, R., Butler, P., Jr., Meyer, C., Jr., Reid, A. M., Takeda, H., and Williams, R. J. (1971b), Apollo 12 Igneous Rocks 12004, 12008, 12009, and 12022: Metal Grains and their Relation to the Crystallization History, in *Lunar and Planetary Science Conference*, vol. 2, pp. 212–212.

Brown, G. M. (1960), The effect of ion substitution on the unit cell dimensions of the common clinopyroxenes, *American Mineralogist*, *45*, 15–38.

Brown, G. M., Emeleus, C. H., Holland, J. G., Peckett, A., and Phillips, R. (1971), Picrite basalts, ferrobasalts, feldspathic norites, and rhyolites in a strongly fractionated lunar crust, in *Lunar and Planetary Science Conference*, vol. 2, p. 583.

Brunfelt, A. O., Heier, K. S., and Steinnes, E. (1971), Determination of 40 elements in Apollo 12 materials by neutron activation analysis, in *Lunar and Planetary Science Conference*, vol. 2, pp. 1281–1290.

Bunch, T. E., Keil, K., and Prinz, M. (1972), Mineralogy, Petrology and Chemistry of Lunar Rock 12039, *Meteoritics*, *7*, 245.

Busche, F. D., Conrad, G. H., Keil, K., Prinz, M., Bunch, T. E., Erlichman, J., and Quaide, W. L. (1971), Electron microprobe analysis of minerals from Apollo 12 lunar samples, *UNM Institute of Meteoritics*, *Special Pub. No. 3*.

Busche, F. D., Prinz, M., Keil, K., and Bunch, T. E. (1972), Spinels and the petrogenesis of some Apollo 12 igneous rocks, *American Mineralogist*, *57*, 1729–1747.

Butler, P., Jr. (1972), Compositional characteristics of olivines from Apollo 12 samples, *Geochimica et Cosmochimica Acta*, *36*, 773–785, doi:10.1016/0016-7037(72)90087-7.

Butler, P., Jr. (1978), Recognition of lunar glass droplets produced directly from endogenous liquids - The evidence from S-ZN coatings, in *Lunar and Planetary Science Conference*, vol. 9, pp. 1459–1471.

Cahill, J. T., Floss, C., Anand, M., Taylor, L. A., Nazarov, M. A., and Cohen, B. A. (2004), Petrogenesis of lunar highlands meteorites: Dhofar 025, Dhofar 081 Dar al Gani 262, and Dar al Gani 400, *Meteoritics and Planetary Science*, *39*(4), 503–529, doi:10.1111/j.1945-5100.2004.tb00916.x.

Cahill, J. T. S., Lucey, P. G., and Wieczorek, M. A. (2009), Compositional variations of the lunar crust: Results from radiative transfer modeling of central peak spectra, *Journal of Geophysical Research (Planets)*, *114*, E09001, doi:10.1029/2008JE003282.

Cameron, A. G. W. (1997), The Origin of the Moon and the Single Impact Hypothesis V, *Icarus*, *126*, 126–137, doi:10.1006/icar.1996.5642.

Cameron, A. G. W., and Benz, W. (1991), The origin of the moon and the single impact hypothesis. IV, *Icarus*, *92*, 204–216, doi:10.1016/0019-1035(91)90046-V.

Cameron, A. G. W., and Ward, W. R. (1976), The Origin of the Moon, in *Lunar and Planetary Science Conference*, vol. 7, pp. 120–122.

Cameron, E. N. (1971), Opaque minerals in certain lunar rocks from Apollo 12, in *Lunar and Planetary Science Conference*, vol. 2, pp. 193–206.

Canup, R. M. (2004), Simulations of a late lunar-forming impact, *Icarus*, *168*(2), 433–456, doi:10.1016/j.icarus.2003.09.028.

Canup, R. M., and Esposito, L. W. (1996), Accretion of the Moon from an Impact-Generated Disk, *Icarus*, *119*(2), 427–446, doi:10.1006/icar.1996.0028.

Canup, R. M., Levison, H. F., and Stewart, G. R. (1999), Evolution of a Terrestrial Multiple-Moon System, *The Astronomical Journal*, *117*, 603–620, doi:10.1086/300667.

Carpenter, P. K., Zeigler, R. A., Jolliff, B. L., Vicenzi, E. P., Davis, J. M., and Donovan, J. J. (2009a), Advances in Electron-Probe Microanalysis and Compositional Mapping: Applications to Lunar Samples, in *Lunar and Planetary Science Conference*, vol. 40, p. 2531.

Carpenter, P. K., Zeigler, R. A., Jolliff, B. L., Vicenzi, E. P., Davis, J. M., Macrae, C. M., Wilson, N. C., Kotula, P. G., and Donovan, J. J. (2009b), Advances in Electron-Probe Microanalysis and Compositional Mapping: Applications to the Analysis of Meteorites, *Microscopy and Microanalysis*, *15*, 534, doi:10.1017/S1431927609098882.

Carrier, D. W., Olhoeft, G. R., and Mendell, W. (1991), *The Lunar Sourcebook - Physical Properties of the Lunar Surface*, chap. 9, pp. 475–594, Cambridge University Press, Cambridge.

Champness, P. E., Dunham, A. C., Gibb, F. G. F., Giles, H. N., MacKenzie, W. S., Stumpfl, E. F., and Zussman, J. (1971), Mineralogy and petrology of some Apollo 12 lunar samples, in *Lunar and Planetary Science Conference*, vol. 2, pp. 359–376.

Christie, J. M., Lally, J. S., Heuer, A. H., Fisher, R. M., Griggs, D. T., and Radcliffe, S. V. (1971), Comparative electron petrography of Apollo 11, Apollo 12, and terrestrial rocks, in *Lunar and Planetary Science Conference*, vol. 2, pp. 69–89.

Cliff, R. A., Lee-Hu, C., and Wetherill, G. W. (1971), Rb-Sr and U, Th-Pb measurements on Apollo 12 materials, in *Lunar and Planetary Science Conference*, vol. 2, pp. 1493–1502.

Cohen, B. A., Swindle, T. D., and Kring, D. A. (2000), Support for the Lunar Cataclysm Hypothesis from Lunar Meteorite Impact Melt Ages, *Science*, *290*, 1754–1756, doi: 10.1126/science.290.5497.1754.

Cohen, B. A., James, O. B., Taylor, L. A., Nazarov, M. A., and Barsukova, L. D. (2004), Lunar highland meteorite Dhofar 026 and Apollo sample 15418: Two strongly shocked, partially melted, granulitic breccias, *Meteoritics and Planetary Science*, *39*(9), 1419–1447, doi:10.1111/j.1945-5100.2004.tb00120.x.

Compston, W., Chappell, B. W., Arriens, P. A., and Vernon, M. J. (1970), The chemistry and age of Apollo 11 lunar material, *Geochimica et Cosmochimica Acta Supplement*, *1*, 1007.

Compston, W., Berry, H., Vernon, M. J., Chappell, B. W., and Kaye, M. J. (1971), Rubidium-strontium chronology and chemistry of lunar material from the Ocean of Storms, in *Lunar and Planetary Science Conference*, vol. 2, pp. 1471–1485.

Crawford, M. L. (1973), Crystallization of plagioclase in mare basalts, in *Lunar and Planetary Science Conference*, vol. 4, p. 705.

Crozaz, c. d. G., Floss, C., and Wadhwa, M. (2003), Chemical alteration and REE mobilization in meteorites from hot and cold deserts, *Geochimica et Cosmochimica Acta*, *67*, 4727–4741, doi:10.1016/j.gca.2003.08.008.

Cushing, J. A., Taylor, G. J., Norman, M. D., and Keil, K. (1999), The granulitic impactite suite: Impact melts and metamorphic breccias of the early lunar crust, *Meteoritics and Planetary Science*, *34*, 185–195, doi:10.1111/j.1945-5100.1999.tb01745.x.

Cuttitta, F., Rose, H. J., Jr., Annell, C. S., Carron, M. K., Christian, R. P., Dwornik, E. J., Greenland, L. P., Helz, A. W., and Ligon, D. T., Jr. (1971), Elemental composition of some Apollo 12 lunar rocks and soils, in *Lunar and Planetary Science Conference*, vol. 2, p. 1217.

Dasch, E. J., Shih, C.-Y., Bansal, B. M., Wiesmann, H., and Nyquist, L. E. (1987), Isotopic analysis of basaltic fragments from lunar breccia 14321 - Chronology and petrogenesis of pre-Imbrium mare volcanism, *Geochimica et Cosmochimica Acta*, *51*, 3241–3254, doi:10.1016/0016-7037(87)90132-3.

Davis, P. A. (1980), Iron and titanium distribution on the moon from orbital gamma ray spectrometry with implications for crustal evolutionary models, *Journal of Geophysical Research*, *85*, 3209–3224, doi:10.1029/JB085iB06p03209.

Day, J. M. D., Taylor, L. A., Floss, C., Patchen, A. D., Schnare, D. W., and Pearson, D. G. (2006a), Comparative petrology, geochemistry, and petrogenesis of evolved, low-Ti lunar mare basalt meteorites from the LaPaz Icefield, Antarctica, *Geochimica et Cosmochimica Acta*, *70*, 1581–1600, doi:10.1016/j.gca.2005.11.015.

Day, J. M. D., Floss, C., Taylor, L. A., Anand, M., and Patchen, A. D. (2006b), Evolved mare basalt magmatism, high Mg/Fe feldspathic crust, chondritic impactors, and the petrogenesis of Antarctic lunar breccia meteorites Meteorite Hills 01210 and Pecora Escarpment 02007, *Geochimica et Cosmochimica Acta*, *70*(24), 5957–5989, doi:10.1016/j.gca.2006.05.001.

Day, J. M. D., Walker, R. J., James, O. B., and Puchtel, I. S. (2010), Osmium isotope and highly siderophile element systematics of the lunar crust, *Earth and Planetary Science Letters*, *289*, 595–605, doi:10.1016/j.epsl.2009.12.001.

De Hon, R. A. (1979), Thickness of the western mare basalts, in *Lunar and Planetary Science Conference*, vol. 10, edited by Hinners, N. W., pp. 2935–2955.

Deer, W. A., Howie, R. A., and Zussman, J. (1966), *An Introduction to the Rock-Forming Minerals*, Longman, London.

Delano, J. W. (1980), Apollo 15 Red Glass: Chemistry and Liquidus Phase Relations, in *Lunar and Planetary Science Conference*, vol. 11, pp. 210–212.

Delano, J. W. (1986), Pristine lunar glasses - Criteria, data, and implications, *Journal of Geophysical Research*, *91*, 201–213, doi:10.1029/JB091iB04p0D201.

Delano, J. W., and Livi, K. (1981), Lunar volcanic glasses and their constraints on mare petrogenesis, *Geochimica et Cosmochimica Acta*, *45*, 2137–2149, doi:10.1016/0016-7037(81)90066-1.

Demidova, S. I., Nazarov, M. A., Anand, M., and Taylor, L. A. (2003), Lunar regolith breccia Dhofar 287B: A record of lunar volcanism, *Meteoritics and Planetary Science*, *38*, 501–514, doi:10.1111/j.1945-5100.2003.tb00023.x.

Dence, M. R., Douglas, J. A. V., Plant, A. G., and Traill, R. J. (1971), Mineralogy and petrology of some Apollo 12 samples, in *Lunar and Planetary Science Conference*, vol. 2, p. 285.

Dhingra, D., Pieters, C. M., Isaacson, P., Staid, M., Mustard, J., Klima, R., Taylor, L. A., Kramer, G., Nettles, J., and M3 Team (2010), Spectroscopic Signature of the

High Titanium Basalts at Mare Tranquillitatis from Moon Mineralogy Mapper (M3), in *Lunar and Planetary Science Conference*, vol. 41, p. 2494.

Dickinson, T., Taylor, G. J., Keil, K., Schmitt, R. A., Hughes, S. S., and Smith, M. R. (1985), Apollo 14 aluminous mare basalts and their possible relationship to KREEP, *Journal of Geophysical Research*, *90*, C365–C374.

Dickinson, T., Taylor, G. J., and Keil, K. (1989), Germanium abundances in lunar basalts - Evidence of mantle metasomatism?, in *Lunar and Planetary Science Conference*, vol. 19, edited by Ryder, G. and Sharpton, V. L., pp. 189–198.

Dowty, E., Prinz, M., and Keil, K. (1973), Composition, mineralogy, and petrology of 28 mare basalts from Apollo 15 rake samples, in *Lunar and Planetary Science Conference*, vol. 4, pp. 423–444.

Dowty, E., Prinz, M., and Keil, K. (1974), Ferroan anorthosite - A widespread and distinctive lunar rock type, *Earth and Planetary Science Letters*, *24*, 15–25, doi: 10.1016/0012-821X(74)90003-X.

Drever, H. I., Johnston, R., Butler, P., Jr., and Gibb, F. G. F. (1972), Some textures in Apollo 12 lunar igneous rocks and in terrestrial analogs, in *Lunar and Planetary Science Conference*, vol. 3, edited by Metzger, A. E. and Trombka, J. I. and Peterson, L. E. and Reedy, R. C. and Arnold, J. R., pp. 171–184.

Drever, H. I., Johnston, R., and Brebner, G. (1973), Radiate Texture in Lunar Igneous Rocks and Terrestrial Analogs, in *Lunar and Planetary Science Conference*, vol. 4, p. 187.

Duke, M. B., Woo, C. C., Sellers, G. A., Bird, M. L., and Finkelman, R. B. (1970), Genesis of lunar soil at Tranquillity Base, *Geochimica et Cosmochimica Acta Supplement*, *1*, 347–361.

Dungan, M. A., and Brown, R. W. (1977), The petrology of the Apollo 12 ilmenite basalt suite, in *Lunar and Planetary Science Conference*, vol. 8, edited by Merril, R. B., pp. 1339–1381.

Ehmann, W. D., and Morgan, J. W. (1971), Major element abundances in Apollo 12 rocks and fines by 14 MeV neutron activation, in *Lunar and Planetary Science Conference*, vol. 2, pp. 1237–1245.

El Goresy, A., Ramdohr, P., and Taylor, L. A. (1971), The opaque minerals in the lunar rocks from Oceanus Procellarum, in *Lunar and Planetary Science Conference*, vol. 2, p. 219.

Elkins-Tanton, L. T., Chatterjee, N., and Grove, T. L. (2003), Magmatic processes that produced lunar fire fountains, *Geophysical Research Letters*, *30*(10), 1513, doi: 10.1029/2003GL017082.

Elkins-Tanton, L. T., Hager, B. H., and Grove, T. L. (2004), Magmatic effects of the lunar late heavy bombardment, *Earth and Planetary Science Letters*, *222*, 17–27, doi:10.1016/j.epsl.2004.02.017.

Elkins-Tanton, L. T., Burgess, S., and Yin, Q.-Z. (2011), The lunar magma ocean: Reconciling the solidification process with lunar petrology and geochronology, *Earth and Planetary Science Letters*, *304*, 326–336, doi:10.1016/j.epsl.2011.02.004.

Engel, A. E. J., Engel, C. G., Sutton, A. L., and Myers, A. T. (1971), Composition of five Apollo 11 and Apollo 12 rocks and one Apollo 11 soil and some petrogenic considerations, in *Lunar and Planetary Science Conference*, vol. 2, p. 439.

Eugster, O. (2003), Cosmic-ray Exposure Ages of Meteorites and Lunar Rocks and Their Significance, *Chemie der Erde - Geochemistry*, *63*(1), 3–30, doi:10.1078/0009-2819-00021.

Fagan, A. L., Neal, C. R., Simonetti, A., Donohue, P. H., and O'Sullivan, K. M. (2012), Distinguishing between Apollo 14 impact melt and pristine mare basalt samples by geochemical and textural analyses of olivine, *Geochimica et Cosmochimica Acta*, *In review*.

Fagan, T. J., Taylor, G. J., Keil, K., Hicks, T. L., Killgore, M., Bunch, T. E., Wittke, J. H., Mittlefehldt, D. W., Clayton, R. N., Mayeda, T. K., Eugster, O., Lorenzetti, S., and Norman, M. D. (2003), Northwest Africa 773: Lunar origin and iron-enrichment trend, *Meteoritics and Planetary Science*, *38*, 529–554, doi: 10.1111/j.1945-5100.2003.tb00025.x.

Fernandes, V. A., Burgess, R., and Turner, G. (2003), ^{40}Ar-^{39}Ar chronology of lunar meteorites Northwest Africa 032 and 773, *Meteoritics and Planetary Science*, *38*(4), 555–564, doi:10.1111/j.1945-5100.2003.tb00026.x.

Fitzgerald, M. J., and Jones, J. B. (1977), Adelaide and Bench Crater - Members of a new subgroup of the carbonaceous chondrites, *Meteoritics*, *12*, 443–458.

Fruland, R. M., Morris, R. V., McKay, D. S., and Clanton, U. S. (1977), Apollo 17 ropy glasses, in *Lunar and Planetary Science Conference*, vol. 8, edited by Merril, R. B., pp. 3095–3111.

Gallant, J., Gladman, B., and Ćuk, M. (2009), Current bombardment of the Earth-Moon system: Emphasis on cratering asymmetries, *Icarus*, *202*, 371–382, doi: 10.1016/j.icarus.2009.03.025.

Garrick-Bethell, I., Wisdom, J., and Zuber, M. T. (2006), Evidence for a Past High-Eccentricity Lunar Orbit, *Science*, *313*, 652–655, doi:10.1126/science.1128237.

Gast, P., and Hubbard, N. (1970), Rare earth abundances in soil and rocks from the ocean of storms, *Earth and Planetary Science Letters*, *10*(1), 94–100, doi: 10.1016/0012-821X(70)90069-5.

Gault, D. E., Hoerz, F., Brownlee, D. E., and Hartung, J. B. (1974), Mixing of the lunar regolith, in *Lunar and Planetary Science Conference*, vol. 5, pp. 2365–2386.

GEMOC (2002), Glitter software program (Version 4.5), http://www.glitter-gemoc.com/.

Ghiorso, M. S., and Sack, R. O. (1995), Chemical mass transfer in magmatic processes. IV. a revised and internally consistent thermodynamic model for the interpolation and extrapolation of liquid-solid equilibria in magmatic systems at elevated temperatures and pressure, *Contributions to Mineralogy and Petrology*, *119*, 197–212.

Gibb, F. G. F., Stumpfl, E. F., and Zussman, J. (1970), Opaque minerals in an Apollo 12 rock, *Earth and Planetary Science Letters*, *9*, 217, doi:10.1016/0012-821X(70)90031-2.

Giguere, T. A., Taylor, G. J., Hawke, B. R., and Lucey, P. G. (2000), The titanium contents of lunar mare basalts, *Meteoritics and Planetary Science*, *35*, 193–200, doi: 10.1111/j.1945-5100.2000.tb01985.x.

Giguere, T. A., Hawke, B. R., Blewett, D. T., Bussey, D. B. J., Lucey, P. G., Smith, G. A., Spudis, P. D., and Taylor, G. J. (2003), Remote sensing studies of the Lomonosov-Fleming region of the Moon, *Journal of Geophysical Research (Planets)*, *108*, 5118, doi:10.1029/2003JE002069.

Gillis, J. J., Jolliff, B. L., and Elphic, R. C. (2003), A revised algorithm for calculating TiO_2 from Clementine uvvis data: A synthesis of rock, soil, and remotely

sensed TiO_2 concentrations, *Journal of Geophysical Research*, *108*(E2), 5009–5027, doi:10.1029/2001JE001515.

Gillis, J. J., Jolliff, B. L., and Korotev, R. L. (2004), Lunar surface geochemistry: Global concentrations of Th, K, and FeO, *Geochimica et Cosmochimica Acta*, *68*, 3791–3805.

GIMP (2010), The GNU Image Manipulation Program, http://www.gimp.org/.

Gnos, E., Hofmann, B. A., Al-Kathiri, A., Lorenzetti, S., Eugster, O., Whitehouse, M. J., Villa, I. M., Jull, A. J. T., Eikenberg, J., Spettel, B., Krähenbühl, U., Franchi, I. A., and Greenwood, R. C. (2004), Pinpointing the Source of a Lunar Meteorite: Implications for the Evolution of the Moon, *Science*, *305*, 657–660, doi: 10.1126/science.1099397.

Goles, G. G., Duncan, A. R., Lindstrom, D. J., Martin, M. R., Beyer, R. L., Osawa, M., Randle, K., Meek, L. T., Steinborn, T. L., and McKay, S. M. (1971), Analyses of Apollo 12 specimens: Compositional variations, differentiation processes, and lunar soil mixing models, in *Lunar and Planetary Science Conference*, vol. 2, pp. 1063–1081.

Goodrich, C. A., and Keil, K. (1987), Mare basalt and other clasts in Yamato lunar meteorites Y-791197 -82192 and -82193, *National Institute Polar Research Memoirs*, *46*, 56–70.

Green, D. H., Ringwood, A. E., Ware, N. G., Hibberson, W. O., Major, A., and Kiss, E. (1971), Experimental petrology and petrogenesis of Apollo 12 basalts, in *Lunar and Planetary Science Conference*, vol. 2, pp. 601–615.

Greenwood, J. P., Itoh, S., Sakamoto, N., Warren, P., Taylor, L., and Yurimoto, H. (2011), Hydrogen isotope ratios in lunar rocks indicate delivery of cometary water to the Moon, *Nature Geoscience*, *4*, 79–82, doi:10.1038/ngeo1050.

Gross, J., and Treiman, A. H. (2010), New Insights into the Complex History of Lunar Highlands: ALHA 81005 Under Reinvestigation, in *Lunar and Planetary Science Conference*, vol. 41, p. 2180.

Grossman, J. N., Alexander, C. M. O., Wang, J., and Brearley, A. J. (2000), Bleached chondrules: Evidence for widespread aqueous processes on the parent asteroids of ordinary chondrites, *Meteoritics and Planetary Science*, *35*, 467–486, doi: 10.1111/j.1945-5100.2000.tb01429.x.

Grove, T. L., and Krawczynski, M. J. (2009), Lunar Mare Volcanism: Where Did the Magmas Come From?, *Elements*, *5*, 29–34, doi:10:2113/gselements.5.1.29.

Grove, T. L., and Vaniman, D. T. (1978), Experimental petrology of very low ti /VLT/ basalts, in *Mare Crisium: The view from Luna 24*, edited by Merrill, R. B. and Papike, J. J., pp. 445–471, Pergamon Press, New York.

Grove, T. L., Walker, D., Longhi, J., Stolper, E., and Hays, J. F. (1973), Petrology of rock 12002 and origin of picritic basalts at Oceanus Procellarum, in *Lunar and Planetary Science Conference*, vol. 4, pp. 995–1011.

Haggerty, S. E., and Meyer, H. O. A. (1970), Apollo 12: opaque oxides, *Earth and Planetary Science Letters*, *9*, 379, doi:10.1016/0012-821X(70)90001-4.

Haloda, J., Irving, A. J., and Tycova, P. (2005), Lunar meteorite Northeast Africa 001: An anorthositic regolith breccia with mixed highland/mare components, in *36th Annual Lunar and Planetary Science Conference*, vol. 36, p. 1487.

Hartmann, W. K., and Davis, D. R. (1975), Satellite-Sized Planetesimals and Lunar Origin, *Icarus*, *24*(4), 504–515, doi:10.1016/0019-1035(75)90070-6.

Hartmann, W. K., Phillips, R. J., and Taylor, G. J. (Eds.) (1986), *Origin of the Moon.*

Haskin, L., and Warren, P. (1991), *The Lunar Sourcebook - Lunar Chemistry*, chap. 8, pp. 357–474, Cambridge University Press, Cambridge.

Haskin, L. A. (1978), Trace element composition of Luna 24 Crisium VLT basalt, in *Mare Crisium: The view from Luna 24*, edited by Merrill, R. B. and Papike, J. J., pp. 593–611, Pergamon Press, New York.

Haskin, L. A., Allen, R. O., Helmke, P. A., Paster, T. P., Anderson, M. R., Korotev, R. L., and Zweifel, K. A. (1970), Rare-earths and other trace elements in Apollo 11 lunar samples, *Geochimica et Cosmochimica Acta Supplement*, *1*, 1213–1231.

Haskin, L. A., Helmke, P. A., Allen, R. O., Anderson, M. R., Korotev, R. L., and Zweifel, K. A. (1971), Rare-earth elements in Apollo 12 lunar materials, in *Lunar and Planetary Science Conference*, vol. 2, pp. 1307–1317.

Hawke, B. R., and Head, J. W. (1978), Lunar KREEP volcanism - Geologic evidence for history and mode of emplacement, in *Lunar and Planetary Science Conference*, vol. 9, pp. 3285–3309.

Hawke, B. R., Gillis, J. J., Giguere, T. A., Blewett, D. T., Lawrence, D. J., Lucey, P. G., Smith, G. A., Spudis, P. D., and Taylor, G. J. (2005a), Remote sensing and geologic studies of the Balmer-Kapteyn region of the Moon, *Journal of Geophysical Research (Planets)*, *110*, E06004, doi:10.1029/2004JE002383.

Hawke, B. R., Gillis, J. J., Giguere, T. A., Blewett, D. T., Lawrence, D. J., Lucey, P. G., Peterson, C. A., Smith, G. A., Spudis, P. D., and Taylor, G. J. (2005b), The Earliest Mare Basalts, in *36th Annual Lunar and Planetary Science Conference*, vol. 36, edited by Mackwell, S. and Stansbery, E., p. 1642.

Head, J. W. (1974), Lunar dark-mantle deposits - Possible clues to the distribution of early mare deposits, in *Lunar and Planetary Science Conference*, vol. 5, pp. 207–222.

Head, J. W., Murchie, S., Mustard, J. F., Pieters, C. M., Neukum, G., McEwen, A., Greeley, R., Nagel, E., and Belton, M. J. S. (1993), Lunar impact basins: New data for the western limb and far side (Orientale and South Pole-Aitken basins) from the first Galileo flyby, *Journal of Geophysical Research*, *98*, 17,149–17,182, doi: 10.1029/93JE01278.

Head, J. W., III (1976), Lunar volcanism in space and time, *Reviews of Geophysics and Space Physics*, *14*, 265–300, doi:10.1029/RG014i002p00265.

Head, J. W., III, and Wilson, L. (1992), Lunar mare volcanism - Stratigraphy, eruption conditions, and the evolution of secondary crusts, *Geochimica et Cosmochimica Acta*, *56*(6), 2155–2175, doi:10.1016/0016-7037(92)90183-J.

Heiken, G. (1975), Petrology of lunar soils, *Reviews of Geophysics and Space Physics*, *13*, 567–587, doi:10.1029/RG013i004p00567.

Heiken, G. H., McKay, D. S., and Brown, R. W. (1974), Lunar deposits of possible pyroclastic origin, *Geochimica et Cosmochimica Acta*, *38*, 1703–1718, doi:10.1016/0016-7037(74)90187-2.

Herbert, F., Drake, M. J., and Sonett, C. P. (1978), Geophysical and geochemical evolution of the lunar magma ocean, in *Lunar and Planetary Science Conference*, vol. 9, pp. 249–262.

Hess, P. C., and Parmentier, E. M. (1995), A model for the thermal and chemical evolution of the Moon's interior: implications for the onset of mare volcanism, *Earth and Planetary Science Letters*, *134*, 501–514, doi:10.1016/0012-821X(95)00138-3.

Hiesinger, H., and Head, J. W. (2006), *New views of lunar geoscience: An introduction and overview*, vol. 60, chap. 1, pp. 1–83, Mineralogical Society of America, Washington, D.C., doi:10.2138/rmg.2006.60.1.

Hiesinger, H., Jaumann, R., Neukam, G., and Head, J. W. (2000), Ages of mare basalts on the lunar nearside, *Journal of Geophysical Research*, *105*, 29,239–29,276, doi:10.1029/2000JE001244.

Hiesinger, H., Head, J. W., Wolf, U., Jaumann, R., and Neukum, G. (2003), Ages and stratigraphy of mare basalts in Oceanus Procellarum, Mare Nubium, Mare Cognitum, and Mare Insularum, *Journal of Geophysical Research (Planets)*, *108*(E7), 5065, doi:10.1029/2002JE001985.

Hiesinger, H., Head, J. W., Wolf, U., Neukum, G., and Jaumann, R. (2008), Ages of Mare Basalts on the Lunar Nearside: A Synthesis, in *Lunar and Planetary Science Conference*, vol. 39, p. 1269.

Hiesinger, H., Head, J. W., Wolf, U., Jaumann, R., and Neukum, G. (2010), Ages and stratigraphy of lunar mare basalts in Mare Frigoris and other nearside maria based on crater size-frequency distribution measurements, *Journal of Geophysical Research (Planets)*, *115*, E03,003, doi:10.1029/2009JE003380.

Hollister, L. S., Trzcienski, W. E., Jr., Hargraves, R. B., and Kulick, C. G. (1971), Petrogenetic significance of pyroxenes in two Apollo 12 samples, in *Lunar and Planetary Science Conference*, vol. 2, p. 529.

Horn, P., Kirsten, T., and Jessberger, E. K. (1975a), Are there a 12 mare basalts younger than 3.1 b.y. unsuccessful search for a 12 mare basalts with crystallization ages below 3.1 b.y., *Meteoritics*, *10*, 417.

Horn, P., Jessberger, E. K., Kirsten, T., and Richter, H. (1975b), ^{39}Ar-^{40} dating of lunar rocks - Effects of grain size and neutron irradiation, in *Lunar and Planetary Science Conference*, vol. 6, pp. 1563–1591.

Hörz, F., Grieve, R., Heiken, G., Spudis, P., and Binder, A. (1991), *The Lunar Sourcebook - Lunar Surface Processes*, chap. 4, pp. 61–120, Cambridge University Press, Cambridge.

Hubbard, N. J., Jr., C. M., Gast, P. W., and Wiesmann, H. (1971), The composition and derivation of Apollo 12 soils, *Earth and Planetary Science Letters*, *10*(3), 341 – 350, doi:10.1016/0012-821X(71)90040-9.

Hupe, G. (website), Lunar Rock - Home of the Northwest Africa 482 (NWA 482) Lunar Meteorite - last accessed: 2011, http://www.lunarrock.com/.

Ida, S., Canup, R. M., and Stewart, G. R. (1997), Lunar accretion from an impact-generated disk, *Nature*, *389*, 353–357, doi:10.1038/38669.

ImageJ (2011), Developed at the National Institutes of Health, http://rsbweb.nih.gov/ij/.

Irving, A. J., Kuehner, S. M., Korotev, R. L., Rumble, D., III, and Hupé, G. M. (2006), Mafic Granulitic Impactite Northwest Africa 3163: A Unique Meteorite from the Deep Lunar Crust, in *37th Annual Lunar and Planetary Science Conference*, vol. 37, edited by Mackwell, S. and Stansbery, E., p. 1365.

James, O. B., and Flohr, M. K. (1983), Subdivision of the Mg-suite noritic rocks into Mg-gabbronorites and Mg-norites, in *Lunar and Planetary Science Conference*, vol. 13, p. 603.

James, O. B., and Wright, T. L. (1972), Apollo 11 and 12 mare basalts and gabbros: Classification, compositional variations, and possible petrogenetic relations, *Geological Society of America bulletin*, *83*, 2357–2382.

Jolliff, B. (1998), Large-scale separation of K-frac and REEP-frac in the source regions of Apollo impact-melt breccias, and a revised estimate of the KREEP composition, *International Geology Review*, *40*, 916–935.

Jolliff, B. L., Korotev, R. L., and Rockow, K. M. (1998), Geochemistry and petrology of lunar meteorite Queen Alexandra Range 94281, a mixed mare and highland regolith breccia, with special emphasis on very-low-Ti mafic components, *Meteoritics and Planetary Science*, *33*, 581–601, doi:10.1111/j.1945-5100.1998.tb01666.x.

Jolliff, B. L., Floss, C., McCallum, I. S., and Schwartz, J. M. (1999), Geochemistry, petrology, and cooling history of 14161,7373: A plutonic lunar sample with textural evidence of granitic-fraction separation by silicate-liquid immiscibility, *American Mineralogist*, *84*, 821–837.

Jolliff, B. L., Gillis, J. J., Haskin, L. A., Korotev, R. L., and Wieczorek, M. A. (2000), Major lunar crustal terranes: Surface expressions and crust-mantle origins, *Journal of Geophysical Research*, *105*, 4197–4216, doi:10.1029/1999JE001103.

Jolliff, B. L., Korotev, R. L., Zeigler, R. A., and Floss, C. (2003a), Northwest Africa 773: lunar mare breccia with a shallow-formed olivine-cumulate component, inferred very-low-Ti (VLT) heritage, and a KREEP connection, *Geochimica et Cosmochimica Acta*, *67*, 4857–4879.

Jolliff, B. L., Haskin, L. A., Korotev, R. L., Papike, J. J., Shearer, C. K., Pieters, C. M., and Cohen, B. A. (2003b), Scientific expectations from a sample of regolith and rock fragments from the interior of the lunar South Pole-Aitken basin, in *Lunar and Planetary Science Conference*, vol. 34, p. 1989.

Joy, K. H., Crawford, I. A., Downes, H., Russell, S. S., and Kearsley, A. T. (2006), A petrological, mineralogical, and chemical analysis of the lunar mare basalt meteorite LaPaz Icefield 02205, 02224, and 02226, *Meteoritics and Planetary Science*, *41*(7), 1003–1025, doi:10.1111/j.1945-5100.2006.tb00500.x.

Joy, K. H., Crawford, I. A., Anand, M., Greenwood, R. C., Franchi, I. A., and Russell, S. S. (2008), The petrology and geochemistry of Miller Range 05035: A new lunar gabbroic meteorite, *Geochimica et Cosmochimica Acta*, *72*(15), 3822–3844, doi:10.1016/j.gca.2008.04.032.

Joy, K. H., Crawford, I. A., Russell, S. S., and Kearsley, A. T. (2010), Lunar meteorite regolith breccias: An in situ study of impact melt composition using LA-ICP-MS with implications for the composition of the lunar crust, *Meteoritics and Planetary Science*, *45*, 917–946, doi:10.1111/j.1945-5100.2010.01067.x.

Joy, K. H., Kring, D. A., Bogard, D. D., McKay, D. S., and Zolensky, M. E. (2011a), Re-examination of the formation ages of the Apollo 16 regolith breccias, *Geochimica et Cosmochimica Acta*, *75*, 7208–7225, doi:10.1016/j.gca.2011.09.018.

Joy, K. H., Burgess, R., Hinton, R., Fernandes, V. A., Crawford, I. A., Kearsley, A. T., and Irving, A. J. (2011b), Petrogenesis and chronology of lunar meteorite Northwest Africa 4472: A KREEPy regolith breccia from the Moon, *Geochimica et Cosmochimica Acta*, *75*, 2420–2452, doi:10.1016/j.gca.2011.02.018.

Jutzi, M., and Asphaug, E. (2011), Forming the lunar farside highlands by accretion of a companion moon, *Nature*, *476*, 69–72, doi:10.1038/nature10289.

Kallemeyn, G. W., and Warren, P. H. (1983), Compositional implications regarding the lunar origin of the ALHA 81005 meteorite, *Geophysical Research Letters*, *10*(9), 833–836, doi:10.1029/GL010i009p00833.

Karner, J., Papike, J. J., and Shearer, C. K. (2003), Olivine from planetary basalts: Chemical signatures that indicate planetary parentage and those that record igneous setting and process, *American Mineralogist*, *88*(5-6), 806–816.

Karner, J., Papike, J. J., and Shearer, C. K. (2004), Plagioclase from planetary basalts: Chemical signatures that reflect planetary volatile budgets, oxygen fugacity, and styles of igneous differentiation, *American Mineralogist*, *89*(7), 1101–1109.

Keil, K., Prinz, M., and Bunch, T. E. (1971), Mineralogy, petrology, and chemistry of some Apollo 12 samples, in *Lunar and Planetary Science Conference*, vol. 2, pp. 319–341.

Kharkar, D. P., and Turekian, K. K. (1971), Analyses of Apollo 11 and Apollo 12 rocks and soils by neutron activation, in *Lunar and Planetary Science Conference*, vol. 2, pp. 1301–1305.

Kieffer, S. W. (1975), From regolith to rock by shock, *Moon*, *13*, 301–320, doi: 10.1007/BF00567522.

Kiely, C., Greenberg, G., and Kiely, C. J. (2011), A New Look at Lunar Soil Collected from the Sea of Tranquility during the Apollo 11 Mission, *Microscopy and Microanalysis*, *17*, 34–48, doi:10.1017/S1431927610093979.

Klein, C., Jr., Drake, J. C., and Frondel, C. (1971), Mineralogical, petrological, and chemical features of four Apollo 12 lunar microgabbros, in *Lunar and Planetary Science Conference*, vol. 2, pp. 265–284.

Korotev, R. (2005), Lunar geochemistry as told by lunar meteorites, *Chemie der Erde / Geochemistry*, *65*(4), 297–346, doi:10.1016/j.chemer.2005.07.001.

Korotev, R. L. (1994), Compositional Variation in Apollo 16 Impact-Melt Breccias and Inferences for the Geology and Bombardment History of the Central Highlands of the Moon, *Geochimica et Cosmochimica Acta*, *58*, 3931–3969, doi:10.1016/0016-7037(94)90372-7.

Korotev, R. L. (2006), Geochemistry of a unique lunar meteorite from oman, a crystalline impact-melt breccia dominated by magnesian anorthosite, in *37th Annual Lunar and Planetary Science Conference*, vol. 37, p. 1402.

Korotev, R. L. (2012), Dr. Randy Korotev's lunar meteorite website, http://meteorites.wustl.edu/.

Korotev, R. L., and Irving, A. J. (2005), Compositions of three lunar meteorites: Meteorite Hills 01210, Northeast Africa 001, and Northwest Africa 3136, in *36th Annual Lunar and Planetary Science Conference*, vol. 36, p. 1220.

Korotev, R. L., Jolliff, B. L., Zeigler, R. A., Gillis, J. J., and Haskin, L. A. (2003), Feldspathic lunar meteorites and their implications for compositional remote sensing of the lunar surface and the composition of the lunar crust, *Geochimica et Cosmochimica Acta*, *67*(24), 4895–4923, doi:10.1016/j.gca.2003.08.001.

Korotev, R. L., Zeigler, R. A., and Jolliff, B. L. (2006), Feldspathic lunar meteorites Pecora Escarpment 02007 and Dhofar 489: Contamination of the surface of the lunar highlands by post-basin impacts, *Geochimica et Cosmochimica Acta*, *70*, 5935–5956, doi:10.1016/j.gca.2006.09.016.

Korotev, R. L., Zeigler, R. A., Jolliff, B. L., Irving, A. J., and Bunch, T. E. (2009), Compositional and lithological diversity among brecciated lunar meteorites of intermediate iron concentration, *Meteoritics and Planetary Science*, *44*, 1287–1322, doi:10.1111/j.1945-5100.2009.tb01223.x.

Korotev, R. L., Jolliff, B. L., Zeigler, R. A., Seddio, S. M., and Haskin, L. A. (2011), Apollo 12 revisited, *Geochimica et Cosmochimica Acta*, *75*, 1540–1573, doi:10.1016/j.gca.2010.12.018.

Krawczynski, M. J., and Grove, T. L. (2008), Experimental Investigations of fO_2 Control on Apollo 17 Orange Glass Phase Equilibria, in *Lunar and Planetary Science Conference*, vol. 39, p. 1231.

Kushiro, I., and Haramura, H. (1971), Major Element Variation and Possible Source Materials of Apollo 12 Crystalline Rocks, *Science*, *171*, 1235–1237, doi:10.1126/science.171.3977.1235.

Kushiro, I., Nakamura, Y., Kitayama, K., and Akimoto, S.-I. (1971), Petrology of some Apollo 12 crystalline rocks, in *Lunar and Planetary Science Conference*, vol. 2, pp. 481–495.

Lally, J. S., Heuer, A. H., Nord, G. L., and Christie, J. M. (1975), Subsolidus reactions in lunar pyroxenes: An electron petrographic study, *Contributions to Mineralogy and Petrology*, *51*, 263–281, doi:10.1007/BF00372145.

Laul, J. C., Vaniman, D. T., and Papike, J. J. (1978), Chemistry, mineralogy and petrology of seven >1 mm fragments from Mare Crisium, *Geochimica et Cosmochimica Acta Supplement*, *9*, 537–568.

Lawrence, D. J., Feldman, W. C., Barraclough, B. L., Binder, A. B., Elphic, R. C., Maurice, S., and Thomsen, D. R. (1998), Global Elemental Maps of the Moon: The Lunar Prospector Gamma-Ray Spectrometer, *Science*, *281*, 1484, doi: 10.1126/science.281.5382.1484.

Li, L., and Mustard, J. F. (2005), On lateral mixing efficiency of lunar regolith, *Journal of Geophysical Research (Planets)*, *110*, E11002, doi:10.1029/2004JE002295.

Lindstrom, D. J. (1999), Accuracy of rastered-beam analysis (RBA) of lunar breccia clasts by electron microprobe, in *Lunar and Planetary Science Conference*, vol. 30, p. 1917.

Lindstrom, M. M., Lindstrom, D. J., Korotev, R. L., and Haskin, L. A. (1986), Lunar meteorite Yamato-791197: A polymict anorthositic norite breccia, *National Institute Polar Research Memoirs*, *41*, 58–75.

Liu, Y., Floss, C., . Day, J., James, M., Hill, E., and Taylor, L. (2009), Petrogenesis of lunar mare basalt meteorite Miller Range 05035, *Meteoritics and Planetary Science*, *44*, 261–284, doi:10.1111/j.1945-5100.2009.tb00733.x.

Longhi, J. (1992a), Experimental petrology and petrogenesis of mare volcanics, *Geochimica et Cosmochimica Acta*, *56*, 2235–2251, doi:10.1016/0016-7037(92)90186-M.

Longhi, J. (1992b), Origin of picritic green glass magmas by polybaric fractional fusion, in *Lunar and Planetary Science Conference*, vol. 22, edited by Ryder, G. and Sharpton, V. L., pp. 343–353.

Lucey, P. G. (2004), Mineral maps of the Moon, *Geophysical Research Letters*, *31*, L08701, doi:10.1029/2003GL019406.

Lucey, P. G., Blewett, D. T., and Hawke, B. R. (1998), Mapping the FeO and TiO2 content of the lunar surface with multispectral imagery, *Journal of Geophysical Research*, *103*, 3679–3699, doi:10.1029/97JE03019.

Lucey, P. G., Blewett, D. T., and Jolliff, B. L. (2000), Lunar iron and titanium abundance algorithms based on final processing of Clementine ultraviolet-visible images, *Journal of Geophysical Research*, *105*(E8), 20,297–20,306, doi: 10.1029/1999JE001117.

Lucey, P. G., Korotev, R. L., Gillis, J. J., Taylor, L. A., Lawrence, D., Campbell, B. A., Elphic, R., Feldman, B., Hood, L. L., Hunten, D., Mendillo, M., Noble, S., Papike, J. J., Reedy, R. C., Lawson, S., Prettyman, T., Gasnault, O., and Maurice, S. (2006), *Understanding the lunar surface and space-moon interactions*, vol. 60, chap. 2, pp. 83–219, Mineralogical Society of America, Washington, D.C., doi:10.2138/rmg.2006.60.2.

Lunar Sample Preliminary Examination Team (1969), Preliminary Examination of Lunar Samples from Apollo 11, *Science*, *165*, 1211–1227, doi: 10.1126/science.165.3899.1211.

Lunar Sample Preliminary Examination Team (1970a), Preliminary Examination of Lunar Samples from Apollo 12, *Science*, *167*, 1325–1339, doi: 10.1126/science.167.3923.1325.

Lunar Sample Preliminary Examination Team (1970b), Preliminary examination of lunar samples. Apollo 12 preliminary science report 189-216, *Tech. rep.*, National Aeronautics and Space Administration.

Lunar Sample Preliminary Examination Team (1973), Apollo 17 Lunar Samples: Chemical and Petrographic Description, *Science*, *182*(4113), 659–672, doi: 10.1126/science.182.4113.659.

Ma, M.-S., Schmitt, R. A., Taylor, G. J., Warner, R. D., Lange, D. E., and Keil, K. (1978), Chemistry and petrology of Luna 24 lithic fragments and less than 250-micron soils - constraints on the origin of VLT mare basalts, in *Mare Crisium: The view from Luna 24*, edited by Merrill, R. B. and Papike, J. J., pp. 569–592, Pergamon Press, New York.

Marvin, U. B. (1983), The discovery and initial characterization of Allan Hills 81005 - The first lunar meteorite, *Geophysical Research Letters*, *10*(9), 775–778, doi: 10.1029/GL010i009p00775.

Marvin, U. B., and Walker, D. (1985), A transient heating event in the history of a highlands troctolite from Apollo 12 soil 12033, in *Lunar and Planetary Science Conference*, vol. 15, edited by Ryder, G. and Schubert, G., p. 421.

Matsunaga, T., Ohtake, M., Haruyama, J., Ogawa, Y., Nakamura, R., Yokota, Y., Morota, T., Honda, C., Torii, M., Abe, M., Nimura, T., Hiroi, T., Arai, T., Saiki, K., Takeda, H., Hirata, N., Kodama, S., Sugihara, T., Demura, H., Asada, N., Terazono, J., and Otake, H. (2008), Discoveries on the lithology of lunar crater central peaks by SELENE Spectral Profiler, *Geophysical Research Letters*, *35*, L23201, doi: 10.1029/2008GL035868.

Maxwell, J. A., and Wiik, H. B. (1971), Chemical composition of Apollo 12 lunar samples 12004, 12033, 12051 12052 and 12065, *Earth and Planetary Science Letters*, *10*, 285–288, doi:10.1016/0012-821X(71)90032-X.

McCallum, I. S., Domeneghetti, M. C., Schwartz, J. M., Mullen, E. K., Zema, M., Cmara, F., McCammon, C., and Ganguly, J. (2006), Cooling history of lunar mg-suite gabbronorite 76255, troctolite 76535 and stillwater pyroxenite sc-936: The record in exsolution and ordering in pyroxenes, *Geochimica et Cosmochimica Acta*, *70*(24), 6068 – 6078, doi:10.1016/j.gca.2006.08.009.

McCubbin, F. M., Steele, A., Hauri, E. H., Nekvasil, H., Yamashita, S., and Hemley, R. J. (2010), Nominally hydrous magmatism on the Moon, *Proceedings of the National Academy of Science*, *1071*, 11,223–11,228, doi:10.1073/pnas.1006677107.

McGee, P. E., Warner, J. L., and Simonds, C. H. (1977), Introduction to the Apollo collections. Part 1: Lunar igneous rocks, *NASA STI/Recon Technical Report N*, *77*, 22,034.

McGetchin, T. R., Settle, M., and Head, J. W. (1973), Radial thickness variation in impact crater ejecta: Implications for lunar basin deposits, *Earth and Planetary Science Letters*, *20*, 226–236, doi:10.1016/0012-821X(73)90162-3.

McKay, D., Heiken, G., Basu, A., Blanford, G., Simon, S., Reedy, R., French, B. M., and Papike, J. (1991), *The Lunar Sourcebook - The Lunar Regolith*, chap. 7, pp. 285–356, Cambridge University Press, Cambridge.

McKay, D. S., Greenwood, W. R., and Morrison, D. A. (1970), Origin of small lunar particles and breccia from the Apollo 11 site, *Geochimica et Cosmochimica Acta Supplement*, *1*, 673–694.

McKay, D. S., Heiken, G. H., Taylor, R. M., Clanton, U. S., Morrison, D. A., and Ladle, G. H. (1972), Apollo 14 soils: Size distribution and particle types, in *Lunar and Planetary Science Conference*, vol. 3, edited by Metzger, A. E., Trombka, J. I., Peterson, L. E., Reedy, R. C., and Arnold, J. R., pp. 983–994.

McKay, D. S., Fruland, R. M., and Heiken, G. H. (1974), Grain size and the evolution of lunar soils, in *Lunar and Planetary Science Conference*, vol. 5, pp. 887–906.

McKay, D. S., Basu, A., and Waits, G. (1978), Grain size and the evolution of Luna 24 soils, in *Mare Crisium: The view from Luna 24*, edited by Merrill, R. B. and Papike, J. J., pp. 125–136, Pergamon Press, New York.

McKay, D. S., Bogard, D. D., Morris, R. V., Korotev, R. L., and Johnson, P. (1986a), Apollo 16 regolith breccias - Characterization and evidence for early formation in mega-regolith, *Journal of Geophysical Research*, *91*, D277–D303, doi: 10.1029/JB091iB04p0D277.

McKay, G., Wagstaff, J., and Yang, S.-R. (1986b), Clinopyroxene REE distribution coefficients for shergottites The REE content of the Shergotty melt, *Geochimica et Cosmochimica Acta*, *50*, 927–937, doi:10.1016/0016-7037(86)90374-1.

McKinley, J. P., Taylor, G. J., Keil, K., Ma, M.-S., and Schmitt, R. A. (1984), Apollo 16: impact melt sheets, contrasting nature of the Cayley plains and Descartes mountains, and geologic history., *Journal of Geophysical Research*, *89*, B513–B524, doi: 10.1029/JB089iS02p0B513.

McSween, H. Y., Jr. (1976), A new type of chondritic meteorite found in lunar soil, *Earth and Planetary Science Letters*, *31*, 193–199, doi:10.1016/0012-821X(76)90211-9.

Merrill, G. P. (1897), *Rocks, rock-weathering and soils*, Macmillan Company, New York.

Meyer, C. (1978), Ion Microprobe Analyses of Aluminous Lunar Glasses, in *Lunar and Planetary Science Conference*, vol. 9, pp. 738–740.

Meyer, C., Jr., Brett, R., Hubbard, N. J., Morrison, D. A., McKay, D. S., Aitken, F. K., Takeda, H., and Schonfeld, E. (1971), Mineralogy, chemistry, and origin of the KREEP component in soil samples from the Ocean of Storms, in *Lunar and Planetary Science Conference*, vol. 2, p. 393.

Meyer, C., Jr., McKay, D. S., Anderson, D. H., and Butler, P., Jr. (1975), The source of sublimates on the Apollo 15 green and Apollo 17 orange glass samples, in *Lunar and Planetary Science Conference*, vol. 6, pp. 1673–1699.

Meyer, J., Elkins-Tanton, L., and Wisdom, J. (2010), Coupled thermal-orbital evolution of the early Moon, *Icarus*, *208*, 1–10, doi:10.1016/j.icarus.2010.01.029.

Meyer, J., C. (2005), Lunar sample compendium.

Mindat (website), The mineral and locality database - last accessed: 2011, http://www.mindat.org/.

Morota, T., Haruyama, J., Ohtake, M., Matsunaga, T., Honda, C., Yokota, Y., Kimura, J., Ogawa, Y., Hirata, N., Demura, H., Iwasaki, A., Sugihara, T., Saiki, K., Nakamura, R., Kobayashi, S., Ishihara, Y., Takeda, H., and Hiesinger, H. (2011), Timing and characteristics of the latest mare eruption on the Moon, *Earth and Planetary Science Letters*, *302*, 255–266, doi:10.1016/j.epsl.2010.12.028.

Morris, R. V. (1978), In situ reworking (gardening) of the lunar surface - Evidence from the Apollo cores, in *Lunar and Planetary Science Conference*, vol. 9, pp. 1801–1811.

Morrison, G. H., Gerard, J. T., Potter, N. M., Gangadharam, E. V., Rothenberg, A. M., and Burdo, R. A. (1971), Elemental abundances of lunar soil and rocks from Apollo 12, in *Lunar and Planetary Science Conference*, vol. 2, pp. 1169–1185.

Murthy, V., Evensen, N., Jahn, B.-M., and Jr., M. C. (1971), Rb-Sr ages and elemental abundances of K, Rb, Sr, and Ba in samples from the Ocean of Storms, *Geochimica et Cosmochimica Acta*, *35*(11), 1139–1153, doi:10.1016/0016-7037(71)90030-5.

Naney, M. T., Crowl, D. M., and Papike, J. J. (1976), The Apollo 16 drill core - Statistical analysis of glass chemistry and the characterization of a high alumina-silica poor (HASP) glass, in *Lunar and Planetary Science Conference*, vol. 7, edited by Kinsler, D. C., pp. 155–184.

Nazarov, M. A., Ignatenko, K. I., and Shevaleevsky, I. D. (1982), Source of Errors in Defocussed Beam Analysis with the Electron Probe, Revisited, in *Lunar and Planetary Science Conference*, vol. 13, pp. 582–583.

Neal, C. R. (2001), Interior of the Moon: The presence of garnet in the primitive deep lunar mantle, *Journal of Geophysical Research*, *106*, 27,865–27,886, doi: 10.1029/2000JE001386.

Neal, C. R., and Kramer, G. Y. (2006), The petrogenesis of the Apollo 14 high-al mare basalts, *American Mineralogist*, *91*(10), 1521–1535.

Neal, C. R., and Taylor, L. A. (1992), Petrogenesis of mare basalts - A record of lunar volcanism, *Geochimica et Cosmochimica Acta*, *56*(6), 2177–2211, doi:10.1016/0016-7037(92)90184-K.

Neal, C. R., Taylor, L. A., and Lindstrom, M. M. (1988), Apollo 14 mare basalt petrogenesis - assimilation of KREEP-like components by a fractionating magma, in *Lunar and Planetary Science Conference*, vol. 18, pp. 139–153.

Neal, C. R., Taylor, L. A., Schmitt, R. A., Hughes, S. S., and Lindstrom, M. M. (1989), High alumina (HA) and very high potassium (VHK) basalt clasts from Apollo 14 breccias. ii - whole rock geochemistry - further evidence for combined assimilation and fractional crystallization within the lunar crust, in *Lunar and Planetary Science Conference*, vol. 19, pp. 147–161.

Neal, C. R., Hacker, M. D., Snyder, G. A., Taylor, L. A., Liu, Y. G., and Schmitt, R. A. (1994a), Basalt generation at the Apollo 12 site, Part 1: New data, classification, and reevaluation, *Meteoritics*, *29*(3), 334–348.

Neal, C. R., Hacker, M. D., Snyder, G. A., Taylor, L. A., Liu, Y. G., and Schmitt, R. A. (1994b), Basalt generation at the Apollo 12 site, Part 2: Source heterogeneity, multiple melts, and crustal contamination, *Meteoritics*, *29*(3), 349–361.

Nehru, C. E., Warner, R. D., Keil, K., and Taylor, G. J. (1978), Metamorphism of brecciated ANT rocks - Anorthositic troctolite 72559 and norite 78527, in *Lunar and Planetary Science Conference*, vol. 9, pp. 773–788.

Newton, R. C., Anderson, A. T., and Smith, J. V. (1971), Accumulation of olivine in rock 12040 and other basaltic fragments in the light of analysis and syntheses, in *Lunar and Planetary Science Conference*, vol. 2, p. 575.

Nielsen, R. L., and Drake, M. J. (1978), The case for at least three mare basalt magmas at the Luna 24 landing site, in *Mare Crisium: The view from Luna 24*, edited by Merrill, R. B. and Papike, J. J., pp. 419–428, Pergamon Press, New York.

Norman, M. D. (2009), The Lunar Cataclysm: Reality or "Mythconception"?, *Elements*, *5*, 23–28, doi:10:2113/gselements.5.1.23.

Norman, M. D., Borg, L. E., Nyquist, L. E., and Bogard, D. D. (2003), Chronology, geochemistry, and petrology of a ferroan noritic anorthosite clast from Descartes breccia 67215: Clues to the age, origin, structure, and impact history of the lunar crust, *Meteoritics and Planetary Science*, *38*, 645–661, doi:10.1111/j.1945-5100.2003.tb00031.x.

Nyquist, L., Bogard, D., Yamaguchi, A., Shih, C.-Y., Karouji, Y., Ebihara, M., Reese, Y., Garrison, D., McKay, G., and Takeda, H. (2006), Feldspathic clasts

in Yamato-86032: Remnants of the lunar crust with implications for its formation and impact history, *Geochimica et Cosmochimica Acta*, *70*, 5990–6015, doi: 10.1016/j.gca.2006.07.042.

Nyquist, L. E., and Shih, C.-Y. (1992), The isotopic record of lunar volcanism, *Geochimica et Cosmochimica Acta*, *56*, 2213–2234, doi:10.1016/0016-7037(92)90185-L.

Nyquist, L. E., Bansal, B. M., Wooden, J. L., and Wiesmann, H. (1977), Sr-isotopic constraints on the petrogenesis of Apollo 12 mare basalts, in *Lunar and Planetary Science Conference*, vol. 8, edited by Merril, R. B., pp. 1383–1415.

Nyquist, L. E., Shih, C.-Y., Wooden, J. L., Bansal, B. M., and Wiesmann, H. (1979), The Sr and Nd isotopic record of Apollo 12 basalts - implications for lunar geochemical evolution, in *Lunar and Planetary Science Conference*, vol. 10, pp. 77–114.

Nyquist, L. E., Wooden, J. L., Shih, C.-Y., Wiesmann, H., and Bansal, B. M. (1981), Isotopic and REE studies of lunar basalt 12038 - Implications for petrogenesis of aluminous mare basalts, *Earth and Planetary Science Letters*, *55*, 335–355, doi: 10.1016/0012-821X(81)90162-X.

Nyquist, L. E., Shih, C.-Y., Reese, Y. D., Park, J., Bogard, D. D., Garrison, D. H., and Yamaguchi, A. (2011), Sm-Nd and Ar-Ar Studies of Dho 908 and 489: Implications for Lunar Crustal History, in *Lunar and Planetary Science Conference*, vol. 42, p. 2368.

O'Sullivan, K. M., and Neal, C. R. (2008), Insights to the Petrogenesis of Apollo 12 Basalts from Crystal Size Distributions and Mineral Geochemistry, in *Lunar and Planetary Science Conference*, vol. 39, p. 1537.

O'Sullivan, K. M., and Neal, C. R. (2010a), Petrogenesis of Apollo 12 Basalts 12031 and 12038, in *Lunar and Planetary Science Conference*, vol. 41, p. 2307.

O'Sullivan, K. M., and Neal, C. R. (2010b), Exploring the Petrogenesis of Apollo 12 Ilmenite Suite Basalts, in *Lunar and Planetary Science Conference*, vol. 41, p. 2322.

O'Sullivan, K. M., Neal, C. R., and Simonetti, A. (2011), Crystal Stratigraphy of Apollo 12 Basalts, in *Lunar and Planetary Science Conference*, vol. 42, p. 2172.

O'Sullivan, K. M., Neal, C. R., and Simonetti, A. (2012), A Crystal Stratigraphy Approach to Understanding Melt Evolution in the Apollo 12 Ilmenite Suite Basalts, in *Lunar and Planetary Science Conference*, vol. 43, p. 2431.

Oxford Instruments (2006), INCAEnergy (Version 4.08), http://www.oxinst.com/.

Papanastassiou, D. A., and Wasserburg, G. J. (1970), Rb-Sr ages from the Ocean of Storms, *Earth and Planetary Science Letters*, *8*(4), 269–278, doi:10.1016/0012-821X(70)90111-1.

Papanastassiou, D. A., and Wasserburg, G. J. (1971a), Lunar chronology and evolution from Rb-Sr studies of Apollo 11 and 12 samples, *Earth and Planetary Science Letters*, *11*, 37–62, doi:10.1016/0012-821X(71)90139-7.

Papanastassiou, D. A., and Wasserburg, G. J. (1971b), Rb-Sr ages of igneous rocks from the Apollo 14 mission and the age of the Fra Mauro formation, *Earth and Planetary Science Letters*, *12*(1), 36–48, doi:10.1016/0012-821X(71)90052-5.

Papike, J. J., and Vaniman, D. T. (1978a), Luna 24 ferrobasalts and the mare basalt suite - Comparative chemistry, mineralogy, and petrology, in *Mare Crisium: The view from Luna 24*, edited by Merrill, R. B. and Papike, J. J., pp. 371–401.

Papike, J. J., and Vaniman, D. T. (1978b), The lunar mare basalt suite, *Geophysical Research Letters*, *5*, 433–436, doi:10.1029/GL005i006p00433.

Papike, J. J., Hodges, F. N., Bence, A. E., Cameron, M., and Rhodes, J. M. (1976), Mare basalts - Crystal chemistry, mineralogy, and petrology, *Reviews of Geophysics and Space Physics*, *14*, 475–540, doi:10.1029/RG014i004p00475.

Papike, J. J., Taylor, L., and Simon, S. (1991), *The Lunar Sourcebook - Lunar Minerals*, chap. 5, pp. 121–181, Cambridge University Press, Cambridge.

Papike, J. J., Ryder, G., and Shearer, C. K. (1998), *Lunar samples*, vol. 36, pp. 5.1–5234, Mineralogical Society of America, Washington, D.C.

Papike, J. J., Karner, J. M., and Shearer, C. K. (2003), Determination of Planetary Basalt Parentage: A Simple Technique Using the Electron Microprobe, in *Lunar and Planetary Science Conference*, vol. 34, edited by Mackwell, S. and Stansbery, E., p. 1018.

Pearce, N. J., Perkins, W. T., Westgate, J. A., Gorton, M. P., Jackson, S. E., Neal, C. R., and Chenery, S. P. (1997), A compilation of new and published major and trace element data for NIST SRM 610 and NIST SRM 612 glass reference materials, *Geostandards and Geoanalytical Research*, *21*(1), 115–144, doi:10.1111/j.1751-908X.1997.tb00538.x.

Peckett, A., and Brown, G. M. (1973), Plutonic or Metamorphic Equilibration in Apollo 16 Lunar Pyroxenes, *Nature*, *242*(5395), 252–255, doi:10.1038/242252a0.

Petro, N. E., and Pieters, C. M. (2007), Foreign Material in the Lunar Regolith: Lateral Transport by Post-Basin Cratering, in *Lunar and Planetary Science Conference*, vol. 38, p. 2069.

Philpotts, J. A., and Schnetzler, C. C. (1970), Apollo 11 lunar samples: K, Rb, Sr, Ba and rare-earth concentrations in some rocks and separated phases, *Geochimica et Cosmochimica Acta Supplement*, *1*, 1471–1486.

Pieters, C., McCord, T. B., Zisk, S., and Adams, J. B. (1973), Lunar Black Spots and Nature of the Apollo 17 Landing Area, *Journal of Geophysical Research*, *78*, 5867–5875, doi:10.1029/JB078i026p05867.

Pieters, C., McCord, T. B., Charette, M. P., and Adams, J. B. (1974), Lunar Surface: Identification of the Dark Mantling Material in the Apollo 17 Soil Samples, *Science*, *183*, 1191–1194, doi:10.1126/science.183.4130.1191.

Pieters, C. M., Sunshine, J. M., Fischer, E. M., Murchie, S. L., Belton, M., McEwen, A., Gaddis, L., Greeley, R., Neukum, G., Jaumann, R., and Hoffmann, H. (1993), Crustal diversity of the Moon: Compositional analyses of Galileo solid state imaging data, *Journal of Geophysical Research*, *98*, 17,127–17,148, doi:10.1029/93JE01221.

Pieters, C. M., Tompkins, S., Head, J. W., and Hess, P. C. (1997), Mineralogy of the mafic anomaly in the South Pole-Aitken Basin: Implications for excavation of the lunar mantle, *Geophysical Research Letters*, *24*, 1903–1906, doi:10.1029/97GL01718.

Pieters, C. M., Gaddis, L., Jolliff, B., and Duke, M. (2001), Rock types of South Pole-Aitken basin and extent of basaltic volcanism, *Journal of Geophysical Research*, *106*, 28,001–28,022, doi:10.1029/2000JE001414.

Pieters, C. M., Boardman, J., Buratti, B., Clark, R., Combe, J. P., Green, R., Goswami, J. N., Head, J. W., Hicks, M., Isaacson, P., Klima, R., Kramer, G., Kumar, K., Lundeen, S., Malaret, E., McCord, T. B., Mustard, J., Nettles, J., Petro, N., Runyon, C., Staid, M., Sunshine, J., Taylor, L. A., Thaisen, K., Tompkins, S., and Varanasi, P. (2010), Identification of a New Spinel-rich Lunar Rock Type by the Moon Mineralogy Mapper (M3), in *Lunar and Planetary Science Conference*, vol. 41, p. 1854.

Pieters, C. M., Besse, S., Boardman, J., Buratti, B., Cheek, L., Clark, R. N., Combe, J. P., Dhingra, D., Goswami, J. N., Green, R. O., Head, J. W., Isaacson, P., Klima,

R., Kramer, G., Lundeen, S., Malaret, E., McCord, T., Mustard, J., Nettles, J., Petro, N., Runyon, C., Staid, M., Sunshine, J., Taylor, L. A., Thaisen, K., Tompkins, S., and Whitten, J. (2011), Mg-spinel lithology: A new rock type on the lunar farside, *Journal of Geophysical Research (Planets)*, *116*, E00G08, doi:10.1029/2010JE003727.

Prettyman, T. H., Hagerty, J. J., Elphic, R. C., Feldman, W. C., Lawrence, D. J., McKinney, G. W., and Vaniman, D. T. (2006), Elemental composition of the lunar surface: Analysis of gamma ray spectroscopy data from Lunar Prospector, *Journal of Geophysical Research (Planets)*, *111*, E12007, doi:10.1029/2005JE002656.

Quaide, W., and Oberbeck, V. (1975), Development of the mare regolith - Some model considerations, *Moon*, *13*, 27–55, doi:10.1007/BF00567506.

Quick, J. E., Albee, A. L., Ma, M.-S., Murali, A. V., and Schmitt, R. A. (1977), Chemical compositions and possible immiscibility of two silicate melts in 12013, in *Lunar and Planetary Science Conference*, vol. 8, edited by Merril, R. B., pp. 2153–2189.

Reid, J. B., Jr. (1971), Apollo 12 spinels as petrogenetic indicators, *Earth and Planetary Science Letters*, *10*, 351–356, doi:10.1016/0012-821X(71)90041-0.

Reufer, A., Meier, M. M. M., Benz, W., and Wieler, R. (2012), A hit-and-run giant impact scenario, *Icarus*, *221*, 296–299, doi:10.1016/j.icarus.2012.07.021.

Rhodes, J. M. (1977), Some compositional aspects of lunar regolith evolution, *Royal Society of London Philosophical Transactions Series A*, *285*, 293–301, doi:10.1098/rsta.1977.0068.

Rhodes, J. M., Wiesmann, H., Rodgers, K. V., Brannon, J. C., Bansal, B. M., and Hubbard, N. J. (1976), Chemistry, classification, and petrogenesis of Apollo 17 mare basalts, in *Lunar and Planetary Science Conference*, vol. 7, edited by Kinsler, D. C., pp. 1467–1489.

Rhodes, J. M., Brannon, J. C., Rodgers, K. V., Blanchard, D. P., and Dungan, M. A. (1977), Chemistry of Apollo 12 mare basalts - Magma types and fractionation processes, in *Lunar and Planetary Science Conference*, vol. 8, edited by Merril, R. B., pp. 1305–1338.

Righter, K., Collins, S. J., and Brandon, A. D. (2005), Mineralogy and petrology of the LaPaz Icefield lunar mare basaltic meteorites, *Meteoritics and Planetary Science*, *40*, 1703–1722, doi:10.1111/j.1945-5100.2005.tb00139.x.

Ringwood, A. E., and Essene, E. (1970), Petrogenesis of Lunar Basalts and the Internal Constitution and Origin of the Moon, *Science*, *167*(3918), 607–610, doi: 10.1126/science.167.3918.607.

Ringwood, A. E., and Kesson, S. E. (1976), A dynamic model for mare basalt petrogenesis, in *Lunar and Planetary Science Conference*, vol. 7, edited by Kinsler, D. C., pp. 1697–1722.

Robinson, K. L., and Treiman, A. H. (2010), Mare Basalt Fragments in Lunar Highlands Meteorites: Connecting Measured Ti Abundances with Orbital Remote Sensing, in *Lunar and Planetary Science Conference Abstracts*, vol. 41, p. 1788.

Rubin, A. E., Scott, E. R. D., and Keil, K. (1997), Shock metamorphism of enstatite chondrites, *Geochimica et Cosmochimica Acta*, *61*, 847–858, doi:10.1016/S0016-7037(96)00364-X.

Russell, S. S., Zolensky, M., Righter, K., Folco, L., Jones, R., Connolly, H. C., Jr., Grady, M. M., and Grossman, J. N. (2005), The Meteoritical Bulletin, No. 89, 2005 September, *Meteoritics and Planetary Science*, *40*(9), 201–263, doi:10.1111/j.1945-5100.2005.tb00425.x.

Saal, A. E., Hauri, E. H., Cascio, M. L., van Orman, J. A., Rutherford, M. C., and Cooper, R. F. (2008), Volatile content of lunar volcanic glasses and the presence of water in the Moon's interior, *Nature*, *454*, 192–195, doi:10.1038/nature07047.

Schnare, D. W., Day, J. M. D., Norman, M. D., Liu, Y., and Taylor, L. A. (2008), A laser-ablation ICP-MS study of Apollo 15 low-titanium olivine-normative and quartz-normative mare basalts, *Geochimica et Cosmochimica Acta*, *72*, 2556–2572, doi:10.1016/j.gca.2008.02.021.

Schnetzler, C. C., and Philpotts, J. A. (1971), Alkali, alkaline earth and rare-earth element concentrations in some Apollo 12 soils, rocks, and separated phases, in *Lunar and Planetary Science Conference*, vol. 2, pp. 1101–1122.

Schonfeld, E., and Bielefeld, M. J. (1978), Correlation of dark mantle deposits with high Mg/Al ratios, in *Lunar and Planetary Science Conference*, vol. 9, pp. 3037–3048.

Schultz, P. H., and Spudis, P. D. (1979), Evidence for ancient mare volcanism, in *Lunar and Planetary Science Conference*, vol. 10, edited by Hinners, N. W., pp. 2899–2918.

Schultz, P. H., and Spudis, P. D. (1983), Beginning and end of lunar mare volcanism, *Nature*, *302*(5905), 233–236, doi:10.1038/302233a0.

Score, R., and Mason, B. (1983), ALHA 81005, *Antarctic Meteorite Newsletter*, *6*, 11.

Shearer, C. K., and Papike, J. J. (1999), Magmatic evolution of the Moon, *American Mineralogist*, *84*(10), 1469–1494.

Shearer, C. K., and Papike, J. J. (2005), Early crustal building processes on the moon: Models for the petrogenesis of the magnesian suite, *Geochimica et Cosmochimica Acta*, *69*, 3445–3461, doi:10.1016/j.gca.2005.02.025.

Shearer, C. K., Papike, J. J., Simon, S. B., and Shimizu, N. (1989), An ion microprobe study of the intra-crystalline behavior of REE and selected trace elements in pyroxene from mare basalts with different cooling and crystallization histories, *Geochimica et Cosmochimica Acta*, *53*, 1041–1054, doi:10.1016/0016-7037(89)90209-3.

Shearer, C. K., Hess, P. C., Wieczorek, M. A., Pritchard, M. E., Parmentier, E. M., Borg, L. E., Longhi, J., Elkins-Tanton, L. T., Neal, C. R., Antonenko, I., Canup, R. M., Halliday, A. N., Grove, T. L., Hager, B. H., Lee, D. C., and Wiechert, U. (2006), *Thermal and magmatic evolution of the moon*, vol. 60, chap. 4, pp. 365–518, Mineralogical Society of America, Washington, D.C., doi:10.2138/rmg.2006.60.4.

Shervais, J. W., and McGee, J. J. (1999), KREEP cumulates in the western lunar highlands: Ion and electron microprobe study of alkali-suite anorthosite and norites from Apollo 12 and 14, *American Mineralogist*, *84*, 806–820.

Shervais, J. W., Taylor, L. A., and Lindstrom, M. M. (1985), Apollo 14 mare basalts: Petrology and geochemistry of clasts from consortium breccia 14321, *Journal of Geophysical Research*, *90*, 375.

Shih, C.-Y., Nyquist, L. E., Reese, Y., Wiesmann, H., Nazarov, M. A., and Taylor, L. A. (2002), The Chronology and Petrogenesis of the Mare Basalt Clast from Lunar Meteorite Dhofar 287: Rb-Sr and Sm-Nd Isotopic Studies, in *Lunar and Planetary Science Conference Abstracts*, vol. 33, p. 1344.

Shkuratov, Y. G., and Bondarenko, N. V. (2001), Regolith layer thickness mapping of the moon by radar and optical data, *Icarus*, *149*(2), 329–338, doi:10.1006/icar.2000.6545.

Simon, S. B., and Papike, J. J. (1985), Petrology of the Apollo 12 Highland Component, in *Lunar and Planetary Science Conference*, vol. 16, pp. 781–782.

Simpson, P. R., and Bowie, S. H. U. (1971), Opaque phases in Apollo 12 samples, in *Lunar and Planetary Science Conference*, vol. 2, pp. 207–218.

Smales, A. A., Mapper, D., Webb, M. S. W., Webster, R. K., Wilson, J. D., and Hislop, J. S. (1971), Elemental composition of lunar surface material (Part 2), in *Lunar and Planetary Science Conference*, vol. 2, pp. 1253–1258.

Snape, J. F., Joy, K. H., and Crawford, I. A. (2011a), Characterization of multiple lithologies within the lunar feldspathic regolith breccia meteorite Northeast Africa 001, *Meteoritics and Planetary Science*, *46*, 1288–1312, doi:10.1111/j.1945-5100.2011.01230.x.

Snape, J. F., Beaumont, S., Burgess, R., Crawford, I. A., and Joy, K. H. (2011b), An evaluation of techniques used in the age and petrologic analysis of Apollo 12 basalts, in *Lunar and Planetary Science Conference*, vol. 42, p. 2011.

Snape, J. F., Crawford, I. A., Joy, K. H., and Burgess, R. (2011c), A petrographic study of basalt fragments in Apollo regolith sample 12003, in *Lunar and Planetary Science Conference*, vol. 42, p. 2020.

Snyder, G. A., Taylor, L. A., and Halliday, A. N. (1995), Chronology and petrogenesis of the lunar highlands alkali suite: Cumulates from KREEP basalt crystallization, *Geochimica et Cosmochimica Acta*, *59*, 1185–1203, doi:10.1016/0016-7037(95)00034-W.

Snyder, G. A., Neal, C. R., Taylor, L. A., and Halliday, A. N. (1997), Anatexis of lunar cumulate mantle in time and space: Clues from trace-element, strontium, and neodymium isotopic chemistry of parental Apollo 12 basalts, *Geochimica et Cosmochimica Acta*, *61*, 2731–2747, doi:10.1016/S0016-7037(97)00082-3.

Sokol, A. K., Fernandes, V. A., Schulz, T., Bischoff, A., Burgess, R., Clayton, R. N., Münker, C., Nishiizumi, K., Palme, H., Schultz, L., Weckwerth, G., Mezger, K., and Horstmann, M. (2008), Geochemistry, petrology and ages of the lunar meteorites Kalahari 008 and 009: New constraints on early lunar evolution, *Geochimica et Cosmochimica Acta*, *72*, 4845–4873, doi:10.1016/j.gca.2008.07.012.

Spera, F. J. (1992), Lunar magma transport phenomena, *Geochimica et Cosmochimica Acta*, *56*, 2253–2265, doi:10.1016/0016-7037(92)90187-N.

Spudis, P. D., Zellner, N. E. B., Delano, J. W., Whittet, D. C. B., and Fessler, B. (2002), Petrologic Mapping of the Moon: A New Approach, in *Lunar and Planetary Science Conference Abstracts*, vol. 33, p. 1104.

Stettler, A., Eberhardt, P., Geiss, J., Grögler, N., and Maurer, P. (1973), Ar^{39}-Ar^{40} ages and Ar^{37}-Ar^{38} exposure ages of lunar rocks, in *Lunar and Planetary Science Conference*, vol. 4, pp. 1865–1888.

Stöffler, D., and Ryder, G. (2001), Stratigraphy and Isotope Ages of Lunar Geologic Units: Chronological Standard for the Inner Solar System, *Space Science Reviews*, *96*, 9–54.

Stöffler, D., Knoell, H.-D., and Maerz, U. (1979), Terrestrial and lunar impact breccias and the classification of lunar highland rocks, in *Lunar and Planetary Science Conference*, vol. 10, edited by Hinners, N. W., pp. 639–675.

Stöffler, D., Keil, K., and Scott, E. R. D. (1991), Shock metamorphism of ordinary chondrites, *Geochimica et Cosmochimica Acta*, *55*, 3845–3867, doi:10.1016/0016-7037(91)90078-J.

Sutton, R. L., and Schaber, G. G. (1971), Lunar locations and orientations of rock samples from Apollo missions 11 and 12, in *Lunar and Planetary Science Conference*, vol. 2, pp. 17–26.

Takeda, H., Yamaguchi, A., Bogard, D. D., Karouji, Y., Ebihara, M., Ohtake, M., Saiki, K., and Arai, T. (2006), Magnesian anorthosites and a deep crustal rock from the farside crust of the moon, *Earth and Planetary Science Letters*, *247*, 171–184, doi:10.1016/j.epsl.2006.04.004.

Takeda, H., Arai, T., Yamaguchi, A., Otuki, M., and Ishii, T. (2007), Mineralogy of Dhofar 309, 489, and Yamato-86032 and Varieties of Lithologies of the Lunar Farside Crust, in *Lunar and Planetary Science Conference Abstracts*, vol. 38, p. 1607.

Taylor, G., Warren, P., Ryder, G., Delano, J., Pieters, C., and Lofgren, G. (1991), *The Lunar Sourcebook - Lunar Rocks*, chap. 6, pp. 183–284, Cambridge University Press, Cambridge.

Taylor, G. J., Martel, L. M. V., and Spudis, P. D. (2012), The Hadley-Apennine KREEP basalt igneous province, *Meteoritics and Planetary Science*, *47*, 861–879, doi:10.1111/j.1945-5100.2012.01364.x.

Taylor, J. G. (2009), Ancient Lunar Crust: Origin, Composition, and Implications, *Elements*, *5*, 17–22, doi:10:2113/gselements.5.1.17.

Taylor, L. A., Kullerud, G., and Bryan, W. B. (1971a), Opaque mineralogy and textural features of Apollo 12 samples and a comparison with Apollo 11 rocks, in *Lunar and Planetary Science Conference*, vol. 2, p. 855.

Taylor, L. A., Shervais, J. W., Hunter, R. H., Shih, C.-Y., Bansal, B. M., Wooden, J., Nyquist, L. E., and Laul, L. C. (1983), Pre-4.2 AE mare-basalt volcanism in the lunar highlands, *Earth and Planetary Science Letters*, *66*, 33–47, doi:10.1016/0012-821X(83)90124-3.

Taylor, S. R. (1982), *Planetary science: A lunar perspective*, *Research supported by NASA. Houston, TX, Lunar and Planetary Institute, 1982, 502 p.*, vol. 38.

Taylor, S. R., and Bence, A. E. (1975), Trace Element Characteristics of the Mare Basalt Source Region: Implications of the Cumulate Versus Primitive Source Model, *LPI Contributions*, *234*, 159–163.

Taylor, S. R., and Jakes, P. (1974), The geochemical evolution of the moon, in *Lunar and Planetary Science Conference*, vol. 5, pp. 1287–1305.

Taylor, S. R., Rudowski, R., Muir, P., Graham, A., and Kaye, M. (1971b), Trace element chemistry of lunar samples from the Ocean of Storms, in *Lunar and Planetary Science Conference*, vol. 2, pp. 1083–1099.

Taylor, S. R., Taylor, G. J., and Taylor, L. A. (2006), The Moon: A Taylor perspective, *Geochimica et Cosmochimica Acta*, *70*, 5904–5918, doi:10.1016/j.gca.2006.06.262.

Taylor, S. R., Pieters, C. M., and MacPherson, G. J. (2006), *Earth-Moon System, Planetary Science, and Lessons Learned*, vol. 60, chap. 7, pp. 657–704, Mineralogical Society of America, Washington, D.C., doi:10.2138/rmg.2006.60.7.

Terada, K., Anand, M., Sokol, A. K., Bischoff, A., and Sano, Y. (2007), Cryptomare magmatism 4.35Gyr ago recorded in lunar meteorite Kalahari 009, *Nature*, *450*(7171), 849–852, doi:10.1038/nature06356.

Touma, J., and Wisdom, J. (1998), Resonances in the Early Evolution of the Earth-Moon System, *The Astronomical Journal*, *115*, 1653–1663, doi:10.1086/300312.

Treiman, A. H. (1996), The perils of partition: Difficulties in retrieving magma compositions from chemically equilibrated basaltic meteorites, *Geochimica et Cosmochimica Acta*, *60*(1), 147–155, doi:10.1016/0016-7037(95)00393-2.

Turner, G. (1970a), ^{40}Ar-^{39}Ar age determination of lunar rock 12013, *Earth and Planetary Science Letters*, *9*(2), 177 – 180, doi:10.1016/0012-821X(70)90049-X.

Turner, G. (1970b), Argon-40/Argon-39 dating of lunar rock samples, *Geochimica et Cosmochimica Acta Supplement*, *1*, 1665–1684.

Turner, G. (1971), ^{40}Ar-^{39}Ar ages from the lunar maria, *Earth and Planetary Science Letters*, *11*(15), 169 – 191, doi:10.1016/0012-821X(71)90161-0.

Unruh, D. M., Stille, P., Patchett, P. J., and Tatsumoto, M. (1984), Lu-Hf and Sm-Nd evolution in lunar mare basalts., *Journal of Geophysical Research*, *89*, 459, doi:10.1029/JB089iS02p0B459.

USGS (2009), Basalt, Columbia River, BCR-2 - U.S. Geological Survey Certificate of Analysis, http://minerals.cr.usgs.gov/geo_chem_stand/basaltbcr2.html.

Vaniman, D., Dietrich, J., Taylor, G., and Heiken, G. (1991), *The Lunar Sourcebook - Exploration, Samples, and Recent Concepts of The Moon*, chap. 2, pp. 5–26, Cambridge University Press.

Wakita, H., and Schmitt, R. A. (1971), Bulk elemental composition of Apollo 12 samples: Five igneous and one breccia rocks and four soils, in *Lunar and Planetary Science Conference*, vol. 2, pp. 1231–1236.

Wakita, H., Rey, P., and Schmitt, R. A. (1971), Abundances of the 14 rare-earth elements and 12 other trace elements in Apollo 12 samples: Five igneous and one breccia rocks and four soils, in *Lunar and Planetary Science Conference*, vol. 2, p. 1319.

Walker, D., Longhi, J., and Hays, J. F. (1972), Experimental petrology and origin of Fra Mauro rocks and soil, in *Lunar and Planetary Science Conference*, vol. 3, p. 797.

Walker, D., Kirkpatrick, R. J., Longhi, J., and Hays, J. F. (1976a), Crystallization history of lunar picritic basalt sample 12002 - Phase-equilibria and cooling-rate studies, *Geological Society of America Bulletin*, *87*, 646–656.

Walker, D., Hays, J. F., Longhi, J., and Kirkpatrick, R. J. (1976b), Differentiation of an Apollo 12 picrite magma, in *Lunar and Planetary Science Conference*, vol. 7, edited by Kinsler, D. C., pp. 1365–1389.

Walker, D., Lasaga, A. C., Stolper, E. M., Hays, J. F., Longhi, J., and Grove, T. L. (1977), Slowly cooled microgabbros 15555 and 15065, in *Lunar and Planetary Science Conference*, vol. 8, edited by Merril, R. B., pp. 1521–1547.

Wänke, H., Wlotzka, F., Baddenhausen, H., Balacescu, A., Spettel, B., Teschke, F., Jagoutz, E., Kruse, H., Quijano-Rico, M., and Rieder, R. (1971), Apollo 12 samples: Chemical composition and its relation to sample locations and exposure ages, the two-component origin of the various soil samples and studies on lunar metallic particles, in *Lunar and Planetary Science Conference*, vol. 2, pp. 1187–1208.

Warner, J. (1970), Apollo 12 lunar sample information., *NASA Tech. Rep., NASA-TR–353*, *353*.

Warner, J. L. (1971), Lunar crystalline rocks: Petrology and geology, in *Lunar and Planetary Science Conference*, vol. 2, pp. 469–480.

Warren, P. H. (1985), The magma ocean concept and lunar evolution, *Annual Review of Earth and Planetary Sciences*, *13*, 201–240, doi: 10.1146/annurev.ea.13.050185.001221.

Warren, P. H. (1989), *KREEP: Major-Element Diversity, Trace-Element Uniformity (Almost)*, pp. 149–153, Lunar and Planetary Institute, Houston, TX.

Warren, P. H. (1993), A Concise Compilation of Petrologic Information on Possibly Pristine Nonmare Moon Rocks, *American Mineralogist*, *78*(3-4), 360–376.

Warren, P. H. (1994), Lunar and martian meteorite delivery services, *Icarus*, *111*, 338–363, doi:10.1006/icar.1994.1149.

Warren, P. H. (1997), The Unequal Host-Phase Density Effect in Electron Probe Defocused Beam Analysis: an Easily Correctable Problem, in *Lunar and Planetary Science Conference Abstracts*, vol. 28, p. 1497.

Warren, P. H., and Kallemeyn, G. W. (1991a), The MacAlpine Hills lunar meteorite and implications of the lunar meteorites collectively for the composition and origin of the moon, *Geochimica et Cosmochimica Acta*, *55*, 3123–3138, doi:10.1016/0016-7037(91)90477-M.

Warren, P. H., and Kallemeyn, G. W. (1991b), Geochemical investigation of five lunar meteorites: Implications for the composition, origin and evolution of the lunar crust, *Antarctic Meteorite Research*, *4*, 91–117.

Warren, P. H., and Kallemeyn, G. W. (1993), Geochemical investigation of two lunar mare meteorites: Yamato-793169 and Asuka-881757, *Antarctic Meteorite Research*, *6*, 35–57.

Warren, P. H., and Wasson, J. T. (1977), Pristine nonmare rocks and the nature of the lunar crust, in *Lunar and Planetary Science Conference*, vol. 8, edited by Merril, R. B., pp. 2215–2235.

Warren, P. H., and Wasson, J. T. (1979), The origin of KREEP, *Reviews of Geophysics and Space Physics*, *17*, 73–88, doi:10.1029/RG017i001p00073.

Warren, P. H., Shirley, D. N., and Kallemeyn, G. W. (1986), A Potpourri of Pristine Moon Rocks, Including a VHK Mare Basalt and a Unique, Augite-rich Apollo 17 Anorthosite, *J. Geophys. Res.*, *91*(B4), D319–D330.

Wasson, J. T., and Baedecker, P. A. (1972), Provenance of Apollo 12 KREEP, in *Lunar and Planetary Science Conference*, vol. 3, edited by Metzger, A. E., Trombka, J. I., Peterson, L. E., Reedy, R. C., and Arnold, J. R., p. 1315.

Wasson, J. T., Warren, P. H., Kallemeyn, G. W., McEwing, C. E., Mittlefehldt, D. W., and Boynton, W. V. (1977), SCCRV, a major component of highlands rocks, in *Lunar and Planetary Science Conference*, vol. 8, edited by Merril, R. B., pp. 2237–2252.

Webmineral (website), Mineralogy Database - last accessed: 2011, http://webmineral.com/.

Weider, S. Z., Crawford, I. A., and Joy, K. H. (2010), Individual lava flow thicknesses in Oceanus Procellarum and Mare Serenitatis determined from Clementine multispectral data, *Icarus*, *209*(2), 323 – 336, doi:10.1016/j.icarus.2010.05.010.

Weill, D. F., Grieve, R. A., McCallum, I. S., and Bottinga, Y. (1971), Mineralogy-petrology of lunar samples. Microprobe studies of samples 12021 and 12022; viscosity of melts of selected lunar compositions, in *Lunar and Planetary Science Conference*, vol. 2, pp. 413–430.

Wentworth, S., Taylor, G. J., Warner, R. D., Keil, K., Ma, M.-S., and Schmitt, R. A. (1979), The unique nature of Apollo 17 VLT mare basalts, in *Lunar and Planetary Science Conference*, vol. 10, edited by Hinners, N. W., pp. 207–223.

Wentworth, S. J., McKay, D. S., Lindstrom, D. J., Basu, A., Martinez, R. R., Bogard, D. D., and Garrison, D. H. (1994), Apollo 12 ropy glasses revisited, *Meteoritics*, *29*, 323–333.

Wetherill, G. W. (1980), Formation of the terrestrial planets, *Annual Review of Astronomy and Astrophysics*, *18*, 77–113, doi:10.1146/annurev.aa.18.090180.000453.

Whitford-Stark, J. L., and Head, J. W. (1980), Stratigraphy of Oceanus Procellarum basalts - Sources and styles of emplacement, *Journal of Geophysical Research*, *85*, 6579–6609, doi:10.1029/JB085iB11p06579.

Wieczorek, M. A., and Zuber, M. T. (2001), The composition and origin of the lunar crust: Constraints from central peaks and crustal thickness modeling, *Geophysical Research Letters*, *28*, 4023–4026, doi:10.1029/2001GL012918.

Wieczorek, M. A., Phillips, R. J., Korotev, R. L., Jolliff, B. L., and Haskin, L. A. (1999), Geophysical Evidence for the Existence of the Lunar "Procellarum KREEP Terrane", in *Lunar and Planetary Science Conference Abstracts*, vol. 30, p. 1548.

Wieczorek, M. A., Jolliff, B. L., Khan, A., Pritchard, M. E., Weiss, B. P., Williams, J. G., Hood, L. L., Righter, K., Neal, C. R., Shearer, C. K., McCallum, I. S., Tompkins, S., Hawke, B. R., Peterson, C., Gillis, J. J., and Bussey, B. (2006), *The constitution and structure of the lunar interior*, vol. 60, chap. 3, pp. 221–364, Mineralogical Society of America, Washington, D.C., doi:10.2138/rmg.2006.60.3.

Willis, J. P., Ahrens, L. H., Danchin, R. V., Erlank, A. J., Gurney, J. J., Hofmeyr, P. K., McCarthy, T. S., and Orren, M. J. (1971), Some interelement relationships between lunar rocks and fines, and stony meteorites, in *Lunar and Planetary Science Conference*, vol. 2, pp. 1123–1138.

Willis, J. P., Erlank, A. J., Gurney, J. J., Theil, R. H., and Ahrens, L. H. (1972), Major, minor, and trace element data for some Apollo 11, 12, 14 and 15 samples, in *Lunar and Planetary Science Conference*, vol. 3, edited by Metzger, A. E. and Trombka, J. I. and Peterson, L. E. and Reedy, R. C. and Arnold, J. R., pp. 1269–1273.

Wood, J. A., Dickey, J. S., Jr., Marvin, U. B., and Powell, B. N. (1970a), Lunar anorthosites and a geophysical model of the moon, *Geochimica et Cosmochimica Acta Supplement*, *1*, 965–988.

Wood, J. A., Dickey, J. S., Jr., Marvin, U. B., and Powell, B. N. (1970b), Lunar Anorthosites, *Science*, *167*, 602–604, doi:10.1126/science.167.3918.602.

Wu, Y., Xue, B., Zhao, B., Lucey, P., Chen, J., Xu, X., Li, C., and Ouyang, Z. (2012), Global estimates of lunar iron and titanium contents from the Chang' E-1 IIM data, *Journal of Geophysical Research (Planets)*, *117*, E02001, doi:10.1029/2011JE003879.

Yamaguchi, A., Karouji, Y., Takeda, H., Nyquist, L., Bogard, D., Ebihara, M., Shih, C.-Y., Reese, Y., Garrison, D., Park, J., and McKay, G. (2010), The variety of lithologies in the Yamato-86032 lunar meteorite: Implications for formation processes of the lunar crust, *Geochimica et Cosmochimica Acta*, *74*, 4507–4530.

Yan, B., Xiong, S. Q., Wu, Y., Wang, Z., Dong, L., Gan, F., Yang, S., and Wang, R. (2012), Mapping Lunar global chemical composition from Chang'E-1 IIM data, *Planetary and Space Science*, *67*, 119–129, doi:10.1016/j.pss.2012.03.010.

Yanai, K., and Kojima, H. (1985), Yamato-82193 Meteorite: The Third Lunar Meteorite Collected at the Yamato Mountains, Antarctica, *Meteoritics*, *20*, 790–791.

Yanai, K., and Kojima, H. (1991), Varieties of lunar meteorites recovered from Antarctica, *Antarctic Meteorite Research*, *4*, 70–90.

Yanai, K., Kojima, H., and Katsushima, T. (1984), Lunar Meteorites in Japanese Collection of the Yamato Meteorites, *Meteoritics*, *19*, 342.

Zeigler, R. A., Korotev, R. L., Haskin, L. A., Jolliff, B. L., and Gillis, J. J. (2006), Petrography and geochemistry of five new Apollo 16 mare basalts and evidence for post-basin deposition of basaltic material at the site, *Meteoritics and Planetary Science*, *41*(2), 263–284, doi:10.1111/j.1945-5100.2006.tb00209.x.

Zhang, A.-C., Hsu, W.-B., Floss, C., Li, X.-H., Li, Q.-L., Liu, Y., and Taylor, L. A. (2010), Petrogenesis of lunar meteorite Northwest Africa 2977: Constraints from in situ microprobe results, *Meteoritics and Planetary Science*, *45*, 1929–1947, doi: 10.1111/j.1945-5100.2010.01131.x.